

European School for Advanced Studies
in Reduction of Seismic Risk

Research Report No. ROSE-2008/0X

**Seismic design of torsionally eccentric
buildings with U-shaped RC Walls**

by

Katrin Beyer

Doctoral Student, ROSE School, Pavia, Italy

Alessandro Dazio

Professor, ETH Zürich, Switzerland

M. J. Nigel Priestley

Co-Director, ROSE School, Pavia, Italy

ROSE School
c/o EUCENTRE
Via Ferrata 1, 27100 Pavia, Italy

December 2007

ABSTRACT

The objective of this report is to make a contribution to the performance-based seismic design of RC buildings with U-shaped walls. Since U-shaped walls are often placed at the perimeter of a building and are typically stiffer and stronger than other lateral strength providing structural elements, many of these buildings possess in-plan strength and stiffness eccentricities and are therefore prone to damage due to twist-induced displacements. The report focuses on two aspects of the design of such buildings for which the knowledge state was judged unsatisfactory. These are: (i) the inelastic behaviour of U-shaped walls under different directions of seismic loading and (ii) the estimation of displacement demands on structural elements in torsionally eccentric buildings.

Although U-shaped walls are frequently used structural elements, only relatively little research has been carried out on their inelastic behaviour. One reason for the restricted research efforts were most likely the scarce experimental evidence – previous to this project only one test series on a single configuration of a U-shaped wall had been carried out. This project aimed at improving the situation by testing two U-shaped walls under a quasi-static cyclic, bi-directional loading regime. The two test units were analysed using plastic hinge models and wide-column models. From the comparison with the experimental results, modelling guidelines for U-shaped walls were developed. The experimental results showed that shear deformations of U-shaped walls can be significantly larger than those of rectangular walls. To model the overall stiffness of the U-shaped wall correctly, appropriate assumptions regarding the shear stiffness of such walls are required. Since existing equations failed to predict the shear stiffnesses of U-shaped walls with adequate accuracy, a new empirical equation was derived from the experimental data of 29 quasi-static cyclic tests of RC walls with rectangular, barbelled, flanged and U-shaped sections.

Modern seismic design approaches focus on displacements rather than force demands. One of the most completely developed approaches that uses displacements and drifts as target parameters in the design process is the direct displacement-based design method, which was developed by Priestley and his co-workers. However, at present, this approach cannot be applied to structures that are asymmetric in plan. In this report the torsional response of inelastic structural wall buildings is investigated and a semi-empirical method for estimating the twist-induced displacements developed. The method can be used to extend the application of the direct

displacement-based design approach to the class of torsionally restrained structures that are asymmetric in-plan but regular over the height.

ACKNOWLEDGEMENTS

The authors would like to acknowledge all researchers who have taken an interest in their research work over the course of the project. The lively discussions on different aspects of seismic behaviour of reinforced concrete structures have provided very valuable insight into various topics of this research. In particular we would like to mention Prof. Hugo Bachmann, Prof. Michael Collins, Prof. Rui Pinho and Prof. José Restrepo. The authors would like to thank especially Prof. Tom Paulay for all his contributions over the past years, in particular regarding the work on torsion presented in this report which is largely based on his original work and ideas.

Mr. Markus Baumann's help and the support of the staff of the structural engineering laboratory at the ETH Zürich were crucial to the successful completion of the experimental work and the authors would like to thank them for their help and dedication.

The experimental part of the project was funded by the ETH Zürich. The first author was awarded a scholarship by the Università degli Studi di Pavia and a research contract by the ETH Zürich. All financial support is gratefully acknowledged.

TABLE OF CONTENTS

ABSTRACT	i
ACKNOWLEDGEMENTS	iii
TABLE OF CONTENTS	iv
LIST OF TABLES	xiii
LIST OF FIGURES	xvii
NOTATION	xxxi
1. INTRODUCTION	1
1.1. Problem statement	3
1.2. Objectives and scope of the study	3
1.3. Outline of report	4
2. LITERATURE REVIEW ON DIFFERENT MODELLING APPROACHES FOR U-SHAPED WALLS	7
2.1. Lumped plasticity models	8
2.1.1. Force-displacement characterisation	8
2.1.2. Yield curvature	10
2.1.3. Plastic hinge length	11
2.2. Stick models	15

2.3. Wide-column models	17
2.3.1. Historical development of WCMs	17
2.3.2. Advantages of WCMs for today's analyses of structural walls	17
2.3.3. Drawbacks of WCMs with linear-elastic properties	19
2.3.4. Studies on WCMs of U-shaped walls with elastic properties	23
2.3.5. WCMs with inelastic properties	23
2.4. Shell element models	24
2.4.1. Shell elements	24
2.4.2. Material models	25
2.4.3. Comparison with experimental results	26
2.5. Defining the ultimate limit state	27
2.5.1. Ultimate concrete strain limit	27
2.5.2. Ultimate reinforcement strain limit	29
2.5.3. Shear capacity as a function of ductility demand	31
2.6. Literature review on estimates for shear deformations	34
3. QUASI-STATIC CYCLIC TESTS OF TWO U-SHAPED WALLS.....	39
3.1. Previous experimental work on U-shaped walls: Tests in Ispra and Saclay	40
3.2. Experimental program	42
3.3. Test setup, loading history and instrumentation	46
3.4. Design of test units	51

3.4.1. Flexural design	51
3.4.2. Shear design	52
3.4.3. Detailing	56
3.5. Experimental results: Failure mechanisms	56
3.5.1. TUA	57
3.5.2. TUB	61
3.6. Experimental results: Force-displacement hysteresees	64
3.6.1. Cycles with $\mu_{\Delta} = 4.0$	65
3.6.2. Cycles in the EW, NS and diagonal directions	68
3.7. Summary of the experimental work	71
4. COMPARISON OF PREDICTED QUANTITIES USED IN PLASTIC HINGE ANALYSIS WITH EXPERIMENTAL RESULTS	75
4.1. Yield curvatures	75
4.2. Strain limits	78
4.2.1. Ultimate concrete strain	79
4.2.2. Longitudinal bar buckling and fracture	81
4.3. Plastic hinge lengths	83
4.3.1. Predicted values of plastic hinge lengths	83
4.3.2. Experimentally determined values of the plastic hinge lengths	84
4.3.3. Comparison of analytical and experimental values	85

4.4. Shear deformations of TUA and TUB	88
4.4.1. Determining the different displacement components	89
4.4.2. Experimentally derived ratios of Δ_s/Δ_f for TUA and TUB.	92
4.4.3. Predicting the shear deformations of TUA and TUB with existing methods	97
4.5. Summary and Conclusions	98
5. SHEAR DEFORMATIONS OF REINFORCED CONCRETE WALLS	101
5.1. An empirical investigation into shear displacements of RC walls	101
5.1.1. Variation of the ratios Δ_s/Δ_f with ductility demand	102
5.1.2. Making the ratios Δ_s/Δ_f of different walls comparable	106
5.1.3. Effect of shear stresses on shear deformations	107
5.1.4. Effect of axial strains: Coupling of shear and flexural deformations	110
5.1.5. An empirical relationship for the ratio Δ_s/Δ_f	113
5.2. Numerical modelling of shear displacements	117
5.2.1. Introduction to the Modified Compression Field Theory	118
5.2.2. VecTor2: A shell element analysis program based on the MCFT	120
5.2.3. Response2000: A section analysis program based on the MCFT	128
5.2.4. Discussion of the numerical results	133
5.3. Summary and conclusions	135
6. NUMERICAL MODELS OF TUA AND TUB	137
6.1. Plastic hinge analysis of TUA and TUB	137

6.1.1. Moment-curvature relationships	138
6.1.2. Force-displacement relationships	142
6.1.3. Moment capacities	153
6.1.4. Summary of findings from plastic hinge analysis	155
6.2. Wide-column models	156
6.2.1. Description of the reference WCM for TUA and TUB	157
6.2.2. Sensitivity of the WCM analysis to the geometry of the model	165
6.2.3. Shear and torsional stiffness of wall elements	173
6.2.4. Link properties	182
6.2.5. Summary of findings and recommendations for properties of WCMs of U-shaped walls	187
6.3. Discussion of results from plastic hinge and wide-column models and outlook on future research	194
7. ACCOUNTING FOR TORSIONAL RESPONSE IN DDBD	195
7.1. Introduction	195
7.1.1. Objectives of this chapter and limitations to the study	197
7.1.2. Layout of this chapter	198
7.2. Literature review on DDBD and torsional response of in-plan asymmetric struc- tures	198
7.2.1. Direct displacement-based design	198
7.2.2. Selected studies describing the torsional response of buildings	199

7.2.3. Simple 2D models and the definition of terms relevant to torsional response	201
7.2.4. Previous studies on torsional response of 2D models	208
7.2.5. Different design approaches for estimating the torsional response	213
7.3. Analysis method applied in this study and earthquake records for dynamic analyses	215
7.3.1. Design spectrum and artificial accelerograms with a corner period of $T_D = 4s$ (Set A)	216
7.3.2. Artificial accelerograms with a corner period of $T_D = 2s$ (Set B)	217
7.3.3. Real records for bi-direction analysis (Set C)	218
7.4. Torsional response of 2D systems	219
7.4.1. TR and TU 2D systems for parametric study	219
7.4.2. Strength eccentricity	224
7.4.3. Effect of the rotational inertia	229
7.4.4. Different seismic intensities	231
7.4.5. Long-period structures ($T_{eff} > T_D$)	235
7.4.6. TR systems with uni- and bi-directional strength and stiffness eccentricities under skew attack	236
7.4.7. Bi-directional input motion	241
7.4.8. Summary of the results from the parametric study on 2D systems	251
7.5. Accounting for torsional response in DDBD	253
7.5.1. Extending the DDBD approach to in-plan asymmetric buildings	253
7.5.2. Examples illustrating the design approach	255

7.6. Summary and recommendations for future research	261
8. SUMMARY, CONCLUSIONS AND OUTLOOK ON FUTURE RESEARCH	265
8.1. Summary	265
8.1.1. Seismic behaviour of U-shaped walls	265
8.1.2. Displacement demands on in-plan asymmetric structures.....	270
8.2. Conclusions	271
8.3. Outlook on future research	274
REFERENCES	277
A. EXPERIMENTALLY DETERMINED RATIOS OF SHEAR TO FLEXURAL DISPLACEMENTS FOR RC WALLS	287
A.1.PCA Tests, Phase I	288
A.2.PCA Tests, Phase II	291
A.3.Tests by Dazio	294
A.4.Tests by Hines	297
A.5.Ispra-Tests on U-shaped walls	300
A.6.Tests of TUA and TUB	300
A.7.Summary of quantities used for the empirical study	301

LIST OF TABLES

2.1	Proportionality factor K_1 for the nominal yield curvature.	11
3.1	U-shaped walls: Comparison of cross sections of TUA, TUB and the units tested in Ispra.	44
3.2	Properties of reinforcing steel used for construction of TUA and TUB.	46
3.3	Predicted nominal and ultimate moment capacities for TUA and TUB.	52
3.4	Nominal and ultimate shear force demands on the web and the critical flange. .	54
3.5	Shear force capacities of the web and the critical flange.	54
3.6	TUA and TUB: Yield displacements and drifts and maximum displacements and drifts for the different directions of loading.	57
4.1	Comparison of predicted, experimental and numerical values for the constant K_1 (Equation 2.7).	78
4.2	Experimental flexural strain values (average strain between $h = 50 - 150$ mm): Maximum tensile, compressive and total excursion strains for different directions of loading.	80
4.3	Comparison of predicted and measured compressive strain values.	81
4.4	Plastic hinge lengths for TUA and TUB according to empirical equations given in Section 2.1.3.	84
4.5	TUA and TUB: Comparison of the ratios of shear to flexural deformations for different methods of evaluating the shear displacements.	97
4.6	Ratios of shear to flexural displacement for TUA and TUB according to Priestley <i>et al.</i> [2007] and Hines <i>et al.</i> [2004].	98

5.1	TUA and TUB: Comparison of the experimentally determined and predicted Δ_s/Δ_f -ratios for the different wall sections (predicted ratios were estimated with Equation 5.9).	115
6.1	Comparison of the curvatures at first yield obtained from experiments and moment-curvature analysis.	141
6.2	Comparison of ratios M_n/M'_y obtained from experiments and moment-curvature analysis.	141
6.3	Comparison of nominal yield curvatures from experiments and moment-curvature analysis.	142
6.4	Comparison of the experimental and analytical flexural top displacements at first yield (excluding the displacement due to strain penetration into the foundation); the analytical displacements were computed for the experimentally determined base curvature.	145
6.5	Comparison of the nominal yield displacements obtained from the experiments and from the section analysis.	146
6.6	Comparison of maximum moments at Positions E and F obtained from the experiments and the section analysis.	154
6.7	Equivalent elastic shear stiffnesses of TUA and TUB in the EW and NS directions for different ductilities levels.	175
7.1	2D parametric study on TR systems: Properties of the walls when designed for zero strength eccentricity.	223
7.2	2D parametric study on TR systems: Properties of the system when designed for zero strength eccentricity.	223
7.3	2D systems with different strength eccentricities.	224
7.4	2D systems with different rotational inertias.	230
7.5	TR system: Displacement demands at zero strength eccentricity for different seismic intensities.	234

7.6	TU system: Displacement demands at zero strength eccentricity for different seismic intensities.	234
A.1	PCA, Phase I: Comparison of ratios of shear to flexural deformations for the different methods of evaluating the shear displacements.	289
A.2	PCA Tests, Phase I: Characteristics of walls [Oesterle <i>et al.</i> , 1976].	290
A.3	PCA, Phase II: Comparison of ratios of shear to flexural deformations for the different methods of evaluating the shear displacements.	291
A.4	PCA Tests, Phase II: Characteristics of walls [Oesterle <i>et al.</i> , 1979].	293
A.5	Dazio: Comparison of ratios of shear to flexural deformations for the different methods of evaluating the shear displacements.	294
A.6	Dazio <i>et al.</i> [1999]: Characteristics of walls WSH ₂ -WSH ₆	296
A.7	Hines: Comparison of ratios of shear to flexural deformations for different methods of evaluating the shear displacements.	298
A.8	Hines: Characteristics of walls with highly-confined boundary elements [Hines <i>et al.</i> , 1999, 2002b].	299
A.9	Ispra: Δ_s/Δ_f -ratios for the different wall sections for different directions of loading (flange labels correspond to those of TUA and TUB).	301
A.10	Summary of experimental and analytical quantities used for the empirical study on the ratio of shear to flexural displacements for RC walls.	303

LIST OF FIGURES

1.1	Cross section of core structures (a-c) and examples of an open (d) and a partially closed core (e); cross section c: Victoria tower block in Mannheim, Germany [Bergmeister and Wörner, 2003].	1
1.2	Seismic response of a RC building with a U-shaped wall.	2
2.1	Plastic hinge analysis: Theoretical curvature distribution due to flexural deformations only, modified distribution accounting for shear spread and strain penetration into the foundation and curvature distribution assumed in plastic hinge analysis (adapted from Priestley and Park [1987]).	9
2.2	Evolution of strains with increasing displacements (a) and geometry of discrete crack model (b); figures from Greifenhagen [2006].	14
2.3	WCMS of coupled wall systems (a), WCMS of non-planar structural walls (b) and the classical wide-column module by MacLeod and Hosny [1977] (c).	18
2.4	Parasitic moment and artificial flexure in conventional wide column frame analogy (a) and examples of modified wide column modules (b); figures adopted from Stafford-Smith and Abate [1981], Stafford-Smith and Girgis [1984] and Kwan [1993].	20
2.5	Incompatibility between beam and wall elements when joint rotations are defined as the horizontal fibre rotations (a) and beam element with vertical rigid arms (b) (after Kwan [1994]).	22
2.6	Ile and Reynouard [2005]: Shell model of the U-shaped wall tested in Ispra (a) and the cyclic material model for concrete (b).	25
2.7	Ile and Reynouard [2005]: Cyclic material model for reinforcing bars.	26
2.8	Shear displacement vs. top displacement for two rectangular walls tested by Dazio <i>et al.</i> [1999] showing the nearly linear relationship between Δ_s and Δ_{top} for peak displacements (adapted from Dazio [2000]).	36

3.1	U-shaped walls tested in Ispra: Cross section (a) and elevation (b); all dimensions are in millimetres.	41
3.2	Test design: Six-storey reference building: Isometric (a) and plan view (b); all dimensions are in metres.	43
3.3	Cross section, shear keys and elevation of TUA (top row) and TUB (bottom row); all dimensions are in millimetres.	45
3.4	Isometric view of the test setup for TUA and TUB.	47
3.5	Photo of the test setup for TUA and TUB.	47
3.6	Cardinal points and labelling of different wall sections (a) and target displacement pattern (b).	48
3.7	Instrumentation of TUA and TUB.	50
3.8	Predicted moment-curvature relationships for TUA and TUB	52
3.9	TUA and TUB: Actual imposed displacement history as seen from the top.	57
3.10	TUA: Longitudinal bars that fractured during the cycles of $\mu_{\Delta} = 8.0$	58
3.11	TUA: Crack pattern towards the end of the test (photos taken at Position A and B during EW cycle with $\mu_{\Delta} = 6.0$): South face (a), West face (b), North face (c) and East face (d).	59
3.12	TUA: West flange end showing the ruptured D12 bars (a) and the lower part of the West flange and the web (b) at Position F during the diagonal cycle with $\mu_{\Delta} = 8.0$ (point of failure).	60
3.13	TUB: Crack pattern towards the end of the test (photos taken at Position B during EW cycle with $\mu_{\Delta} = 6.0$): South face (a), West face (b), North face (c) and East face (d).	62
3.14	TUB: South face (a) and North face (b) at Position B during the sweep at $\mu_{\Delta} = 6.0$ (point of failure).	63

3.15	TUA, $\mu_{\Delta} = 4.0$: Forces applied to flanges and web at different positions.	66
3.16	TUB, $\mu_{\Delta} = 4.0$: Forces applied to flanges and web at different positions.	66
3.17	Qualitative sketch of the forces at Positions E and F (grey patches: concrete area that is according to section analysis in compression).	68
3.18	TUA and TUB: SRSS moment-displacement hysteresis and force-displacement hysteresees of the three actuators for the cycles at $\mu_{\Delta} = 4.0$	69
3.19	TUA: Force-displacement hysteresees for cycles in the EW direction (a+b), in the NS direction (c+d) and in the diagonal direction (e-h).	72
3.20	TUB: Force-displacement hysteresees for cycles in the EW direction (a+b), in the NS direction (c+d) and in the diagonal direction (e-h).	73
4.1	TUA and TUB: Curvature profiles at first yield for the different positions.	77
4.2	TUA and TUB: Comparison of the experimentally derived plastic hinge length due to strain penetration (L_{sp}) to the predicted value $0.022d_b f_y$	86
4.3	TUA and TUB: Comparison of the experimentally derived values for $L_{ph} - L_{sp}$ to values from empirical equations for plastic hinge lengths (excluding the term $0.022d_b f_y$ for strain penetration). The filled and unfilled markers represent values that were computed from plastic displacements according to Equations 4.4a and 4.4b, respectively.	87
4.4	Original method for evaluating the shear displacements: Assumed variation of lengths of diagonals for shear deformations (a), flexural deformations (b) and vertical and horizontal elongation (c).	90
4.5	Modified method by Hiraishi [1984] for evaluating the shear displacements: Assumed variation of lengths of diagonals for shear deformations (a), flexural deformations (b) and vertical and horizontal elongation (c).	91
4.6	TUA: Displacement components for cycles in the EW (a), NS (b) and diagonal (c-e) directions.	93

4.7	TUB: Displacement components for cycles in the EW (a), NS (b) and diagonal (c-e) directions.....	94
4.8	TUA: Average ratios of Δ_s/Δ_f for different directions of loading (shear deformations were determined according to the indirect method).	96
4.9	TUB: Average ratios of Δ_s/Δ_f for different directions of loading (shear deformations were determined according to the indirect method).	96
4.10	TUA and TUB: Comparison of the experimentally determined Δ_s/Δ_f -ratios to the predicted ratios according to Priestley <i>et al.</i> [2007] and Hines <i>et al.</i> [2004].	98
5.1	PCA, Phase I: Variation of the ratio Δ_s/Δ_f with top displacement (a) and displacement ductility (b).	103
5.2	Truss analogy model for a wall element with parallel compression struts (a, adapted from Oesterle <i>et al.</i> [1984]) and Mohr's circle representing the strain state at the centre line of the wall (b, adapted from Rabbat and Collins [1978]).	104
5.3	Shear deformations: The ratio Δ_s/Δ_f as a function of three different shear stress parameters: τ (a), τ/v_n (b) and $(\tau - \tau_P)/v_n$ (c).	108
5.4	Effect of compression zone depth c on the mean axial strain ε_m	110
5.5	Shear deformations: The ratio Δ_s/Δ_f as a function of three different flexural strain parameters: $1 - c/l_w$ (a), $\varepsilon_m/(\tan\theta \cdot \varphi \cdot l_w/2)$ (b) and $\varepsilon_m/(\tan\theta \cdot \varphi \cdot L_{ph})$ (c).	111
5.6	Shear deformations: The ratio Δ_s/Δ_f as a function of the stress parameter $(\tau - \tau_P)/v_n$ and three different flexural strain parameters: $1 - c/l_w$ (a), $\varepsilon_m/(\tan\theta \cdot \varphi \cdot l_w/2)$ (b) and $\varepsilon_m/(\tan\theta \cdot \varphi \cdot L_{ph})$ (c).	114
5.7	Prediction of the shear deformations: Using Equation 5.9 for the entire dataset (a) and comparison of the predictions by Priestley <i>et al.</i> [2007], Hines <i>et al.</i> [2004] and Equation 5.9 for TUA and TUB (b).	116
5.8	Cracking angle θ as a function of the shear stress ratio $(\tau - \tau_P)/v_n$	117
5.9	Prediction of the shear deformation with Equation 5.9 assuming $\theta = 45^\circ$	117

5.10	MCFT: Loading (a), deformation (b), Mohr's circle of average strains (c) and average strains in the cracked element (d); figures from Vecchio and Collins [1986].	119
5.11	WSH ₃ : Cross section (a), instrumentation (b) and finite element mesh and virtual instruments in VecTor2 (c).	121
5.12	WSH ₃ : Comparison of results of cyclic and pushover analyses with VecTor2 to experimental force-displacement hysteresees.	122
5.13	WSH ₃ (cyclic loading), VecTor2 (pushover analysis): Displacement components (a+c) and ratio of shear to flexural displacements (b+d) for shear displacements computed from virtual instruments (first row) and element shear strains (second row); (e) comparison of experimental and numerical ratios of shear to flexural displacements.	125
5.14	WSH ₃ , VecTor2 analysis: Displacement components (a) and ratio of shear to flexural displacements (b) for cyclic analysis; comparison of Δ_s/Δ_f -ratios from pushover analysis and cyclic analysis (c) and comparison of Δ_s/Δ_f -ratios from cyclic analysis to experimentally determined ratios (d).	127
5.15	Test Units B ₃ and B ₄ : Comparison of numerical and experimental force-displacement hysteresees of test unit B ₃ (a); comparison of numerically and experimentally determined ratios of shear to flexural deformations for specimens B ₃ and B ₄ , which were identical in their configuration but were subjected to cyclic and monotonic loading, respectively (b).	129
5.16	Response2000: Clipping of the active shear forces in Response2000 for a simply supported beam (a) and a cantilever wall (b).	130
5.17	Test Unit WSH ₃ : Comparison of Response2000 analysis results to the experimental force-displacement hysteresis.	131
5.18	Test Unit WSH ₃ , Response2000 and VecTor2 analyses: Ratio of shear to flexural displacements obtained experimentally and numerically. For the Response2000 analysis the flexural displacements were computed once with (label 'Response2000') and once without accounting for strain penetration into the foundation (label 'Response2000 (NSP)').	132

5.19	Comparison of ratios of shear to flexural displacements obtained from experiments and Response2000 analysis.	133
6.1	TUA and TUB: Material models for section analysis (a-d, as an example for the concrete materials the stress-strain curves for the flange ends are shown) and the subdivision of the sections into concrete and reinforcement fibres (e and f, the different shades of grey indicate the areas with different concrete properties).	138
6.2	TUA and TUB: Moment-curvature relationships for the five different directions of loading that were examined during the experimental testing.	139
6.3	TUA and TUB: Moment-curvature relationships for bending in the diagonal direction for displacement- and force-controlled pushover analysis (a,b) and orientation of the neutral axes for the two types of analyses (c,d).	143
6.4	TUA and TUB: Comparison of the analytically with the experimentally obtained nominal yield displacements. Two types of different analytical approaches are included in the plot: (i) predicting the single components of the yield displacements and combining these according to Equation 6.2 and (ii) estimating the total displacement from a linear curvature profile (Equation 2.5).	147
6.5	TUA: Comparison of results of pushover analyses to experimental force-displacement hysteresees for loading parallel to the web (a), the flanges (b) and in the diagonal direction (c).	151
6.6	TUB: Comparison of results of pushover analyses to experimental force-displacement hysteresees for loading parallel to the web (a), the flanges (b) and in the diagonal direction (c).	152
6.7	TUB, EW cycle: Comparison of results of pushover analyses to experimental force-displacement hysteresees including the capacity curves for web crushing (Legend: Oe84=Oesterle <i>et al.</i> [1984], PP92=Paulay and Priestley [1992]).	153
6.8	TUA and TUB: First yield and nominal yield moments for all directions of loading.	154
6.9	WCM: Isometric view (a), wide-column model (b), fibre cross sections of TUA (c) and details of collar of WCM where the lateral displacements are imposed (d).	159

6.10	TUA, WCM: Internal forces at Position A at $\mu_{\Delta} = 4.0$; the forces are given in the global coordinate system.....	162
6.11	TUA, WCM with state-of-the-art properties: Comparison of analysis and experimental results for cycles in the EW, NS and diagonal directions (a-c, also included are the results of the pushover analyses of the WCM) and comparison of actuator forces obtained from analysis and experiment during the cycles of $\mu_{\Delta} = 4.0$ (d-f).	163
6.12	TUB, WCM with state-of-the-art properties: Comparison of analysis and experimental results for cycles in the EW, NS and diagonal directions (a-c, also included are the results of the pushover analyses of the WCM) and comparison of actuator forces obtained from analysis and experiment during the cycles of $\mu_{\Delta} = 4.0$ (d-f).	164
6.13	TUA: Different schemes for subdividing the U-shaped section into planar wall sections (all dimensions are in millimetres).....	166
6.14	TUA: Influence of the subdivision of the section on the pushover curves in the EW direction (a) and in the Direction F (b).	166
6.15	TUA: Influence of the subdivision of the section on the hysteresis curves for the diagonal cycles (a) and the force of the NS-W actuator for cycles with $\mu_{\Delta} = 4.0$ (b).....	167
6.16	TUA: Wide-column models with link spacings of 1360mm (a), 680mm (b) and 453mm (c).	168
6.17	TUA: Influence of the spacing of the horizontal links on the pushover curves (a) and the moment distribution (b); as an example the pushover curves for loading in the EW direction (Positions A and B) and the moments in the web at Position A at $\mu_{\Delta} = 4.0$ are plotted.....	169
6.18	TUA: Influence of the spacing of the horizontal links on the hysteresis curves for the diagonal cycles (a) and the force of the NS-W actuator for cycles with $\mu_{\Delta} = 4.0$ (b).	170

- 6.19 TUA, $h_{sp} = 680\text{mm}$: Influence of the number of elements between horizontal links on the pushover curves (a) and the moment distribution (b); as an example the pushover curves for loading in the EW direction (Positions A and B) and the moments in the web at Position A at $\mu_{\Delta} = 4.0$ are plotted (fb=force-based element formulation)..... 172
- 6.20 TUA: Influence of the number of elements between horizontal links on the hysteresis curves for the diagonal cycles (a) and the force of the NS-W actuator for cycles with $\mu_{\Delta} = 4.0$ (b). 172
- 6.21 TUA, Direction A, B: WCMs with different shear stiffnesses (stiffness of uncracked section and equivalent linear-elastic stiffnesses for different ductility levels); pushover curves in the EW direction (a) and ratio of shear to flexural displacements (b). 175
- 6.22 TUA, Direction E: WCMs with different shear stiffnesses (stiffness of uncracked section and equivalent linear-elastic stiffnesses for $\mu_{\Delta} = 4.0$); pushover curves for displacement in the diagonal direction towards Position E (a) and actuator forces (b). 176
- 6.23 TUA, WCM with improved shear stiffness of wall elements: Comparison of analysis and experimental results for cycles in the EW, NS and diagonal directions (a-c); comparison of actuator forces obtained from analysis and experiment during the cycles at $\mu_{\Delta} = 4.0$ (d-f). 177
- 6.24 TUA: Influence of the distribution of the shear flexibility over the wall height (shear flexibility evenly distributed between $h = 0 - 2.72\text{m}$ and shear flexibility concentrated in the plastic hinge zone) on the hysteresis curves for the diagonal cycles (a) and the force in the NS-W actuator for cycles with $\mu_{\Delta} = 4.0$. 179
- 6.25 TUA: Influence of the out-of-plane shear stiffness of the wall elements on the hysteresis curves for the diagonal cycles (a) and the force of the NS-W actuator for cycles with $\mu_{\Delta} = 4.0$ (b). 180

- 6.26 TUA: Influence of the torsional stiffness of the wall and collar elements on the hysteresis curves for the diagonal cycles (a) and the force of the NS-W actuator for cycles with $\mu_{\Delta} = 4.0$ (b). The term "large GK" refers to the torsional stiffness of uncracked, homogenous sections and "small GK" refers to the rotational stiffness of cracked sections (as an approximation the torsional stiffness was reduced by the same ratio as the shear stiffness). 182
- 6.27 TUA: Influence of the torsional stiffness of the wall and collar elements on the actuator forces (a) and the torsional stiffness (b) when the WCM is first subjected to a translation in the Direction D and then to a rotation of the wall head. 183
- 6.28 TUA, Direction E: WCMs with different torsional stiffnesses of the horizontal links: Pushover curves for displacement in the diagonal direction towards Position E (a) and actuator forces (b). 184
- 6.29 TUA: Influence of the torsional stiffnesses of the horizontal links on the hysteresis curves for the diagonal cycles (a) and the force of the NS-W actuator for cycles with $\mu_{\Delta} = 4.0$ (b). 184
- 6.30 TUA: Influence of the shear flexibility of the horizontal links on the hysteresis curves for the diagonal cycles (a) and the force of the NS-W actuator for cycles with $\mu_{\Delta} = 4.0$ (b). 185
- 6.31 TUA: Vertical strain profile of TUA at Position E with $\mu_{\Delta} = 3.0$ (at Position E the West flange end was in compression). The grey lines represent the grid of the Demec measurements, the grey shaded areas the vertical strains and the dashed black lines the best fit linear strain profiles over one wall section. 187
- 6.32 TUA, final WCM with in-plane shear stiffnesses derived from experimentally determined and predicted Δ_s/Δ_f -ratios: Comparison of analysis and experimental results for cycles in the EW, NS and diagonal directions (a-c); comparison of actuator forces obtained from analysis and experiment during the cycles of $\mu_{\Delta} = 4.0$ (d-f). 192

6.33	TUB, final WCM with in-plane shear stiffnesses derived from experimentally determined and predicted Δ_s/Δ_f -ratios: Comparison of analysis and experimental results for cycles in the EW, NS and diagonal directions (a-c); comparison of actuator forces obtained from analysis and experiment during the cycles of $\mu_\Delta = 4.0$ (d-f).	193
7.1	Photo of a RC structure with flat slabs and gravity columns and a very eccentric core structure, which is the only member providing lateral strength (photo by the courtesy of H. Bachmann).	197
7.2	Torsionally unrestrained and torsionally restrained systems: Examples of systems that are for excitation in the x direction classified as TU system (a) and TR system (b).	202
7.3	Maximum displacement profiles if rotational inertia is considered or neglected (a) and example of a system for which the definition of TR or TU is dependent on the direction of excitation (b): Direction 1: TU, direction 2: TR, direction 3: The system is symmetric.	203
7.4	"Balanced CV-CR location criterion" according to Myslimaj and Tso [2002] for the TR system (a) and wall layout for which it might be feasible to satisfy this criterion without excessive reinforcement ratios in the short walls (b). . . .	214
7.5	Acceleration and displacement spectra for the five artificial records of Set A. . . .	217
7.6	Acceleration and displacement spectra for the five artificial records of Set B. . . .	218
7.7	Acceleration (a and b), and displacement spectra (c-f) for the 20 artificial records of Set C. Plots a-d show the geometric mean of the spectral acceleration and the spectral displacement respectively. Plots e and f show the displacement spectra for the horizontal ground motion components in x and z direction. . . .	220
7.8	Approximation of a 3D system by a 2D system with springs and lumped mass: Example of a 3D wall-type structure (a), plan view of the asymmetric system (b), 2D system with springs and lumped mass (c).	221
7.9	TR system for parametric study: Plan layout of floor system (a) and 2D representation of the structure with springs and lumped mass (b).	222

7.10	TU system for parametric study: Plan layout of floor system (a) and 2D representation of the structure with springs and lumped mass (b).	222
7.11	2D systems with strength eccentricity: stiffness and strength eccentricity (a) and element and system strength (b) as a function of the excess strength ratio λ_1	225
7.12	TR system: Displacement demand on CoM, stiff and soft edge (a) and maximum and nominal rotation (b) for different strength eccentricity ratios e_{vz}/b_z	226
7.13	TU system: Displacement demand on CoM (solid line), stiff edge (dashed line) and soft edge (dotted line) (a) and maximum and nominal rotation for different strength eccentricity ratios e_{vz}/b_z (b).	226
7.14	TR system: Comparison of displacement (a) and rotation (b) demand for elastic (grey lines) and inelastic (black lines) systems.	227
7.15	TU system: Comparison of displacement (a) and rotation (b) demand for elastic (grey lines) and inelastic (black lines) systems. For the legend the reader is referred to Figure 7.14.	228
7.16	TR systems with constant base shear: Displacement demand on CoM (solid line), stiff edge (dashed line) and soft edge (dotted line) (a) and maximum and nominal rotation for different values of e_{vz}/b_z (b).	228
7.17	TR system: Comparison of displacement demands on CoM (a) and stiff and soft edges (b) for different values of rotational inertia expressed in terms of r_m/r_0 -ratios.	230
7.18	TU system: Comparison of displacement demands on CoM (a) and stiff and soft edges (b) for different values of rotational inertia expressed in terms of r_m/r_0 -ratios.	230
7.19	TR system: Comparison of displacement (a-c) and ductility (d-f) demands on CoM and stiff and soft edges for different seismic intensities.	232
7.20	TU system: Comparison of displacement (a-c) and ductility (d-f) demands on CoM and stiff and soft edges for different seismic intensities.	233

7.21	TR systems analysed for skew attack with uni-directional strength and stiffness eccentricity (a) and bi-directional strength and stiffness eccentricity (b).	236
7.22	TR systems analysed for skew attack with uni-directional strength and stiffness eccentricity (a) and bi-directional strength and stiffness eccentricity (b).	237
7.23	Skew attack of TR system with uni-directional strength and stiffness eccentricity: Displacement demand in the x direction (a-c) and the z direction (d-f) for different excess strength ratios λ_1	239
7.24	Skew attack of TR system with uni-directional strength and stiffness eccentricity: Maximum (a) and nominal rotation for Wall 1 and 2 (b) for different excess strength ratios λ_1	240
7.25	TR systems with bi-directional strength and stiffness eccentricity: Angle α for which the effective eccentricities are maximum (a) and for which the effective eccentricities diminished (b).	240
7.26	Skew attack of TR system with bi-directional strength and stiffness eccentricity: Displacement demand in the x direction (a-c) and the z direction (d-f) for different excess strength ratios λ_1 and λ_4	242
7.27	Skew attack of TR system with bi-directional strength and stiffness eccentricity: Maximum (a) and nominal rotation for Wall 1 and 2 (b) for different excess strength ratios λ_1 and λ_4	243
7.28	TR system: Analysis with bi-directional (a) and – as an example – analysis with uni-directional excitation for the component in the x direction (b).	243
7.29	TR system: Comparison of analysis results for bi-directional to uni-directional excitation: Examples of records that led to approximately the same (a), a smaller (b), a larger (c) and dependent on the strength eccentricity a larger or a smaller (d) response for bi-directional excitation (black lines) than for uni-directional excitation (grey lines).	244
7.30	TR system: Comparison of bi-directional to uni-directional excitation with respect to the displacement demand in the x direction: Displacement demand on CoM (a-c) and stiff and soft edge (d-f) for $\lambda_1 = 1.0, 1.4$ and 1.8	246

7.31	TR system: Comparison of bi-directional to uni-directional excitation with respect to the displacement demand in the z direction: Displacement demand on CoM (a-c) and Wall 3 and Wall 4 (d-f) for $\lambda_1 = 1.0, 1.4$ and 1.8	247
7.32	TR systems: Plan view of models of set TR Systems 3 (a) and models of set TR Systems 4 (b).	249
7.33	Different TR systems: Comparison of the median bi-directional excitation (black lines) to the median uni-directional excitation (grey lines) with respect to the displacement demand in the x direction (left plots) and in the z direction (right plots).	250
7.34	TR system with different slab lengths b_x : Comparison of analysis results for uni-directional excitation (black lines) to prediction (grey lines).	258
7.35	TR system with constant base shear and different strengths of transverse walls: Comparison of analysis results for uni-directional excitation (black lines) to prediction (grey lines).	259
7.36	TR system with $T_{eff} > T_D$ and different strengths of transverse walls: Comparison of analysis results for uni-directional excitation (black lines) to prediction (grey lines).	260
7.37	Different TR systems: Comparison of analysis results for bi-directional excitation (black lines) to prediction (grey lines).	262
A.1	PCA walls, Phase I: Ratio of shear to flexural displacements as a function of the top displacement if the shear displacements are computed according to the indirect method (a) and the original method (b).	289
A.2	PCA walls, Phase II: Ratio of shear to flexural displacements as a function of the top displacement if the shear displacements are computed according to the indirect method (a) and the original method (b).	292
A.3	Dazio: Ratio of shear to flexural displacements as a function of the top displacement if the shear displacements are computed according to Hiraishi's method (a), the indirect method (b) and the original method (c).	295

A.4 Hines: Ratio of shear to flexural displacements as a function of the top displacement if the shear displacements are computed according to the indirect method (a) and the original method (b).....	298
---	-----

NOTATION

ABBREVIATIONS

EC8	Eurocode 8 (the respective year of publication is given in brackets)
LVDT	Linear Variable Displacement Transformer
MCFT	Modified Compression Field Theory
PHA	Plastic Hinge Analysis
RC	Reinforced Concrete
TUA	Test Unit A
TUB	Test Unit B
WCM	Wide-Column Model

GENERAL NOTATION

Note: Variables that were only used in the literature review sections are defined as they are introduced and are not included in this list.

Capital Latin Letters

A_g	Gross concrete area of a section
A_{sh}	Effective shear area
A_s	Reinforcement area
E	Elastic modulus
EI^I	Flexural stiffness of uncracked section
EI^{II}	Flexural stiffness of cracked section, $EI^{II} = M'_y / \phi'_y$
E_c	Elastic modulus of the concrete
E_s	Elastic modulus of the steel
F_{EW}	Force in EW direction
F_{NS}	Force in NS direction
F'_y	Shear force at first yield
G	Shear modulus
G_c	Shear modulus of the concrete
H	Effective height of a building or height of a wall subjected to a point load at $h = H$
I	Moment of inertia

K	Torsional rigidity (the torsional stiffness is then GK)
K_i	Constants for estimating the yield curvature
K_s	Shear stiffness of test unit
$K_{s,g}$	Shear stiffness of test unit computed for gross sectional properties
$K_{s,\mu_\Delta=x}$	Equivalent elastic shear stiffness computed for $\mu_\Delta = x$
L_{ph}	Plastic hinge length
L_{ph1}, L_{ph2}	Plastic hinge lengths according to Equations 2.10a and 2.10b
$L_{ph3},$	Plastic hinge lengths according to Equations 2.11 and 2.12
$L_{ph3,mod}$	
L_{sp}	Plastic hinge length due to strain penetration into the foundation
L_{spp}	Elastic strain penetration length into the foundation
M	Bending moment (typically at the base of a wall)
M_{EW}	Base moment due to forces in EW direction
M_{NS}	Base moment due to forces in NS direction
M_n	Nominal yield moment
M'_y	First yield moment
M_{SRSS}	SRSS moment at the wall base computed from forces in EW and NS direction (Equation 3.1a)
N	Number of elements per row (FE model)
P	Axial load
V	Shear force
V_c	Shear capacity associated with the shear resistance of the concrete
V_{cr}	Shear force at onset of cracking
V_n	Shear force corresponding to nominal flexural strength
$V_{n,fl}$	Nominal shear force demand on a single flange
$V_{n,web}$	Nominal shear force demand on the web
V_P	Shear capacity associated with an inclined compression strut due to the axial load
V_s	Shear capacity associated with the shear reinforcement
V_{tot}	Total shear capacity, $V_{tot} = V_P + V_c + V_s$
$V_{ult,fl}$	Ultimate shear force demand on a single flange
$V_{ult,web}$	Ultimate shear force demand on the web

Small Latin Letters

b	Width of the shear panel
c	Compression zone depth
d	Length of the diagonal of the shear panel

d_b	Diameter of the main longitudinal reinforcement
f'_c	Cylinder compressive strength of concrete at the day of testing
f_t	Tensile strength of concrete at the day of testing
f_y	Yield strength of longitudinal reinforcement
f_{yh}	Yield strength of horizontal reinforcement
f_u	Ultimate strength of longitudinal reinforcement
h	Height above the base of the wall
h_{cr}	Height over which the wall has cracked
h_i	Height interval covered by the i -th instrument in the LVDT chain
h_{sb}	Height of the shear panel
k_s	Shear stiffness of a vertical element in a wide-column model
h_{sp}	Vertical spacing between horizontal links
l_{el}	Element length
l_{fl}	Length of the flanges of a U-shaped wall
l_{diag}	Length of the diagonal of a U-shaped section, $l_{diag} = \sqrt{l_{fl}^2 + l_{web}^2}$
l_w	Wall length
l_{web}	Length of the web of a U-shaped wall
n	Modular ratio $n = E_s/E_c$
t_w	Wall width (the smallest width if the thickness of the wall varies along the length)
v_n	Shear stress capacity

Capital Greek Letters

Δ_{EW}	Displacement in EW direction
Δ_{NS}	Displacement in NS direction
Δ_f	Flexural displacement (including deformations due to the base rotation)
Δ'_f	Flexural displacement (excluding deformations due to the base rotation)
Δ'_{fy}	Flexural displacement at first yield
Δ_{max}	Maximum attained displacement
Δ'_y	Displacement at first yield
Δ_y	Nominal yield displacement
Δ_{yf}	Flexural displacement at nominal yield
Δ_{top}	Total displacement at the top
Δ_s	Shear displacement
$\Delta_{s1}, \Delta_{s2},$	Shear displacement computed according Hiraishi, the indirect method and the
Δ_{s3}	original method (Section 4.4.1)
Δ_{sl}	Displacement due to sliding at the wall base

Δ_{SRSS}	SRSS displacement of TUA and TUB at $h = 2.95\text{m}$ (Equation 3.1b)
Δ_{θ}	Top displacement due to opening of the joint between wall base and foundation

Small Greek Letters

α	Measure for the variation of the curvature over the height of a shear panel (Equation 4.8)
α	Ratio of cracked to uncracked flexural stiffness, $\alpha = EI^I / EI^I$
δ_i	Variation in length of the diagonal i of the shear panel
δ_{max}	Drift at the maximum attained displacement
$\delta_{NW,i}$	Elongation measured by the i -th instrument of the LVDT chain along edge NW (accordingly for edges NE, SW, SE)
δ_y	Nominal yield drift
ε_c	Maximum compressive strain of a section at the location of a reinforcement bar
ε_{cu}	Ultimate compressive strain capacity of concrete
ε_d	Axial strain in the compression strut ($\varepsilon_d < 0$)
ε_h	Horizontal strain
ε_m	Mean axial strain of a section
ε_s	Maximum tensile strain of a section at the location of a reinforcement bar
ε_{su}	Tensile strain capacity of a reinforcement bar (defined as strain at maximum stress)
ε_{sy}	Yield strain of the longitudinal reinforcement
γ	Shear strain
γ_i	Shear strain within element i (FE model)
$\gamma_{m,0.45}$	Average shear strain of a wall section computed over the central 45% of the wall length
γ_{VW}	Average shear strain of a wall section computed from the principle of virtual work
κ	Ratio of displacements computed for different curvature profiles (Equation 6.3)
μ_{Δ}	Displacement ductility
ν	Poisson's ratio
φ	Curvature of a wall section
φ_b	Base curvature of a wall
φ_y	Yield curvature of a wall section
φ_p	Plastic curvature of a wall section
φ_{ult}	Ultimate curvature of a wall section
ρ_h	Horizontal reinforcement ratio, excluding confinement reinforcement
ρ_{tot}	Total vertical reinforcement ratio

τ	Average shear stress
τ_i	Shear stress within element i (FE model)
τ_P	Shear stress associated with the shear capacity V_P
θ	Rotation of the wall section
θ	Cracking angle measured against the element axis
θ_b	Base curvature measured over the interval $h = 0 - 50\text{mm}$ (TUA and TUB)

ADDITIONAL NOTATION FOR CHAPTER 7

Abbreviations

CoM	Centre of Mass
CR	Centre of Stiffness
CV	Centre of Strength
DDBD	Direct Displacement-Based Design
MDoF	Multi Degree of Freedom
SDoF	Single Degree of Freedom
TR	Torsionally Restrained
TU	Torsionally Unrestrained

Capital Latin Letters

I_{rot}	Rotational inertia
$K_{rot,eff}$	Rotational stiffness about the centre of stiffness based on the secant stiffnesses of the elements
K_{rot}	Rotational stiffness about the centre of stiffness
$K_{rot,CoM}$	Rotational stiffness about the centre of mass
$K_{rot,x}$	Rotational stiffness about the centre of stiffness provided by the elements acting in x -direction
$K_{rot,z}$	Rotational stiffness about the centre of stiffness provided by the elements acting in z -direction
K_x	Translational stiffness of the system in x -direction
K_z	Translational stiffness of the system in z -direction
L_i	Length of the lever arm between element i at the centre of strength
M	Mass
$S_{a,GM}$	Geometric mean of the spectral acceleration of the x component of the ground motion

$S_{d,GM}$	Geometric mean of the spectral displacement of the x component of the ground motion
$S_{d,x}$	Spectral displacement of the x component of the ground motion
$S_{d,z}$	Spectral displacement of the z component of the ground motion
$S_{d,5\%}$	Spectral displacement for 5% viscous damping
$S_{d,\xi}$	Spectral displacement for a viscous damping of ξ
T_C	Corner period of the spectrum
T_{eff}	Effective period of the system
T_0	Uncoupled translational period of the system
$V_{n,xs}$	Nominal base shear of the system in x -direction
$V_{n,xi}$	Nominal base shear of wall i in x -direction
$V_{n,zs}$	Nominal base shear of the system in z -direction
$V_{n,zi}$	Nominal base shear of wall i in z -direction
$V_{rot,x}$	Rotational strength provided by the elements acting in x -direction
$V_{rot,z}$	Rotational strength provided by the elements acting in z -direction

Small Latin Letters

b_x, b_z	Dimensions of the slab
e_{rx}	Distance in x -direction of the CR to the CoM
e_{rz}	Distance in z -direction of the CR to the CoM
e_{vx}	Distance in x -direction of the CV to the CoM
e_{vz}	Distance in z -direction of the CV to the CoM
h_{eff}	Effective height of a building
h_n	Total height of the building
k	Equivalent wall stiffness
k_{xi}	Equivalent stiffness of wall i in x -direction
k_{zi}	Equivalent stiffness of wall i in z -direction
m_{eff}	Effective mass of a building
m_j	Mass of storey j
r_F	Post-elastic stiffness ratio
r_m	Radius of gyration of mass
r_{rx}	Radius of gyration of stiffness for elements acting in x -direction
r_{rz}	Radius of gyration of stiffness for elements acting in z -direction
r_{vx}	Radius of gyration of strength for elements acting in x -direction
r_{vz}	Radius of gyration of strength for elements acting in z -direction
r_0	Radius of gyration of mass of a square slab with equal area and uniformly distributed mass

x_i	Distance in x -direction between wall i and the CoM
z_i	Distance in z -direction between wall i and the CoM

Capital Greek Letters

Δ_{CoM}	Displacement at the centre of mass
Δ_d	Design displacement
Δ_i	Displacement of element i
Δ_j	Design displacement at storey j
Δ_p	Plastic displacement
Δ_y	Yield displacement of a wall
Δ_{ys}	Yield displacement of the system
Δ_u	Ultimate displacement

Small Greek Letters

α	Angle enclosed by the ground motion axes and the axes of the structural system
λ_i	Excess strength factor of element i (Equation 7.22)
$\mu_{\Delta s}$	System ductility
μ_{φ}	Curvature ductility
θ	Nominal rotation
ξ	Viscous damping ratio
$\xi_{eff,s}$	Effective damping ratio of the system

1. INTRODUCTION

The lateral strength of reinforced concrete (RC) buildings is often provided by a core, which is well suited to accommodate lift shafts or staircases. A core is a structural element with a cellular section that is typically closed on three sides and is either open or partially closed by deep coupling beams on the fourth. There are numerous possible shapes of such core structures; the simplest one is a U-shaped or channel shaped section (Figure 1.1a) but multicellular sections (Figure 1.1b) are also very common and particular in high-rise buildings even more complex shapes may occur (Figure 1.1c). It is believed that cores with simple shapes can be designed for a predictable and dependable inelastic cyclic behaviour whereas the behaviour of cores with very complex shapes can be hardly understood with the required accuracy, hence calling for an almost elastic design. Figures 1.1d and e show examples of a core that – apart from the floors that are spanning across – is open on one side and a core that is partially closed.

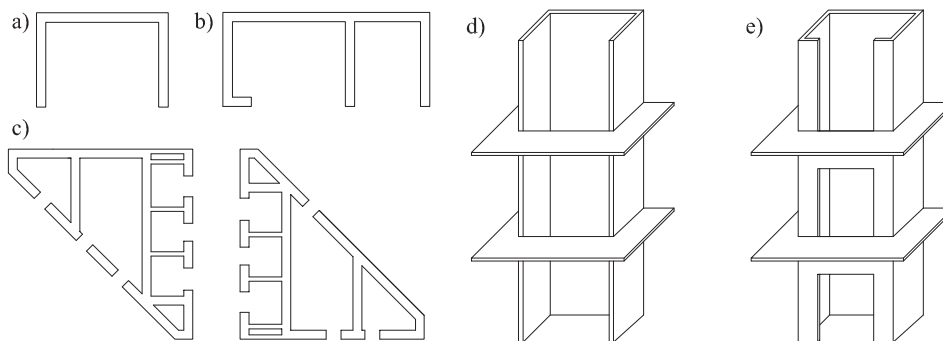


Figure 1.1. Cross section of core structures (a-c) and examples of an open (d) and a partially closed core (e); cross section c: Victoria tower block in Mannheim, Germany [Bergmeister and Wörner, 2003].

Over the last decades the seismic behaviour of RC walls with rectangular cross section has been the subject of extended research and several test series on such walls were conducted. From the results of these experimental studies the key parameters controlling the behaviour

of rectangular walls under seismic excitation could be deduced and the results were adopted in code provisions providing detailed guidelines for designing engineers. Although core walls are very popular in practice their inelastic behaviour under seismic loading has not been examined in detail but only very few experiments on U-shaped walls under cyclic loading (and none on walls with more complex shapes) have been conducted in the past. Hence, there is a lack of experimental evidence of the behaviour of such walls under seismic loading, which prevents a thorough calibration of analytical models and the derivation of appropriate design guidelines.

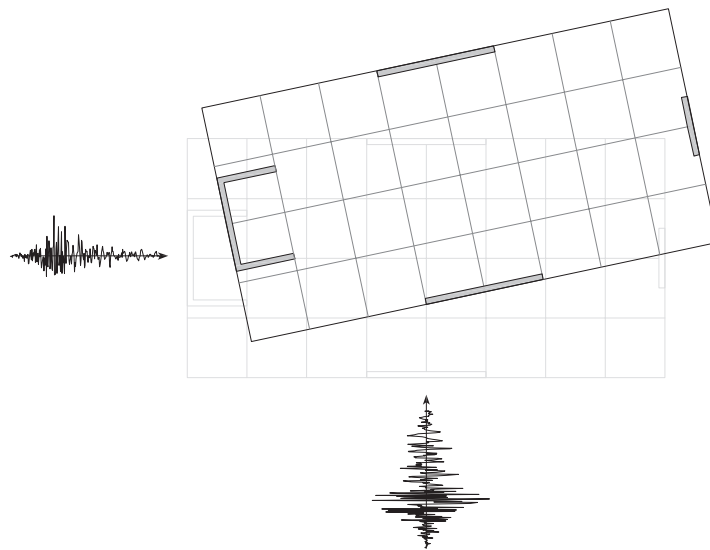


Figure 1.2. Seismic response of a RC building with a U-shaped wall.

Due to the increasing demand of open floor areas, the core structures are often placed at the perimeter of the building. Since other vertical members of the structure are typically less stiff and less strong than the core, the structural system is asymmetric in plan regarding the lateral stiffness and strength distribution. Hence, when subjected to seismic excitation, the building does not only translates but also twists. This is visualised in Figure 1.2. Large rotational displacement demands during a seismic event can make the building vulnerable if the increased displacement demand due to the twist of the system is not considered during the design. To draw a valid comparison of the displacement capacity of a structure with the expected displacement demand during a seismic event it is therefore necessary to account in the design process for the increased displacement demand due to the twist component of the response. Figure 1.2 visualises also the demand on the core structure: Unlike rectangular walls,

which only resist lateral forces in one direction, core structures provide lateral stiffness and strength in both horizontal directions and also possess a torsional stiffness.

1.1 Problem statement

When designing an in-plan asymmetric RC building with a core structure such as the one shown in Figure 1.2 the engineer faces two main problems: The first concerns the design of the core structure. RC design codes tend to be written for rectangular walls. It is often difficult – and sometimes impossible – to extrapolate the formulae that have been developed for rectangular walls to cores since the behaviour of cores under seismic loading is very complex. Although there have been some research efforts in the past to characterise the behaviour of cores, most of these efforts concerned the elastic behaviour of such walls. Only recently one research group addressed the inelastic behaviour of U-shaped walls but limited their study to the behaviour of one particular wall configuration and did not derive general design recommendations. The experimental evidence for the behaviour of such walls when subjected to lateral displacements is therefore very limited.

The second difficulty concerns the conceptual design of buildings with U-shaped walls. Modern seismic design approaches focus on displacement rather than force demands. One of the most completely developed approaches that allows to directly address displacements in the design process is the direct displacement-based design method, which was developed by Priestley and his co-workers. However, at present this approach cannot be applied to structures that are asymmetric in plan.

1.2 Objectives and scope of the study

The general objectives of this project is to contribute to the performance-based seismic design of RC buildings with cores. More specifically, it is aimed (i) at making a contribution to the understanding of the inelastic behaviour of cores under different directions of seismic loading and (ii) to identify a method for estimating the displacement demands of torsionally eccentric buildings during an earthquake. The scope of the first part is limited to U-shaped walls. This is the simplest shape of a core, yet it possesses all the characteristics that make the elastic and inelastic behaviour considerably more complex than that of rectangular walls, i.e. it is a composite section of several rectangular sections that is open on one side and provides flexural resistance in both horizontal directions as well as torsional stiffness. Regarding the seismic design of U-shaped walls this project aims at making the following contributions:

- Additional experimental evidence for the behaviour of U-shaped walls for different directions of loading.
- Development and validation of simple numerical models that can be used by the engineer to analyse U-shaped walls.
- Contribution to the development of design guidelines for U-shaped walls.

The torsional stiffness of U-shaped walls is not addressed within the scope of this project but the focus is set on the flexural and shear behaviour of U-shaped walls. Core configurations with more complex layouts are not considered although it is expected that most of the findings for U-shaped walls would also apply, for example, to E-shaped walls. The numerical modelling of the U-shaped walls is restricted to the analysis of the stand-alone members as they were tested during the experimental part of this thesis, which comprised two quasi-static cyclic tests of U-shaped walls, which were built at half scale. Entire buildings that include U-shaped walls are not considered.

In the second part of the report the response of buildings that are asymmetric in plan is studied. The objective of this part is to identify key parameters influencing the twist of a structure when subjected to seismic excitation and to develop a method for estimating the increased displacement demand on structural elements due to this twist. This method allows to account for torsionally induced displacements when designing a structure according to the direct displacement-based design method.

1.3 Outline of report

The report is divided into eight chapters. This first chapter is an introductory chapter, which briefly describes the challenges involved in designing a plan-asymmetric RC building with U-shaped walls. It also identifies the research need and formulates four key objectives for the thesis. Chapters 2 to 6 relate to different aspects of the seismic behaviour of U-shaped walls while Chapter 7 concerns the conceptual design of plan asymmetric buildings. In the following, each chapter is briefly described.

Chapter 2 reviews existing approaches of numerical models for U-shaped walls. Within this chapter four different types of models are discussed. These are the plastic hinge models, the stick models, the wide-column models and shell element models. Also included in this chapter is a summary of the most commonly used design criteria for determining the displacement capacity of a RC member, a review of the applied models for diagonal tension and diagonal compression shear failure as well as a review of existing methods for estimating the shear deformations of RC walls.

Chapter 3 describes the quasi-static cyclic tests of two U-shaped walls, which were carried out within the scope of this project, in terms of the test setup, the loading history and the main experimental results. The test units were subjected to a bi-directional loading history, hence it was possible to observe the behaviour of the U-shaped wall for different directions of loading. All numerical analyses of U-shaped walls that are presented in this report are based on these two tests. This chapter also includes a comprehensive description of the design of the two test units. The discussion of the design guidelines is extended to the design of U-shaped walls that form part of an entire building and can therefore be applied when a new building with a U-shaped wall is designed.

In Chapter 4 the experimental results are analysed further and compared to existing estimates of quantities that are used in plastic hinge analysis. These are estimates for the yield curvature, strains limits for defining the ultimate displacement capacity, plastic hinge length and shear displacements. Special emphasis is placed on the comparison of quantities for different directions of loading. The existing equations for the plastic hinge analysis were derived for rectangular walls and this chapter concludes with recommendations for their application to U-shaped walls.

From the results in Chapter 4 it was found that from all parameters required for the plastic hinge analysis the available estimates for the shear displacements were the least satisfactory. Chapter 5 aims at improving this situation by deriving a new empirical equation for the prediction of the ratio of shear to flexural displacements for RC walls. In addition, this chapter includes an evaluation of two structural analysis programs regarding their capability of predicting shear displacements. The study on shear displacements builds on the experimental evidence of the two U-shaped walls that were tested within the scope of this project as well as 27 other RC walls that have been tested by other researchers. Out of the 27 walls, three walls are U-shaped walls whereas the others have rectangular, barbelled or flanged sections. Details of these walls are presented in Appendix A.

Out of the four modelling approaches that were reviewed in Chapter 2 the plastic hinge analysis method and the wide-column method were selected and used to analyse the two U-shaped walls that were tested under quasi-static cyclic loading. In Chapter 6 the analysis results are compared against the experimental results and the two methods are assessed regarding their capabilities of modelling the inelastic behaviour of U-shaped walls under lateral loads. Recommendations regarding the choice of modelling parameters are given.

Chapter 7 concerns the torsional response of buildings that are asymmetric in-plan. This chapter includes an extensive 2D parametric study on asymmetric buildings. The objective of

this parametric study is to identify the key parameters controlling the torsional response of inelastic RC buildings. Based on the findings of the parametric study, a method for accounting for the displacement demands due to twist of the building within the direct displacement-based design approach is developed.

In the final chapter the main findings of this project are summarised, the motivation for this study reviewed and further research needs related to the design of plan asymmetric buildings with U-shaped walls are identified.

2. LITERATURE REVIEW ON DIFFERENT MODELLING APPROACHES FOR U-SHAPED WALLS

In this section different approaches of modelling the behaviour of U-shaped walls under seismic loading are reviewed. They are discussed in the order of their complexity:

- Plastic hinge model (Section 2.1)
- Stick model (Section 2.2)
- Wide-column model (Section 2.3)
- Shell model (Section 2.4)

These modelling approaches are general approaches, which are not limited to U-shaped walls. In the following sections the state-of-the-art of these modelling approaches for general wall sections is briefly summarised and issues particular to the modelling of U-shaped walls or the application of these approaches to U-shaped walls that have been reported in the literature are reviewed.

To establish the ultimate displacement capacity for each of these models, limits on concrete and reinforcement strains are defined that are related to certain types of failure. A summary of different guidelines for the selection of appropriate strain limits is given in Section 2.5. In some cases the tensile shear capacity or the web crushing capacity, which both reduce with curvature ductility, might limit the displacement capacity of a wall section. The state-of-the-art approaches for the assessment of these shear capacities are also summarised in Section 2.5.

Modelling of slender structural walls commonly focuses on flexural deformations while shear deformations are often considered as negligible. It will be shown in Chapter 4 that this assumption does not hold for U-shaped walls but that shear deformations should be included in numerical models of U-shaped walls. A review of different approaches for estimating shear deformations is given in Section 2.6.

2.1 Lumped plasticity models

The lumped plasticity approach assumes that the inelastic deformation can be modelled as concentrated in one flexural plastic hinge that is located near the section subjected to the largest moment demand. The deformations are computed assuming a piecewise-linear curvature profile in which the inelastic curvatures are distributed evenly over a plastic hinge length (Figure 2.1). This is of course only an approximation of the physical behaviour of RC members. However, the plastic hinge model is appealing for the sake of its simplicity and has also been shown to yield good estimates of the displacement capacity of the structural member. Moreover, it is widely accepted and used by the design engineer community. A prerequisite for its application is of course that adequate estimates of the plastic hinge length, the ultimate curvature and the ratio of shear to flexural displacements are available. The ultimate curvature is typically determined from strain limits which are discussed in Section 2.5. In the following the state-of-the-art equations for the principle aspects of plastic hinge analysis are briefly summarised, i.e. the force-displacement characterisation (Section 2.1.1), the yield curvature, which marks the onset of inelastic deformations (Section 2.1.2), and the plastic hinge length (Section 2.1.3). The contribution of shear deformations to the overall deflection is discussed in the last section of this chapter (Section 2.6).

2.1.1 Force-displacement characterisation

The objective of plastic hinge analysis is the transformation of the moment-curvature relationship that can be readily obtained from section analysis into a force-displacement relationship. The proportionality constant between force and moment is simply the shear span, the transformation from curvature to displacement is, however, more elaborate. Within this process it is customary to distinguish between the displacement prior to yielding and the post-yield displacement. The total displacement can therefore be written as:

$$\Delta = \Delta_y + \Delta_p \quad (2.1)$$

where Δ_y is the yield displacement and Δ_p the plastic displacement. In the following, typical approaches for estimating the yield and plastic deformation of cantilever walls from the base curvature φ are described.

For design purposes the yield displacement of a cantilever is often simply estimated on the basis of a triangular curvature distribution [Paulay and Priestley, 1992]:

$$\Delta_y = \frac{\varphi_y}{3} H^2 \quad (2.2)$$

where φ_y is the yield curvature and H the effective height of the wall. Since the moment distribution is also triangular this equation effectively assumes that the stiffness is constant

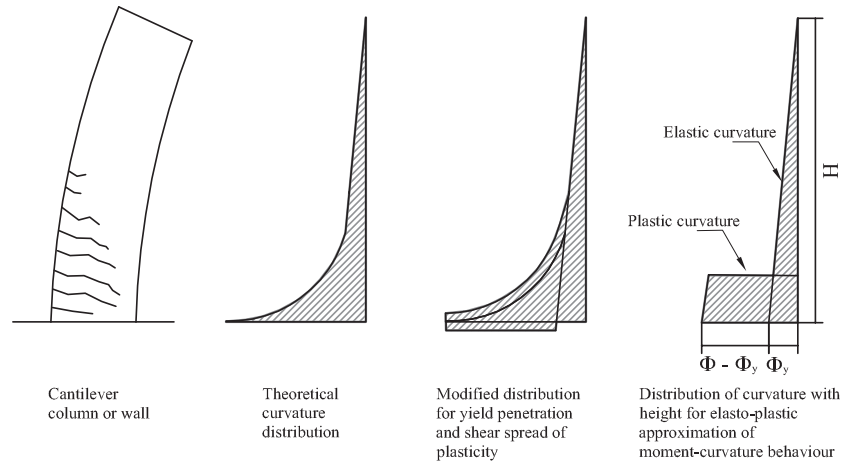


Figure 2.1. Plastic hinge analysis: Theoretical curvature distribution due to flexural deformations only, modified distribution accounting for shear spread and strain penetration into the foundation and curvature distribution assumed in plastic hinge analysis (adapted from Priestley and Park [1987]).

along the structural member. At some distance from the base the wall will probably be uncracked and hence it is likely that the flexural deformations are overestimated by Equation 2.2. However, the shear displacements and the strain penetration are not explicitly accounted for.

Hines [2002] developed a more elaborate approach for estimating the yield displacement. He distinguished between the deformation due to flexure of the wall, the rigid body rotation due to strain penetration into the foundation, and the shear deformation. From the experiments he conducted, Hines found that the strain penetration prior to yielding of the longitudinal bars can make a significant contribution to the flexural displacement at yield. He suggested adding a term to the flexural yield displacement Δ_{yf} to account for the base rotation due to strain penetration:

$$\Delta_{yf} = \frac{\varphi_y}{3} H^2 + \varphi_y L_{spsy} H \quad (2.3)$$

where L_{spsy} is the equivalent plastic hinge length to account for strain penetration prior to yielding. From his experiments, Hines found that L_{spsy} could be approximated as 1.5 times the strain penetration length after yielding, which is often estimated as $L_{sp} = 0.022d_b f_y$ (Equation 2.10a). Hines gave the following explanation for the fact that the strain penetration lengths prior to yielding are larger than the post yield lengths: Before yielding, the strain penetration into the foundation is almost linear. After yielding the strain penetrates only slightly further into the foundation since the forces in the reinforcing bars do not increase substantially. Before yielding the overall deformations are fairly small and hence the contribution of the strain penetration to the overall displacement – which is expressed in terms of $\varphi L_{spsy} H$

– is comparatively larger. The total yield displacement including the shear component Hines described by the following equation:

$$\Delta_y = \Delta_{yf} \cdot \left(1 + \frac{\Delta_s}{\Delta_f}\right) \quad (2.4)$$

where Δ_s/Δ_f is the ratio of the shear to the flexural displacements. Note that, although Hines accounted explicitly for the shear deformation and strain penetration, he computed the flexural deformations at yield Δ_{yf} on the basis of a linear curvature profile over the height of the wall (Equation 2.3).

The plastic displacement is obtained from the plastic hinge length L_{ph} , the plastic curvature φ_p and the effective height H of the wall. A well known equation for the plastic displacement is the following [Paulay and Priestley, 1992]:

$$\Delta_p = \varphi_{ult} \cdot L_{ph} \cdot (H - 0.5L_{ph}) = (\varphi_{ult} - \varphi_y) \cdot L_{ph} \cdot (H - 0.5L_{ph}) \quad (2.5)$$

where φ_{ult} is the ultimate curvature. In this equation the term describing the plastic deformation is formulated as a rotation with the centre of the plastic hinge at midheight of the plastic hinge. Hines [2002] noted that a centre of rotation for the plastic deformation at midheight of the plastic hinge is a conservative assumption, which might be suitable for design, but that a centre of rotation at the base is a more suitable assumption for assessment purposes. Within the scope of this project the objective is to compare analytical to experimental results and hence the most realistic assumptions should be adopted. Following Hines' argumentation it is therefore assumed that the displacement capacity is best estimated if the plastic hinge is placed at the base of the wall.

Considering that the ratio of shear to flexural displacement remains approximately constant over the entire ductility range (see Section 2.6) the ultimate displacement can – as the yield displacement – be written as the product of the flexural displacement and the shear ratio Δ_s/Δ_f [Hines, 2002]:

$$\Delta = (\Delta_{yf} + (\varphi_{ult} - \varphi_y) \cdot L_{ph} \cdot H) \cdot \left(1 + \frac{\Delta_s}{\Delta_f}\right) \quad (2.6)$$

2.1.2 Yield curvature

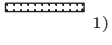
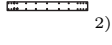
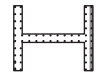
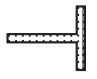
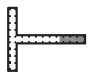
It has been accepted for some time that the yield curvature φ_y of a RC structural member is, for most practical design applications, only related to the geometry of the structural member and the yield strain ε_{sy} of the longitudinal reinforcement. Priestley *et al.* [1996] were the first to publish data that showed that the stiffness of a concrete section was directly related to its strength and therefore the yield curvature of the concrete section was in fact relatively

independent of the section's strength. Priestley and Kowalsky [1998] introduced the following expression for the yield curvatures of structural walls:

$$\varphi_y = K_1 \cdot \frac{\varepsilon_{sy}}{l_w} \quad (2.7)$$

where l_w is the wall length and K_1 a proportionality factor depending on the shape of the cross section of the wall and the longitudinal reinforcement layout. Several researchers have derived expressions for the K_1 -factor from moment-curvature analysis for a number of different wall geometries; a summary of these is given in Table 2.1.

Table 2.1. Proportionality factor K_1 for the nominal yield curvature.

	 1)	 2)			
Priestley and Kowalsky [1998]	2.25 ± 15%	2.0 ± 5%			
Dazio [2000]		~ 1.8			
Paulay [2002]	~ 2.0	~ 1.8	~ 1.4	~ 1.4	~ 1.8

1) Rectangular section without concentrated end reinforcement.

2) Rectangular section with concentrated end reinforcement.

At present, K_1 -factors have not been derived for U-shaped sections. However, for bending parallel to the web and the flanges K_1 -factors for I-shaped and T-shaped walls, respectively, can serve as approximations:

Bending parallel to the web:
$$\varphi_y = 1.4 \cdot \frac{\varepsilon_{sy}}{l_{web}}$$

Bending parallel to the flanges, web in compression:
$$\varphi_y = 1.4 \cdot \frac{\varepsilon_{sy}}{l_{fl}} \quad (2.8)$$

Bending parallel to the flanges, flange ends in compression:
$$\varphi_y = 1.8 \cdot \frac{\varepsilon_{sy}}{l_{fl}}$$

where l_{web} is the length of the web and l_{fl} the length of the flanges. For bending in the diagonal direction the yield curvature of a U-shaped section cannot be approximated by the yield curvature of a section of simpler shape, such as an I- or T-shaped section.

2.1.3 Plastic hinge length

a) State-of-the-art equations for plastic hinge lengths for design purposes.

RC structural members that respond in the inelastic range show a concentration of plastic strains around the section with the largest moment. However, unlike an elasto-plastic model of

a structural member under the Bernoulli-hypothesis of plane sections remaining plane would suggest, the inelastic deformations are not concentrated in one single section but are spread over a certain length of the structural member. The reasons for the spreading of the plastic strains are threefold [Priestley and Park, 1987]:

- The increase in capacity between the moment at first yield M'_y and the ultimate moment M_u combined with the moment gradient results in spreading of the plastic deformations over a certain length of the structural member. The length of the region over which plasticity spreads due to this mechanism is commonly expressed as a ratio of the effective height H while the ratio of M'_y/M_n , i.e. the hardening of the section, is often not explicitly taken into account.
- The inclined flexural-shear cracks lead also to a spread of the plastic deformation since the steel strains above the section of the largest moment will be increased (tension shift).
- Strain penetration along the reinforcement bars into the adjacent elastic member (e.g. the foundation) is the third mechanism that increases the plastic deformation capacity of the structural member. The strain along the anchorage length of the reinforcing bar in the foundation leads to a slip between the reinforcing bar and the foundation, which results in uplift at the structural wall or column base implying additional base rotation. This can be expressed as the product of a plastic curvature times an additional plastic hinge length increment.

Priestley and Park [1987] were the first to express the plastic hinge length as the sum of the three aforementioned contributions (for a complete history on the development of the plastic hinge analysis in earthquake engineering the reader is referred to Hines [2002]). For walls the general equation for the plastic hinge length can be written as:

$$L_{ph} = C_1 \cdot H + C_2 \cdot l_w + C_3 \cdot d_b \quad (2.9)$$

where d_b is the bar diameter of the main longitudinal reinforcement, l_w the wall length and C_1 , C_2 and C_3 constants. The first term represents the spread of plasticity due to the moment gradient, the second the spread of plasticity due to inclined flexural-shear cracking and the third term the increased rotation capacity due to strain penetration into the foundation. The total plastic hinge length will be at least twice the length due to strain penetration since slippage of the reinforcement may also increase the strain at sections above the base [Priestley *et al.*, 1994]. Paulay and Priestley [1992] presented two equations as estimates for the plastic hinge length of structural walls. Each included only two of the aforementioned contributions

to the plastic hinge length:

$$L_{ph} = 0.08H + 0.022d_b f_y \quad (2.10a)$$

$$L_{ph} = 0.2l_w + 0.044H \quad (2.10b)$$

where H is the *effective* height of the wall. The same equations were given for the total wall height $h_n = H/0.675$ in Priestley and Kowalsky [2000]. According to Paulay and Priestley [1992] the length of the plastic hinge L_{ph} corresponds typically to 30 – 80% of the wall length l_w . For slender flexural walls Priestley and Kowalsky [2000] used the maximum value of L_{ph} resulting from the two equations. In the new book on displacement-based design [Priestley *et al.*, 2007] a revised form of the equation for the plastic hinge length was published, which contains a term for each of the three mechanisms contributing to the spread of plasticity:

$$L_{ph} = kH + 0.1l_w + 0.022d_b f_y \quad (2.11)$$

where $k = 0.2(f_u/f_y - 1) \leq 0.08$ with f_y and f_u being the yield and ultimate strengths of the longitudinal reinforcement, respectively. Priestley *et al.* [2007] based the shear lag term $0.1l_w$ on research by Paulay and Priestley [1992], who had suggested $0.2l_w$. For design purposes they reduced it to half the length. Hence, some conservatism can be removed by resubstituting $0.1l_w$ with $0.2l_w$. The resulting equation might be more appropriate for assessment purposes including the prediction of experimental results:

$$L_{ph} = kH + 0.2l_w + 0.022d_b f_y \quad (2.12)$$

According to Priestley (private communication, 2007) the plastic hinge lengths given in Equations 2.10 and 2.11 should yield – in conjunction with ultimate strain limits as given in Section 2.5.1 – displacement capacities that are considerably lower than the displacement that would lead to collapse of the structural members. Hence, at present, the safety margin between design displacement capacities and ultimate displacement capacities is introduced by using conservative estimates of the plastic hinge length. This should be kept in mind when comparing the plastic hinge lengths derived from Equations 2.10 and 2.11 to experimentally-determined plastic hinge lengths.

b) Criticism levelled at the plastic hinge model and emerging modified approaches of the plastic hinge model.

The plastic hinge approach has been mainly criticised for the use of curvatures within the heavily cracked plastic zone. The crack pattern is typically fan-like due to the interaction of

flexure and shear. The Bernoulli assumption of plane sections remaining plane does not hold and therefore the definition of curvatures seems doubtful. In addition, the plastic hinge lengths have been typically calibrated for the tension side. This becomes evident in the strain penetration term $C_2 d_b$, which is irrelevant if the rotation capacity is limited by compressive strains [Priestley *et al.*, 1994]. Most published plastic hinge equations are therefore not applicable if failure on the compression side of the wall is anticipated.

The plastic hinge lengths in Equations 2.10 and 2.11 are empirical relationships and thus their effectiveness depends on the data they have been calibrated against, which were chiefly walls and columns with round or rectangular cross sections. Therefore, before the equations are applied in the design of U-shaped walls, they should be validated against experimental data for U-shaped walls. Hines [2002] tried to overcome the drawbacks of an empirical relationship by developing a method for deriving the plastic hinge length of structural walls or columns from first principles, accounting for the moment gradient and tension shift. The approach is based on moment equilibrium about the centre of the compression zone at the wall base considering the wall part above the top crack of the fanned crack pattern. It also includes the ratio of the maximum moment to the moment at first yield M'_y . Up to now, this approach has only been applied to barbelled walls with heavily confined boundary elements.

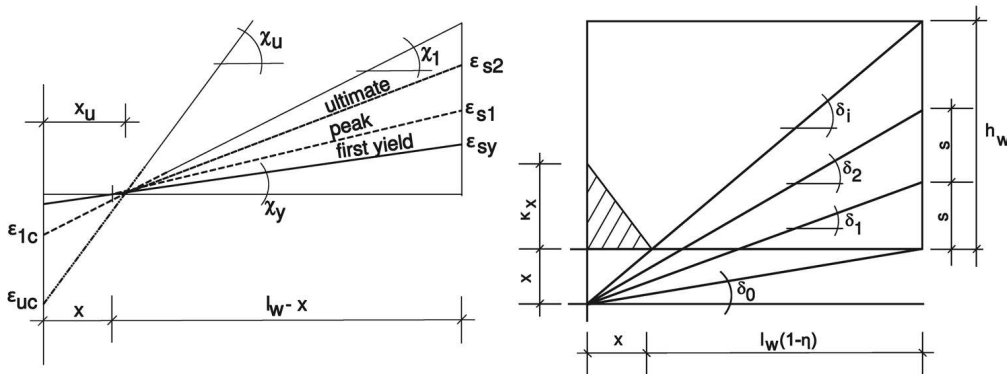


Figure 2.2. Evolution of strains with increasing displacements (a) and geometry of discrete crack model (b); figures from Greifenhagen [2006].

Based on the work by Bachmann [1967], Greifenhagen [2006] developed a new approach for estimating the plastic rotation capacity of the inelastic zone, which abandons the assumption of plane sections. He developed equations for the rotation capacity of the plastic zone that consider the compression side and the tension side of the base section separately. By doing so, for curvatures larger than φ'_y , he dropped the assumption of plane sections and postulated

that the behaviour can be described by assuming different curvatures for the compression and tension side (Figure 2.2). For both sides Greifenhagen derived ultimate rotation capacities for compression and tension failure. For tension failure the ultimate rotation capacity is expressed as the sum of crack widths $\sum w_j$ along the tension edge divided by the lever arm ($l_w - c$), where c is the depth of the compression zone (for convenience Greifenhagen assumed that the depth of the compression zone is the same as at first yield when the section is still assumed as plane):

$$\theta_s = \frac{\sum w_j}{l_w - c} \quad (2.13)$$

The crack widths w_j are estimated on the basis of the tension chord model and different bond models. For the compression side the ultimate curvature is expressed as

$$\theta_c = \kappa \cdot \varepsilon_{cu} \quad (2.14)$$

where κ is a factor accounting for the strain localisation due to longitudinal reinforcement and axial force. Greifenhagen's approach seems appealing since the separate consideration of the compression and tension side makes allowance for the fact that limits on the tensile and compressive strains cannot be treated with the same plastic hinge length. In this way, ultimate compressive and tensile strain levels can be addressed directly rather than considering average quantities over the plastic hinge length. A drawback of the approach is the large sensitivity to the assumed bond stress and ultimate steel strains, which control the crack width estimates. The uncertainties related to these two quantities are significant. Greifenhagen developed and applied the approach to squat walls that he had tested. However, when comparing the prediction to the experimental results he only included the tension side criterion, although failure of the compression side had been observed for two out of the four tested walls (i.e. M3 and to a limited extent also for M4). Hence, although the concept of this approach is appealing, the large uncertainties render its practical application difficult.

2.2 Stick models

In stick models the wall section is modelled by a single element. General aspects that require attention when modelling a structural wall as a stick are the number of elements along the wall height and the choice of the element type. The required number of elements over the wall height depends on the formulation of the element and the number of integration points per element. The formulation of the element determines whether the elements are based on displacement shape functions (stiffness- or displacement-based elements) or interpolation functions for forces (flexibility- or force-based elements). Details on these two types of element

can be found in Bathe [1996] and Taucer *et al.* [1991]. The consideration of the element type is important since it controls the distribution of the inelastic strains. If the displacement capacity of the wall is estimated for example from the push-over analysis of a stick model, strain criteria are typically employed for the definition of limit states. The outcome of the analysis will strongly depend on the chosen element formulation, the number and position of integration points along the element and the element length. In particular, the length of the element near the wall base, where the plastic deformations are concentrated, can have a significant effect on the analysis results. The classical type of elements are displacement-based elements. For most displacement-based elements cubic Hermitian polynomials are used as shape functions; for these elements the curvature variation along the length is linear. Analogous to the plastic hinge model, which was discussed in the previous section, the base element is often assigned the estimated length of the plastic hinge. For the bi-directional analysis of walls with different plastic hinge lengths in the two directions a compromise might be required and an intermediate element length chosen.

U-shaped walls can be subjected simultaneously to bi-axial shear forces and bending moments, torsional moments and axial forces. Most programs do not allow for the interaction of shear forces and torsional moments with bending moments and axial forces. The interaction of axial force and bi-axial bending moments is best accounted for in fibre-sections. Shear stiffness and torsional stiffness are often modelled as elastic properties although at least the shear stiffness of structural walls tends to decrease when the wall is subjected to inelastic deformations (see Section 2.6).

When the U-shaped wall is modelled as part of a larger structure additional issues require attention, such as the in-plan position of the stick and the connection of the stick to other structural members. If stick models are placed at the centroid of their section, lateral forces applied to the stick model will not cause a torsional moment – this is not correct since the shear centre of U-shaped walls does not coincide with the centroid of the section. For an elastic homogenous section, the shear centre lies outside the U-shaped section. Placing the stick at the shear centre of the U-shaped wall instead would improve the model regarding its torsional properties [Reynouard and Fardis, 2001]. However, when the U-shaped wall undergoes inelastic flexural deformations, the shear centre is likely to move towards the web [Pégon *et al.*, 2000c] and it is therefore not possible to place the stick at the correct effective shear centre throughout the analysis. In addition, Reynouard and Fardis [2001] pointed out that placing the stick at the shear centre also introduces errors in the vertical displacements at the end of beams framing into the stick. Reynouard and Fardis [2001] recommended using stick models of U-shaped walls only if the torsional rigidity of the U-shaped wall is small with

respect to the torsional rigidity of the building. In this case the stick can be placed at the centroid of the section.

2.3 Wide-column models

Despite the frequent use of wide-column models (WCMs) in engineering practice, recent literature on wide-column models is scarce. The objective of this section is to present an overview on different aspects of WCMs starting with their historical development (Section 2.3.1) and then discussing today's use of such models (Section 2.3.2), their drawbacks (Section 2.3.3), their application to U-shaped walls with elastic properties (Section 2.3.4) and their application to structures that behave inelastically (Section 2.3.5).

2.3.1 Historical development of WCMs

Already in the past non-planar walls have been common structural elements providing lateral stiffness and strength to RC buildings. Since even within elastic systems the force distribution between the different components (webs and flanges) of non-planar walls can be quite complex, the development of simple, computational inexpensive analysis models for such structures was a research objective from the early beginnings of computational structural analysis. One of the modelling approaches that found broad application was the "wide-column analogy" (known also as the "equivalent frame method"). It was originally developed for planar wall structures such as structural walls with openings and structural walls coupled by beams or slabs (e.g. Clough *et al.* [1964]; MacLeod [1974]) and was later extended to non-planar structures (e.g. MacLeod and Hosny [1977]; Stafford-Smith and Abate [1981]). Examples of WCMs of structural walls coupled by deep beams and of a U-shaped wall are shown in Figures 2.3a and 2.3b, respectively. In WCMs of non-planar walls the web and flange sections are represented by vertical column elements located at the centroid of the web and flange sections. These vertical elements are then connected by horizontal links running along the weak axis of the sections having common nodes at the corners. Except for a torsional flexibility, which they are typically assigned, these links are modelled as rigid.

2.3.2 Advantages of WCMs for today's analyses of structural walls

Today, with the rapid increase in computer power, computational expense receives less consideration when a computer model for the analysis of a structure is set up. Nevertheless, WCMs of structural walls still appeal and are often preferred to models with 2D or 3D elements for the following reasons:

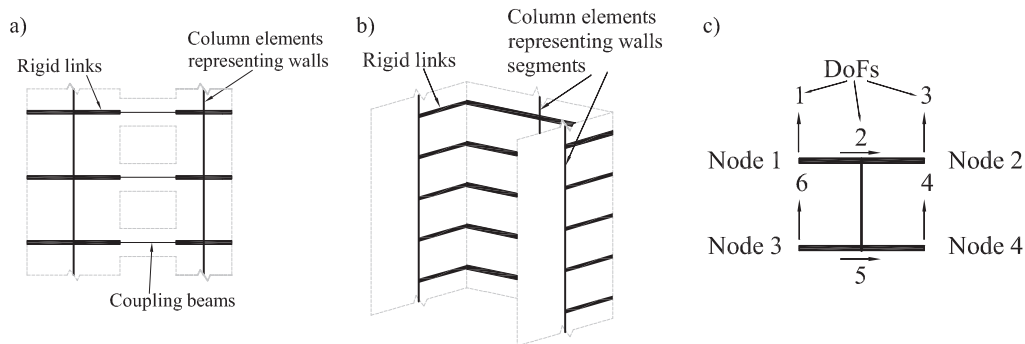


Figure 2.3. WCMs of coupled wall systems (a), WCMs of non-planar structural walls (b) and the classical wide-column module by MacLeod and Hosny [1977] (c).

- For seismic design, the nonlinear behaviour of walls and beams is of prime interest. There are few structural software packages with adequate nonlinear RC material models for 2D or 3D elements. The available packages are in general sophisticated and not suited for design purposes in engineering offices.
- The engineer needs moment, shear force and axial force to design a wall. This output can be obtained directly from frame analysis while models with 2D or 3D elements require the integration over the section to obtain the section forces and moments.

An alternative modelling approach, which is even more simple than WCMs, are stick models, which were discussed in Section 2.2. If stick models are assigned fibre sections they are – as WCMs – able to capture the interaction of axial and flexural capacity and to model the moment capacities for different directions of bending. However, WCMs of non-planar walls have a number of advantages when compared to stick models:

- Many structural analysis programs have predefined libraries of cross section geometries; it is hence not always possible to analyse a stick model with the section of one's choice. An exception is the program "Opensees" [Mazzoni *et al.*, 2005] which allows defining fibre sections by means of single fibres to which size, location and stress-strain relations are assigned; any section layout can therefore be analysed.
- Stick models are one-dimensional models, and hence they cannot reflect the distribution of the shear force over the web and flanges of the U-shaped section. Therefore, the shear deformation will be the same whether the total shear force is in reality carried by one

flange alone or equally distributed between the two flanges. WCMs, however, are able to represent the distribution of the shear forces over the cross section area.

- Stick models of U-shaped walls have no inherent torsional stiffness; this property needs to be assigned separately and is not related to the flexural and shear strength of the model. WCMs have an inherent torsional stiffness due to the flexural stiffness of the two flanges and the lever arm between them.
- When the U-shaped wall forms part of a larger structure, stick models representing the U-shaped wall can be placed at either the centroid or the shear centre of the section. Both positions bear disadvantages depending on the applied type of loading [Reynouard and Fardis, 2001].
- While stick models yield only total sectional forces, WCMs provide the sectional forces acting on the individual components of the wall [Avramidis, 1991]; these are exactly the quantities needed by design engineers. For example, in the case of U-shaped walls, the distribution of the total base shear force between the web and the two flanges is an important parameter for their shear strength design.

For these reasons, WCMs of structural wall systems with nonlinear beam-column elements are often used for structural analyses. However, they are, of course, only approximations of the real structural system and also exhibit some drawbacks.

2.3.3 Drawbacks of WCMs with linear-elastic properties

The three main drawbacks of WCMs with elastic properties concern the parasitic bending moments due to shear stresses along the wall edges, the response to torsional loading and the rotation demand on coupling beams. The latter does not concern U-shaped walls that are completely open on one side. However, for the sake of completion, it is briefly discussed.

a) Parasitic moments.

A wide-column module for wall sections comprises one flexible column element and two rigid links which extend over the width of the wall. Stafford-Smith and Girgis [1986] found that such elements are afflicted by parasitic bending moments when continuous shear stresses along the wall edges are modelled. Since continuous distributed shear stresses along a wall edge will be lumped into discrete shear forces at the rigid links these shear forces will cause reverse bending of the column element (Figure 2.4a). The parasitic moment is

$$M_{par} = \tau t_w \frac{h_{sp}}{2} l_w \quad (2.15)$$

where τ is the constant shear stress along the wall edges, t_w the wall thickness, h_{sp} the vertical spacing between rigid links and l_w the wall length. The flexural displacement associated with the reverse bending is

$$\Delta_{par} = \frac{M_{par}h_{sp}^2}{6EI} \quad (2.16)$$

where EI is the flexural stiffness of the wall. The deformation due to parasitic bending moments can be considered as an apparent shear deformation that is dependent on the bending stiffness of the column element and the spacing of the rigid links. Hence, it is only related to the modelling approach and has no physical meaning. The apparent shear displacement Δ'_s of the wall due to the parasitic moments of the wall and the true shear flexibility is

$$\Delta'_s = \Delta_s + \Delta_{par} = \frac{\tau}{G}h_{sp} + \frac{\tau t_w l_w h_{sp}^3}{12EI} = \frac{\tau}{G}h_{sp} \left(1 + \frac{t_w l_w G h_{sp}^2}{12EI}\right) \quad (2.17)$$

If the shear modulus G is rewritten in terms of the Young's modulus E and the Poisson's ratio ν and the moment of inertia I is replaced by the expression for the gross section, an apparent shear modulus G' can be defined as (after Kwan [1993]):

$$G' = \frac{G}{1 + \frac{h_{sp}^2}{2(1+\nu)l_w^2}} \quad (2.18)$$

Equation 2.18 shows that for a homogenous wall section modelled with the wide-column approach the apparent shear modulus depends on the square of the ratio of the vertical link spacing and the wall width. Stafford-Smith and Girgis [1986] suggested to limit the link spacing to one fifth of the overall wall height to ensure that the bending stiffness of the reverse bending is larger when compared to the overall bending stiffness of the structure. Although the equations above have been derived for pure shear, parasitic bending moments also occur under all other types of loading that include shear stresses.

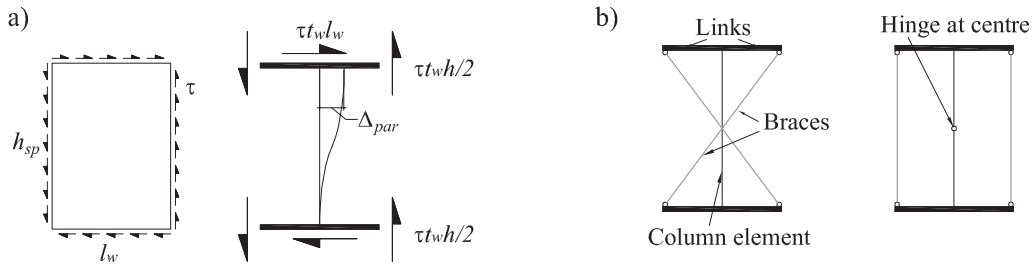


Figure 2.4. Parasitic moment and artificial flexure in conventional wide column frame analogy (a) and examples of modified wide column modules (b); figures adopted from Stafford-Smith and Abate [1981], Stafford-Smith and Girgis [1984] and Kwan [1993].

Considerable efforts by a number of researchers have been undertaken to improve the wide-column model and to overcome its shortcomings related to the parasitic bending moments. Kwan [1993] suggested altering the shear modulus G so that the apparent shear modulus G' becomes equal to the true shear modulus G . Kwan demonstrated that with the classical wide-column element by MacLeod and Hosny [1977] and the adjusted shear modulus, the model yields in exact results for shear, bending moment and axial force. This approach does not eliminate the parasitic moments. Instead, the bending moments are evaluated at the midheight of the elements where the parasitic moments according to Kwan [1993] are zero; if necessary these moments can be extrapolated to the element ends.

Other approaches (e.g. Stafford-Smith and Abate [1981]; Stafford-Smith and Girgis [1984]; Kwan [1994]) suggested modifying the WCM by adding additional braces to the wide-column modules in order to eliminate the displacements due to the parasitic bending moments (Figure 2.4b). However, WCMs with braces have several drawbacks: Firstly, the stiffness of the braces and the stiffness of the column element need to be determined such that the sum of the stiffnesses is equal to the true wall stiffness. Hence, the column element is no longer the direct model of the wall section. Secondly, the internal forces of the wall can no longer be directly obtained from the internal forces of the column element, but equilibrium needs to be computed on the entire wide-column module including the braces. Thirdly, more elements and nodes are required than for the classical WCM. Although the capacity of today's structural analysis programs is sufficient, it renders the setting up of the numerical model more difficult. Finally, WCMs with braces are only practical for elastic analysis because it seems very improbable to find an appropriate combination of inelastic properties of the braces and the column element, which represent correctly the bending moment-axial force interaction of the wall section. This applies in particular to WCMs which are subjected to cyclic loading in the inelastic range. Kwan [1994] later showed that the wide column modules of Figures 2.4b are equivalent to each other and the choice is only a matter of personal preferences.

b) WCMs of cores under torsional loading.

WCMs of cores which are partially closed by deep beams may lead to erroneous results for torsional loading since a large portion of the torsional resistance is attributed to Saint-Venant shear stresses rather than warping of the section [Stafford-Smith and Girgis, 1986]. The Saint-Venant shear stresses cause parasitic bending moments, which lead to reverse bending of the web and flanges. As a consequence the behaviour of the WCM might be dominated by the reverse bending rather than deformations that account for physical-meaningful stresses. A more in-depth discussion of the torsional behaviour of U-shaped walls and related modelling aspects will be considered in a future project but is beyond the scope of this study (see Section 1.2).

c) Rotation demand on coupling beams.

The second short coming of the WCM concerns the beam end rotations. Figure 2.5a shows that in the conventional WCM the flexible beams are connected to the rigid links. In standard frame programs the rotation of the rigid links depend only on the flexural deformation of the column and not on the shear deformations of the column [Rutenberg *et al.*, 1986]. The rotation of the coupling beam is, however, dependent on the rotation of the vertical edge of the wall (Figure 2.5b), which is generally larger than the flexural rotation of the wall.

Kwan suggested two different approaches to overcome this problem [Kwan, 1991, 1994]. In 1991, Kwan proposed that the shear deformations of the wall should be accounted for by making the link from the wall centre to the wall perimeter flexible in shear. In return the wall element was assigned an infinite (or very large) shear stiffness. The approach bears the disadvantage that due to the high shear stiffness of the wall the lateral shear deflection of the wall is not modelled correctly. The shear stiffness of the links is further discussed in Section 6.2.4.

In 1994 Kwan developed a coupling beam model in which the coupling beam ends were not only linked to a single rigid link but to two consecutive rigid links (Figure 2.5b). In this way, the rotation of the coupling beam end was linked to the rotation of the vertical edge of the wall.

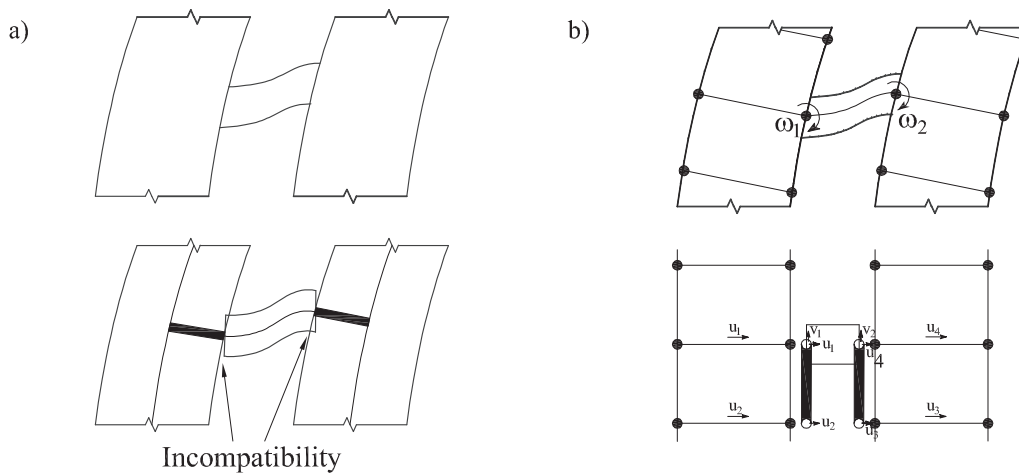


Figure 2.5. Incompatibility between beam and wall elements when joint rotations are defined as the horizontal fibre rotations (a) and beam element with vertical rigid arms (b) (after Kwan [1994]).

2.3.4 Studies on WCMs of U-shaped walls with elastic properties

While many studies focused on the development of modified WCMs with braces in order to overcome the drawbacks associated with the classical WCMs, some other studies tried to define limits on the applicability of the original WCM with no braces. Avramidis [1991], for example, stated that the original WCMs led to good results for walls with relatively simple cross sections and walls subjected to predominantly flexural action. He also stated that the wide-column analogy should not be used for walls with irregular cross sections, squat walls and partially or completely closed cores under torsional loading. Further studies concentrated on the choice of modelling parameters. Xenidis *et al.* [1993], for example, benchmarked the results of classical WCMs of U-shaped walls with elastic properties against results obtained from shell element models of the same walls. They compared the results regarding the modal displacement profiles and maximum stresses at the wall base for response spectrum analysis focussing their investigation on the torsional stiffness of the links and on the torsional stiffness of the column elements representing the web and the flanges, respectively. The analysis results were not sensitive to the torsional stiffness of the column elements and the authors recommended setting their torsional stiffness to zero. Regarding the torsional stiffness of the links Xenidis *et al.* [1993] concluded that for the links in the web a value representative of the section with elastic properties was most appropriate (though they did not state which value) while the links in the flanges should be modelled as rigid. Torsionally flexible web links imply that the core sections are not forced to remain plane but are allowed to warp. Some years earlier Avramidis, who is a co-author of the study by Xenidis *et al.* [1993], had suggested setting the torsional stiffness of the links in the web to [Avramidis, 1991]:

$$GK = \frac{G_c h_{sp} t_w^3}{3} \quad (2.19)$$

where h_{sp} is the link spacing, which Avramidis chose to be equal to the storey height. Avramidis stated that in engineering practice the torsional rigidity of the links in the web is often set to zero but found from parametric studies that this led in many cases to a considerable overestimation of deformations under torsional loading.

2.3.5 WCMs with inelastic properties

Although it is believed that WCMs with inelastic properties are widely used in practice, there is very little literature on such models. In the report accompanying the research project on the U-shape walls tested in Ispra and Saclay [Reynouard and Fardis, 2001] the use of inelastic WCMs is discussed, although it seems that such models were not used for the analysis carried out within the scope of the research project. The authors suggested that WCMs should be used instead of a stick model if it was felt that modelling of the torsional response was important (see also Section 2.2). Reynouard and Fardis [2001] suggested that the horizontal arms "should

be absolutely rigid in bending, shear and axial extensions, but should have a finite torsional rigidity". As a value for the torsional rigidity GK they used the same value for the torsional rigidity as Avramidis (Equation 2.19). In contrast to Avramidis [1991] and Xenidis *et al.* [1993], Reynouard and Fardis did not distinguish between the torsional stiffness of the links in the web and in the flanges.

To our knowledge the appropriateness of the link properties suggested by Reynouard and Fardis [2001] has never been checked against experimental results of U-shaped walls responding in the inelastic range. Apart from the link properties, the engineer needs guidelines on the best way to subdivide the U-shaped section into planar sections, on the vertical spacing of the links, on the number of elements between links and on the shear and torsional stiffness of the wall sections. These issues will be addressed in Section 6.2.

2.4 Shell element models

A large number of different finite element codes including 2D or 3D elements and sophisticated material models have been developed in recent years [Shing and Tanabe, 2001]. Since the field of shell models in seismic analysis is too broad to be summarised in full, this section concentrates on shell models of U-shaped walls with inelastic properties and their application to U-shaped walls. More specifically, this consists of the work by Ile and Reynouard, who have developed a shell model of the U-shaped walls tested at Ispra and Saclay using the finite element program CASTEM 2000. The following paragraphs describe the formulation of the shell elements, the constitutive models for concrete and reinforcement, and the match of the analysis results to the experimental data.

2.4.1 Shell elements

Ile and Reynouard [2005] devised shell element models with several layers of thin shell elements for the concrete. Using several layers of thin shell elements allowed Ile and Reynouard to capture the stress variation in the concrete over the thickness of the wall and to model the out-of-plane bending stiffness of the wall sections. The vertical and horizontal reinforcing bars were modelled as truss elements and perfect bond between reinforcement and concrete was assumed. Note that for his Ph.D. thesis Ile [2000] applied a cyclic bond-law, in which the bond stress degraded with bond-slip. The same model had been used by Ile *et al.* [2002b] when modelling rectangular walls with plain bars.

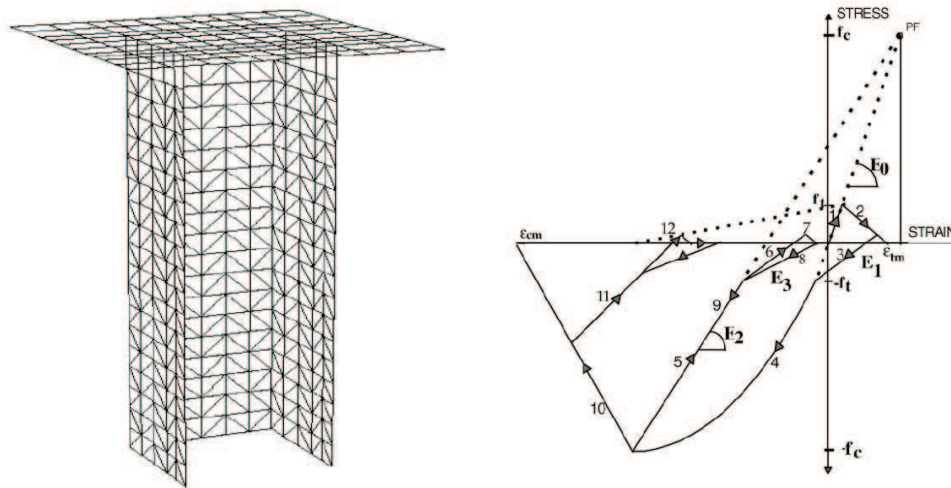


Figure 2.6. Ile and Reynouard [2005]: Shell model of the U-shaped wall tested in Ispra (a) and the cyclic material model for concrete (b).

2.4.2 Material models

For their analyses Ile and Reynouard [2005] used a biaxial concrete model, which they had developed some years earlier [Ile and Reynouard, 2000]. During the uncracked state the concrete material model was based on plasticity theory. The concrete was considered as uncracked as long as the yield surface in tension had not been reached. When it was reached, a crack formed perpendicular to the principle direction in tension. For the cracked state a smeared cracking model was adopted. Cracks were not allowed to rotate, and a further crack could only form at right-angles to the first crack. After the concrete had cracked, the two directions (parallel and perpendicular to the crack) were considered independently and were represented by a cyclic uni-axial material law. The shear transfer across the crack was modelled by a reduced shear modulus μG . In their first paper in 2000, Ile and Reynouard had used a constant value of μ throughout the analyses. In their later paper in 2005, the reduction factor μ was formulated as a function of the total strain, the residual strain after unloading in compression, and the crack opening strain. The reinforcing bars were modelled adopting a cyclic material model which could account for softening due to the Bauschinger effect and buckling of the reinforcing bars [Ile and Reynouard, 2005].

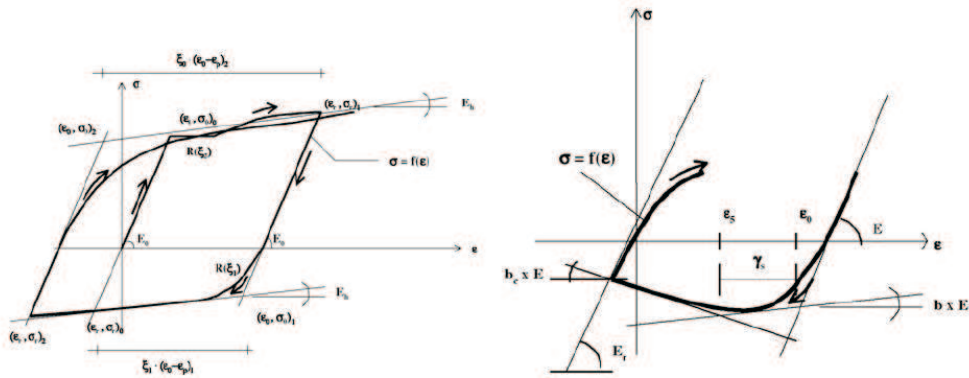


Figure 2.7. Ile and Reynouard [2005]: Cyclic material model for reinforcing bars.

2.4.3 Comparison with experimental results

With the exception of the last cycles in which strong strength degradation was observed during the experiments, Ile and Reynouard [2005] were able to achieve a good match between the numerical and experimental results in terms of the global displacements and forces. Ile and Reynouard [2005] attributed discrepancies between the shell element model and the experimental evidence to strong damage to the concrete and buckling of the bars of the physical wall; these two effects could not be adequately accounted for in the finite element model. A source of flexibility that was also not accounted for in the finite element model was the rigid body rotation due to strain penetration into the foundation; this might have caused a further discrepancy between the analytical results and the experimental results [Ile and Reynouard, 2005].

In addition to the force-displacement hysteresis, the results of the analytical model and the experiments were compared on a more local level in terms of the elongation of diagonal transducers [Pégon *et al.*, 2000b]. For the test in the X-direction (displacement parallel to the web) the agreement between analytical and experimental results was very satisfactory, but for the bi-directional test (butterfly pattern) the agreement was not as good [Ile, 2000]. On the whole, the shell model seems, however, capable of reflecting the shear deformation of the walls in a satisfactory manner.

Ile [2000] also modelled the U-shaped wall that was tested on the shaking table in Saclay [Combescuré *et al.*, 1999b]. For the motions with small peak ground accelerations ($PGA \leq$

0.26g) in which the reinforcing steel remained elastic, the top displacement time histories and the overturning moments were well represented by the analytical model. For larger peak ground accelerations ($0.63g \leq PGA \leq 1.00g$) the agreement was less satisfactory. For these input motions significant inelastic deformation occurred. At 1.0g some bars ruptured; this effect could not be represented in the model.

The appealing characteristic of this modelling method is the interaction of shear and flexural behaviour. In all of the previously described types of model (plastic hinge analysis, stick model and wide-column model) it is impossible or very difficult to account, for example, for the dependence of the shear stiffness on the axial force and the flexural stiffness. It also appears that the cyclic material models employed for the shell models, which were partly newly developed by Ile and Reynouard [2005], are powerful for large cycle inelastic displacements. Although computer become increasingly powerful, it seems unlikely that such elaborate models of structural walls will become a standard for design engineers in the near future. The setting up and checking of the model – particular if an entire building rather than an isolated component has to be analysed – requires a large amount of expertise in numerical modelling. The focus of this study will therefore be placed on simpler numerical models (Chapter 6).

2.5 Defining the ultimate limit state

The damage state of a structural element is best characterised by peak strains in the most critical section. Hence, in plastic hinge analysis it is common practice to link the displacement capacity of structural elements to the ultimate strain limits of concrete and longitudinal reinforcement. A review of proposed strain limits for concrete and reinforcement is presented in Sections 2.5.1 and 2.5.2, respectively. Alternatively, the displacement capacity can be limited by the shear capacity of the section (both diagonal tension and compression shear failure) which reduces with increasing inelastic deformations. Different models for the ductility dependent shear capacity are discussed in Section 2.5.3.

2.5.1 Ultimate concrete strain limit

RC walls that have been designed according to state-of-the-art principles have typically confined boundary elements. The loss of the unconfined cover concrete is in general not considered as an ultimate limit state but as a serviceability limit state. The ultimate strain capacity of unconfined concrete is often estimated as $\varepsilon_{cu} = 0.004$ [Scott *et al.*, 1982].

The strain capacity of confined concrete depends on a number of parameters, such as the confinement ratio, the spacing of hoops and the yield strength of the confining reinforcement.

Two of the most widely used approaches for estimating the strain capacity of confined concrete are summarised in the following: The first is the approach by Scott *et al.* [1982], which is an empirical relationship between the ultimate strain ε_{cu} of confined concrete and the confining reinforcement. The second approach is by Mander *et al.* [1988a,b], which is based on mechanical principles.

Scott *et al.* [1982] tested a series of 25 square, confined RC columns under monotonic axial loading, which was applied concentrically (21 specimens) or eccentrically (4 specimens). They found that the ultimate compressive strain in the confined concrete core could be estimated as the strain at which the first hoop fractured. All tested columns had inner and outer hoops. Fracture of the outer hoops occurred not at all or considerably later than fracture of the inner hoops. This observation was linked to the loss of bond of the outer hoops after the cover concrete had spalled off leading to a more equal spread of the strains in the hoops. From the test results on concentrically loaded columns Scott *et al.* [1982] derived an empirical relationship between the concrete strain capacity ε_{cu} , the volume ratio of transverse reinforcement ρ_s , and the yield strength of the transverse reinforcement f_{yh} :

$$\varepsilon_{cu} = 0.004 + 0.9\rho_s \frac{f_{yh}}{300\text{MPa}} \quad (2.20)$$

From the experiments maximum concrete compressive strain within the range 0.017 to 0.038 were obtained. The equation was derived for columns tested under strain rates representative of those under real seismic loading. Scott *et al.* [1982] stated that for structural members under flexural loading the peak concrete compressive strain in the non-uniform stress field would be significantly larger (2 to 3 times) than under concentric axial load. Hence, displacement capacities of flexural members computed on the basis of the strain limit given in Equation 2.20 will be conservative estimates.

Mander *et al.* [1988a,b] developed an expression for the ultimate strain capacity of confined concrete that is based on strain energy considerations. They postulated that the ultimate volumetric strain energy of the confined concrete core equals the ultimate strain capacity of the confining reinforcement minus the strain energy stored in the longitudinal bars in compression plus the ultimate strain energy required to crush unconfined concrete. The equation proposed by Mander *et al.* [1988b] was later simplified and is nowadays used in the following form [Paulay and Priestley, 1992]:

$$\varepsilon_{cu} = 0.004 + \frac{1.4\rho_s f_{yh} \varepsilon_{su}}{f'_{cc}} \quad (2.21)$$

where ρ_s and f_{yh} are defined as in Equation 2.20, ε_{su} is the steel strain at maximum tensile stress and f'_{cc} is the compression strength of the confined section. For rectangular sections

the volumetric ratio of confining steel is $\rho_s = \rho_x + \rho_y$ where ρ_x and ρ_y are the area ratios of transverse reinforcement to core concrete cut by planes perpendicular to the x and y directions. The approach was experimentally validated against 31 RC columns of different cross sections under concentric, monotonic axial load at similar strain rates to those used by Scott *et al.* [1982].

Hines [2002] criticised the approach by Mander *et al.* [1988a,b] since it does not account for the effect of longitudinal bar buckling. According to Hines [2002], buckling of the longitudinal reinforcement may lead to local yielding and subsequent fracture of the hoops. Hines [2002] argued that if bar buckling rather than expansion of the confined concrete under compression leads to hoop fracture, the energy balance approach by Mander *et al.* [1988a,b] is incorrect. Priestley *et al.* [2007] also identified a couple of reasons why Equation 2.21 is only approximate and suggested that compressive strains of walls under axial load and flexure might exceed the predicted strain limits by a factor of about 1.3 – 1.6.

Although there are some reservations within the engineering community regarding the mechanical principles behind Equation 2.21, it remains one of the most widely used equations for estimating the strain capacity of confined concrete sections. The applicability of both approaches (Equations 2.20 and 2.21) to the quasi-static cyclic tests on U-shaped walls is limited due to strain gradient effects, differences as a consequence of monotonic and cyclic loading, and strain rate effects. Due to the lack of more appropriate equations they are used despite these shortcomings.

2.5.2 Ultimate reinforcement strain limit

Longitudinal reinforcing bars in flexural walls fail typically in one of the two following modes:

- The bar ruptures in tension with no preceding buckling. This failure mechanism has been observed for bars whose cover concrete had not spalled off. As a consequence the strains within the bar were concentrated within a very short section of the bar.
- The bar ruptured in tension after having buckled in compression. This failure mechanism is often observed for the main longitudinal reinforcement at the wall ends.

The second of these failure modes is more typical for longitudinal reinforcing bars in the boundary elements since cover concrete tends to spall off at displacement demands smaller than the ultimate displacement capacity and therefore the strain concentration is less significant. Restrepo [1993] was the first to describe the mechanism behind the fracture of bars after

buckling: Buckling leads to microcracks on the compressed side of the bar. Upon load reversal these cracks might propagate and lead to premature fracture of the reinforcing bar.

Restrepo found that the total excursion strain $\varepsilon_s - \varepsilon_c$, i.e. the absolute sum of the strains in the compressive and tensile range, was better suited as a failure criterion than the isolated consideration of ε_s . Since the computation of the total strain excursion, for example, is in plastic hinge analysis rather difficult, Priestley *et al.* [1996] proposed to simply limit the tensile strain to $0.75\varepsilon_{su}$. Later, Priestley *et al.* [2007] suggested a reduction factor of 0.6 for design. Apart from the effects of compressive strains, this reduction accounts for the effects of buckling on the tensile strain capacity [Priestley *et al.*, 2007].

Several other studies proposed alternative strain limits for the buckling and rupture of longitudinal reinforcing bars: From his experiments on bridge piers, Hines [2002] found that total excursion strains in the range of 0.035 to 0.05 lead to the onset of bar buckling. Restrepo [2006] proposed the following equation as a strain limit on total excursion strain for the onset of bar buckling:

$$\varepsilon_s - \varepsilon_c \geq \frac{10 - \frac{s_h}{d_b}}{100} \quad (2.22)$$

where s_h is the spacing of the confining reinforcement and d_b the diameters of the main longitudinal reinforcement. As a strain limit on bar fracture Restrepo [2006] suggested:

$$\varepsilon_s - \varepsilon_c = \frac{14 - \frac{4s_h}{3d_b}}{100} \leq \frac{\varepsilon_{su}}{2} \text{ and } \varepsilon_c \leq -0.004 \quad (2.23)$$

Berry and Eberhard [2005] used a set of 104 circular and rectangular columns which have been tested under cyclic loading during which the longitudinal reinforcement bars buckled. Rather than defining a strain for which bar buckling is expected they proposed an empirical relationship linking the drift ratio over the effective height H to bar buckling:

$$\frac{\Delta}{H} \% = 3.25(1 + k_{e_bb}\rho_{eff}\frac{d_b}{l_w})(1 - \frac{P}{A_g f'_c})(1 + \frac{H}{10l_w}) \quad (2.24)$$

where $k_{e_bb} = 40$ for rectangular walls, $k_{e_bb} = 150$ for circular, spiral-reinforced columns and $k_{e_bb} = 0$ if $s_h/d_b > 6$ since only little data was available for this range; $\rho_{eff} = \rho_s f_{ys} / f'_c$ the effective confinement ratio; ρ_s the volumetric reinforcement ratio and f_{ys} the yield strength of the transverse reinforcement.

Dazio [2000] carried out analytical studies on the buckling of reinforcement bars. He found that besides the spacing of the confining reinforcement the post-elastic properties, i.e. the tangent-modulus, of the reinforcing bar controls the inelastic buckling behaviour of reinforcing bars. The work on buckling of reinforcing bars has been based mainly on reinforcing bars

used in New Zealand and the United States. Typically, the hardening ratios of these steels is higher than those used in Europe and therefore these equations might be unconservative for European reinforcing steels.

Priestley *et al.* [2007] developed an equation for the damage control curvature for which buckling occurs. This equation accounts directly for the effect of the post-yield stiffness on inelastic buckling. For spacings of the horizontal confinement smaller than the threshold $s_{b,max}$ the maximum steel strain of $0.6\varepsilon_{su}$ can be attained without buckling of the reinforcement. For spacings between $s_{b,max} \leq s \leq 16d_b$ the curvature at which reinforcement buckling occurs can be estimated as:

$$\begin{aligned}\varphi_{ls} &= \varphi_s + \left(\frac{16d_b - s}{16d_b - s_{b,max}}\right) \cdot (12\varphi_y - \varphi_s) \\ s_{b,max} &= \left(3 + 6\left(\frac{f_u}{f_y} - 1\right)\right)d_b \leq 6d_b\end{aligned}\quad (2.25)$$

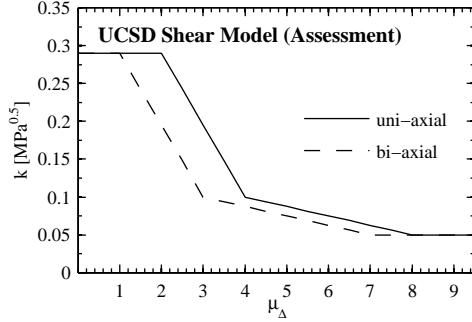
where φ_s is the serviceability limit-state curvature which is defined by the limit strains $\varepsilon_s = 1.5\%$ or $\varepsilon_c = 0.4\%$ whichever is reached first. For structural walls the serviceability limit-state curvature can be estimated as $\varphi_s = 0.01755/l_w$.

The range of values proposed for maximum tensile strains reflects the uncertainties associated with strain limits for reinforcing bars subjected to alternating compressive and tensile stresses and strains. To identify a limit that is appropriate for the experiments conducted described in Chapter 3, the different strain limits will be compared against experimentally determined strain values in Section 4.2.2.

2.5.3 Shear capacity as a function of ductility demand

Three different types of shear failure in a RC member can be distinguished: Diagonal tension failure, diagonal compression failure (also referred to as web crushing), and sliding shear failure at the base of the wall. Typically, only the diagonal tension and diagonal compression shear capacity are formulated as ductility-dependent, while the sliding shear capacity is often assumed as constant over the entire ductility range. In this section a summary of the diagonal tension and diagonal compression shear capacity equations that were used for the design and post-testing assessment of the two tested U-shaped walls is presented.

A number of shear capacity models for RC members undergoing inelastic flexural deformations have been developed in the past. Of these, the UCSD shear model [Priestley *et al.*, 1996] was chosen for the design of the U-shaped walls. According to this model a reinforcing steel component V_s , a concrete component V_c , and an axial load component V_p contribute to the total shear resistance V_n of a wall. Whereas the steel and axial load components are independent of the ductility demand, the concrete component reduces with increasing ductility:



$$V_n = V_s + V_c + V_p \quad (2.26a)$$

$$V_s = f_{yh} d \frac{A_v}{s} \cot(\theta) \quad (2.26b)$$

$$V_c = k(\mu_{\Delta}) \cdot \sqrt{f'_c} \cdot A_{sb} \quad (2.26c)$$

$$V_p = P \cdot \frac{\Delta l}{\Delta h_p} \quad (2.26d)$$

f_{yt}	Yield strength of the transverse reinforcement.
d	Effective depth of the section (commonly taken as $0.8l_w$).
A_v	Area of the transverse reinforcement.
s	Vertical spacing of the transverse reinforcement.
θ	Cracking angle measured with respect to the element axis.
$k(\mu_{\Delta})$	Factor accounting for effect of ductility demand, loading history (uni-/bi-directional) and extent of conservatism (design/assessment).
A_s	Effective shear area taken as $A_{sb} = 0.8 \cdot l_w t_w$.
P	Axial load.
Δl	Horizontal distance between point of application of axial load and centre of compression zone.
Δh_p	Vertical distance between point of application of axial load and centre of compression zone.

For the assessment of web crushing, three different approaches were employed. During the design stage the diagonal compression demand was checked against the web crushing capacity within the plastic hinge region according to EC8 [CEN, 2003], which is not dependent on the displacement ductility demand (note that in the draft version of EC8 from 2001 [CEN, 2001] the resistance to web crushing was twice the resistance given in the final version of the EC8 [CEN, 2003]):

$$V_{Rd} = 40\% \cdot \nu_1 \cdot b_w \cdot 0.8l_w \cdot f_{cd} / (\cot\theta + \tan\theta) \quad (2.27)$$

$$\nu_1 = 0.6 \quad \text{For } f_{ck} \leq 60 \text{ MPa.}$$

$$\nu_1 = 0.9 - f_{ck}/200 \quad \text{For } f_{ck} > 60 \text{ MPa.}$$

$$f_{cd} \quad \text{Design value of concrete compressive strength.}$$

$$f_{ck} \quad \text{Characteristic compressive cylinder strength of concrete at 28 days.}$$

In the literature there are a number of approaches that explicitly account for a reduction in web crushing capacity with ductility demand. These have not been considered during the design stage of the walls but will be used in Chapter 6 – in addition to the strain limits described in Section 2.5 – when determining the displacement capacity of the walls by means of plastic hinge analysis. The two approaches discussed in the following are those by Oesterle *et al.* [1984] and Paulay and Priestley [1992].

Oesterle *et al.* [1984] tested a series of flanged and barbelled walls, of which some failed due to crushing of the diagonal in compression. They observed that crushing occurred only after significant flexural and shear yielding had taken place. Instead of relating the loss of diagonal compression capacity to strains, as the modified compression field theory does, they proposed to link the capacity to the drift demand δ_{pb} in the plastic hinge zone since drift is a more readily available parameter in seismic design. For axial load ratios of $0 < P/A_g f'_c \leq 0.09$ they gave the following expression for the maximum shear force sustained prior to web crushing:

$$V_{Rd} = 0.8l_w t_w \cdot \frac{1.8f'_c}{1 + (600 - 2000 \cdot \frac{P}{A_g f'_c})\delta_{pb}} \quad (2.28)$$

Hines and Seible [2004] argued that the web crushing capacity should not be a function of the axial force in the wall section. From their experiments they found that the load path of the axial force did not interfere with the critical compression strut in the plastic hinge zone and hence they concluded that the two mechanisms should be considered independently.

Paulay and Priestley [1992] linked the loss of the diagonal compression capacity to the over-strength factor $\Phi_{o,w}$ and the displacement ductility μ_Δ – two design quantities that are even more readily available than the drift over the plastic hinge region used by Oesterle *et al.* [1984]. For design, Paulay and Priestley suggested to limit the nominal shear stress $v_i = V/b_w d$ to

$$v_i \leq \left(\frac{0.22\Phi_{o,w}}{\mu_\Delta} + 0.03 \right) f'_c \leq 0.16f'_c \leq 6MPa \quad (2.29)$$

The limit of $0.16f'_c$ was the minimum nominal shear stress for which web crushing was observed in the experiments conducted by Oesterle *et al.* [1984] indicating that the equation proposed by Paulay and Priestley [1992] is a design equation that aims at a certain degree of conservatism. Hines and Seible [2004] criticised the design approaches by Oesterle *et al.* [1984] and Paulay and Priestley [1992] for assuming evenly distributed shear stresses across an effective section and found from comparison with experiments that the two approaches led to very conservative estimates of the web crushing capacity.

2.6 Literature review on estimates for shear deformations

Unlike the flexural stiffness, the shear stiffness typically receives relatively little attention when slender RC structural walls are modelled. For such members shear deformations are often assumed as being insignificant and crude assumptions regarding the shear stiffness are common. In FEMA 356 [American Society of Civil Engineers (ASCE), 2000], for example, it is recommended to assign RC members a shear rigidity of $0.4E_cA_w$, where A_w is the area of the web cross section between the extreme compression fibre and the centroid of the tension reinforcement. Assuming that the shear modulus is $G_c \cong 0.4E_c$ the proposed rigidity corresponds approximately to the shear stiffness of an uncracked, elastic member. This certainly overestimates the actual stiffness of cracked RC members considerably and therefore the importance of shear deformations will be underestimated.

Although they have not found their way into all modelling guidelines, different approaches for treating shear deformations of RC walls subjected to inelastic deformations have been developed in the past. One of the earliest approaches was to reduce the effective shear area A_{sb} to a fraction of the gross area A_g , similar to what has been done in the past to account for the effect of cracking on the flexural stiffness:

$$A_{sb} = 0.5 - 0.8A_g \quad (2.30)$$

Note that the reduction factor of 0.8 originates from the theory of elasticity and does not account for cracking. For elastic, homogenous sections with a greater length than width the effective shear strain can be estimated as $\gamma = V/(5/6 \cdot A_g G_c)$, with the factor $5/6$ ¹ accounting for the increase of shear deformations due to the non-uniform shear stress distribution over the section. If the shear area is estimated according to Equation 2.30, the shear area is therefore reduced to 60 – 96% of the shear area of the elastic, homogenous section. The shear modulus is defined as

$$G_c = \frac{E_c}{2(1 + \nu)} \quad (2.31)$$

For concrete a Poisson's ratio ν between 0.2 – 0.25 is commonly assumed. The approach of reducing the shear area does not make allowance for the load transfer mechanism for shear forces in RC members after onset of cracking, which is generally attributed to shear reinforcement in tension and concrete struts in compression and is therefore not directly related to the shear stiffness of the concrete. Park and Paulay [1975] derived an equation for the shear stiffness on the basis of an analogous truss. They assumed the chord members as infinitely rigid and also neglected any deformations at the anchorage of the stirrups. For shear reinforcement

¹The factor of $5/6$ is only correct for materials with zero Poisson ratio, for other materials the factor is $(5 + 5\nu)/(6 + 5\nu)$ [Kaneko, 1975].

perpendicular to the element axis the shear stiffness per length can be written as

$$K_v = \frac{\sin^2(\theta) \cos^2(\theta)}{\sin^4(\theta) + n\rho_h} \cdot \rho_h E_s t_w d \quad (2.32)$$

where α is the inclination of the compression struts with respect to the element axis, ρ_v the shear reinforcement ratio $\rho_v = A_v/(sb_w)$, n the modular ratio E_s/E_c , t_w the wall width, and d the effective depth of the wall. Note that the units of K_v are those of a force. To obtain the shear stiffness of a member of the length h , the shear stiffness K_v has to be divided by h .

Both, the traditional approach and the approach by Park and Paulay [1975], assume that the shear stiffness remains constant when the wall is loaded in the inelastic range. Since the shear force carried by a wall increases only marginally once the nominal yield force has been reached, both approaches predict that for displacements beyond the nominal yield displacement the shear displacements remain approximately constant while the flexural deformations increase. Hence, according to these two approaches the ratio of shear to flexural deformations would decrease for increasing ductility demands. From experimental results Dazio [2000] found that this is not the case: When analysing rectangular walls that he had tested under quasi-static cyclic loading, Dazio observed that the ratio of shear to flexural displacements remained approximately constant for the peak displacements of all cycles in the inelastic range. Figure 2.8a and b are graphs reproduced from Dazio [2000]². The graphs show that the contribution of the shear displacements to the total displacements at peak values remains approximately constant over the entire ductility range and hence also the ratio of shear to flexural displacements remains approximately constant. This finding is important for the analysis and modelling of walls in which the shear displacements constitute a significant proportion of the total displacements.

Priestley *et al.* [2007] developed a shear model, which joins the truss model by Park and Paulay [1975] with Dazio's finding of the constant ratio Δ_s/Δ_f . In their model Priestley *et al.* [2007] distinguished between the state before and after shear cracking. The shear displacement at shear cracking was estimated as

$$\Delta_{s,1} = \frac{V_{cr}}{G_c A_{sb}} H \quad (2.33)$$

where Priestley *et al.* [2007] recommended estimating the shear modulus as $G_c = 0.43E_c$ and the shear area of solid sections as $A_{sb} = 0.87A_g$. The model developed by Park and Paulay [1975] applied to concrete sections that were cracked in shear. The shear force V_{cr} for which

²The graphs are not identical to the graphs in Dazio [2000] since the shear displacements in Dazio [2000] had been computed using the original method (Section 4.4.1) while the shear displacements shown in Figure 2.8 were computed using the method proposed by Hiraishi [1984].

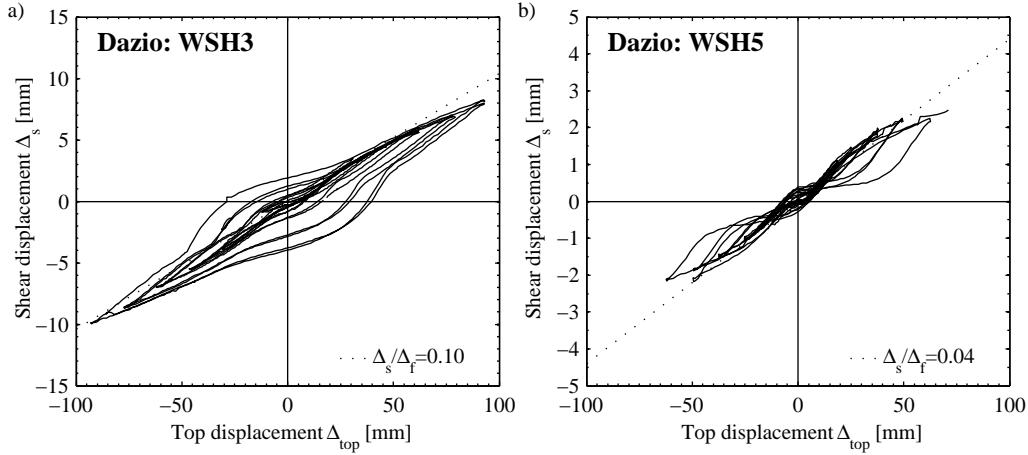


Figure 2.8. Shear displacement vs. top displacement for two rectangular walls tested by Dazio *et al.* [1999] showing the nearly linear relationship between Δ_s and Δ_{top} for peak displacements (adapted from Dazio [2000]).

onset of shear cracking occurs is estimated as the concrete contribution to the shear capacity for $\mu_{\Delta} = 1.0$ [Priestley *et al.*, 2007]:

$$V_{cr} = 0.29 \sqrt{f'_c} \cdot A_{sb} \quad (2.34)$$

Priestley *et al.* [2007] recommended using Equation 2.32 only in conjunction with $\theta = 45^\circ$ since for typical values of n and ρ_v the shear stiffness according to Equation 2.32 increases as the cracking angle θ reduces from 45° to 30° , which is in conflict with most observations from testing. Priestley *et al.* [2007] also suggested that the increase in modular ratio due to the softening of the diagonal concrete strut should be considered and proposed an average value of $n = 10$ for analysis purposes.

Between the instant of shear cracking and a displacement ductility of 1.0 the shear displacement is computed as the sum of the elastic shear displacement and a shear displacement component derived from the truss model. For a cantilever wall of height H the total shear displacement is:

$$\Delta_{s,n} = \Delta_{s1} + \frac{V_n - V_{cr}}{K_v} \cdot H \quad (2.35)$$

where V_n is the shear force corresponding to nominal flexural strength. From plastic hinge analysis or a comparable analysis approach the flexural displacement $\Delta_{f,n}$ at $\mu_{\Delta} = 1.0$ can be computed. For the post-yield phase Priestley *et al.* [2007] estimate the shear displacements as the flexural displacements multiplied by the ratio $\Delta_{s,n}/\Delta_{f,n}$:

$$\Delta_s = \Delta_f \cdot \frac{\Delta_{s,n}}{\Delta_{f,n}} \quad (2.36)$$

In the truss model by Park and Paulay [1975] the compression struts are assumed to be parallel. This assumption does not hold for the plastic hinge regions, where a fan-like crack pattern is typical. Hines [2002] derived an equation for shear displacements on the basis of this fan mechanism. The shear displacements Δ_s are expressed as a ratio of the flexural displacements Δ'_f that is associated with the same fan-like mechanism:

$$\frac{\Delta_s}{\Delta'_f} = \frac{l_w}{H} \quad (2.37)$$

where H is the shear span and l_w the wall length. Hence, as the approach proposed by Priestley *et al.* [2007], Hines' model for shear deformations follows Dazio's observation [2000] that the ratio of shear displacements to flexural displacements of structural walls is relatively constant over the entire displacement range, i.e. between yield displacement and ultimate displacement capacity of the structural walls.

Hines [2002] further assumed that the flexural displacement Δ'_f due to the fan mechanism accounts for about 25% of the total flexural displacement; the remaining 75% was linked to the very lowest cracks, which were not included in the fan mechanism, rotation of the column base due to strain penetration, and elastic displacements. With these assumptions the shear displacements Δ_s can be written as a function of the total flexural displacements Δ_f :

$$\frac{\Delta_s}{\Delta_f} = 0.25 \frac{l_w}{H} \quad (2.38)$$

By adding an empirical factor Hines *et al.* [2004] included two phenomena: First, that shear cracks tend to be wider when the shear demand is close to the shear capacity, and second, that shear cracks also tend to be larger for large cracking angles θ :

$$\frac{\Delta_s}{\Delta_f} = \alpha \cdot 0.35(1.6 - 0.02\theta) \frac{l_w}{H} \quad (2.39)$$

$$1 \leq \alpha = \left(\frac{V}{V_s} + \frac{V}{V_{sc}} \right) \leq 2$$

where θ is the angle in degrees to the vertical of cracks outside the fan mechanism measured at maximum displacement, V_s is the capacity to resist diagonal tension (capacity limited by yielding of stirrups) and V_{sc} is the capacity to resist diagonal compression (capacity limited by web crushing). Although Hines' model was derived from a mechanical model for the plastic hinge zone, the assumption regarding the sources of flexural displacements (25% from the fan mechanism) and the introduction of the factor to account for the opening of the shear cracks renders it effectively a semi-empirical model. So far, the model has been tested against eleven quasi-static cyclic tests on shear walls and bridge piers [Hines, 2002]; the comparison showed a good agreement between experimental and analytical results. Note, however, that the same tests were used to derive the semi-empirical model and hence further validation is required. Hines' model and the model by Priestley *et al.* [2007] will be applied to the two U-shaped

walls, which were tested within the scope of this project; the comparison of the predicted and experimentally determined Δ_s/Δ_f -ratios is presented in Section 4.4.2.

3. QUASI-STATIC CYCLIC TESTS OF TWO U-SHAPED WALLS

Within the scope of this project two U-shaped walls were tested under quasi-static cyclic loading. The key objective of these tests was to provide additional experimental evidence for U-shaped walls, which could promote the general understanding of their seismic behaviour. To our knowledge, the only previous test series on U-shaped walls under seismic loading was a joint research project between the laboratories in Ispra and Saclay; a brief summary of these experiments is given in Section 3.1. Unlike the walls tested in Ispra and Saclay, which were designed according to draft versions of the EC8, the test units of this project were not designed following a particular code but following principles that were judged "reasonable" to ensure a ductile behaviour without being unnecessarily conservative with respect to the shear and sliding shear design. It was believed that such test units would yield the best insight into the load transfer mechanisms of U-shaped walls and help to reveal critical aspects in their design.

Naturally, with two test units only a limited number of aspects could be investigated. The main focus of the experiments was set on the behaviour of U-shaped walls for loading in different directions. Based on this focus the following tasks were identified:

- Assess the failure mechanisms of U-shaped walls. In particular observe whether the U-shaped walls are susceptible to shear or sliding shear failure.
- Gain experimental evidence for the stiffness, strength and displacement capacity of U-shaped walls when loaded in different directions.
- Determine the magnitude of the different displacement components (flexure, shear and sliding component) of U-shaped walls for different directions of loading.
- Determine the torsional stiffness of the U-shaped walls.

These objectives were used as guidelines for all steps during the planning phase of the experiments, which concerned the test setup, the instrumentation, the loading history and the design of the test units. These steps are described in Sections 3.2, 3.3 and 3.4. In the final two sections

of this chapter selected results of the two tests are presented first in written form in terms of a description of the failure mechanisms (Section 3.5) and then in the form of force-displacement hystereses (Section 3.6). Note that the torsional stiffness of the U-shaped walls is not covered within this report but the experimental evidence on the torsional stiffness was gained for reasons of completeness and will be analysed at a later stage. The objective of this chapter is to provide some information on the experimental work on which the modelling and design chapters are based; a complete description and discussion of the experiments is beyond the scope of this document. For a complete presentation of the test set-up and the experimental results the reader is referred to the test report [Beyer *et al.*, 2008].

3.1 Previous experimental work on U-shaped walls: Tests in Ispra and Saclay

Within the scope of the joint research project of the laboratories in Ispra and Saclay one configuration of a U-shaped wall was tested under different loading schemes [Reynouard and Fardis, 2001]. The experiments were carried out in Ispra and Saclay in the years 1999 and 2000. The key objective of these tests on U-shaped walls was the validation of the design guidelines in the new Eurocode 8 [Combescure *et al.*, 1999a]. According to Ile *et al.* [2002a] eight walls were tested; out of these two walls were used for "calibration purposes" and results of these tests are not reported in the literature (one of these two walls had been tested on the shaking table and the other pseudo-dynamically). From the remaining six walls half were tested under quasi-static cyclic loading (Ispra-tests) and the other half on the shaking table (Saclay-tests).

All test units were based on the same prototype that represented a small elevator shaft. While the test units that were tested quasi-statically were full-scale models of the prototype the size of the test units that were tested on the shaking table was reduced to 60%. The cross-section of the prototype and therefore also of all test units was very compact due to the large wall thickness compared to the web or flange lengths (Figure 3.1a); this choice in the geometry rendered the test units rather particular and not very representative for most U-shaped walls used in practice.

The shaking table tests of the three down-sized test units were performed at the CEA-Saclay laboratory [Combescure *et al.*, 1999a]. Aside from the spacing of the confining reinforcement at the corners and flange ends, the three units were identical. The intensity of the input motion was increased stepwise from 0.1g to 1.0g. The units were loaded uni-directionally along their axes of symmetry. Due to very small ultimate strain capacities of the reinforcing steel ($\varepsilon_{su} = 2.5 - 2.6\%$) all units failed prematurely due to fracture of the main longitudinal bars. At failure concrete crushing was still very limited [Combescure *et al.*, 1999a]. Since the units were only loaded parallel to the flanges, the results provided little information regarding the behaviour of U-shaped walls under different directions of loading, which is the focus of

the study presented here. The Saclay-tests will therefore not be considered in the following chapters.

The full-size specimens of the prototype were tested under quasi-static loading regimes at the laboratories in Ispra. Apart from the scale, the Ispra- and Saclay test units differed regarding the shear span ratio, the axial load ratio, and the strain capacity of the reinforcement: For the Ispra-test units a very ductile steel was used, which had an ultimate strain capacity of $\varepsilon_{su} \cong 25\%$ [Pégon *et al.*, 2000b]. The three units tested in Ispra were identical; the cross section and elevation of the Ispra-tests are shown in Figure 3.1. According to Ile and Reynouard [2005] the U-shaped walls have been designed and detailed according to the old EC8 (ENV 1998-1-3:1994, CEN [1994]) and its proposed revision (prEN 1998-1:2001, CEN [2001]). Strictly speaking, however, the sections do not even comply with the detailing requirements for the medium ductility class since according to EC8 every other longitudinal bar within the boundary elements should be engaged by a hoop or a cross tie. At the flange ends, however, six longitudinal bars were placed in one line and only the outer two bars were stabilised by the confining hoops. The shear strength of the web and particular the flanges was in excess of what EC8 required. Each of the flanges were designed for the full shear demand in the y -direction to account for the fact that for bi-directional loading the flange in tension might not contribute much to the shear capacity [Ile and Reynouard, 2005]. Note that the reinforcement drawings of the test units, which are shown for example in Ile and Reynouard [2005], suggest that the shear reinforcing bars were straight bars that ended 160mm away from the flange end

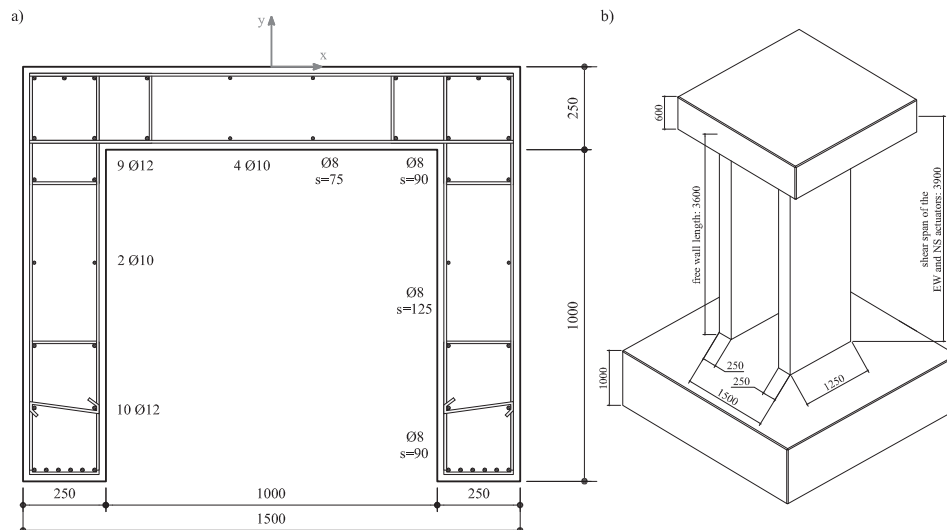


Figure 3.1. U-shaped walls tested in Ispra: Cross section (a) and elevation (b); all dimensions are in millimetres.

and 80mm away from the corner without being anchored around longitudinal bars. This reinforcement detail does not seem to be in conflict with EC8, since no specification regarding the anchorage of shear reinforcements are provided, but it does not comply with good detailing practice for ductile walls.

The three test units that were tested in Ispra were subjected to different quasi-static cyclic loading histories. During the tests the axial load was kept constant. At the base level the axial load was 2120kN, which corresponded to an axial load ratio between $P/f'_c A_g = 0.10 - 0.12$ for the three test units. The first test unit was subjected to a uni-axial cyclic loading scheme along the symmetry axis ("Ispra Y"), the second test unit to the same scheme but this time the unit was loaded parallel to the web ("Ispra X"), and the third test unit was loaded with a bi-directional clover leaf pattern ("Ispra XY"). The first test unit, which was loaded in the y -direction, failed at $\mu_\Delta = 6.0$ due to buckling and rupture of longitudinal reinforcing bars at one flange end, rupture of one hoop at the same flange end and concrete degradation [Pégon *et al.*, 2000d]. The failure was also caused by a missing hoop just above the wall base in the flange end that finally failed; the hoop had been forgotten during the construction of the test unit. The second test unit, which was loaded in the x -direction, failed at $\mu_\Delta = 6.0$ due to buckling and rupture of longitudinal reinforcing bars and fracture of a hoop at one flange end [Pégon *et al.*, 2000a]. During the bi-directional test the test unit failed during the fourth loop at $\mu_\Delta = 4.0$ [Pégon *et al.*, 2000c]. The failure began with the rupture of longitudinal reinforcing bars but ended in a shear failure of the flange that was in compression.

The test conducted in Ispra were the first tests on U-shaped walls under quasi-static cyclic loading and set a milestone in testing of structural walls. However, the choice of the very compact wall section, the insufficient detailing, and the high axial load that led to pinched hysteresis loops make the Ispra-test units fairly specific. The objective of the test series carried out within the project here is to extend the range of experimentally tested U-shaped sections to more commonly used layouts.

3.2 Experimental program

The two U-shaped walls that were tested within the scope of this project were both half-scale models of a typical lift shaft housing an 8-person elevator. The effective heights of the walls were determined from time-history analysis of a six-storey reference building shown in Figure 3.2. Details on the time-history analyses are given in Beyer *et al.* [2006]. The final shear spans of the half-scale walls were 2.95m in the direction parallel to the flanges and 3.35m in the direction parallel to the web. During testing of the walls the applied axial load was kept constant; the axial load at the base of the walls (i.e. including self-weight and weight of any

installations mounted onto the wall) was 780kN. The axial load was applied at the approximate centre of the gross sections.

The principle parameter distinguishing the two units was the wall thickness. The wall thickness of Test Unit A was 0.15m corresponding to 0.30m at full-scale, while the wall thickness of Test Unit B was 0.10m, which corresponds to 0.20m at full-scale; the latter can be regarded as a lower bound used in RC construction. The wall thickness was chosen as parameter because it influences the overall behaviour of the U-shaped walls. More specifically it affects – together with the concrete strength – the shear capacity of the wall, the compression zone depths and hence the strain demand on the concrete. The compression zone depth might become fairly deep for loading in the diagonal direction when only one flange end is in compression. In addition, the wall thickness controls possible out-of-plane shear, bending and stability effects. These effects are also difficult to model numerically and hence numerical parameter studies cannot substitute experimental results. Table 3.1 shows the cross sections and some characteristic values of Test Units A and B in comparison to those of the units tested in Ispra. In particular Test Unit B is considerably less compact than the Ispra-section and it is believed that the new experimental results will nicely complement the test series from Ispra.

Figure 3.3a and d show the reinforcement layout of Test Unit A and B (hereafter called TUA and TUB). Note that the cross section of TUB has been slightly revised since published in Beyer *et al.* [2006]. The longitudinal reinforcement was kept the same over the entire height of the wall. Only the spacing of the confining reinforcement was increased for $h \geq 1.70\text{m}$ above the wall base. The total area of the vertical reinforcement was approximately the same for the two test units (TUA: $A_s = 3281\text{mm}^2$, TUB: $A_s = 3224\text{mm}^2$). The horizontal reinforcement was identical for the two walls. Both the corners and the flanges were strongly confined

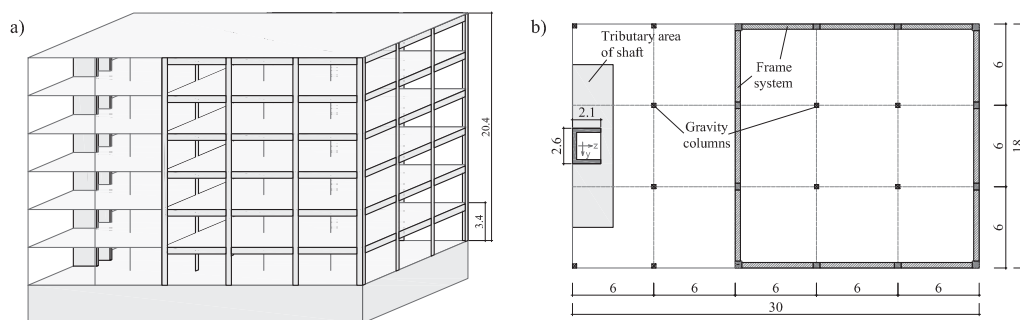
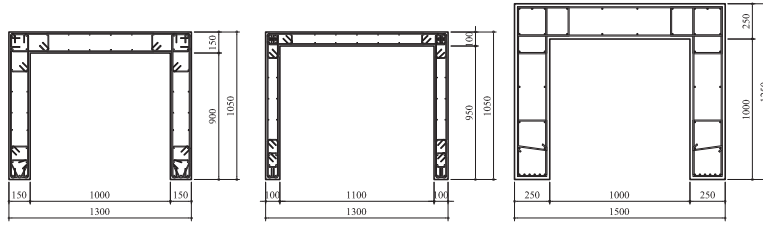


Figure 3.2. Test design: Six-storey reference building: Isometric (a) and plan view (b); all dimensions are in metres.

Table 3.1. U-shaped walls: Comparison of cross sections of TUA, TUB and the units tested in Ispra.



	TUA	TUB	Ispra
Scale	1 : 2	1 : 2	1 : 1
Shear span M/V	$2.95\text{m}^1/3.35\text{m}^2$	$2.95\text{m}^1/3.35\text{m}^2$	$3.90\text{m}^{1,2}$
Shear span ratio h/l_w	$2.81^1/2.58^2$	$2.81^1/2.58^2$	$3.12^1/2.60^2$
Axial load ratio $P/f'_c A_g$	0.02	0.04	0.10 – 0.12
Slenderness ratios:			
l_{web}/t_w	8.7	13.0	6.0
l_{fl}/t_w	7.0	10.5	5.0
Vertical reinforcement:			
ρ_{tot}	0.71%	1.00%	0.56%
Horizontal reinforcement:			
Web: ρ_b	0.30%	0.45%	0.54%
Flanges: ρ_b	0.30%	0.45%	0.32%

¹⁾ for displacements parallel to the flanges (NS direction)

²⁾ for displacements parallel to the web (EW direction)

to increase the compressive stress and in particular the compressive strain capacity of the concrete. The design approach adopted for TUA and TUB is summarised in Section 3.4.

As a measure against sliding shear failure the walls were equipped with shear keys at their bases (Figure 3.3b and e). The shear keys were unreinforced concrete studs, which were formed by moulds in the foundation. The foundation was cast before the wall. Prior to casting of the wall the moulds were lined with grease to prevent the fresh concrete from sticking to the moulds. When the wall was cast these moulds filled with concrete and thus provided an additional interlock between the wall base and the foundation.

Since the test units were half-scale models of the prototype wall the maximum aggregate size was also reduced from 32mm to 16mm in order to keep scale effects to a minimum. For the reinforcement, bars with 6 and 12mm diameter were used. Smaller diameter were not employed since in most cases the strain capacity of such bars is very limited. The concrete

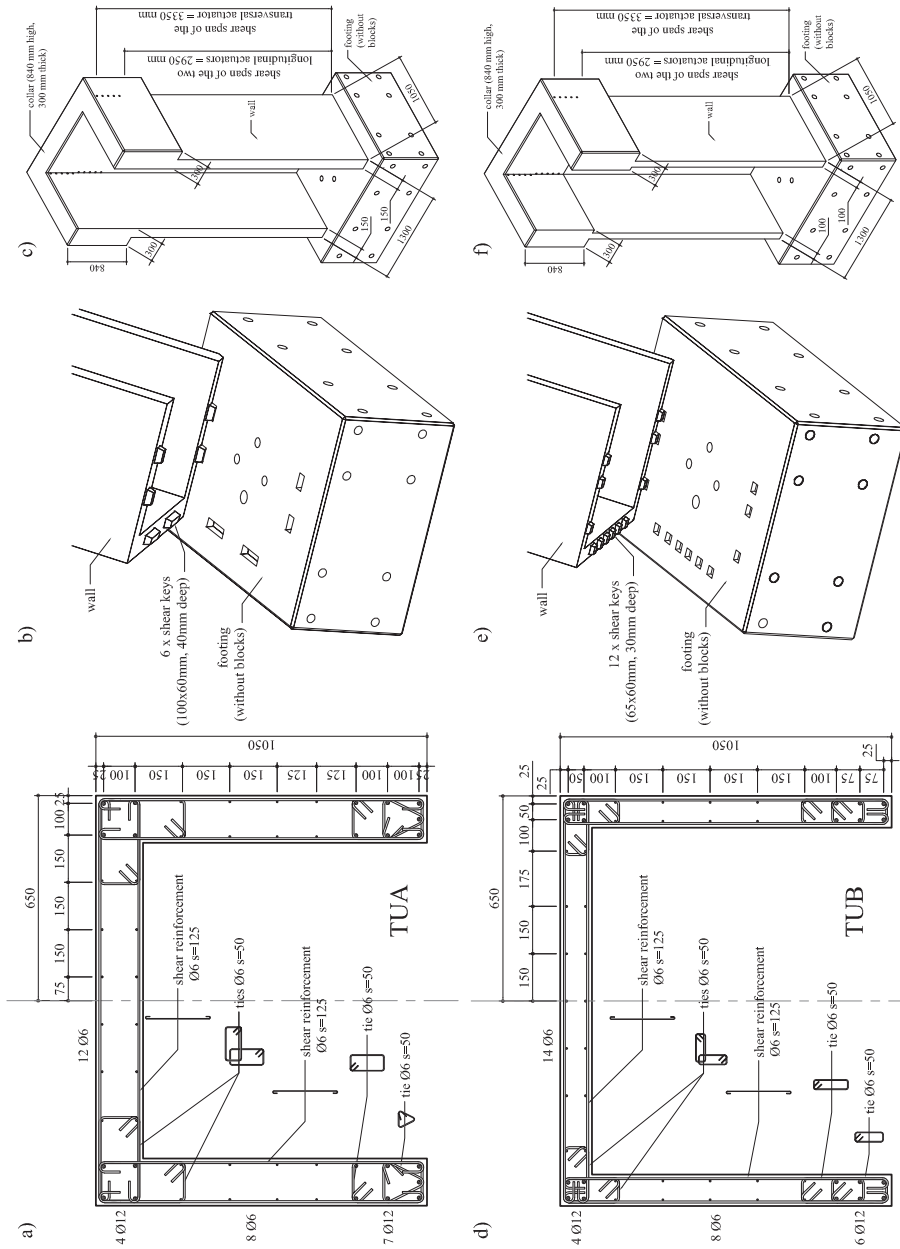


Figure 3.3: Cross section, shear keys and elevation of TUA (top row) and TUB (bottom row); all dimensions are in millimetres.

cylinder strengths of TUA and TUB at the day of testing were 77.9MPa and 54.7MPa respectively. In particular the concrete strength of TUA turned out significantly higher than intended. The objective had been to aim for $f'_c = 45\text{MPa}$, which would be representative of a concrete C30/37 that is several years of age. The larger concrete strength increased the shear capacity of TUA and hence rendered it less susceptible to shear failure. On the other hand the large concrete strength reduced the number of cracks outside the boundary elements since the tensile strength of the concrete was also large. As a consequence, the crack widths were larger than for normal strength concrete, which in return reduced the shear strength due to aggregate interlocking. Due to the high concrete strength cracks often propagated through aggregates, which further reduced the shear capacity due to aggregate interlock. On the whole, however, the shear strength of TUA probably benefited from the high concrete strength. The large crack widths also placed a high strain demand on the longitudinal 6mm bars. As a consequence, some of the 6mm bars fractured towards the end of the test without prior buckling. The properties of the reinforcing bars are given in Table 3.2 (note that the material tests have been reevaluated since they have been published in Beyer *et al.* [2006]).

Table 3.2. Properties of reinforcing steel used for construction of TUA and TUB.

	f_y [MPa]	f_u [MPa]	f_u/f_y [-]	ε_{su} ¹⁾ [%]
TUA: D12 bars	488	595	1.22	12.6
TUB: D12 bars	471	574	1.22	12.7
TUA and TUB: D6 bars	518	681	1.32	8.4

¹⁾ The strain capacity ε_{su} was defined as the strain at maximum stress.

3.3 Test setup, loading history and instrumentation

An isometric view of the test setup for TUA and TUB is shown in Figure 3.4; a photo of it is shown in Figure 3.5. To control the two horizontal, translational and one twisting degrees of freedom of the wall heads, the walls were loaded with three actuators: The EW actuator, which loaded the web, and the NS actuators, which loaded the flanges. The alignment of the test units with the directions as well as the labelling of different web and flange regions is shown in Figure 3.6a. The force on the web (EW actuator) was applied at $h = 3.35\text{m}$ while the forces on the flanges (NS actuators) were applied at $h = 2.95\text{m}$ (Figure 3.3c and f). At the top of the wall – where the actuators were connected to the wall – the wall thickness was increased to 0.3m. This collar replaced the solid slab, which had been used as a load stub in the tests at Ispra (Figure 3.1); reasons for the choice of the collar instead of the solid slab are given in Beyer *et al.* [2006].

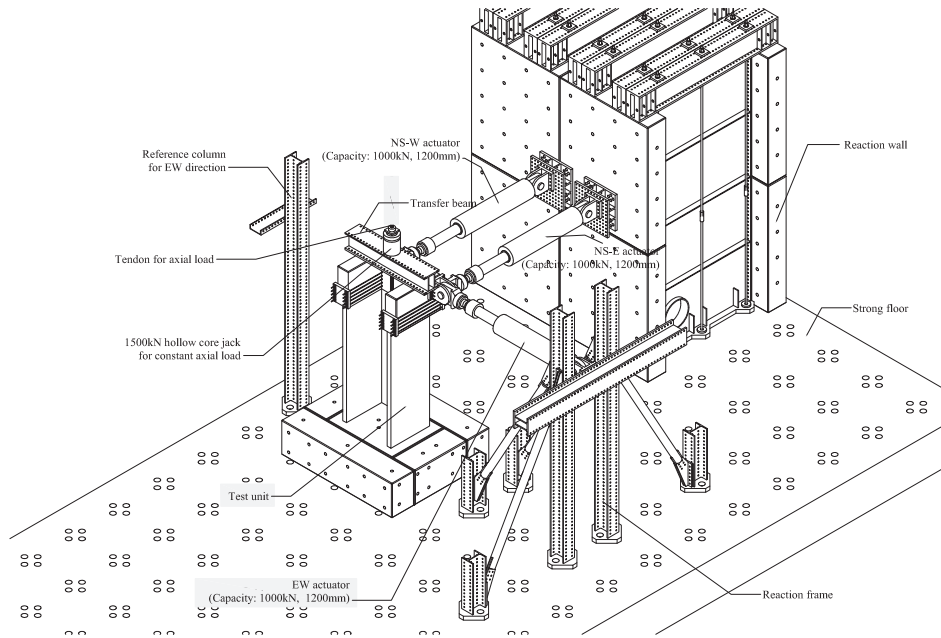


Figure 3.4. Isometric view of the test setup for TUA and TUB.

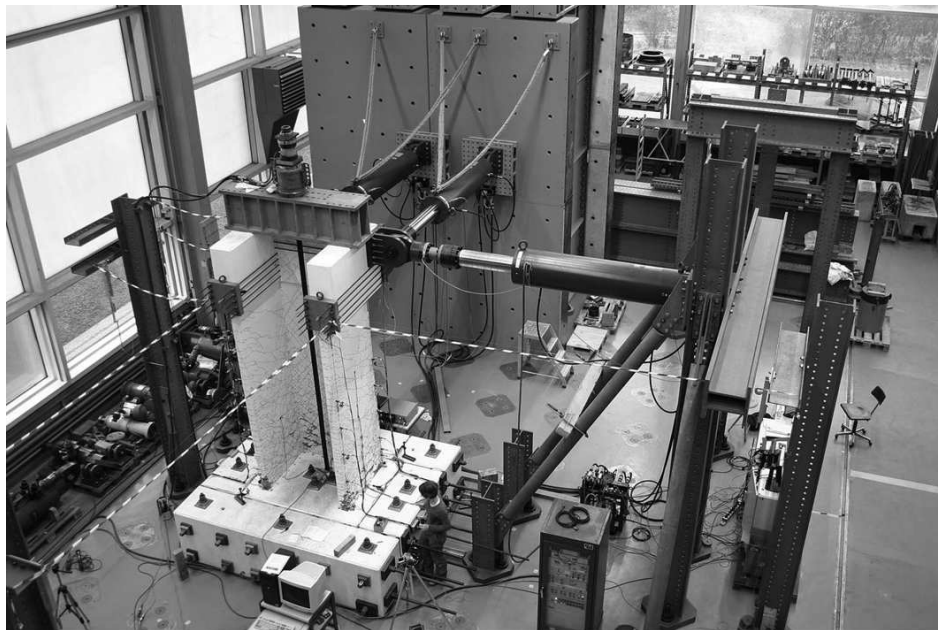


Figure 3.5. Photo of the test setup for TUA and TUB.

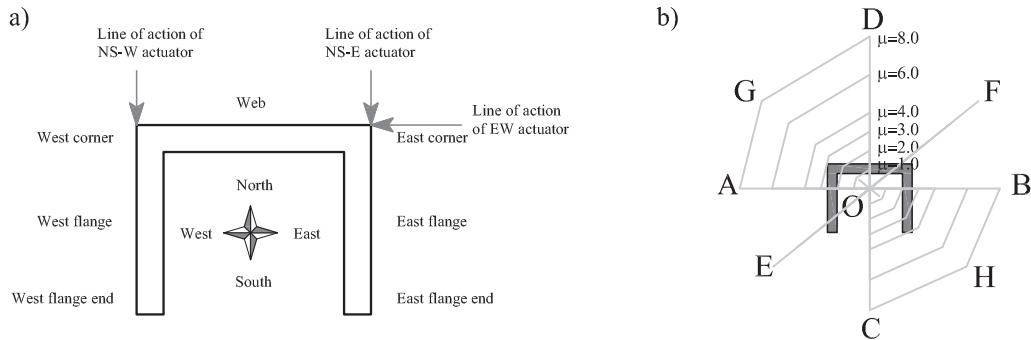


Figure 3.6. Cardinal points and labelling of different wall sections (a) and target displacement pattern (b).

As outlined in the introduction to this chapter the key objective of the experimental work was to characterise the behaviour of U-shaped walls for different directions of loading. Five different directions of loading were distinguished within this study and labelled with different letters (Figure 3.6b):

- Parallel to the web (Positions A and B),
- Parallel to the flanges, flange ends in compression (Position C),
- Parallel to the flanges, web in compression (Position D),
- In the diagonal direction, one flange end in compression (Position E and H),
- In the diagonal direction, one corner in compression (Position F and G).

When loading in the NS or the diagonal direction the displacement was controlled at $h = 2.95\text{m}$, for loading in the EW direction the displacement was controlled at $h = 3.35\text{m}$. The diagonal direction was defined as the geometric diagonal of the section that joins the outer corner with the outer edge of the flange end. Hence, for the diagonal movement the ratio of the displacements parallel to the web and flanges corresponded to the ratio of the web and flange lengths, i.e. $1.3 : 1.05$. Due to money and time constraints only one specimen of each of the two test units could be built and tested. Since the objective of the project was to assess the behaviour of the walls for different directions of loading, the test units had to be subjected to a bi-directional loading history. The chosen loading history is based on a pattern developed by Hines *et al.* [2002a] who proposed a history comprising a "sweep" and a diagonal at each level. The particularity of the "sweep" is that a yield displacement is also defined for the diagonal direction and hence the pattern seems to be more rounded than the

rectangular clover leaf pattern. The clover leaf pattern leads to large displacements in the diagonal directions and tends to impose higher ductility demands in the diagonal directions than in the principal directions. In the tests described here, the pattern developed by Hines *et al.* [2002a] is preceded by a full cycle parallel to the web and a full cycle parallel to the flanges. The complete loading history for one cycle is hence (see Figure 3.6b):

- EW cycle: Full cycle parallel to the web (O→A→B→O),
- NS cycle: Full cycle parallel to the flanges (O→C→D→O),
- Diagonal cycle: Full cycle in the diagonal direction (O→E→F→O),
- "Sweep" (O→A→G→D→C→H→B→O).

During these cycles the twist of the wall head was restrained. Only at Positions O, A, B, C and D during the cycles of ductility levels 1.0 and 4.0 small rotations were applied in order to determine the torsional stiffness of the walls. Altogether, the load pattern corresponded to three cycles parallel to the web and the flanges if the diagonal and the "sweep" were projected onto the principal directions. In terms of the number of plastic excursions (NPE) and the sum of normalised plastic deformation ranges (SNPDR) [Applied Technology Council, 1992; Krawinkler, 1996] the loading regime was hence more severe than the loading regime of the bi-directional test at Ispra, in which the wall was loaded with a full clover leaf pattern, which corresponded to two cycles in the two principal directions at each ductility level. The total loading history that was applied to TUA and TUB was the repetition of the load pattern at different ductility levels (Figure 3.6b). The first four levels were within the elastic range of the wall. The amplitudes of these cycles were force-controlled with limits of 25%, 50%, 75% and 100% of the lateral forces at first yield according to the prediction. During these cycles the sweep was replaced by the second diagonal (O→H→G→O). After first yield of the longitudinal reinforcing bars had been reached the nominal yield displacements in the five directions were determined on the basis of mean strains of vertical bars at the wall base in conjunction with the prediction made prior to the test (Table 3.6). The loading pattern was then repeated at displacement ductility levels of 1, 2, 3, 4, 6, 8 until failure occurred.

During the testing the behaviour of the walls was documented by taking notes and photographs as well as a large number of measurements. In total, 120 hard-wired instruments were installed, which measured local and global deformations, strains of selected transverse reinforcing bars as well as the applied forces. In addition, Demec measurements from Whitmore plugs were taken on the inside faces of the web and flanges in order to record the deformation pattern of the lower half of the wall. Finally, the width of selected cracks was measured manually at instants of peak displacements and zero loads.

The most important measurements were the actuator forces, the displacements of the wall head, the sliding displacements at the wall base, the elongation of the wall edges, and the shear displacements (Figure 3.7). The elongation of the edges was measured by four chains of linear variable displacement transducers (LVDTs). Each chain consisted of eight devices; the base length of the devices varied between 50mm at the base and 1000mm at the top. The lowest device measured the variation in length between $h = 50$ mm and the foundation, i.e. the measured displacement included the opening of the base joint due to strain penetration into the foundation. The shear displacements were measured by diagonal string pots on the outer faces of the web and the two flanges. Each face was covered by three crosses; the first cross covered the height interval between $h = 50 - 850$ mm, the second between $h = 850 - 1650$ mm and the third between $h = 1650 - 2650$ mm. With this instrumentation it was possible to determine the shear deformations for the web, the West and the East flange independently. A more detailed description of the instrumentation and the data acquisition systems can be found in Beyer *et al.* [2008].

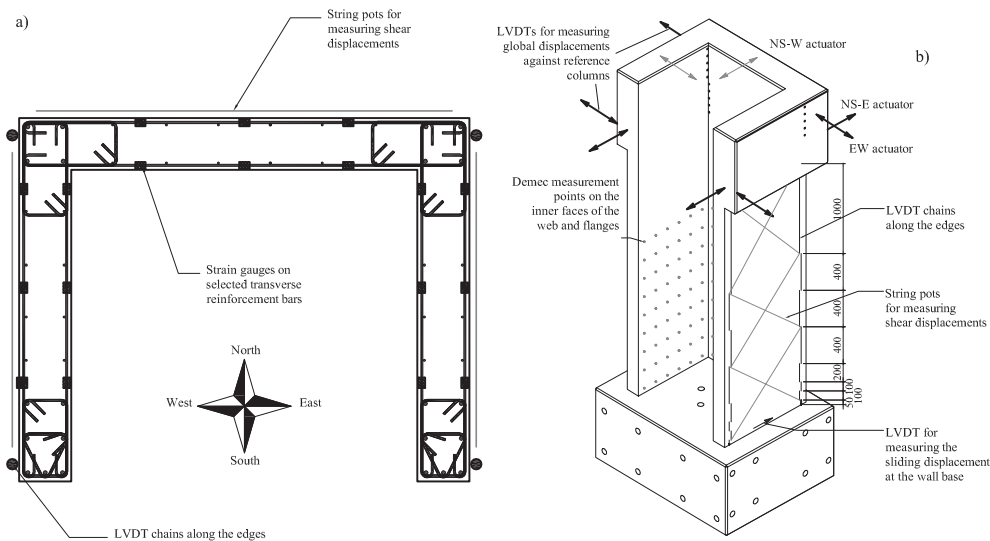


Figure 3.7. Instrumentation of TUA and TUB.

3.4 Design of test units

The design of the two test units did not follow a particular code but design approaches were selected that were judged reasonable in order to achieve a ductile behaviour of the test units. In this section the key aspects of the design process are described and discussed. The discussion is extended to aspects that concern the design of real U-shaped walls rather than test units and also includes further insights and considerations regarding the design of U-shaped walls that resulted from observations of the experiments. The section is divided into three parts covering the flexural design (Section 3.4.1), the shear design (Section 3.4.2), and the detailing of U-shaped walls (Section 3.4.3).

3.4.1 Flexural design

When designing the test units care was taken that the moment resistance about the positive and negative axis parallel to the web were approximately the same. For loading about the symmetry axis the positive and negative moment capacity were naturally identical. Equal moments in positive and negative direction are desirable in order to avoid an accumulation of maximum and residual displacements on the side with the smaller resistance over the course of the seismic excitation. If the U-shaped wall forms part of a larger lateral load resisting system, the moment resistance of the equilibrium of the entire structure should be considered. However, most structural elements that are used in combination with U-shaped walls (e.g. frames, rectangular walls) provide equal resistance in the positive and negative direction of loading and hence the U-shaped wall should likewise provide similar moment resistances in the positive and negative direction.

Figure 3.8 shows the moment-curvature relationships for TUA and TUB. These curves were computed before carrying out the experiments; updated moment-curvature relationships that were computed after completion of the experiments are included in Section 6.1.1. Before the experiments were carried out only first estimates of the strain capacity of the reinforcing bars were available. From these preliminary tests the strain capacity was estimated as 10%. The curvature was therefore limited to a curvature associated with $0.6 \times 10\% = 6\%$ maximum steel strain [Priestley *et al.*, 2007]. The reduction of the ultimate steel strain capacity by 40% accounts, for example, for effects on the tensile strain capacity due to buckling and compressive strains (see also Section 2.5.2). Table 3.3 summarises the nominal and ultimate moment capacities. The nominal moment was determined as the moment for which the maximum steel strain reached 1.5% or the concrete compressive strain 0.4%, whichever occurred first [Priestley *et al.*, 2007].

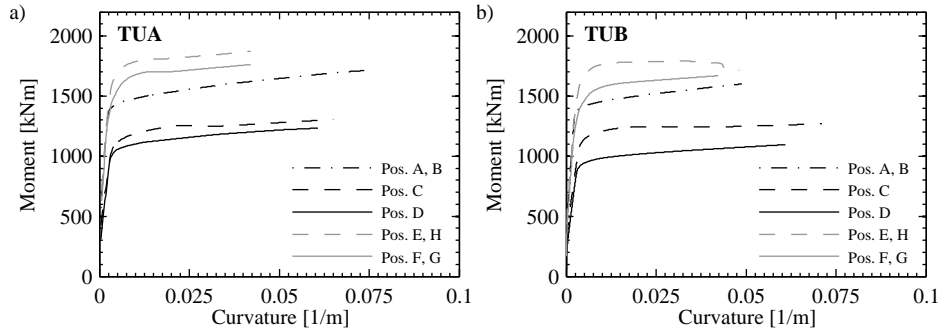


Figure 3.8. Predicted moment-curvature relationships for TUA and TUB

Table 3.3. Predicted nominal and ultimate moment capacities for TUA and TUB.

	Nominal moment			Ultimate moment		
	M_{EW} [kNm]	M_{NS} [kNm]	M_{SRSS} [kNm]	M_{EW} [kNm]	M_{NS} [kNm]	M_{SRSS} [kNm]
TUA						
Position A, B	1500			1640		
Position C		1230			1310	
Position D		1130			1230	
Position E, H	1430	1080	1790	1490	1130	1870
Position F, G	1390	960	1690	1440	1020	1760
TUB						
Position A, B	1470			1620		
Position C		1240			1340	
Position D		1010			1190	
Position E, H	1430	1040	1770	1480	1010	1790
Position F, G	1350	830	1580	1440	880	1690

M_{EW} Moment due to forces in the EW direction.

M_{NS} Moment due to forces in the NS direction.

M_{SRSS} Moment resulting from the vectorial addition of M_{EW} and M_{NS} .

3.4.2 Shear design

a) Shear demand.

For the shear design of TUA and TUB it was assumed that shear forces are carried as in-plane forces only, i.e. the shear force parallel to the web was entirely attributed to the web while the shear force parallel to the flanges was distributed between the two flanges. For loading parallel to the flanges, the shear force was distributed equally between the two flanges. For

loading in the diagonal direction, however, the shear force parallel to the flanges was entirely attributed to the flange in compression while the flange in tension was assumed to carry no significant portion of the lateral load. This load distribution scheme for the diagonal direction was proposed by Reynouard and Fardis [2001]. Table 3.4 summarises the nominal and ultimate shear demands on the web and on one flange for the different directions of loading. For loading in the diagonal direction the shear force demand on the critical flange, i.e. the flange in compression, is given.

b) Diagonal tension shear capacity.

Once the shear demand on the web and flanges was determined, the web and flanges of the U-shaped walls were designed as independent rectangular wall sections according to the modified UCSD shear model (Section 2.5.3). For the design a cracking angle of 30° with respect to the element axis was assumed. Table 3.5 summarises the different contributions to the shear resistance dependent on the direction of loading for the web and one flange. For loading in the diagonal direction the resistance of the critical flange, i.e. the flange in compression, which is assumed to carry the entire shear force in the NS direction, is given. The values were computed with the final material properties summarised in Section 3.2; safety factors were not included in the calculations. The contribution of the concrete to the shear resistance (Equation 2.26c) was computed for $\mu_\Delta = 6.0$ and bi-directional loading, thus leading to $k = 0.0625$. When the web was in tension (Position E) any contribution of the concrete to the shear resistance was disregarded since large crack widths were expected to reduce the shear resistance of the concrete considerably. The relatively large safety margin between demand and capacity was originally not intended but resulted mainly from a smaller yield strength of the D12mm longitudinal bars (Table 3.5). While according to the steel mill the characteristic strength, i.e. the 5%-fractile, of the Topar-S 500C, which was used as main longitudinal reinforcing bar, is $f_y = 500\text{MPa}$, the actual strengths of the batches used for construction of TUA and TUB were 488MPa and 471MPa respectively. For the design of the construction units a yield strength of 580MPa had been assumed. As a consequence, the shear capacity was less critical than originally intended.

While for the design of the test units the contribution of the axial load to the shear capacity was considered in order to omit unnecessary conservatism, it is questionable whether it should also be considered when designing U-shaped walls that form part of a real structure. There are several reasons for this reservation: In the experiment the axial load was applied at the centroid of the section but in most real structures (e.g. Fig. 3.2) the centroid of the U-shaped wall does not coincide with its centre of the tributary area. Hence, if the axial load is accounted for in shear design, the actual location of the resultant axial force should be considered. However, while for the experiments the location of the resultant axial force was known, in real, statically

Table 3.4. Nominal and ultimate shear force demands on the web and the critical flange.

	Nominal shear force demands				Ultimate shear force demands			
	TUA		TUB		TUA		TUB	
	$V_{n,web}$ [kN]	$V_{n,fl}$ [kN]	$V_{n,web}$ [kN]	$V_{n,fl}$ [kN]	$V_{ult,web}$ [kN]	$V_{ult,fl}$ [kN]	$V_{ult,web}$ [kN]	$V_{ult,fl}$ [kN]
Pos. A, B	447		439		490		484	
Pos. C		209		210		222		227
Pos. D		191		170		208		202
Pos. E, H	427	367	428	353	445	383	442	342
Pos. F, G	414	325	404	280	430	346	430	298

Table 3.5. Shear force capacities of the web and the critical flange.

	Web					Critical flange				
	V_p	V_c	V_s	V_{tot}	V_{tot}/V_{ult}	V_p	V_c	V_s	V_{tot}	V_{tot}/V_{ult}
	[kN]	[kN]	[kN]	[kN]	[-]	[kN]	[kN]	[kN]	[kN]	[-]
TUA										
Position A, B	133	86	423	642	1.31					
Position C						68	70	341	479	2.16
Position D						37	70	341	448	2.15
Position E, H	123	0	423	546	1.22	125	70	341	536	1.40
Position F, G	111	86	423	620	1.44	66	70	341	477	1.38
TUB										
Position A, B	133	48	423	604	1.25					
Position C						68	39	341	448	1.97
Position D						37	39	341	417	2.06
Position E, H	123	0	423	546	1.24	125	39	341	505	1.43
Position F, G	111	48	423	582	1.35	66	39	341	446	1.59

indeterminate structures, it can only be estimated. The magnitude and location of the resultant axial force is influenced by internal forces due to creeping and shrinking of the concrete. The redistribution might be particularly strong if the core wall is slip-formed before the rest of the structure is constructed. Apart from the shear capacity the eccentricity of the axial load also influences the flexural capacity, which contributes to the lateral load resistance of the system. When computing the flexural capacity, it is suggested to neglect the axial load eccentricity and consider the axial load applied at the centroid of the section.

c) Diagonal compression shear capacity (web crushing).

When designing the test units the web crushing capacity of TUA and TUB was assessed according to the formula given in the final version of EC8 (see Section 2.5.3). For TUA the diagonal compression capacities of the web and a single flange were 860kN and 694kN, respectively. For TUB these values reduced to 473kN and 382kN. For both TUA and TUB the capacity checks regarding web crushing were therefore satisfied even though the capacity estimates given in the final version of EC8 were rather low when compared to its draft version (Section 2.5.3).

When reassessing the web crushing after the experiments had been completed, alternative approaches were considered that accounted for the effect of the ductility demand on the web crushing capacity. From the observations during the experiments it was concluded that web crushing might become particularly important in the unconfined parts of the web and flanges. Due to the bi-directional loading, spalling of the concrete tends to extend deeper into these parts of the wall than into confined wall parts. The effective thickness of the unconfined wall sections is therefore considerably reduced. As a remedy the boundary elements could be extended further into the web and flange sections in order to confine and therefore protect a larger part of the wall from extensive spalling. Alternatively, a reduced wall thickness should be considered when the web crushing capacity is checked. As a first estimate the wall thickness could be reduced by four times the maximum aggregate size.

d) Sliding shear capacity.

For typical floor layouts, the tributary area for gravity loads of a U-shaped wall is often of similar size to the one of a rectangular wall (Figure 3.2b). Due to their large cross sectional area, when compared to rectangular walls, the axial load ratio $P/A_g f'_c$ of U-shaped walls tends to be quite small. Walls with low axial load ratios are particularly prone to sliding shear failure. Sliding interfaces are typically cold joints where the bond between the two concrete sections is limited, e.g. at the interface between the foundation and the wall. Since sliding was considered to be a potential failure mode care was taken that the interface between wall and foundation was representative of such interfaces in real structures. In order to achieve this, the wall and foundation were cast in two stages: First, the foundation was cast upright. The surface of the foundation forming the interface with the wall was roughened when the concrete began to stiffen. After a couple of days the foundation was turned by 90° and wall and collar were cast horizontally as one entity. Casting the wall upright as well was impossible due to height restrictions in the concrete factory. According to EC8 [CEN, 2003] both TUA and TUB would have failed in sliding shear. To prevent this type of failure diagonal reinforcement in the lower $0.5l_w$ or $0.5H$ (whichever is the smaller) of the wall would have been required. However, diagonal reinforcement is relatively difficult to place and in particular in medium

seismicity regions builders are often not used to such construction details. More importantly, it was felt that the design approach in EC8 does not reflect important parameters that influence sliding shear failure. Therefore, an alternative design approach was developed, which will be presented in a future study.

3.4.3 Detailing

The test units were detailed for large ductility demands. This meant that (i) all large diameter bars were stabilised by hoops, (ii) the spacing of the hoops was selected to prevent premature buckling of the longitudinal bars, and (iii) the confinement ensured the integrity of the concrete compression zone up to large compressive strains. A 50mm spacing of the hoops was chosen, which corresponded to 4.2 times the diameter of the main longitudinal reinforcing bars (12mm). The hoops were closed by 135°-hooks while the shear reinforcement had 180°-hooks at both ends. To ease the construction of the units the confinement was limited to boundary elements at the corners and flange ends; this is also the typical detail used for real constructions. The extent of the boundary elements into the web and flanges were determined from section analysis as the area where the maximum compression strain exceeds 0.004; also considered were other restraints as, for example, the layout of the vertical reinforcement. Loading in the diagonal direction caused the deepest compression zones in both the flange ends and the corners and therefore dictated the size of the confined zones.

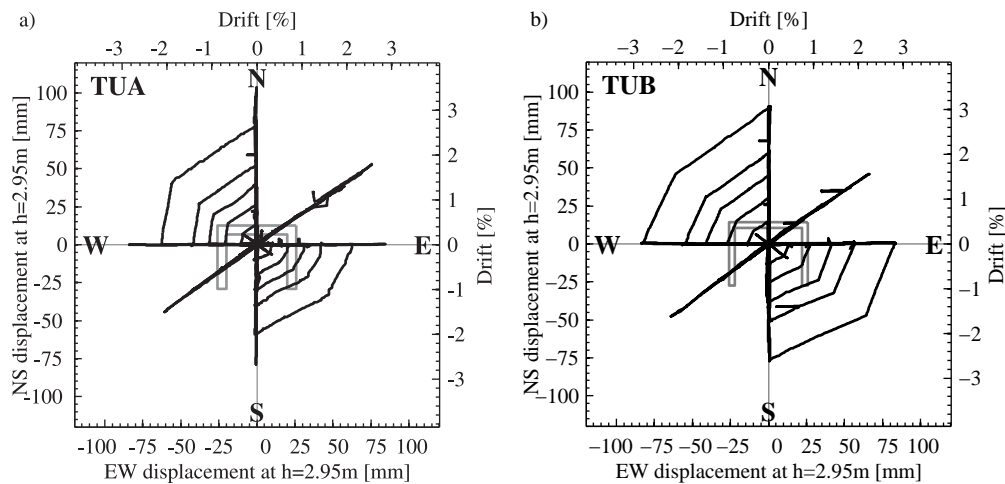
Based on the observations during testing it is now believed that in particular the boundary elements in the corners were essential for the integrity of the section when the wall was subjected to large lateral displacement demands. When designing a U-shaped wall it is therefore recommended to pay particular attention to this detail.

3.5 Experimental results: Failure mechanisms

In this section a brief description of the failure mechanisms of TUA and TUB is given. Emphasis is placed on the description of the damage state indicators, such as concrete spalling, concrete crushing and reinforcing bar buckling and fracture. In Chapter 4 these indicators will be related to strain limits, which are employed to define displacement limits in plastic hinge analysis. Also included in the present chapter is a discussion on the significance of out-of-plane deformations of the web and flanges and sliding shear displacements along the wall base. Table 3.6 summarises the yield displacements of TUA and TUB in the five directions of loading and also lists maximum attained displacements and drifts. A discussion of the magnitude of the yield displacements is given in Section 6.1.2b. Figure 3.9 shows the actual imposed displacement pattern as seen from the top. The comparison to the target displacement pattern (Figure 3.6b) shows that the actuator control system worked very effectively.

Table 3.6. TUA and TUB: Yield displacements and drifts and maximum displacements and drifts for the different directions of loading.

	TUA				TUB			
	Δ_y [mm]	δ_y [%]	Δ_{max} [mm]	δ_{max} [%]	Δ_y [mm]	δ_y [%]	Δ_{max} [mm]	δ_{max} [%]
Position A, B ($h = 3.35\text{m}$)	10.4	0.31	83.2	2.48	13.5	0.40	81.0	2.42
Position C ($h = 2.95\text{m}$)	9.8	0.33	78.4	2.66	12.7	0.43	76.2	2.58
Position D ($h = 2.95\text{m}$)	13.0	0.44	104.0	3.53	15.0	0.51	90.0	3.05
Position E ($h = 2.95\text{m}$)	8.8	0.30	70.4	2.39	12.7	0.43	76.2	2.58
Position F ($h = 2.95\text{m}$)	10.5	0.36	84.0	2.85	12.1	0.41	72.6	2.46

**Figure 3.9. TUA and TUB: Actual imposed displacement history as seen from the top.**

3.5.1 TUA

Test Unit A failed due to fracture of the longitudinal bars. Buckling of the longitudinal bars was observed for the first time at $\mu_{\Delta} = 6.0$ during the cycle in the diagonal direction. At Position E the buckled D12 bar in the outer corner of the West flange buckled; at this time the curvature of the bar was still fairly moderate. The first bar fractures occurred in the EW cycle at $\mu_{\Delta} = 8.0$ when loading to Position B: Two D6 bars in the West flange ruptured (Figure 3.10); these bars had previously buckled because their cover concrete had been lost. During the following NS cycle a distinct "bang" during the loading from O→C indicated that

a further D6 bar must have ruptured. However, the ruptured bar could not be identified. It was probably a bar in the web that had not previously buckled but which strain capacity had been exceeded due to the large crack spacings. The first D12 bar ruptured when loading from C→D at $\mu_{\Delta} = 8.0$. It was the outermost D12 bar in the West flange end, which had previously buckled. The then following cycle in the diagonal direction at $\mu_{\Delta} = 8.0$ was the final cycle: When loading to Position E (flange end in compression) two further D6 bars in the web ruptured that had buckled during preceding cycles. The two D12 bars at the West flange end, which had not yet ruptured, kinked very much towards the inside of the wall. Upon load reversal (E→F) these two bars ruptured. In addition, one further D12 and all remaining D6 bars in the West flange ruptured causing the final failure of the TUA.

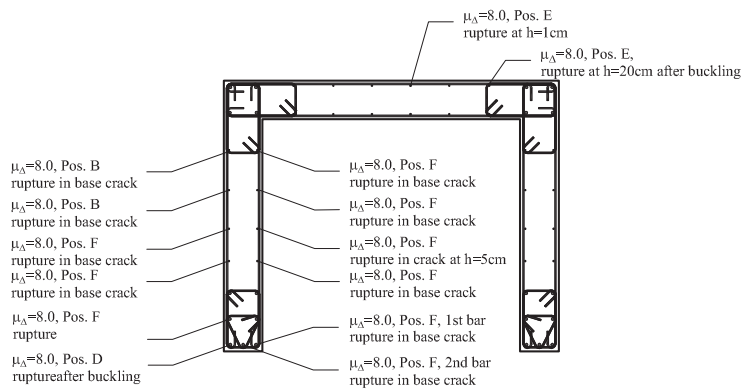


Figure 3.10. TUA: Longitudinal bars that fractured during the cycles of $\mu_{\Delta} = 8.0$.

Failure of concrete in compression was not observed for TUA. Onset of concrete spalling was observed at $\mu_{\Delta} = 3.0$ during the sweeping motion. However, spalling at this stage was still very limited and became only significant from the diagonal cycle at $\mu_{\Delta} = 4.0$ onwards. Until the end of the test the concrete in all four confined boundary elements was in a fairly good condition whereas the unconfined concrete of the flanges and the web seemed to "decompose" during the cycles at $\mu_{\Delta} = 8.0$, i.e. it did not form a unit anymore but was divided by cracks into pieces that moved relative to each other. Due to the bi-directional loading history a complex crack pattern on the web and flanges had formed (Figure 3.11). While the crack pattern of the web looked fairly similar to the typical crack pattern of a rectangular wall under uni-directional excitation, the flanges showed cracks of very different angles for the different directions of loading. The steepest cracks occurred at Position E and H, respectively, within the flange whose end was in compression.

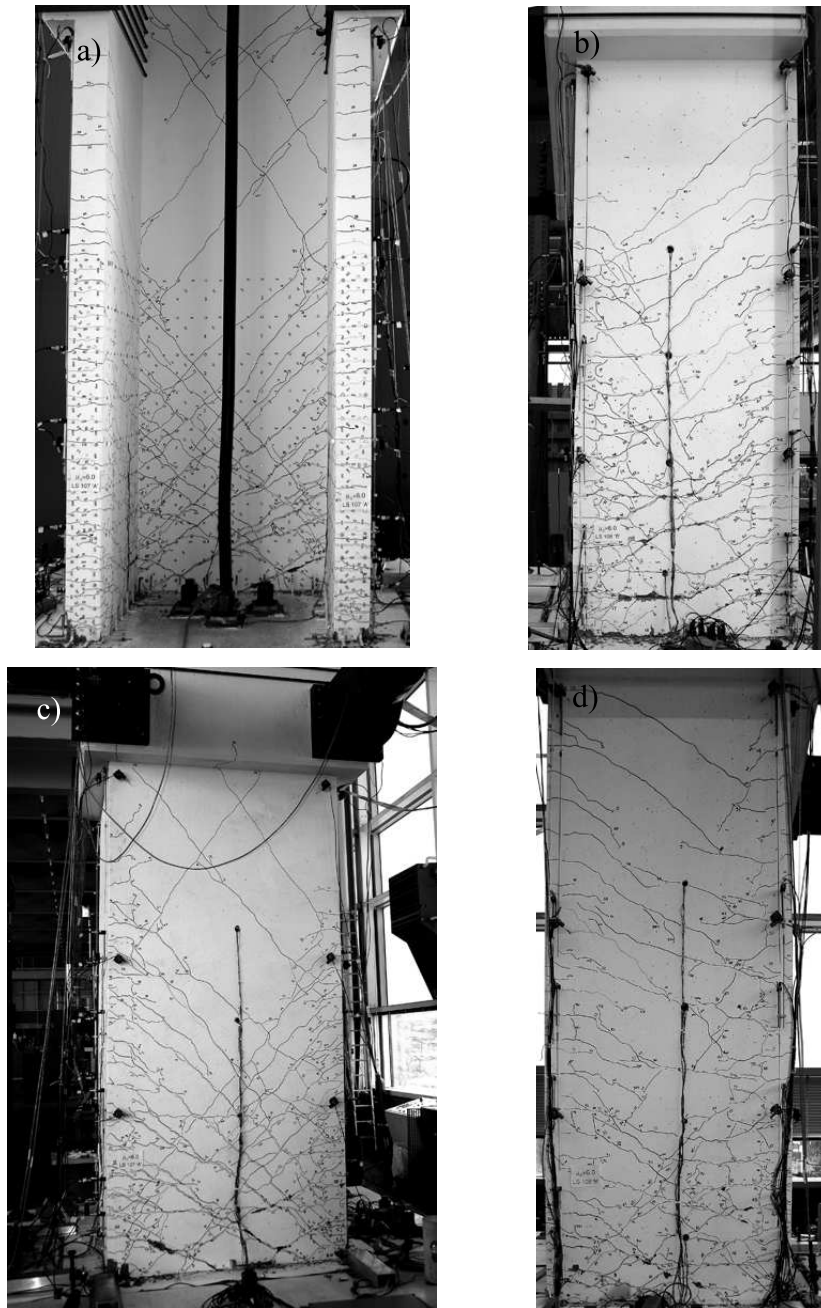


Figure 3.11. TUA: Crack pattern towards the end of the test (photos taken at Position A and B during EW cycle with $\mu_{\Delta} = 6.0$): South face (a), West face (b), North face (c) and East face (d).



Figure 3.12. TUA: West flange end showing the ruptured D12 bars (a) and the lower part of the West flange and the web (b) at Position F during the diagonal cycle with $\mu_{\Delta} = 8.0$ (point of failure).

Due to restrictions to the instrumentation, out-of-plane movements were not measured but could only be observed visually. Out-of-plane deformations were only observed within the lowest 50cm of the wall where crack widths were wide enough to accommodate lateral movements. The first out-of-plane deformations that were noted during testing of TUA occurred at Position B during the sweep at $\mu_{\Delta} = 3.0$: In the vicinity to the West corner, which was at this instant under tension, the West flange and the web moved inwards. Along two cracks at heights of $h \cong 20\text{cm}$ and 44cm the horizontal offset along the crack was about 0.5mm . During later cycles the same out-of-plane movement could be observed when the wall was pushed towards Position B. During the cycles of ductility level 6.0 out-of-plane movements were observed in further wall sections: At Position E during the diagonal cycle at $\mu_{\Delta} = 6.0$ a slight outward movement of the West flange end occurred. The crack in which the out-of-plane movement was concentrated was 30cm above the wall base. It is likely that the movement took place during the unloading phase from D to E when the cracks in the flange end were still open because at Position D (during the NS cycle) the flange ends had been in tension. The lateral movement was, however, so small that it did not cause a stability problem. At Position G the West corner moved outwards by about $\sim 2\text{mm}$. The crack in which the lateral movement was located was at $h \cong 20\text{cm}$ above the wall base. At Position B out-of-plane movements were also observed for the East flange: The part of the flange above a crack at $h \cong 20\text{cm}$ moved outwards; the offset was approximately $\sim 5\text{mm}$. Finally, large out-of-plane deformations within the web occurred during the final cycle. At the point of failure (Position F) the maximum lateral offset within the web was $\sim 15\text{mm}$. The presence of out-of-plane deformations showed that out-of-plane forces played a role in the load transfer mechanism when the wall was not loaded along its symmetry axis. In particular loading in the diagonal direction caused out-of-plane deformations. However, during all but the final cycle the out-of-plane deformations were relatively small and did not impair the capacity of the wall.

Throughout the test, sliding shear displacements at the wall base were fairly small. At peak displacements of the EW, NS and diagonal cycles at $\mu_{\Delta} = 6.0$ the maximum sliding displacement of the web, West and East flange were 2.5mm, 1.2mm and 1.6mm, respectively, which corresponded to 4.4%, 3.0% and 2.0% of the top displacements at these instants. For cycles of smaller ductilities the sliding displacement were considerably smaller. As described before, during the cycles at $\mu_{\Delta} = 8.0$ the unconfined concrete near the wall base degraded considerably. The devices that measured the sliding shear displacements were fixed to the unconfined concrete. Due to the relative movement of the pieces, the sliding displacement measurements became less reliable and the intensive cracking caused some instruments measuring the sliding displacement to fall off. At the end of the test, when the base crack was in some parts about one centimetre wide, one could see that at least one of the shear keys in the West flange had sheared off. The condition of the other shear keys could not be inspected.

3.5.2 TUB

TUB failed due to crushing of compression diagonals in the unconfined part of the web when loading from H→B during the sweep at $\mu_{\Delta} = 6.0$. For TUB concrete spalling initiated already during the cycles at $\mu_{\Delta} = 2.0$ but longitudinal reinforcement did not become visible until the NS cycles at $\mu_{\Delta} = 4.0$. As a result of the bi-axial loading, spalling of the concrete spread from the boundary elements towards the unconfined regions. In the unconfined regions the loss of section width due to spalling was significantly greater than in the confined regions (Figure 3.14). The reduction of the wall width led eventually to the web crushing failure. In the region where the compression struts finally failed the width of the wall had in some parts been reduced to as little as ~ 3 cm. After failure of the compression struts there were even a number of continuous holes through the web. The crack pattern that developed as a result of the bi-directional loading history is shown in Figure 3.13. In comparison to TUA the spacing of the cracks was smaller (see Section 3.2) and the upper part of the wall had cracked more severely. In addition, the steep cracks forming in the West and East flanges at Position E and H, respectively, were even slightly steeper than for TUA ($\sim 25^{\circ}$ compared to $\sim 30^{\circ}$).

Unlike typical web crushing failures the failure of the wall was not very catastrophic since part of the lateral load could be transferred to the well-confined boundary elements at the corners. These then acted as short columns while the web part above the failed compression strut acted like a stiff "beam". Figure 3.14 shows the South and North face of the web at the point of failure. In particular at the East edge a distinct drift of the short column is clearly recognisable. The concrete of the confined corner elements was still in a very good condition. However, the system did become softer and the lateral load dropped by more than 20% with

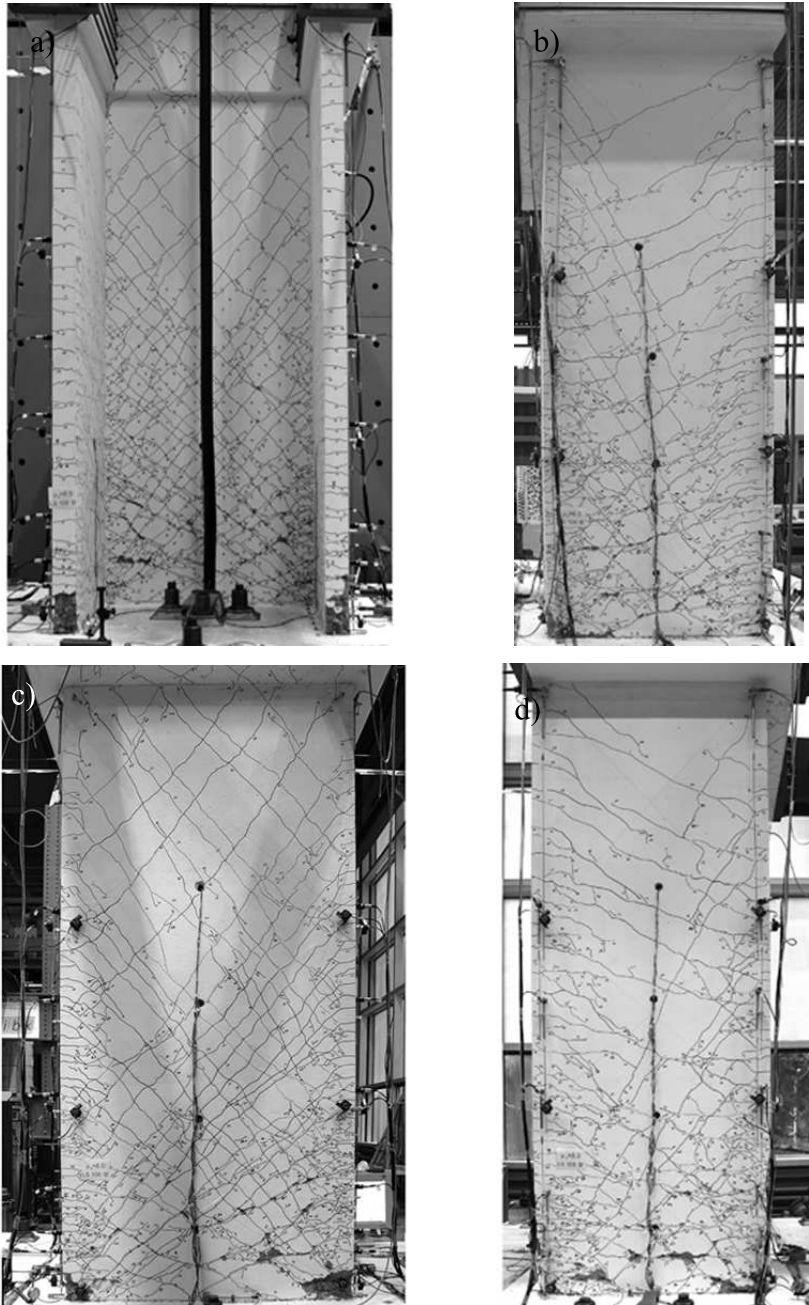


Figure 3.13. TUB: Crack pattern towards the end of the test (photos taken at Position B during EW cycle with $\mu_{\Delta} = 6.0$): South face (a), West face (b), North face (c) and East face (d).

respect to the loads attained at Position B during previous ductility levels. It was therefore decided to stop the test and the wall was unloaded.

As outlined in Section 3.4.2c During the design of the test units the web crushing capacity was determined according to EC8 [CEN, 2003]. According to this approach the web crushing capacity exceeded the shear demand. The following reasons, which had not been considered during design, might explain the discrepancy between predicted and actual web crushing capacity:

- The in some parts of the wall extensive reduction of the wall thickness had not been accounted for when designing the wall against web crushing.
- Independent of the reduction of the wall thickness the web crushing capacity tends to reduce with increasing ductility demand. This is not explicitly accounted for in the equation given in EC8 [CEN, 2003], which is intended for structures of the ductility class DCH. This ductility class corresponds roughly to a maximum displacement ductility of about 3.0¹, which is only half of the ductility that TUB reached. The limited ductility level had not been considered during the design stage; this might partially account for the inadequate web crushing capacity.

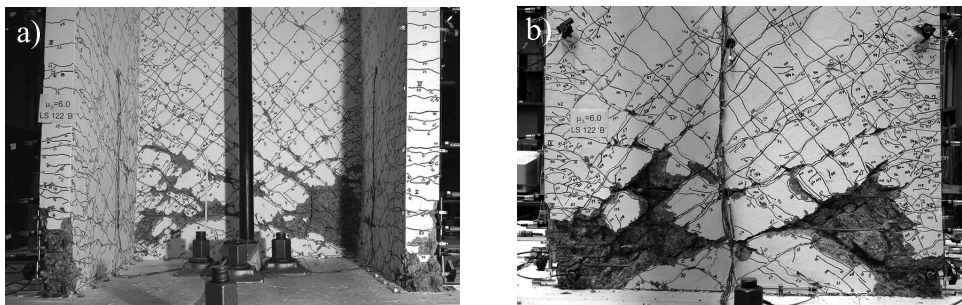


Figure 3.14. TUB: South face (a) and North face (b) at Position B during the sweep at $\mu_{\Delta} = 6.0$ (point of failure).

None of the longitudinal bars of TUB had fractured when the wall failed due to crushing of the compression diagonal in the web. Buckling of the bars had, however, occurred. It was first observed during the diagonal cycle (O→E) at $\mu_{\Delta} = 6.0$ for the two bars of the West flange

¹According to [CEN, 2003] the behaviour factor q for uncoupled slender walls is 4.0 assuming a redundancy factor α_u/α_1 of unity. With a typical overstrength factor of $\Phi_{o,w}$ of 1.5 a q -factor of 4.0 corresponds to a displacement ductility of 2.7 (applicable to period ranges for which the equal displacement approximation holds).

end, which were then under compression. The longitudinal bars were only visible between the first and second hoop (the first being at base level). Hence, the buckling mode was a single bent between these two hoops. During the cycles of the subsequent sweep the cover concrete was lost up to the fourth and fifth hoop at the East and West flange ends respectively. As a consequence, when the flange ends were loaded in compression again, buckling occurred up to the heights where the longitudinal bars were bare.

Although the wall sections of TUB were fairly slender out-of-plane movements were limited. During cycles of smaller ductilities indications for out-of-plane deformations were limited to vertical cracks on the inner faces of the flanges in the vicinity of the corner. Such cracks had not been observed for TUA. The first of the vertical cracks appeared at Position B during the sweep at $\mu_{\Delta} = 2.0$. It appeared on the inner face of the East flange about 21cm away from the corner. From then on, every time the wall was pushed to Position B, some existing vertical cracks on the inner face of the East flange elongated and/or new vertical cracks formed. The same happened at Position A on the inner face of the West flange: The first vertical crack formed at Position A during the EW cycle at $\mu_{\Delta} = 3.0$. The crack was about 23cm away from the corner. During later cycles further vertical cracks appeared and existing ones propagated further up the wall. Apart from the vertical cracks there was only very limited indications for out-of-plane movements. Some lateral displacement of the West flange end could be observed at Position E at $\mu_{\Delta} = 6.0$. Probably due to out-of-plane shear forces that were transferred from the wall to the foundation within the compression zone at the flange end a small lateral movement was recognisable. The lateral movement showed up as two small kinks (i.e. concentrated rotations within cracks) at about 15 and 30cm above the wall base. The magnitude of the lateral movement was a few millimetres. However, the shape of the wall did not give the impression that failure due to out-of-plane movements was imminent.

Sliding displacements at the wall base were even smaller than for TUA. The maximum sliding displacements that were measured before the sweeping motion at $\mu_{\Delta} = 6.0$ was commenced were 1.00mm, 1.70mm and 4.04mm for the web, West and East flange respectively. These sliding displacements made up 1.2%, 2.2% and 4.4% of the top displacements.

3.6 Experimental results: Force-displacement hysterereses

The internal force distribution within the U-shaped walls under bi-directional loading is very complex and requires some consideration when designing U-shaped walls. To give an idea of how the forces varied during the cycles at one ductility level the actuator forces during the $\mu_{\Delta} = 4.0$ cycles are discussed in Section 3.6.1. The forces are considered mostly as individual actuator forces. In addition, the moments and displacements in the EW and the NS direction are combined in SRSS quantities. By definition the SRSS moment and displacement are

always positive quantities. For plotting hysteresis loops the SRSS moment and displacement were multiplied by the sign of the displacement in the NS direction. The SRSS moment and displacement are hence defined as:

$$M_{SRSS} = \sqrt{(F_{EW} \cdot 3.35\text{m})^2 + (F_{NS} \cdot 2.95\text{m})^2} \cdot \text{sign}(F_{NS}) \quad (3.1a)$$

$$\Delta_{SRSS} = \sqrt{\Delta_{EW,2.95m}^2 + \Delta_{NS,2.95m}^2} \cdot \text{sign}(\Delta_{NS}) \quad (3.1b)$$

where F_{EW} is the EW actuator force that was applied at $h = 3.35\text{m}$ and F_{NS} is the sum of the NS actuator forces that were applied at $h = 2.95\text{m}$. The diagonal displacement was computed at the height of the NS actuators ($h = 2.95\text{m}$).

3.6.1 Cycles with $\mu_{\Delta} = 4.0$

In this section, the force distribution during the $\mu_{\Delta} = 4.0$ cycles is discussed in a qualitative manner. Note that during the testing of the walls only the forces applied by the actuators could be measured while the force distribution at the wall base could not be recorded. The forces plotted in the subsequent graphs are hence actuator forces. The actuator forces during the $\mu_{\Delta} = 4.0$ cycles are presented in two types of graphs: Figure 3.15 and 3.16 show a graphical representation of the forces at the peak displacements during the cycles at $\mu_{\Delta} = 4.0$ while Figure 3.18 shows the force-displacement hystereses of TUA and TUB for ductility level 4.0. The force-displacement pairs that belong to peak displacements are marked in the figures with letters corresponding to the respective positions.

When a U-shaped wall is loaded parallel to its flanges (Positions C and D), the force distribution is simple since the wall is displaced parallel to its symmetry axis: The lateral force in the NS direction is split in equal parts between the two flanges while the force applied to the web diminishes. In practice, different states of cracking of the two flanges and different stress states in the preceding cycle lead to slightly different flange forces. For example, at Position C the West flange was typically softer and hence attracted less force. The softness of the West flange was caused by the cracks that had opened at Position B, i.e the loading position that preceded the NS cycle. Although the wall was pushed back to the zero position before the cycle in the NS direction was commenced, the cracks in the West flange were still wider than in the East flange, which had been in compression. As a consequence, at the onset of the NS cycle, the in-plane stiffness of the West flange tended to be smaller than the in-plane stiffness of the East flange and therefore the West flange attracted slightly less force than the East flange.

Unlike loading in the NS direction, loading in the EW direction (Positions A and B) was not parallel to an axis of symmetry. If the wall would have been solely loaded by the actuator loading the web, the wall would have twisted since the shear centre of a homogenous U-shaped

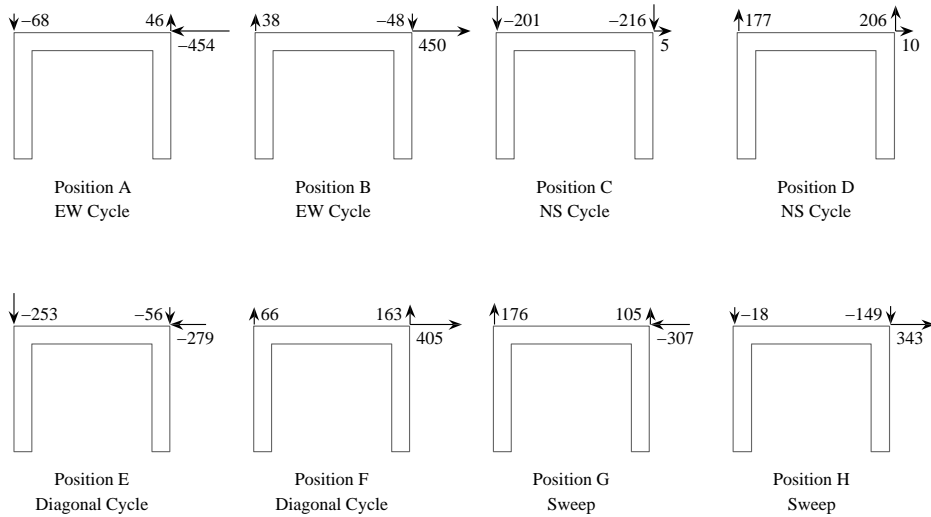


Figure 3.15. TUA, $\mu_{\Delta} = 4.0$: Forces applied to flanges and web at different positions.

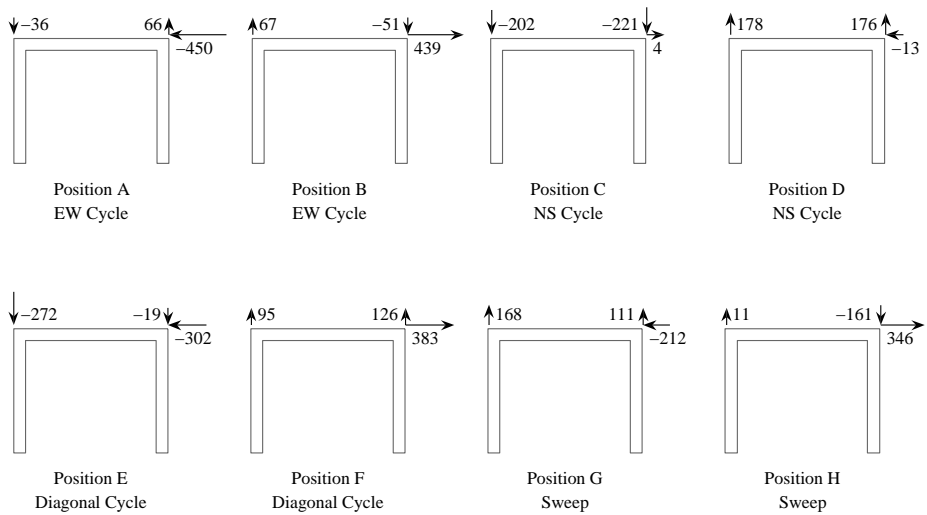


Figure 3.16. TUB, $\mu_{\Delta} = 4.0$: Forces applied to flanges and web at different positions.

wall lies outside the section. Twisting of the wall head was, however, restraint throughout the test – with the exception of those instants during the loading history when a small twist was applied in order to determine the torsional stiffness of the section. To restrain the twist of the wall head, a torsional moment had to be applied by the two actuators in the NS direction at Position A and B. This did, however, not imply that the wall over the entire height did not twist: The position of the shear centre is likely to have varied over the height since it is dependent on the cracking state of the wall [Pégon *et al.*, 2000c]. It should also be noted that the sum of the forces in the NS direction was not zero when the walls were loaded in the EW direction although the NS displacement was kept as close as possible to zero during the EW cycles. Since the reinforcement was not equally distributed along the flanges a moment about the EW axis resulted when for example one flange and the web had yielded. It is interesting to note that the resulting NS forces were of opposite signs for TUA and TUB. This is probably caused by the additional D₁₂ bar at the two flange ends of TUA.

The direction of loading that is the most complex regarding the load transfer is the diagonal direction. The following aspects contribute to this effect:

- The stiffnesses of the flanges are different; the flange in compression is stiffer than the flange in tension.
- The open base crack reduces the locations where shear forces can be effectively transferred to the base.
- Out-of-plane bending is likely to be a relevant part of the load transfer mechanism.

The forces on flanges and web during the diagonal cycles are a result of forces required to push or pull the wall along the diagonal direction and a force couple applied by the NS actuators to restrain the wall head from twisting. At Positions E and H, when one of the flange ends was in compression, the forces from these two origins added up to a large force in the push-direction on the flange in compression and a small force in the push (or even pull) direction in the opposite flange. At Positions F and G, when one of the corners was in compression, the force couple required to restrain the wall from rotating reduced the force in the compression flange and increased the force in the flange in tension; the forces were therefore more equally distributed between the two flanges. The interaction of forces required for bending and for twisting restraint at the Positions E and F is illustrated in Figure 3.17.

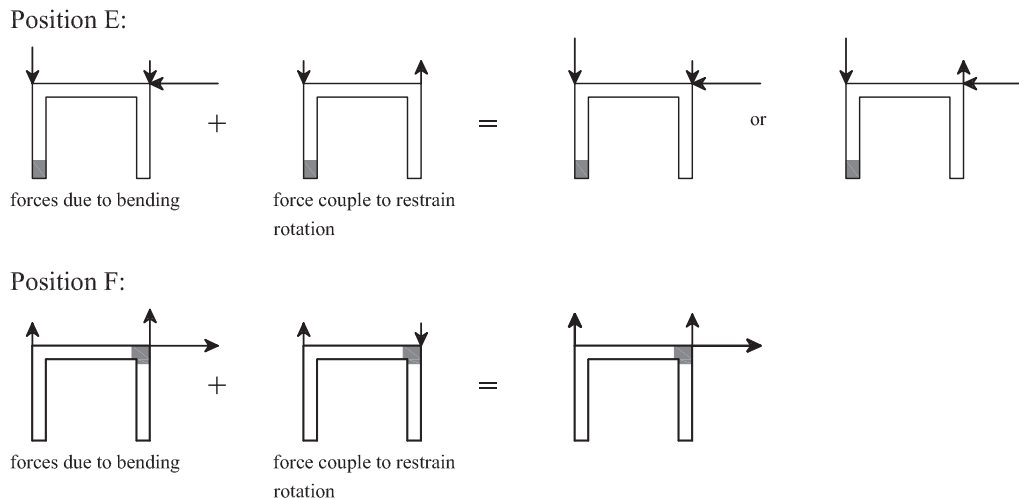


Figure 3.17. Qualitative sketch of the forces at Positions E and F (grey patches: concrete area that is according to section analysis in compression).

3.6.2 Cycles in the EW, NS and diagonal directions

The objective of this section is to give an overview of the force-displacement behaviour of TUA and TUB. The combination of three actuators and cycles in three different directions (EW, NS and diagonal direction) and a sweeping motion led to a large number of potential hysteresis plots. Only the most important ones were included here. The focus is set on the cycles in the EW, NS and diagonal directions; the sweeping motion is not included. For the three directions the hysteretic behaviour is presented in separate graphs, i.e. each graph contains only cycles from one direction. For TUA the force-displacement hysteresses are shown in Figure 3.19; the force-displacement hysteresses for TUB are plotted in Figure 3.20. For both EW and NS cycle two different plots are presented, one that shows the hysteresis loops of the EW actuator and one for the NS actuators. For the diagonal cycles four different hysteresis plots are presented: In the first plot (plot e) the hysteresis in the EW and NS direction are combined in the SRSS moment and the SRSS displacement, which were defined in Equation 3.1; in the three subsequent plots (plots f-h) the hysteresses of the EW and NS actuators are plotted separately. In the following the most important features of the force-displacement hysteresses will be discussed. Unlike the failure mechanisms the main characteristics of the hysteresis curves of TUA and TUB are not very different and therefore only general remarks that apply to both test units will be made.

EW cycle: Figures 3.19a (TUA) and 3.20a (TUB) show the force-displacement curve of the EW actuator for EW cycles only. Although the force-displacement history is assembled

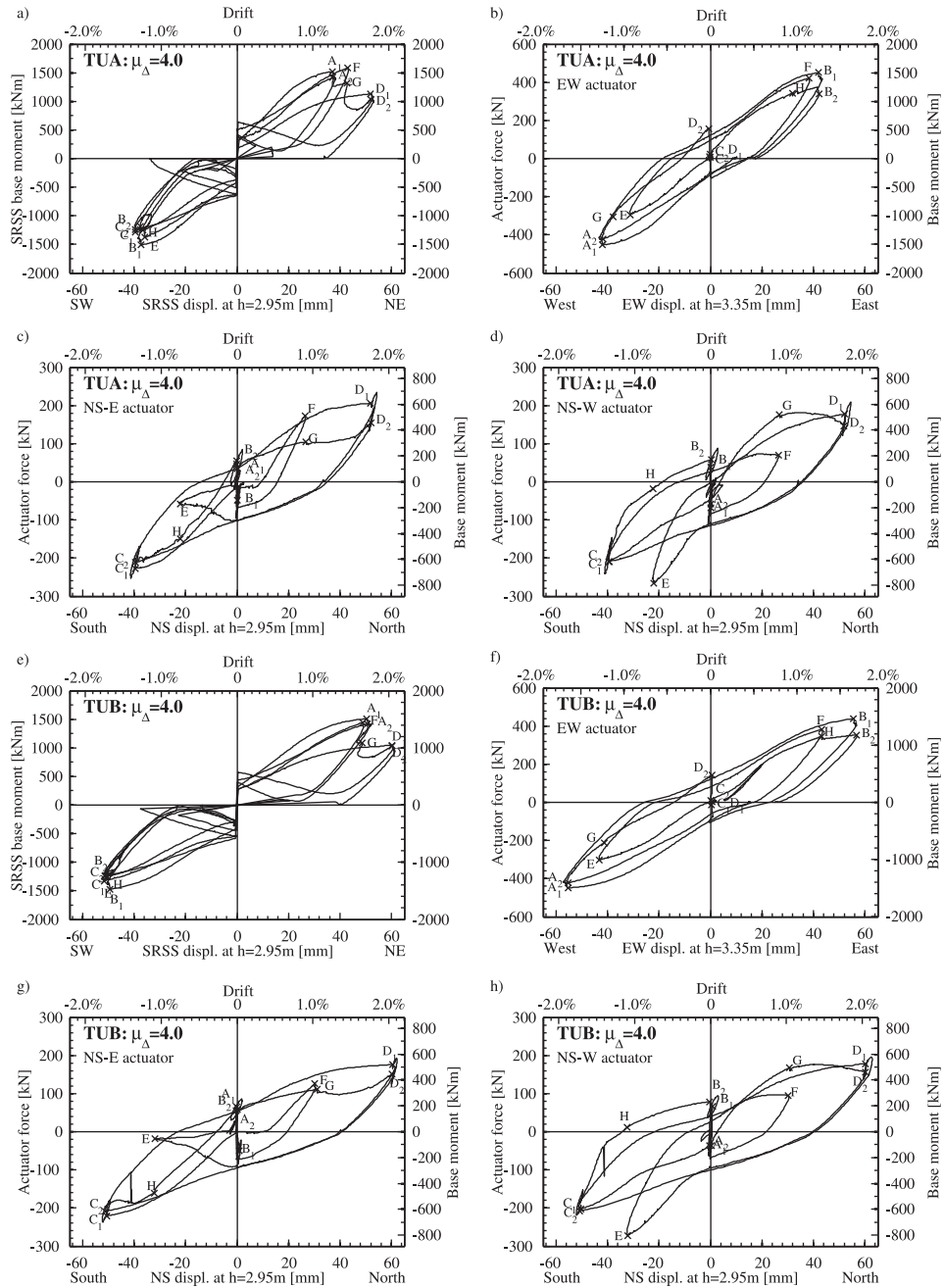


Figure 3.18. TUA and TUB: SRSS moment-displacement hysteresis and force-displacement hystereses of the three actuators for the cycles at $\mu_{\Delta} = 4.0$.

using only the EW cycles from the complex loading history, the hysteresis loops look similar to those of a symmetric rectangular wall that is subjected to uni-axial cyclic loading. When loading in the EW direction, the NS actuators were used to restrain the wall head from twisting. The forces applied by the NS actuators during the EW cycles are shown in Figures 3.19b and 3.20b. The force couple was necessary since the shear centre of the U-shaped wall lay outside the section and hence the applied EW force did not pass through the shear centre. With increasing ductility demand on the wall the magnitude of the required force couple reduced since the shear centre moved closer to the centre of the web [Pégon *et al.*, 2000d].

NS cycle: Figures 3.19c and 3.20c show the force-displacement curves of the two individual NS actuators as well as the total force in the NS direction. Although the moment capacities in the positive and the negative NS direction were approximately the same, the hysteresis loops looked quite different in the two directions: For positive displacements, when the web was in compression, the hysteresis loops were fat. For negative displacements, when the flange end was in compression, the loops looked similar to those for loading in the EW direction. If the wall had just been loaded in the NS direction, in theory, no EW force would have been necessary in order to maintain zero EW displacement. At the beginning of a cycle in the NS direction, however, the force in the EW actuator was always negative (Figures 3.19d and 3.20d). This force resulted from the previous cycle in the EW direction. Since the wall was pushed back to zero EW displacement before starting the NS cycle, the EW force at the beginning of an NS cycle corresponded to the EW force in the EW cycle at zero displacement. This force decayed rapidly during the NS cycle and was usually close to zero when Position C was reached.

Diagonal cycle: Figures 3.19e and 3.20e show the SRSS moment plotted against the SRSS displacement. The shape of the loops is somewhat peculiar. Since the SRSS moment and displacement are by definition positive quantities the SRSS quantities were multiplied by the sign of the NS displacement (Equation 3.1). The jumps in the unloading branches resulted from the fact that the SRSS moment was not zero when the NS displacement was zero. Figures 3.19f and 3.20f show the hysteresis loops of the EW actuator. There is a clear difference to the loops for loading in the EW direction (Figures 3.19a and 3.20a): The loops are more pinched and in particular at Position E the maximum attained force is considerably smaller than at Position A. The opposite holds for the NS direction: At Position E the maximum total force in the NS direction is only slightly smaller than at Position C while at Position F the total NS force is considerably smaller than at Position D. The individual actuator forces are shown in Figures 3.19h and 3.20h. When loading from O→E the maximum force in the East flange was not attained at the peak

displacement but shortly after the zero displacement. The force then dropped continuously and at the peak displacement it was much smaller than the force in the West flange whose flange end was in compression. At Position F the inverse situation occurred for TUA, but for TUB the forces in the two actuators were of similar magnitude. Only the shape of the loops was very different: While the force in the East flange increased towards the peak displacement the force in the West flange reached its maximum at a top displacement corresponding to $\mu_{\Delta} \cong 2.0$.

3.7 Summary of the experimental work

The objective of this chapter was to present selected results of the quasi-static cyclic tests on two U-shaped walls. The results of the experiments on the two U-shaped walls were discussed in terms of failure mechanism and force-displacement hysteresees. The experiments have shown that the adopted design approach led to a ductile behaviour of TUA and TUB, which reached displacement ductilities of 8 and 6 respectively. TUA failed due to rupture of the longitudinal reinforcing bars after buckling – a failure mode that is also often observed for well detailed and capacity designed rectangular walls. TUB failed due to web crushing. This was not the targeted failure mechanism even though the well-confined corner elements prevented sudden crushing. The concrete crushing failure in the web was caused by the reduction of the effective wall thickness due to spalling of the unconfined concrete outside of the boundary elements. During the design it had not been considered that bi-directional loading might favour the spalling of concrete in these regions. The bi-directional loading history was fairly complex involving cycles in three different directions (EW, NS and diagonal) and a sweeping motion. For the design of U-shaped walls, it is important to understand the force distribution between the different wall sections (web and flanges). It was shown that in particular the force distribution between the two flanges during the diagonal cycles was very complex and originated from two sources, i.e. from the forces required to impose the lateral displacements and from the forces required to restrain the wall head from twisting. In the following chapters the experimental results will be analysed further and compared with the numerical predictions.

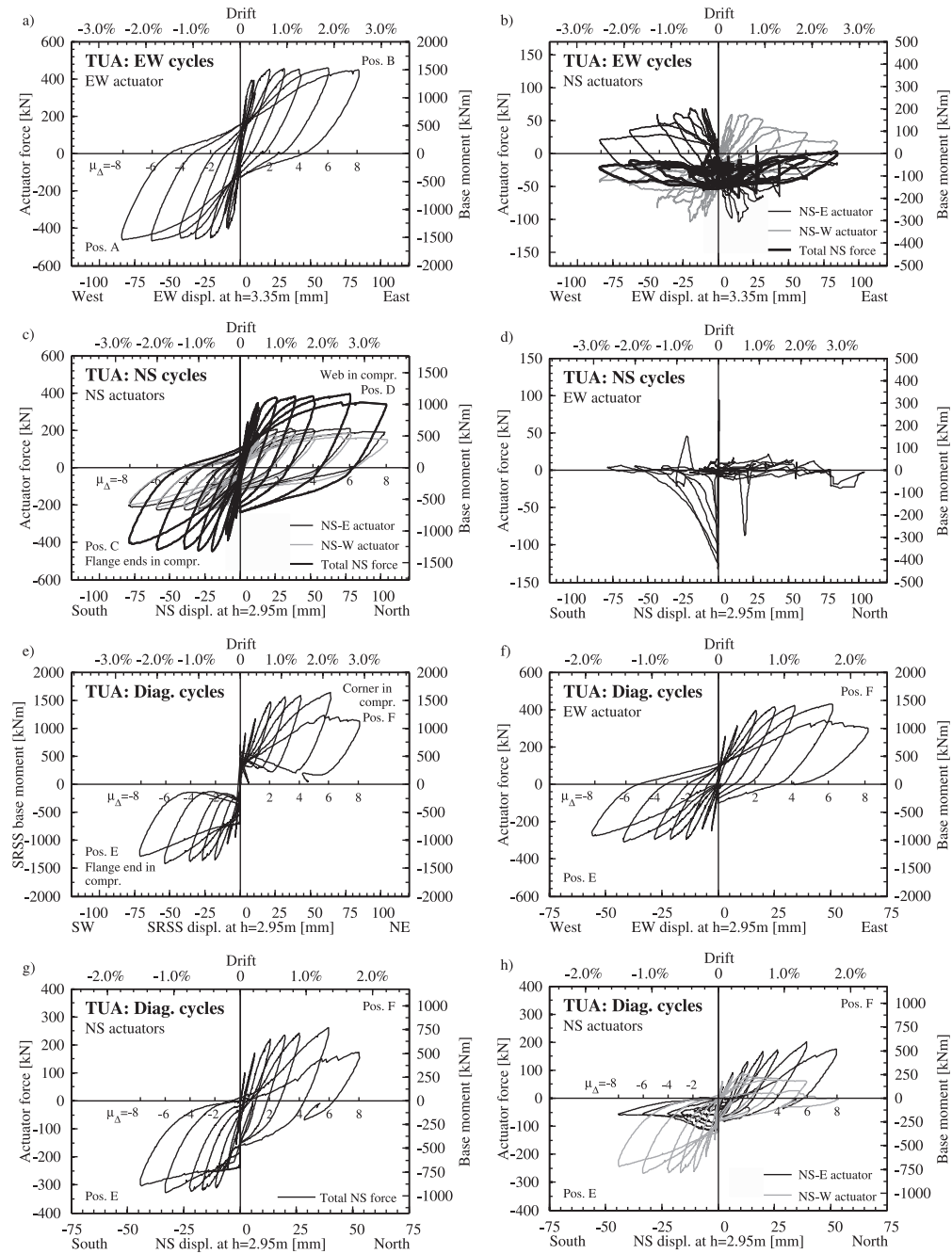


Figure 3.19. TUA: Force-displacement hysteresses for cycles in the EW direction (a+b), in the NS direction (c+d) and in the diagonal direction (e-h).

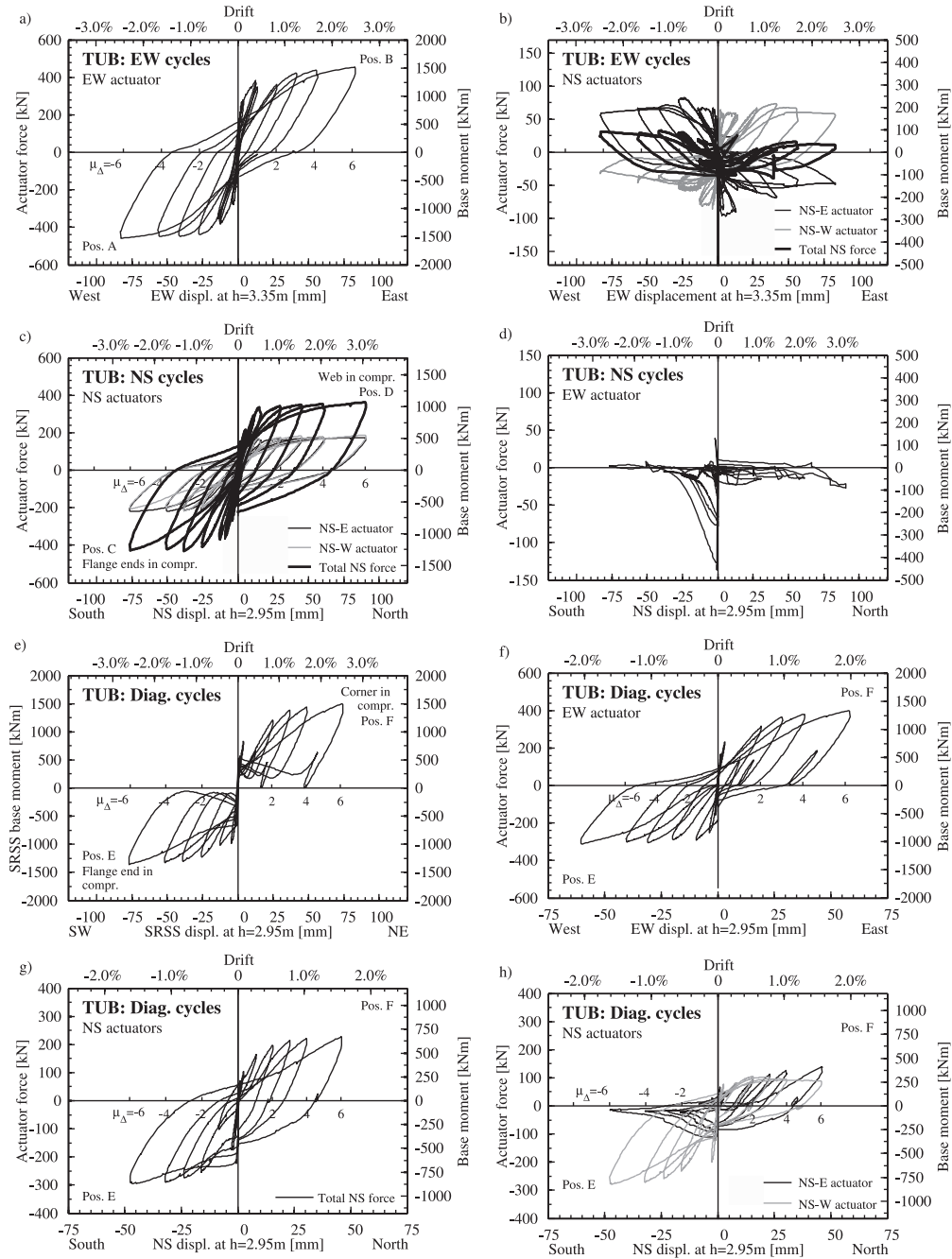


Figure 3.20. TUB: Force-displacement hysteresses for cycles in the EW direction (a+b), in the NS direction (c+d) and in the diagonal direction (e-h).

4. COMPARISON OF PREDICTED QUANTITIES USED IN PLASTIC HINGE ANALYSIS WITH EXPERIMENTAL RESULTS

The state-of-the-art equations for the plastic hinge length and some of the approaches for estimating the shear deformations are empirical equations (Section 2.1). These equations were calibrated with data from uni-axial tests on rectangular or barbelled walls and rectangular or circular columns. Plastic hinge analysis is appealing because it is relatively simple to carry out and yields in general good estimates for the displacement capacity of RC members undergoing inelastic deformations; it is therefore desirable to extend its application to U-shaped walls. However, before the current state-of-the-art equations are applied to U-shaped walls they should be validated against experimental evidence for U-shaped walls; the two quasi-static cyclic tests that were presented in Chapter 3 will be used for this purpose. Naturally, a comparison with the results of two test units cannot constitute a thorough validation but must be considered as a first step within the process.

The objective of this section is therefore to estimate quantities important to plastic hinge analysis from the current equations and compare these estimates with the experimental results. The following variables are considered:

- Yield curvature (Section 4.1)
- Ultimate strain limits (Section 4.2)
- Plastic hinge length (Section 4.3)
- Shear deformations (Section 4.4)

4.1 Yield curvatures

Curvatures of cracked RC sections are more a concept convenient to the design engineer than a determinable quantity from experiments (Section 2.1.3b). Nevertheless, it will be attempted to estimate the yield curvatures from the experimental results and to compare these with

analytical estimates. At the ultimate displacement, however, analysis and experiments will be compared via strains rather than curvatures (Section 4.2).

Curvatures cannot be measured directly but average curvatures are derived from the LVDT measurements along the edges which yield average strains (Section 3.3, Figure 3.7). For example, the curvature of the West flange determined from the measurements of the i -th instruments from the base is:

$$\varphi_i = \frac{\frac{\delta_{NW,i}}{\Delta h_i} - \frac{\delta_{SW,i}}{\Delta h_i}}{l'_f} \quad (4.1)$$

where $\delta_{NW,i}$ and $\delta_{SW,i}$ are the elongations measured by the i -th instruments along the NW edge and the SW edge respectively, Δh_i is the height interval covered by the i -th instrument and l'_f is the horizontal distance between the LVDT chains along the NW and SW edges. For the East flange the LVDT chains along the NE and SE edge were considered and for the web the chains along the NW and NE edge were used. The base curvature cannot, however, be derived in such a way since the lowest devices recorded mainly the effects of strain penetration into the foundation rather than the deformation of the wall section itself. Hence, the base curvature must be estimated from the curvatures at larger heights. Different schemes are possible to derive the base curvature, the following is used here: The base curvature is linearly extrapolated from the curvatures computed at larger heights. The assumption that the curvature profile at yield is approximately linear over the entire wall height could not be confirmed from measurements. Only curvatures from the base up to about midheight of the wall followed an approximately linear trend. Hence, to obtain a realistic estimate of the base curvature only curvatures up to this height are included when extrapolating the linear profile to the base. The curvature profiles of TUA and TUB at first yield are plotted in Figure 4.1. The grey, straight lines indicate the height over which the linear curvature profile was fitted. This linear profile was then extrapolated to the base to determine the base curvature φ'_y .

The points of first yield were determined as the instants when the average strain δ/h between 50 – 250mm above the wall base first exceeded the yield strain of the D12 reinforcing bars. The average strain between $h = 50 - 250$ mm was computed from the LVDT measurements between $h = 50 - 150$ mm and $h = 150 - 250$ mm. Using the strain between $h = 50 - 150$ mm alone yielded unreliable results since the crack spacing at first yield was larger than 100mm. Of course, at the instant when the average strain between $h = 50 - 250$ mm equalled ε_{sy} the longitudinal reinforcement would have already yielded within cracks. The nominal yield curvature φ_y was then computed as the product of the curvature at first yield multiplied by the predicted ratio of nominal moment to first yield moment:

$$\varphi_y = \varphi'_y \cdot \frac{M_n}{M'_y} \quad (4.2)$$

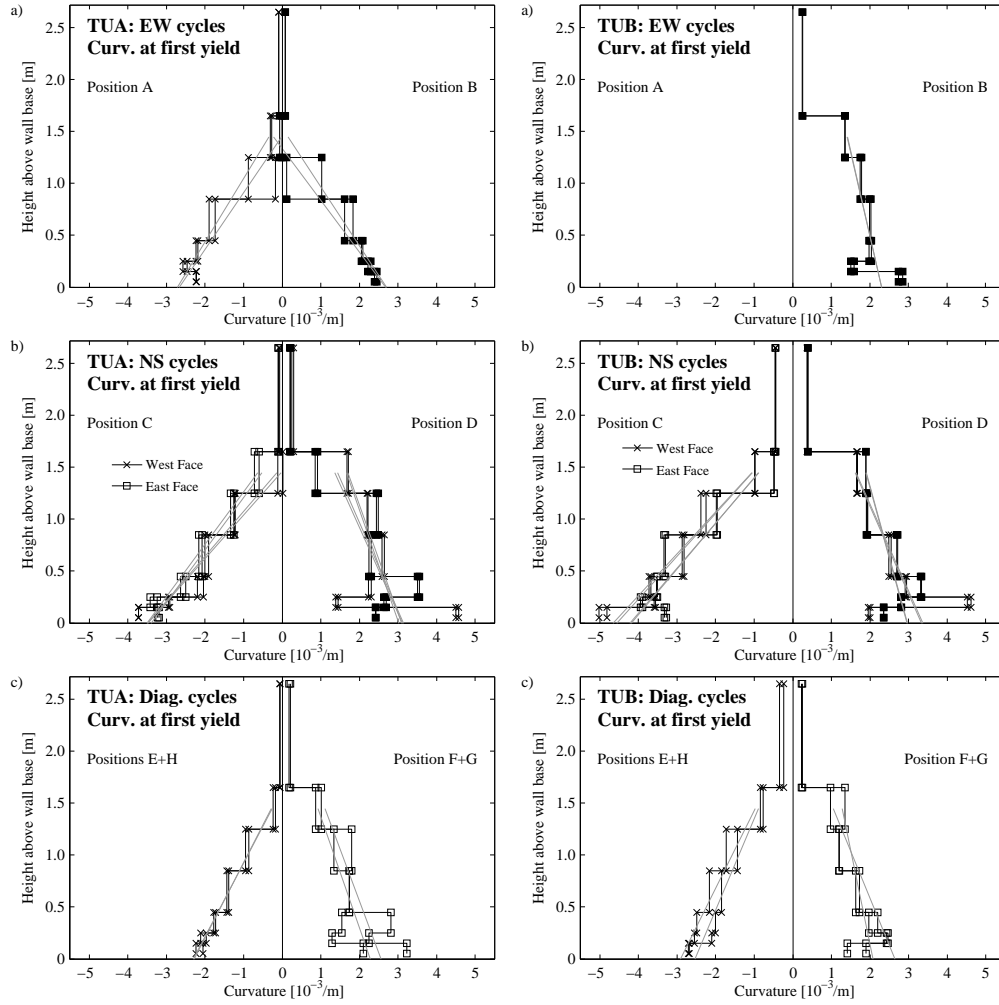


Figure 4.1. TUA and TUB: Curvature profiles at first yield for the different positions.

Table 4.1 summarises for TUA and TUB the experimental yield curvatures in the form of the proportionality constants K_1 (Equation 2.7) which were computed from the experimental data. For the EW, NS and diagonal directions the wall length l_w was taken as l_{web} , l_f and $l_{diag} = \sqrt{l_{web}^2 + l_f^2}$, respectively. The experimental results are compared with the values for I- and T-profiles that were proposed by Paulay [2002] on the basis of a parametric section analysis (Section 2.1.2). Also included in the table are numerical results from section analyses of TUA and TUB that will be presented in Section 6.1.1; the results for the nominal yield curvatures are anticipated here in order to complete the picture regarding the available yield curvature estimates.

Table 4.1. Comparison of predicted, experimental and numerical values for the constant K_1 (Equation 2.7).

	TUA	TUB	TUA	TUB	Prediction
	Exp.	Exp.	Analysis	Analysis	Paulay [2002]
Positions A and B	1.73	1.44	1.42	1.38	1.4
Position C	1.76	2.23	1.67	1.81	1.8
Position D	1.42	1.53	1.46	1.47	1.4
Positions E and H	2.12	2.07	2.04	2.07	-
Positions F and G	2.00	1.87	2.03	1.98	-

With the exception of the yield curvature of TUA at Positions A and B and the yield curvature of TUB at Position C, there is a very good agreement between the experimentally determined yield curvatures and the yield curvatures derived from section analysis. At Positions A and B for TUA and Position C for TUB the experimentally derived yield curvatures are about 20% larger than the yield curvatures derived from section analysis. These are also the only two directions of loading where the experimentally derived yield curvatures for TUA and TUB differ significantly; for all other directions the yield curvatures of TUA and TUB are fairly similar. Hence, it is likely that the experimentally derived yield curvature that deviate strongly from the yield curvature obtained from section analysis were rather high estimates of the actual yield curvatures. This could be, for example, caused by unequal crack spacings. The results of the section analysis compare very well to the estimates by Paulay [2002]. For the diagonal directions such estimates of the coefficient K_1 have not yet been derived; as for the principal directions (Positions A, B, C and D) mean values of the K_1 -coefficients could be derived from parametric section analyses. Such mean values are very convenient in preliminary design stages when the exact layout of the section has not yet been determined. However, as long as such mean coefficients for the diagonal direction of bending are not yet available, section analysis of the individual U-shaped section has been shown to yield good estimates of the yield curvature.

4.2 Strain limits

To draw a comparison between the limits suggested in the literature and experimentally determined values, compressive, tensile, and total excursion strains along the four outer edges of the test units A and B were computed and are summarised in Table 4.2. The given strains are average strains between $h = 50 - 150\text{mm}$. This height interval represents best the actual bar strain at the wall base where bar buckling and fracture was observed and where axial stresses in the concrete were highest. The lowest instrument ($h = 0 - 50\text{mm}$) measured chiefly the elongation of the wall edge due to strain penetration into the foundation rather than the wall deformation between $h = 0 - 50\text{mm}$. The strain values were corrected for the distance

between the LVDT and the edge of the corner or flange end. The given values correspond therefore to strains on the outer, vertical edges of corner and flange ends. Note that, when determining the yield curvature, mean strains were computed over $h = 50 - 250\text{mm}$ whereas the strains for post-yield load steps, which are presented in Table 4.2, are mean strains over $h = 50 - 150\text{mm}$. At first yield the crack spacing was still fairly large and using the mean strain over $h = 50 - 150\text{mm}$ only would have yielded unreliable results. At larger ductility demands the crack spacing reduced and the mean strains over $h = 50 - 150\text{mm}$ yielded the best estimate of the maximum strain.

The tensile and compressive strains are the measured strains at the given load step, i.e. these are *not* necessarily the largest strains measured up to this instant but strains at preceding positions might have been larger. For the total excursion strains, however, the maximum of $\varepsilon_s - \varepsilon_c$ of all the values measured up to the considered load step are given. For each position, the total excursion strain refers to the corner or flange end that is at this position in compression. For example, the total excursion strain at Position E is computed as the absolute maximum compressive strain that was measured up to this moment at the West flange end plus the maximum tensile strain measured up to this moment at the West flange end. At Positions C and D the strains in the two flanges were averaged and for the cycles in the EW direction the strains were computed at the corners and averaged for Positions A and B. For the sweeping motion, the Positions G and H on the second diagonal are considered. The tensile strain capacities of the D12 bars of TUA and TUB were 12.6% and 12.7%, respectively (Table 3.2).

Section 2.5 summarised different values for strain limits on confined concrete crushing, bar buckling and fracture that were found in the literature. In the following sections these limits are compared to the strain values obtained experimentally.

4.2.1 Ultimate concrete strain

Failure of the confined concrete boundary elements was observed for neither TUA nor TUB (Sections 3.5.1 and 3.5.2). Hence, it is not possible to check whether the equations for the compressive strain capacity of the confined concrete, which were given in Section 2.5.1, are appropriate for determining displacement limits for TUA and TUB. The comparison of predicted strain capacities with experimentally obtained strain values shows, however, that the predicted strain capacities are with one exception well above the observed values (Table 4.3). The exception concerns the compressive strain at the NE corner of TUB. The maximum compressive strain of -0.036 was measured at the point of failure of TUB ($\mu_\Delta = 6.0$, Position B during sweeping motion, not included in Table 4.2). Failure of the confined boundary element of the NE corner was not observed but the measured strain exceeds the ultimate strain capacity according to Mander *et al.* [1988b] by about 60%. It is, however, 40% smaller than

Table 4.2. Experimental flexural strain values (average strain between $h = 50 - 150\text{mm}$): Maximum tensile, compressive and total excursion strains for different directions of loading.

Pos.			$\mu_{\Delta} = 1.0$				$\mu_{\Delta} = 3.0$			
			ε_s [‰]	ε_c [‰]	$\varepsilon_s - \varepsilon_c$ [‰]	$\frac{\varepsilon_s - \varepsilon_c}{\varepsilon_{su}}$ [-]	ε_s [‰]	ε_c [‰]	$\varepsilon_s - \varepsilon_c$ [‰]	$\frac{\varepsilon_s - \varepsilon_c}{\varepsilon_{su}}$ [-]
EW cycle	A+B	TUA	2.6	-0.7	4.9	0.039	5.0	-1.5	6.3	0.050
		TUB	4.1	-0.5	7.7	0.061	12.4	-1.8	14.1	0.112
NS cycle	C	TUA	2.9	0.0	4.2	0.033	7.0	-0.4	5.6	0.045
		TUB	4.2	-1.7	3.5	0.028	11.9	-3.2	23.3	0.185
	D	TUA	4.1	-0.8	3.9	0.031	24.7	-2.3	9.3	0.074
		TUB	4.1	0.0	4.8	0.038	25.9	-1.5	13.6	0.108
Diag. cycle	E	TUA	2.9	-1.5	6.3	0.050	13.1	-3.0	30.3	0.241
		TUB	12.9 ¹⁾	-0.7 ¹⁾	33.9 ¹⁾	0.269	25.9	-7.5	39.0	0.310
	F	TUA	3.8	-1.5	5.2	0.041	25.9	-3.7	16.9	0.134
		TUB	7.0	0.0	14.5	0.115	26.2	-2.3	28.6	0.227
Sweep	G	TUA	4.2	-1.4	5.1	0.040	22.1	-3.3	9.6	0.076
		TUB	2.5	-1.3	11.0	0.087	25.5	-5.8	16.4	0.130
	H	TUA	3.4	1.1	6.0	0.047	9.2	0.4	23.9	0.190
		TUB	3.0	-1.4	4.5	0.036	23.4	-2.2	27.9	0.221

Pos.			$\mu_{\Delta} = 6.0$				$\mu_{\Delta} = 8.0$			
			ε_s [‰]	ε_c [‰]	$\varepsilon_s - \varepsilon_c$ [‰]	$\frac{\varepsilon_s - \varepsilon_c}{\varepsilon_{su}}$ [-]	ε_s [‰]	ε_c [‰]	$\varepsilon_s - \varepsilon_c$ [‰]	$\frac{\varepsilon_s - \varepsilon_c}{\varepsilon_{su}}$ [-]
EW cycle	A+B	TUA	33.7	-1.5	33.6	0.267	47.1	2.3	47.4	0.376
		TUB	34.6	-4.1	40.6	0.322	-	-	-	-
NS cycle	C	TUA	30.5	-1.0	31.4	0.249	46.5	5.7	46.4	0.368
		TUB	31.2	-4.4	39.6	0.314	-	-	-	-
	D	TUA	43.2	-1.6	33.0	0.262	86.8	5.3	49.0	0.389
		TUB	48.7	-3.9	36.8	0.292	-	-	-	-
Diag. cycle	E	TUA	48.9	-3.1	56.9	0.452	70.4	-	-	-
		TUB	43.2	-13.7	60.7	0.482	-	-	-	-
	F	TUA	55.3	-2.5	52.7	0.418	-	2.9	74.2	0.589
		TUB	45.1	-8.9	52.5	0.416	-	-	-	-
Sweep	G	TUA	35.3	-3.0	34.7	0.276	-	-	-	-
		TUB	53.0	-16.1	48.9	0.388	-	-	-	-
	H	TUA	33.1	4.3	37.1	0.295	-	-	-	-
		TUB	50.3	-9.1	66.0	0.524	-	-	-	-

¹⁾ Before loading in the diagonal direction at $\mu_{\Delta} = 1.0$ a sudden impact probably due to a fault in the control system loaded the wall beyond $\mu_{\Delta} = 1.0$ [Beyer *et al.*, 2008]. Thus the strain values for TUB at $\mu_{\Delta} = 1.0$ are distorted.

the ultimate strain capacity according to Scott *et al.* [1982]. At the point of failure the concrete in the web crushed and shear deformations at the East corner, where the compressive strain of -0.036 had been measured, were large. These might have influenced the axial strain measurement and hence it is questionable whether the measurement is accurate. For comparison, up to the point of failure the maximum measured compressive strain at the opposite corner of TUB (NW corner) was only -0.016 . While the experimentally determined maximum strain of -0.036 might be biased, the equation by Mander *et al.* [1988b] is also known to underestimate the compressive strain capacity for members under combined axial load and flexure; Priestley *et al.* [2007] quoted a factor of $1.3 - 1.6$ between predicted and actual compressive strain capacity (Section 2.5.1). To summarise, the equations by Scott *et al.* [1982] and Mander *et al.* [1988b] (considering an amplification factor of $1.3 - 1.6$) results in compressive strain capacities of the concrete that are larger than the measured maximum compressive strains; this is consistent with the observation that the confined boundary elements of TUA and TUB were still in very good shape when the test units failed due to longitudinal bar rupture and web crushing, respectively.

Table 4.3. Comparison of predicted and measured compressive strain values.

	TUA		TUB	
	Flange end	Corner	Flange end	Corner
	[‰]	[‰]	[‰]	[‰]
Scott <i>et al.</i> [1982]	46	47	42	60
Mander <i>et al.</i> [1988b]	14	14	17	22
Experiment	3	4	14	36

4.2.2 Longitudinal bar buckling and fracture

The behaviour of the longitudinal bars during testing of TUA and TUB was described in Sections 3.5.1 and 3.5.2. In both tests, the onset of extensive buckling was observed at Position E during cycles with $\mu_{\Delta} = 6.0$. In the case of TUA, bars fractured during cycles at $\mu_{\Delta} = 8.0$ and caused the failure of the wall. In the case of TUB, the test had to be stopped due to compression strut failure in the web just before the wall could be loaded with cycles at $\mu_{\Delta} = 8.0$. The finding that the onset of buckling was associated with cycles at $\mu_{\Delta} = 6.0$ and bar rupture with cycles at $\mu_{\Delta} = 8.0$ is consistent with the observations by Hines [2002]. At the onset of buckling, the total excursion strain was 0.057 and 0.061 for TUA and TUB, respectively. This is just outside the range of strain values characteristic for the onset of bar buckling suggested by Hines ($0.035 \leq \varepsilon_s - \varepsilon_c \leq 0.05$) and it compares fairly well with Restrepo's expression (Equation 2.22) which equates to 0.058 for $s_h = 50\text{mm}$ and $d_b = 12\text{mm}$

(Section 2.5.2). According to Priestley *et al.* [2007] the reinforcing bars should not have buckled before reaching $0.6\varepsilon_{su}$ since the spacing of the stabilising reinforcement $s_h = 50\text{mm}$ was less than $s_{h,max} = 52\text{mm}$.

Fracture of the main longitudinal bars of TUA occurred during the diagonal cycle at $\mu_\Delta = 8.0$ when loading from E to F. The bars that ruptured were situated in the West flange end. During the preceding cycle in the NS direction, they had been subjected to large strains when the wall was pushed to Position D. In the final, diagonal cycle they were first subjected to compressive strains and then, upon load reversal, to tensile strains. During this last cycle the strain measurements are incomplete since due to the large deformations and the significant spalling of the concrete the LVDT measuring the strain at the West flange end between $h = 50 - 150\text{mm}$ had to be dismantled. At Position D, the tensile strain at the flange ends was 0.087. In the cycles at $\mu_\Delta = 6.0$ a maximum total strain excursion for the flange end of 0.057 was recorded at Position E. The strain limits for bar fracture suggested by Restrepo (Equation 2.23), which is here controlled by the upper limit of $0.5\varepsilon_{su} = 0.063$, or by Priestley *et al.* [2007] ($0.6\varepsilon_{su} = 0.076$) yield reasonable estimates for TUA whereas the strain limit by Priestley *et al.* [1996] ($0.75\varepsilon_{su} = 0.095$) seems slightly too high when buckling causes premature fracture of the reinforcing bar.

If the same strain limit is applied for the computation of the pushover curves of TUB, the displacement capacities should be overestimated since none of the longitudinal bars in TUB had fractured. However, from a comparison of the buckling deformations of the longitudinal bars of TUA and TUB at $\mu_\Delta = 6.0$ it is postulated that the bars of TUB would have ruptured during the cycles at $\mu_\Delta = 8.0$ had shear failure not ended the test at the end of the cycles with $\mu_\Delta = 6.0$. At this instant the maximum total strain excursion $\varepsilon_s - \varepsilon_c$ was 0.066, which was measured at the East flange end at Position H during the sweeping motion. This strain value is even slightly larger than the maximum excursion strain measured for TUA at Position E for $\mu_\Delta = 8.0$ (while the ultimate strain capacities ε_{su} of the D12 bars of TUA and TUB were almost equal). Hence, it is very likely that – had TUB been tested beyond cycles at $\mu_\Delta = 6.0$ – the longitudinal bars would have ruptured soon.

To summarise, the estimates on the reinforcement strain capacity by Restrepo [2006] and Priestley *et al.* [2007] yield reasonable results which compare relatively well to the experimental data. Since Restrepo's estimate for the strain limit for bar buckling was closest to the strain at Position E at $\mu_\Delta = 6.0$, his estimate will also be used for predicting the point of reinforcing bar fracture for TUA. Therefore, in the plastic hinge analysis in Section 6.1 a strain limit of $0.5\varepsilon_{su}$ will be employed for computing the displacement capacity of TUA. For TUB, the

displacement capacity was limited by the web crushing capacity, which decreased with the ductility demand.

4.3 Plastic hinge lengths

In Section 2.1.3 the different components of plastic hinge lengths were discussed and the most commonly used empirical equations for plastic hinge lengths were introduced. The objective of this section is to derive plastic hinge lengths from the experimental results of TUA and TUB and compare these to the values from Equations 2.10a and 2.10b, Equation 2.11 and the modified, less conservative version of the latter (Equation 2.12). First, these equations are evaluated for the different directions of loading (Section 4.3.1). Then, in a second step, equivalent plastic hinge lengths are derived from the LVDT measurements (Section 4.3.2). Finally, the experimentally determined plastic hinge lengths are compared with the estimates of the existing empirical equations and conclusions are drawn on whether these equations, which have been derived from data of rectangular, barbelled and circular walls and columns, are also applicable to U-shaped walls (Section 4.3.3).

4.3.1 Predicted values of plastic hinge lengths

A summary of the predicted plastic hinge lengths according to Equations 2.10a and 2.10b and Equation 2.11 is given in Table 4.4; the plastic hinge lengths were once computed for the EW direction ($l_w = l_{web}$) and once for the NS direction ($l_w = l_{fl}$). The comparison of the results for the different equations shows that the new equation for the plastic hinge length (L_{ph3}) gives almost identical values to the maximum of the two established equations ($\max(L_{ph1}, L_{ph2})$). In the equation "modified L_{ph3} " the term for inclined shear cracking was replaced by $0.2l_w$ as originally suggested by Paulay and Priestley [1992].

If the empirical equations for the plastic hinge length are also applied for the prediction of the displacement capacity in the diagonal direction, one needs to decide which measures for the wall length and the wall height are most appropriate. For the wall length, three choices seem possible:

- The length of the diagonal, i.e. $l_{diag} = \sqrt{l_{web}^2 + l_{fl}^2}$, which was also used when deriving the yield curvature.
- The length of either the web or the flanges.
- The arithmetic mean of the length of the web and the length of the flanges, i.e. $(l_{web} + l_{fl})/2$.

Considering that the term in the plastic hinge length equations that includes the wall length represents the spreading of the plasticity due to inclined shear cracking, it seems logical to use a wall length measure that is directly linked to the shear transfer mechanism. Shear forces are assumed to be carried as in-plane forces by either the web or the flanges. It is argued, therefore, that either the length of the web or the length of the flanges should be used when deriving the plastic hinge length for displacement in the diagonal direction. A similar argumentation can be used for the wall height. It is suggested that the plastic hinge length for loading in the diagonal direction should be taken as the maximum of the plastic hinge lengths in the EW and NS directions.

Table 4.4. Plastic hinge lengths for TUA and TUB according to empirical equations given in Section 2.1.3.

	$0.022d_b f_y$ [mm]	L_{ph1} [mm]	L_{ph2} [mm]	L_{ph3} [mm]	$L_{ph3,mod}$ [mm]	$L_{ph3,mod}^*$ [mm]
TUA:						
EW cycle	129	397	407	406	536	471
NS cycle	129	365	340	363	468	404
TUB:						
EW cycle	124	392	407	401	531	469
NS cycle	124	360	340	358	463	401

$$L_{ph1} = 0.08H + 0.022d_b f_y$$

$$L_{ph2} = 0.2l_w + 0.044H$$

$$L_{ph3} = kH + 0.1l_w + 0.022d_b f_y$$

$$L_{ph3,mod} = kH + 0.2l_w + 0.022d_b f_y$$

$$L_{ph3,mod}^* = kH + 0.2l_w + 0.011d_b f_y$$

4.3.2 Experimentally determined values of the plastic hinge lengths

At different ductility levels and for the different positions of the load cycle the plastic hinge length was determined from the plastic displacement Δ_p , the plastic curvature φ_p , and the effective height H of the wall:

$$L_{ph} = \frac{\Delta_p}{\varphi_p H} \quad (4.3)$$

Before the plastic hinge length can be determined, estimates of the plastic displacement Δ_p and the plastic curvature φ_p are required. At first yield it was found that the curvatures obtained from section analyses corresponded well to the experimentally obtained base curvatures if the latter were derived by linearly extrapolating the curvatures between $h = 50 - 1650\text{mm}$ to

the base level (Section 4.1). Therefore, the same procedure was applied when determining the plastic curvature φ_p ; solely the height interval, over which the best-fit linear curvature profile was determined, was reduced to $h = 50 - 1250\text{mm}$ for the EW and NS directions and to $h = 50 - 850\text{mm}$ for the diagonal direction. These are the height intervals for which the curvature profiles of the inelastic walls were approximately linear. The plastic base curvature φ_p was determined as the total base curvature φ_b (gained from extrapolation) minus the nominal yield curvature φ_y (first two K_1 -columns of Table 4.1). The plastic displacement Δ_p was determined in two different ways: (a) in the "indirect" way by subtracting the measured shear displacement Δ_s , the measured sliding shear displacement Δ_{sl} and the flexural displacement at nominal yield Δ_{yf} from the total measured top displacements Δ_{top} and (b) by integrating the mean curvatures derived from LVDT measurements and subtracting the flexural displacement at nominal yield:

$$\Delta_p = \Delta_{top} - \Delta_s - \Delta_{sl} - \Delta_{yf} \quad (4.4a)$$

$$\Delta_p = \int_{h=0}^{h_{top}} \theta(h)dh - \Delta_{yf} \quad (4.4b)$$

A portion of the plastic hinge length according to Equation 4.3 can be attributed to strain penetration into the foundation. This portion, i.e. the equivalent strain penetration length L_{sp} , can be computed separately from the difference between the actual measured rotation θ_b over the base interval ($h = 0 - 50\text{mm}$) and the total curvature $\varphi_y + \varphi_p$, which was derived by linear extrapolation from the curvatures at larger heights, times the length of the base interval:

$$L_{sp} \cdot \varphi_p = \theta_b - 50\text{mm} \cdot (\varphi_y + \varphi_p) \quad (4.5)$$

The portion of the plastic displacement of the wall that is associated with inelastic deformations above the wall base can be computed from the difference of the total plastic hinge length and the equivalent strain penetration length, i.e. $L_{ph} - L_{sp}$.

4.3.3 Comparison of analytical and experimental values

In Figures 4.2a and b experimental values for the post-yield strain penetration length L_{sp} are normalised by the longitudinal bar diameter d_b and their yield strength f_y and compared to the proportionality constant of 0.022 given by Paulay and Priestley [1992]. For $\mu_\Delta \geq 3.0$ the experimentally derived length L_{sp} was in the majority of cases smaller than the predicted length. During testing of TUA and TUB the footing was prestressed horizontally since the entire footing was assembled from the foundation connected to the wall and separate foundation blocks. It is likely that the bi-axial compression state of the foundation reduced the

strain penetration into the foundation. As a first estimate it will be assumed that the strain penetration length L_{sp} for a prestressed foundation is about half the length for a foundation with mild reinforcement only [Hines, 2002]; the modified plastic hinge lengths are included as $L_{ph3,mod}^*$ in Table 4.4. For $\mu_{\Delta} = 2.0$ the values of L_{sp} were in many cases larger than 0.022. At this loading stage the plastic curvatures φ_p were small. Hence, small increases in the base rotation θ_b led to large values of L_{sp} . Since the walls were detailed for high ductility demands, the strain penetration lengths at $\mu_{\Delta} = 2.0$ were not very relevant for determining the ultimate displacement capacity.

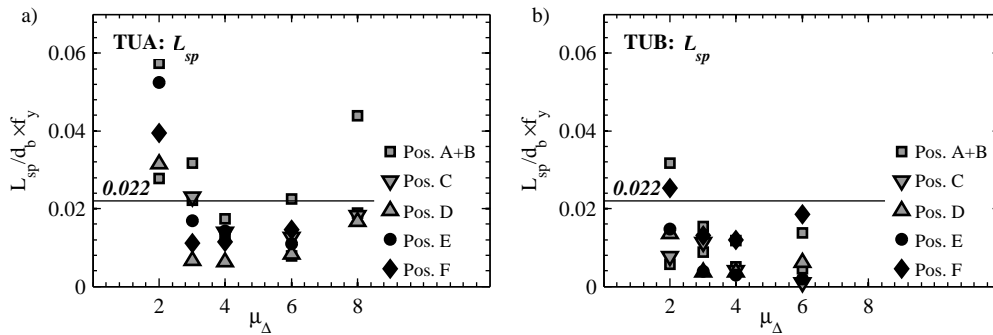


Figure 4.2. TUA and TUB: Comparison of the experimentally derived plastic hinge length due to strain penetration (L_{sp}) to the predicted value $0.022d_b f_y$.

As outlined before, because the foundation was prestressed horizontally, the strain penetration length L_{sp} into the foundation was biased low. It is therefore interesting to compare experimental and empirical values for plastic hinge components other than the strain penetration term. In Figure 4.3 the term for strain penetration is excluded from both the experimental and the predicted values of the plastic hinge length. Note that the equation for L_{ph2} does not include a strain penetration term; this estimate of the plastic hinge length is therefore not included in the following discussion.

The deviation of the experimentally derived values from the empirical equation was greatest for smaller ductilities. For small ductility levels the effect of the uncertainties that were related to the yield displacement and to the shear displacement measurements were greater than for larger ductilities. It is assumed that the conclusions drawn from cycles with $\mu_{\Delta} \geq 4.0$ are more reliable than those from cycles with $\mu_{\Delta} \leq 3.0$. Ductilities smaller than 3.0 are of interest if the structural member is designed for medium ductility levels (as for example in EC8, see footnote on page 63). Figure 4.3 includes values for $L_{pb} - L_{sp}$ that were computed from the two different estimates of the plastic displacement Δ_p according to the indirect method and

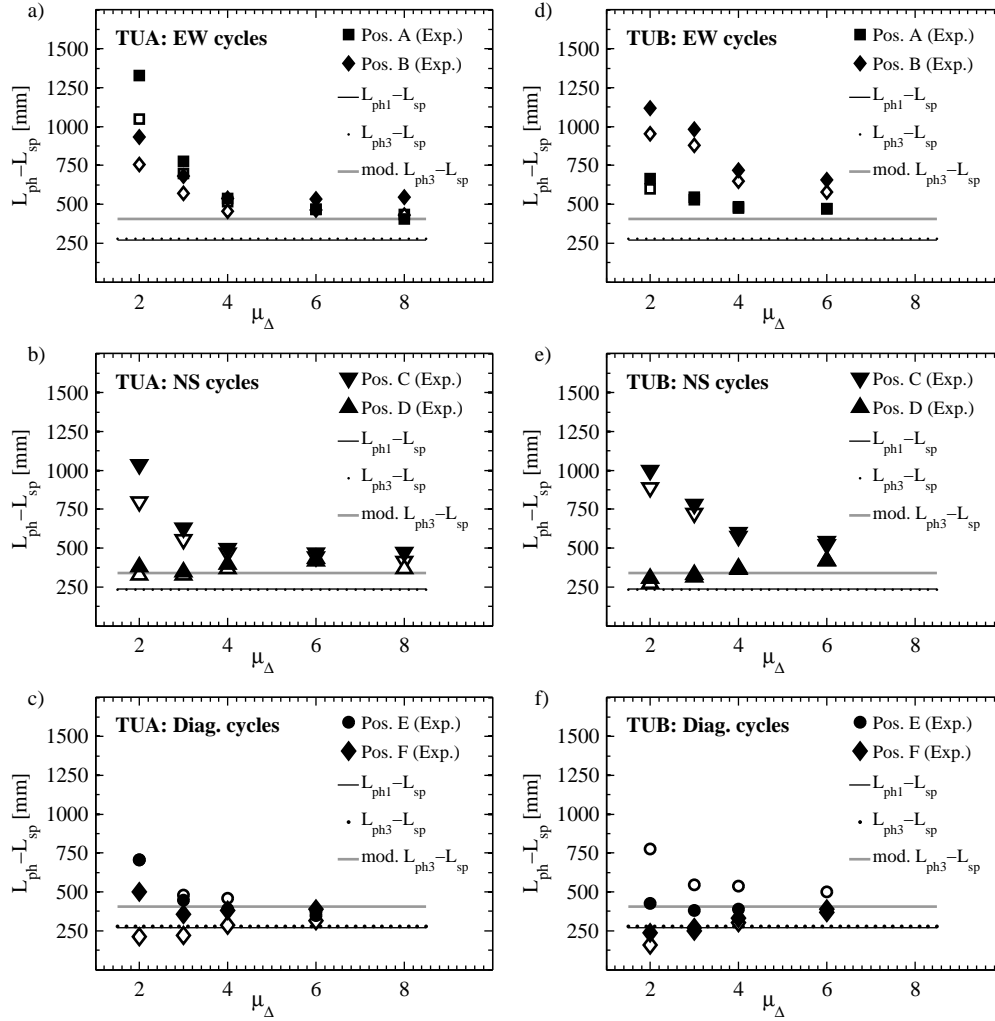


Figure 4.3. TUA and TUB: Comparison of the experimentally derived values for $L_{pb} - L_{sp}$ to values from empirical equations for plastic hinge lengths (excluding the term $0.022d_b f_y$ for strain penetration). The filled and unfilled markers represent values that were computed from plastic displacements according to Equations 4.4a and 4.4b, respectively.

the integration method (Equation 4.4). Ideally, the two methods should yield identical results. For real experiments, this is never the case but the difference is for most directions of loading relatively small.

For $\mu_{\Delta} \geq 4.0$ the design equations for the plastic hinge length minus the strain penetration length (i.e. $L_{pb1} - L_{sp}$, and $L_{pb3} - L_{sp}$) are for the EW and NS directions of loading smaller than the empirically derived equations. It was the intention of Paulay and Priestley [1992] and Priestley *et al.* [2007] that the design equations for the plastic hinge length underestimate the actual plastic hinge length to some extent in order to maintain a safety margin between the ultimate design displacement and the displacement causing collapse. The modified version of L_{pb3} , which is less conservative with respect to the term representing the spreading of plasticity due to inclined shear cracking, yielded estimates that came closer to the experimental values for the EW and NS direction though it still underestimated the experimental values. For the diagonal direction the experimental values were mostly between the lengths predicted by the design equations and the assessment equation.

To summarise, it was proposed that the plastic hinge length for displacements in the diagonal direction should be estimated as the maximum of the plastic hinge length for displacements in the two principal directions. The preceding comparison of predicted and experimental values has shown that the empirical design equations for plastic hinge lengths (L_{pb1} , L_{pb2} and L_{pb3}), which were chiefly derived from rectangular walls and columns, also led for U-shaped walls to estimates of L_{pb} that are smaller than those derived from the experimental data. This applies for all three directions of loading (EW, NS and diagonal direction) and therefore these design equations for L_{pb} should yield safe estimates of the displacement capacity. The plastic hinge length $L_{pb3,mod}$ produced less conservative estimates of the plastic hinge length, which can be used for assessment purposes or the prediction of test results. Although the design and assessment estimates of L_{pb} are suitable for all three directions, the estimates are biased low for the principal directions and slightly biased high for the diagonal direction. To achieve similar ratios of experimentally determined to predicted plastic hinge lengths the predicted plastic hinge lengths for the diagonal direction would need to be reduced by 40 – 50%.

4.4 Shear deformations of TUA and TUB

For plastic hinge analysis it is most convenient to characterise the shear displacements as a ratio of the flexural displacements (Section 2.1.1). Therefore, the ratio Δ_s/Δ_f will be used in the following to characterise the shear deformations of TUA and TUB. Before the experimentally determined ratios Δ_s/Δ_f are presented in Section 4.4.2 it is briefly outlined in Section 4.4.1 how flexural and shear displacements were computed from the experimental measurements.

In Section 4.4.3 existing approaches are employed to predict the Δ_s/Δ_f -ratios and the results are compared to the experimentally determined ratios.

4.4.1 Determining the different displacement components

The total top displacement is typically interpreted as the sum of four displacement components, i.e. (i) the sliding displacement Δ_s at the base of the wall, (ii) the deformation component Δ_θ due to opening of the joint between the wall base and the foundation, (iii) the flexural deformation Δ'_f of the wall and (iv) the shear displacement Δ_s . In the following the displacement components Δ_θ and Δ'_f are treated as the total flexural displacement Δ_f . This corresponds to the approach taken in plastic hinge analysis in which the strain penetration into the foundation is included in the plastic hinge length equation (Equation 2.12). While the top displacements of TUA and TUB were measured directly against reference columns (Section 3.3), the individual displacement components needed to be derived from local displacement measures. For TUA and TUB, the sliding displacement at the wall base could be readily obtained from gauges at the base of the web, the West and the East flange measuring the relative horizontal displacements between the wall and the foundation. The computation of the remaining two displacement components, i.e. the flexural and the shear displacements are described in following two sections.

a) Flexural displacements.

The flexural deformations of the web and the flanges were obtained from the four chains of LVDT devices along the four outer edges of TUA and TUB (Section 3.3, Figure 3.7). From these measurements average curvatures were derived (Equation 4.1) and the flexural deformation of the three wall faces were computed by double integration of the curvature profiles. The LVDT chains only extended to a height of $h = 2650\text{mm}$; between $h = 2650\text{mm}$ and the height where the actuator force was applied ($h_{NS} = 2.95\text{m}$, $h_{EW} = 3.35\text{m}$) the wall was assumed as rigid. The EW flexural deformations of the web were computed from the LVDT chains along the NE and NW edges. The NS flexural deformations of the West and East flanges were derived from the LVDT chains along the NW and SW edges and the NE and SE edges, respectively.

b) Shear displacements.

The shear displacements were determined from the diagonal measurements on the outer faces of the web and the two flanges. Assuming the centre of rotation is at the midheight of the panel, the shear distortion γ can be determined as (e.g. Dazio *et al.* [1999]):

$$\gamma = \frac{\Delta_s}{h_{sb}} = \frac{1}{4bh_{sb}}((d + \delta_2)^2 - (d + \delta_1)^2) \quad (4.6)$$

In some studies this equation is simplified to (e.g. Hines *et al.* [2002b]):

$$\gamma = \frac{d}{2bh_{sh}}(\delta_2 - \delta_1) \quad (4.7)$$

For the definition of the variables see Figure 4.4a. Equation 4.6 can be derived using Pythagoras' theorem within the triangles ABC and DEF. Equation 4.7 corresponds to the zero and first order terms of the Taylor series of Equation 4.6.

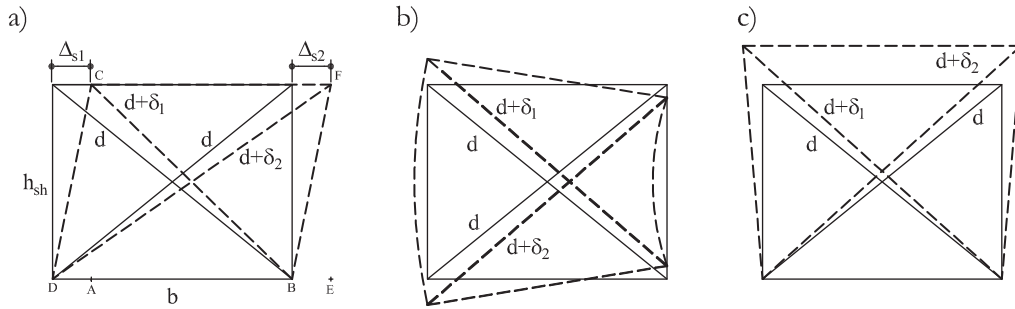


Figure 4.4. Original method for evaluating the shear displacements: Assumed variation of lengths of diagonals for shear deformations (a), flexural deformations (b) and vertical and horizontal elongation (c).

Based on the deformation schemes shown in Figure 4.4 it is often argued that only shear deformations cause a different variation in lengths of the two diagonals d_1 and d_2 whereas flexural deformations and elongations extend the two diagonals by the same amount. Hiraishi [1984] showed that Figure 4.4 reflects the special case of constant curvature over the height of the panel. If the curvature is not constant (Figure 4.5), estimates according to the original equations (Equations 4.6 and 4.7) overestimate the actual shear displacements. Note that this finding is based on the assumption that the curvature decreases from the base to the top. Hiraishi [1984] showed that a term needs to be subtracted from Equation 4.7 in order to account for the variation of curvature:

$$\gamma = \frac{d}{2bh}(\delta_1 - \delta_2) - (\alpha - 0.5)\theta \quad (4.8)$$

where θ is the rotation at the top of the panel and α a measure for the variation of the curvature:

$$\begin{aligned} \theta &= \int_{z=0}^h \varphi(z) dz \\ \alpha &= \frac{\int_{z=0}^h \theta(z) dz}{\theta \cdot z} \end{aligned} \quad (4.9)$$

where $z = [0; h]$ defines the height of the panel and $\varphi(z)$ is the curvature over the height of the panel. For a constant curvature the rotation increases linearly with height and the flexural displacement at the top of the panel is $\theta \cdot h/2$ and hence $\alpha = 0.5$. For this special case, the original method is correct; if the curvature decreases from the bottom to the top, the original method overestimates the actual shear displacements. For TUA and TUB the maximum difference in shear displacements determined according to the two different methods was 70% (Position F, East flange); for most directions of loading the difference was, however, between 10 and 20%. It is obvious that the modified method by Hiraishi [1984] requires the measurement of the flexural deformations of the panel by means of transducers along the two vertical edges of the panel. The finer the subdivision of these two chains of transducers the higher the accuracy with that α can be determined.

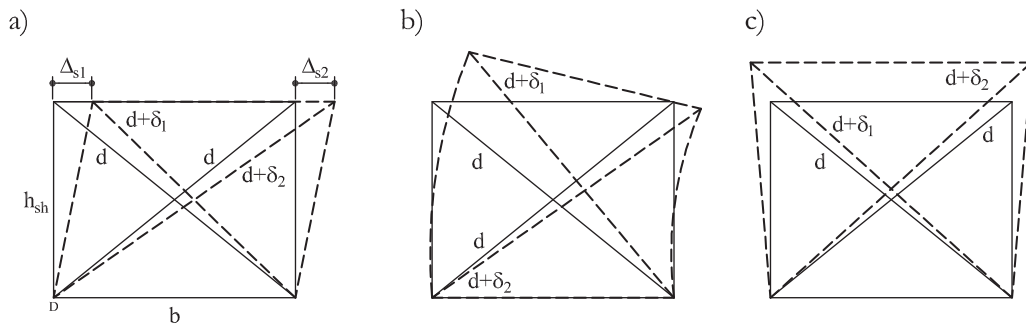


Figure 4.5. Modified method by Hiraishi [1984] for evaluating the shear displacements: Assumed variation of lengths of diagonals for shear deformations (a), flexural deformations (b) and vertical and horizontal elongation (c).

Since Hiraishi's method accounts for the effect of the curvature distribution on the shear displacement measurements it seems superior to the original method. Analysis of the results obtained for TUA and TUB and the rectangular walls tested by Dazio *et al.* [1999] has, however, shown that the sum of the shear displacements according to Hiraishi's method and sliding and flexural displacements is often less than the measured total displacement. However, this was not confirmed by the finite element results presented in Section 5.2.2 (e.g. Figure 5.13a) and might therefore be due to measurement errors or deformations that were not captured. For the sake of completeness it is stated here that the findings by Massone and Wallace [2004] are in contrast to the observations that the sum of the shear displacements according to Hiraishi's method and sliding and flexural displacements is often less than the measured total displacement. Massone and Wallace [2004] found that, if the shear displacements are evaluated according to Hiraishi's method, the total of shear and flexural displacements matches the measured top displacement very well. But it is important to note that Massone and Wallace

[2004] could not compute α from measurements since the vertical elongations of the wall edges were only measured with one device per panel height. Hence, they estimated α as 2/3 and found good agreement. However, verifying Hiraishi's method with a best guess estimate of the all-controlling factor α seems hardly sound. Massone and Wallace [2004] stated themselves that the presented findings would be stronger if α could have been determined directly from measurements.

As alternative to Hiraishi's and the original method, the shear deformations can be determined indirectly as the difference of the total displacement Δ_{top} minus the flexural displacement Δ_f and the sliding displacement along the base of the wall Δ_{sl} :

$$\Delta_s = \Delta_{top} - \Delta_f - \Delta_{sl} \quad (4.10)$$

Although the method by Hiraishi was found to result in low estimates of Δ_s when compared to the indirect method, it is preferred to the original method. Whether Hiraishi's method or the indirect method for determining the shear deformations is better suited depends on the type of measurement available.

4.4.2 Experimentally derived ratios of Δ_s/Δ_f for TUA and TUB

Using the techniques described in the previous section, the flexural, shear and sliding shear displacement components were determined for all peak displacements of the load histories to which TUA and TUB were subjected. Figures 4.6 and 4.7 show for TUA and TUB, respectively, the contribution of the three displacement components to the total displacement for the different directions of loading. The shear displacements which are included in these figures were computed according to Hiraishi's method (Section 4.4.1). In plot a of these figures the displacement components of the web for EW cycles are plotted; plot b shows the average of the displacement components of the West and East flange for NS cycles. For the diagonal cycles the displacement components of the web, the West and East flange are presented in three separate plots (plots c-e). As Dazio [2000] had postulated, the contributions of one displacement component to the total displacement remained approximately constant over the entire ductility range (Section 2.6). Whereas the contributions of the sliding displacements to the total displacements were very small for all directions of loading, the shear displacements constituted for some directions of loading and wall sections a significant part of the total displacements.

To illustrate the variation in Δ_s/Δ_f -ratios for different positions and wall sections the ratios are presented in graphical form in Figures 4.8 and 4.9 for TUA and TUB, respectively. The given Δ_s/Δ_f -ratios are mean ratios, which were computed as the average ratio of the cycles

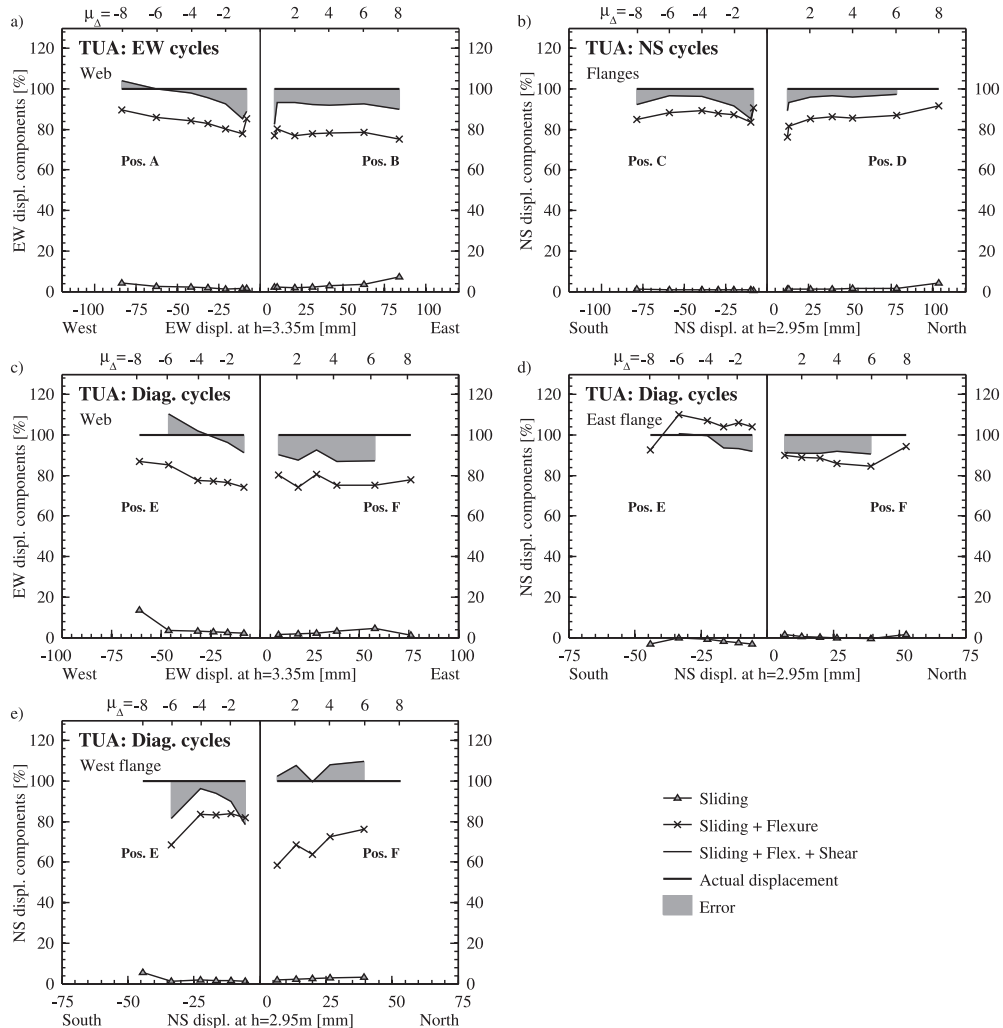


Figure 4.6. TUA: Displacement components for cycles in the EW (a), NS (b) and diagonal (c-e) directions.

with $\mu_{\Delta} = 2.0 - 8.0$ for TUA and as average ratios of the cycles with $\mu_{\Delta} = 2.0 - 6.0$ for TUB. Cycles with $\mu_{\Delta} < 2.0$ were not included when computing the mean Δ_s/Δ_f -ratios since in particular for TUA measuring very small shear displacements led to inaccurate results. During testing of TUA the connection between the string pots measuring the diagonal deformations and the filaments, which were used to elongate the string pots, lacked stiffness. As a consequence the string pot measurements showed signs of a small hysteresis and slip, which affected in particular the measurements at small cycle response, and therefore the small cycles were

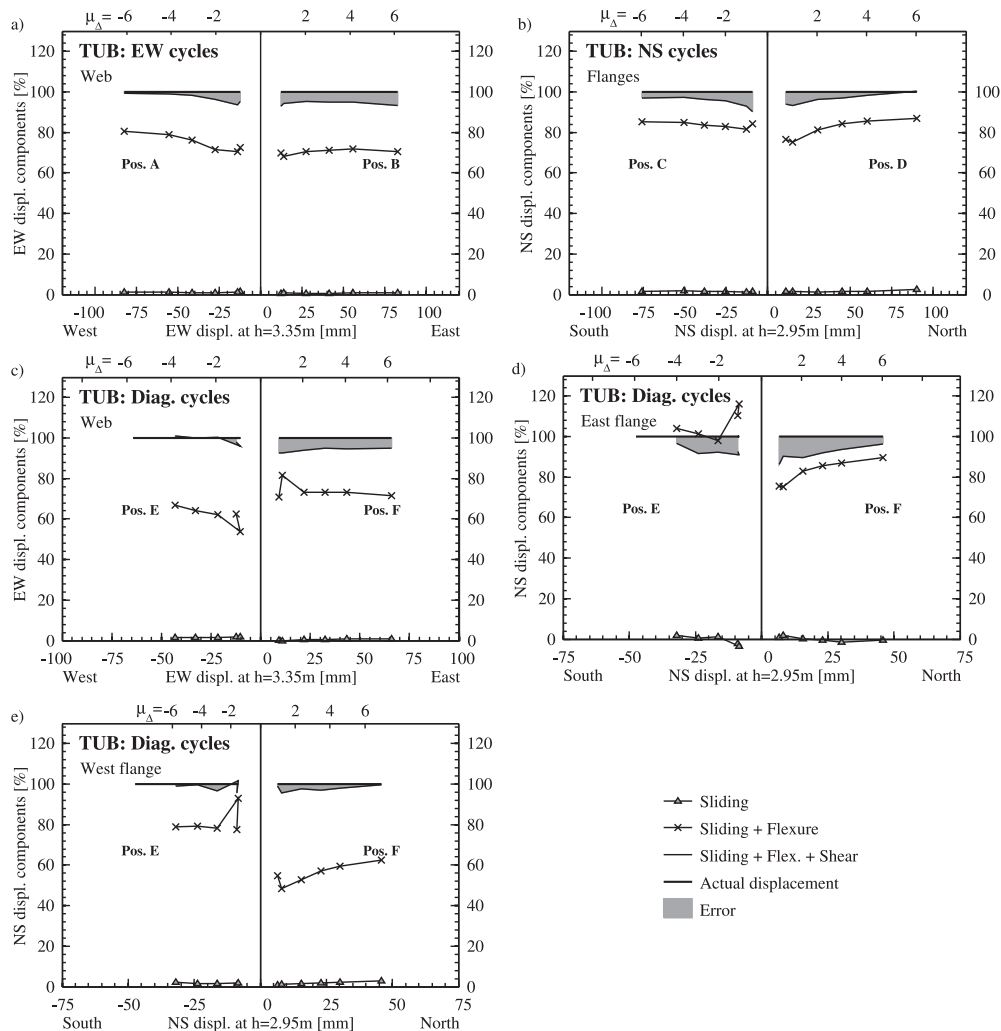


Figure 4.7. TUB: Displacement components for cycles in the EW (a), NS (b) and diagonal (c-e) directions.

not included when computing the mean value. For testing of TUB the setup was improved and the string pot measurements are believed to be fairly accurate for small displacements too. Figures 4.8 and 4.9 show the following:

- Shear displacements constituted a considerably larger portion of the total displacement for the slender wall TUB than for the wall TUA whose wall thickness was 1.5 times the

wall thickness of TUB. For most positions the shear displacement ratio of TUB was 1.4 – 2.0 times greater than the shear displacement ratio of TUA.

- The shear displacement ratio that is most conspicuous is the ratio for the East flange at Position E, which is negative, i.e. the shear displacements and the flexural displacements have opposite signs. When loading in the diagonal direction the force in the East flange did not reach its peak at the maximum displacement (Position E) but dropped from the force at the origin (Position O) to the final value at Position E (Section 3.6.2). This drop in force probably led to a reverse of the shear displacements in the East flange.
- When the wall sections were under net tension (web at Position E, West flange at Position F) the ratio of the shear displacements to flexural displacement was largest.
- When the compression zone passed through the wall section the order of magnitude of the Δ_s/Δ_f -ratio was similar to Δ_s/Δ_f -ratios of rectangular walls.

Table 4.5 summarises the mean ratios of shear to flexural deformations for the web and flanges in the different direction of loading. To demonstrate the sensitivity of the results to the different methods, the Δ_s/Δ_f -ratios for TUA and TUB were computed using all three methods that had been introduced in Section 4.4.1. In most cases the sum of the flexural displacements, sliding displacements and the shear displacements derived according to Hiraishi's method was slightly smaller than the total measured displacement (Figures 4.6 and 4.7). Hence, the indirect method led to ratios that were slightly larger than those derived according to Hiraishi. Only in some cases was the difference significant; these concern mostly cases in which the ratio Δ_s/Δ_f was rather small because in these cases small absolute differences yield large relative differences. As expected, computing the shear displacements according to the original methods led in all cases (apart from the negative ratios) to larger ratios than for Hiraishi's method. Since there is mathematical evidence that the original method overestimates the actual shear displacements these will not be considered in the following. Which of the remaining two methods is more accurate is difficult to determine. In the following the values according to the indirect method will be used. The difference between the ratios clearly shows that the ratios cannot be considered as exact but represent approximate figures only.

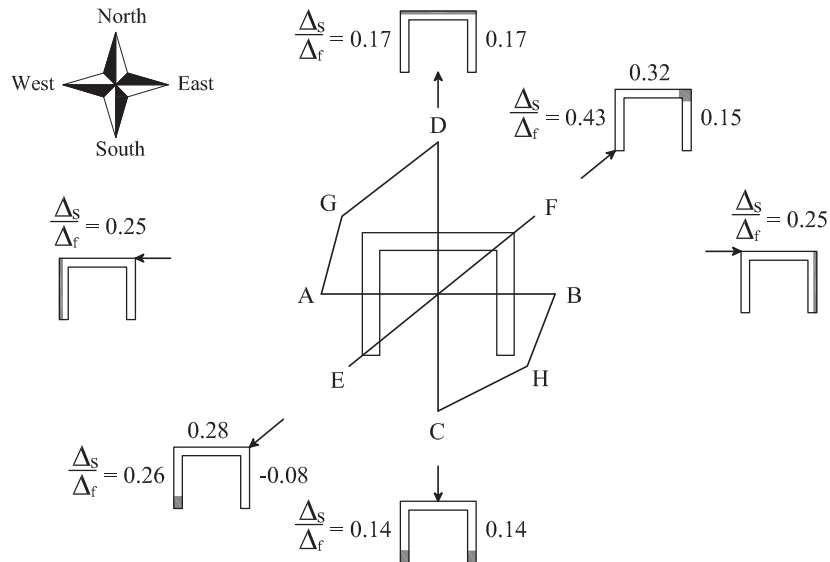


Figure 4.8. TUA: Average ratios of Δ_s/Δ_f for different directions of loading (shear deformations were determined according to the indirect method).

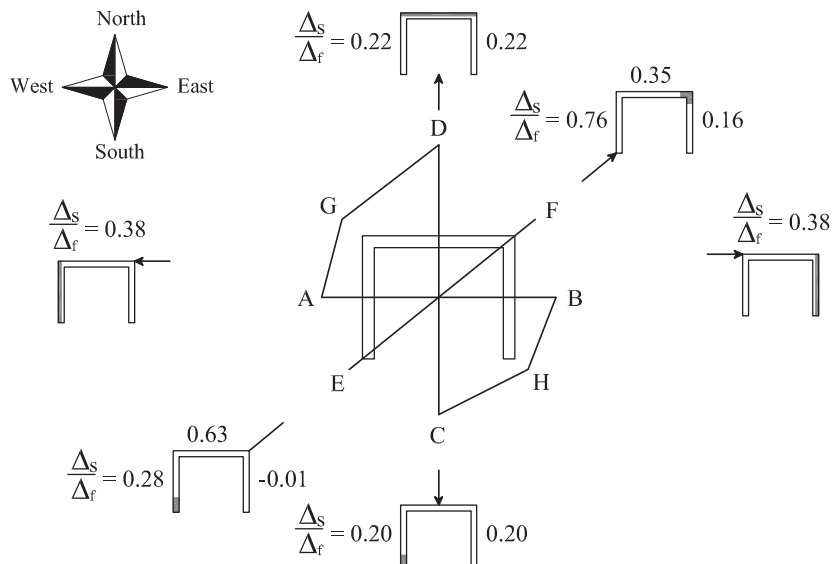


Figure 4.9. TUB: Average ratios of Δ_s/Δ_f for different directions of loading (shear deformations were determined according to the indirect method).

Table 4.5. TUA and TUB: Comparison of the ratios of shear to flexural deformations for different methods of evaluating the shear displacements.

		TUA			TUB		
		$\frac{\Delta_{s1}}{\Delta_f}$	$\frac{\Delta_{s2}}{\Delta_f}$	$\frac{\Delta_{s3}}{\Delta_f}$	$\frac{\Delta_{s1}}{\Delta_f}$	$\frac{\Delta_{s2}}{\Delta_f}$	$\frac{\Delta_{s3}}{\Delta_f}$
Position A, B	Web	0.18	0.25	0.20	0.32	0.38	0.33
Position C	Flanges	0.08	0.14	0.10	0.15	0.20	0.17
Position D	Flanges	0.13	0.17	0.16	0.18	0.22	0.21
Position E	Web	0.30	0.28	0.33	0.61	0.63	0.66
	West flange	0.14	0.26	0.15	0.25	0.28	0.27
	East flange	-0.09	-0.06	-0.08	-0.07	-0.01	-0.07
Position F	Web	0.17	0.32	0.18	0.27	0.35	0.26
	West flange	0.53	0.43	0.59	0.72	0.76	0.83
	East flange	0.05	0.15	0.08	0.08	0.16	0.11
Δ_{s1}	Computed according to Hiraishi [1984]						
Δ_{s2}	Indirection method: $\Delta_{s2} = \Delta_{top} - \Delta_f - \Delta_{sl}$						
Δ_{s3}	Original method						

4.4.3 Predicting the shear deformations of TUA and TUB with existing methods

In Section 2.6 the approaches by Hines *et al.* [2004] and Priestley *et al.* [2007] for predicting shear deformations of RC walls were introduced. These two approaches were applied to TUA and TUB and the predicted Δ_s/Δ_f -ratios are compared with the experimentally determined ratios. Table 4.6 summarises the experimental and predicted ratios; a graphical comparison of the values is shown in Figure 4.10. The approach proposed by Priestley *et al.* [2007] could in many cases not be applied since the shear cracking force V_{cr} was larger than the total shear force demand. Assuming the section remained uncracked in shear led to very small shear displacements; in most cases this approach therefore underestimated the ratio Δ_s/Δ_f . If the shear demand was larger than V_{cr} , the ratio Δ_s/Δ_f was often overestimated. The semi-empirical approach of Hines *et al.* [2004] led to quite good estimates provided that the wall section was not under net tension. When the wall section was under net tension, the ratios Δ_s/Δ_f were grossly underestimated.

Table 4.6. Ratios of shear to flexural displacement for TUA and TUB according to Priestley *et al.* [2007] and Hines *et al.* [2004].

		TUA			TUB		
		Exp.	Hines <i>et al.</i> [2004]	Priestley <i>et al.</i> [2007]	Exp.	Hines <i>et al.</i> [2004]	Priestley <i>et al.</i> [2007]
Position A, B	Web	0.25	0.17	0.15	0.38	0.20	0.93
Position C	Flanges	0.14	0.10	0.02	0.20	0.13	0.10
Position D	Flanges	0.17	0.10	0.02	0.22	0.10	0.04
Position E	Web	0.28	0.13	0.04	0.63	0.16	0.32
	West flange	0.26	0.13	0.05	0.28	0.20	0.49
	East flange	-0.06	0.09	0.01	-0.01	0.09	0.01
Position F	Web	0.32	0.17	0.05	0.35	0.17	0.67
	West flange	0.43	0.07	0.01	0.76	0.09	0.04
	East flange	0.15	0.09	0.03	0.16	0.09	0.04

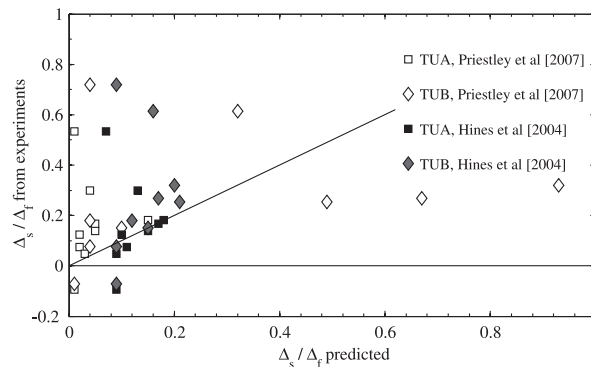


Figure 4.10. TUA and TUB: Comparison of the experimentally determined Δ_s/Δ_f -ratios to the predicted ratios according to Priestley *et al.* [2007] and Hines *et al.* [2004].

4.5 Summary and Conclusions

The objective of this chapter was to evaluate whether the current state-of-the-art equations in plastic hinge analysis could also be used for the plastic hinge analysis of U-shaped walls. This was open to debate since most of these equations are empirical or semi-empirical equations that have been calibrated with databases that did not contain U-shaped walls. Four different aspects of plastic-hinge analysis have been considered; these were: (i) the yield curvature, (ii) the strain limits for ultimate displacement, (iii) the plastic hinge length, and (iv) the ratio of shear to flexural displacements. The findings are briefly recapitulated in the following.

For the yield curvatures ready-made estimates derived from parametric section analyses are currently only available for the two principal directions. For the diagonal direction, the engineer needs to compute the yield curvature from a section analysis of the considered U-shaped section on a case-to-case basis. Both types of estimate compare fairly well to the actually measured yield curvatures and hence one can conclude that at the onset of yielding the assumption of plane sections seems to lead to good results. The strain limits on concrete and reinforcement derived for walls or columns with different cross sections can be applied without limitations to walls with U-shaped cross sections. In the experiments carried out the contribution of the strain penetration to the spreading of inelasticity was small since the foundation had been prestressed laterally. With respect to the other mechanisms contributing to the plastic hinge length the modified and less conservative Equation 2.12 yielded fairly good estimates for all directions. The plastic hinge length in the diagonal direction was estimated as the maximum of the plastic hinge lengths in the two principal directions (EW and NS direction). For the principal directions the estimates were typically slightly on the low side while for the diagonal direction the estimates were slightly larger than the experimentally determined plastic hinge lengths. Hence, although the match between the estimate and the experimentally determined values are satisfactory for all directions, the degree of conservatism using Equation 2.12 will be larger for the principal directions than for the diagonal directions. To remove the bias from the plastic hinge length $L_{ph3,mod}$, the predicted plastic hinge lengths for the diagonal directions of loading would need to be reduced by $\sim 40 - 50\%$.

While the available equations for yield curvatures, strain limits and plastic hinge lengths appear to be also applicable to U-shaped walls, existing empirical methods for estimating shear displacements fail to capture the behaviour of wall sections that are under net tension. These are the web at Position E, the West flange at Position F and the East flange at Position E. The latter is a special case since the ratio of shear to flexural displacements is negative; it is not expected that this ratio can be predicted by any of the empirical methods since the complex force-displacement history of the flange causes the negative ratio. However, the Δ_s/Δ_f -ratios for the web at Position E and the West flange at Position F should be predictable if the effect of the net tension on the section could be captured. It would be desirable to gain a better understanding of the factors controlling the ratio Δ_s/Δ_f and to develop an approach that is applicable independent of the axial strain in the wall section. This is attempted in Chapter 5.

5. SHEAR DEFORMATIONS OF REINFORCED CONCRETE WALLS

The ratio of shear to flexural deformations of a RC wall is an important design parameter, which enters directly into equations for the plastic hinge analysis but is also useful when estimating shear stiffnesses of elements in stick models or wide-column models. The ratio of shear (Δ_s) to flexural deformations (Δ_f) is therefore often used for characterising the shear deformations of RC walls. In Section 4.4.2 the Δ_s/Δ_f -ratios were determined for TUA and TUB and the variation of these ratios between the web and flanges for the different directions of loading were discussed. It has also been shown that neither of the two existing approaches for estimating the ratio of shear to flexural deformation that were introduced in Section 2.6 and applied to TUA and TUB in Section 4.4.3 yielded entirely satisfactory results. The objective of this chapter is to look at shear displacements of RC walls in some more depth than in Chapter 4 and to identify alternative ways of estimating the ratio of shear to flexural displacements. The problem is approached in two different ways: First, in an empirical study key factors affecting the ratio of shear to flexural displacements in RC walls are identified and a new empirical equation for estimating the ratio Δ_s/Δ_f is proposed (Section 5.1). Second, two finite element programs are assessed regarding their capability of modelling shear deformations (Section 5.2). Unlike the discussion in Section 4.4.1 this chapter is not limited to the experimental results of TUA and TUB but results from other experiments on RC walls are also included.

5.1 An empirical investigation into shear displacements of RC walls

This section presents a small investigation into the ratio of shear to flexural deformations of RC walls. The objective is to identify the variables controlling the ratio Δ_s/Δ_f and to derive an empirical relationship between these key variables and Δ_s/Δ_f . For this purpose a database of RC walls was assembled. Apart from TUA and TUB, the database contains experimental and numerical data of 27 walls and columns from five different test series [Oesterle *et al.*, 1976, 1979; Dazio *et al.*, 1999; Hines *et al.*, 1999, 2002b; Reynouard and Fardis, 2001]. All walls were tested under quasi-static cyclic loading. Most of the walls were subjected to uni-directional loading, only test units TUA, TUB and IspraXY had been subjected to bi-directional loading. The walls were built at scale 1 : 3 to 1 : 2 and their cross sections were rectangular, barbelled,

flanged or U-shaped. The shear span ratios varied between 2.00 to 4.04. Details on these walls are summarised in Appendix A.

Squat walls with shear span ratios smaller than 2.00 were excluded from the database because the shear transfer mechanism of squat walls is different to that of slender walls: Squat walls tend to transfer the horizontal load from the top of the wall to its base via a direct, inclined compression strut whereas the shear transfer mechanism of slender walls is chiefly related to the truss mechanism formed by shear reinforcement and compression diagonals. From Demec measurements and nonlinear analysis it was also found that the region where the shear strains are concentrated differs for squat and slender walls: In squat walls the shear strains are concentrated in the region of the compression strut while for slender walls the shear strains are concentrated in the region of the plastic hinge that is under tension.

As stated above this section describes an empirical study on the ratios of shear to flexural deformations for RC cantilever walls. To identify possible variables influencing the magnitude of the shear displacements, the ratios of shear to flexural deformations of the PCA walls (Phase I) are discussed in Section 5.1.1 in terms of the associated failure mechanisms and shear demands. In the same section the strain state of a cracked RC panel is analysed and parallels are drawn to the findings from the PCA-walls. The ratio of shear to flexural deformations will obviously also depend on the slenderness of the wall. An option for normalising the ratios for walls of different geometry is explored in Section 5.1.2. The following two sections discuss two sets of variables that influence the shear deformations, i.e. the magnitude of the shear stresses (Section 5.1.3) and the magnitude of the axial strains (Section 5.1.4). In the final section a new semi-empirical approach for estimating the ratio of shear to flexural deformations is introduced (Section 5.1.5).

5.1.1 Variation of the ratios Δ_s/Δ_f with ductility demand

Dazio [2000] found that the ratio of shear to flexural displacements is approximately constant for peak displacements in the inelastic loading range (Section 2.6). While this finding holds for most of the walls within the database, there are some walls for which the Δ_s/Δ_f -ratio varies significantly with the top displacement. To illustrate the differences of these walls to the others the walls of Phase I of the PCA test series are discussed in the following.

Figures 5.1a and b show the ratio of shear to flexural displacements as a function of the total top displacement and the displacement ductility, respectively. The ratios are plotted for inelastic cycles showing a stable hysteretic behaviour; small amplitude cycles at the beginning of the test and cycles at the end of the test when either bar fracture or web crushing had occurred were omitted. In the following the variation of the Δ_s/Δ_f -ratios for top displacements

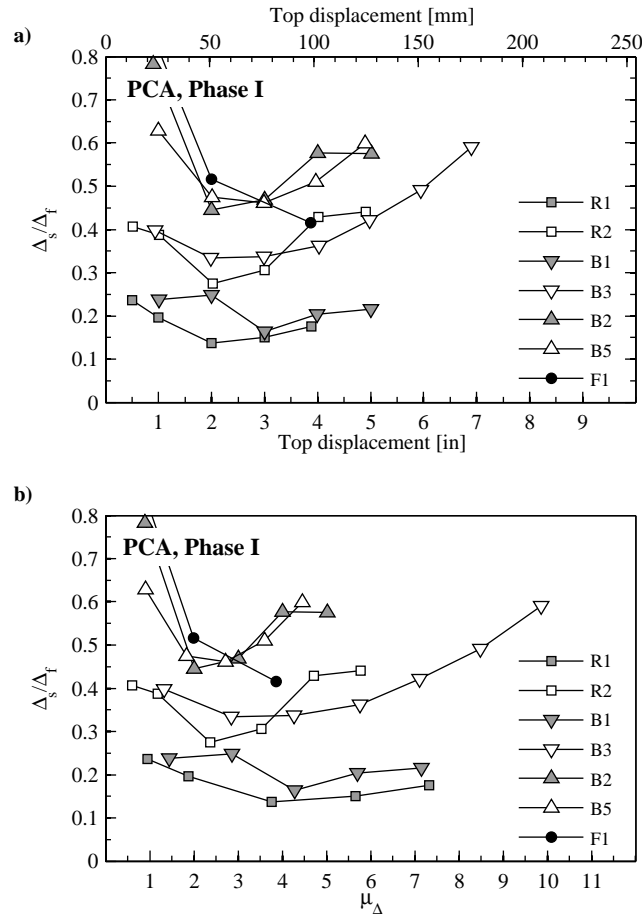


Figure 5.1. PCA, Phase I: Variation of the ratio Δ_s/Δ_f with top displacement (a) and displacement ductility (b).

$\Delta_{top} \geq 2.0$ in is discussed; for cycles with smaller amplitudes the interaction of different effects that control the variation of Δ_s/Δ_f with top displacement is even more complex than for large cycle response (see also discussion later in this section). Figure 5.1 shows that for the walls R1 and B1 the ratio of Δ_s/Δ_f is approximately constant over the entire ductility range. This is in line with Dazio's observation (Section 2.6). For F1 only two data points with $\Delta_{top} \geq 2.0$ in were available and it is therefore not possible to clearly identify a trend. For the other four walls (R2, B3, B2, B5), the ratio Δ_s/Δ_f tended to increase with displacement demand for $\Delta_{top} > 2.0$ in, i.e. with increasing top displacement the shear deformations contributed a larger portion to the total displacement. Specimens R1 and B1 failed in flexure whereas specimen F1 failed suddenly due to web crushing. All these three specimens have

in common that the shear transfer mechanism as such did not deteriorate significantly before failure. Specimens B₃ and B₅ experienced concrete crushing and grinding of the web concrete. From the onset of the crushing of the concrete, the contribution of the shear deformations to the overall deformations increased significantly. Specimen R₂ was subjected to large out-of-plane deformations which might have contributed to a deterioration of the compression struts and other parts of the shear transfer mechanism. Specimen B₂ is an exception since it failed suddenly due to web crushing and hence one might expect that the ratio of shear to flexural deformations remained constant until failure. Yet the ratio constantly increased from about 45% at $\Delta_{top} = 2.0$ in to 58% at $\Delta_{top} = 5.0$ in.

The walls that Dazio tested (Section A.3) were all capacity-designed and hence shear deformations were smaller than for the PCA-walls (the Δ_s/Δ_f -ratios of the walls tested by Dazio varied between 0.12–0.22). Nonetheless, the results from the PCA-walls show that Dazio's finding is applicable to RC walls if the shear transfer mechanism is not degrading significantly. For walls for which the shear transfer mechanism is degrading significantly the ratio Δ_s/Δ_f increases as the top displacement increases. It was found that one arrives at the same conclusion if the stress state due to axial load, shear force and moment of a cracked RC panel with parallel compression struts is considered (Fig. 5.2a). This is outlined in the following paragraphs.

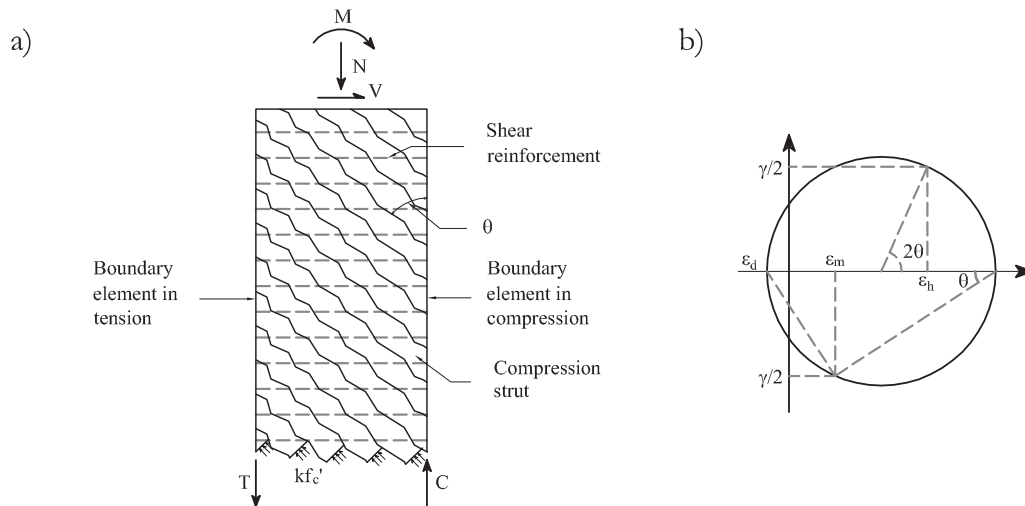


Figure 5.2. Truss analogy model for a wall element with parallel compression struts (a, adapted from Oesterle *et al.* [1984]) and Mohr's circle representing the strain state at the centre line of the wall (b, adapted from Rabbat and Collins [1978]).

Figure 5.2b shows the Mohr's circle representing the average strain state of the wall panel in Figure 5.2a. The variable ε_d refers to the axial strain in the compression strut (hence $\varepsilon_d < 0$), ε_m to the mean axial strain of the section, ε_h to the horizontal strain, and γ to the shear strain. The following two relationships can be readily derived:

$$\begin{aligned} \tan\theta &= \frac{\gamma/2}{\varepsilon_h - \varepsilon_d} \\ \tan\theta &= \frac{\varepsilon_m - \varepsilon_d}{\gamma/2} \end{aligned} \quad (5.1)$$

Solving the two equations for $\gamma/2$, adding the results together and making use of the relationship that $\tan\theta + \cot\theta = 2/\sin 2\theta$, leads to the following expression for γ :

$$\gamma = \frac{\varepsilon_m}{2\tan\theta} + \varepsilon_h \cdot \tan\theta - \frac{2\varepsilon_d}{\sin 2\theta} \quad (5.2)$$

The same equation is quoted in Oesterle *et al.* [1984] but it originates from Rabbat and Collins [1978] where it was given in a slightly different form. The equation can also be derived using principles of virtual works on the truss model shown in Figure 5.2a [Oesterle *et al.*, 1984]. Equation 5.2 visualises that there are three different contributions to the shear strain γ : The first term represents the contribution of the mean axial strain ε_m . In structural walls subjected to seismic loading the axial strains are chiefly caused by flexural deformations. Assuming that the compression zone depth c remains approximately constant, ε_m is directly related to the curvature φ , which determines the flexural deformations. Therefore, the first term of Equation 5.2 shows that the shear strains are directly related to the flexural strains. Hence, if the second and third term are small, the shear displacements are proportional to the flexural displacements – this was the case for Dazio's walls that were capacity designed. The second term represents the contribution of the horizontal strains in the shear reinforcement to the shear strain and the third term the contribution of the strain in the compression diagonal to the shear strain. Thus, if the walls are either not capacity designed and plastic strains are accumulating in the shear reinforcement or if the compression struts are softening considerably the shear strains increase disproportionately to the flexural strains. As a consequence, the ratio Δ_s/Δ_f increases with the top displacement.

The importance of flexural strains on shear strains was already recognised by Oesterle *et al.* [1979], who observed that "Loss of shear stiffness with reversals was primarily dependent on the magnitude of inelastic tensile set in the reinforcement from the previous loading. Abrasion and loss of material from grinding played a secondary role." They also recommended that the "large 'effective' shear distortions" accompanying "flexural hinging (...) should be considered in structures designed to utilize the inelastic capacity of walls" – a recommendation which seemed to have been forgotten over some decades but gains significance in the time of displacement-based design approaches.

Equation 5.2 offers also an explanation for the reduction of the ratio Δ_s/Δ_f with top displacements up to 2in: The walls represented in Figure 5.1 have nominal yield displacements between 0.5 – 1.1in (12.7 – 27.9mm). A top displacement of $\Delta_{top} = 2.0$ in therefore corresponds to a displacement ductility of $\mu_\Delta \cong 2.0 - 4.0$. Up to yield, the forces in the section increase and hence all three components of the shear strain increase (Equation 5.2). Beyond yield, on the premise that the shear transfer mechanism is not yet degrading, only the first component is increasing in proportion to the flexural displacements whereas the magnitude of the last two remains approximately constant. Thus the ratio Δ_s/Δ_f is reducing until the last two components of γ in Equation 5.2 are so small with respect to the first that the ratio is remaining approximately constant.

The largest flexural strains and therefore also the largest shear strains in structural walls occur in the plastic hinge zone. Strictly speaking, Equation 5.2 is not applicable to the plastic hinge zones where compression struts are not parallel but arrayed in a fan-like pattern. However, it is believed that Equation 5.2 can help to understand which parameters influence the shear deformations. In order to increase the chance of identifying trends the study will focus on specimens that showed no signs of a significantly degrading shear mechanism. Since data points are scarce the specimens R2, B3, B2 and B5 are not deleted from the dataset but the ratio of Δ_s/Δ_f at $\Delta_{top} = 2$ in is taken as an approximation of the ratio Δ_s/Δ_f for a wall in which neither the horizontal strain in the shear reinforcement nor the strains in the compressive struts contributed significantly to the shear strains in the inelastic phase of the loading.

5.1.2 Making the ratios Δ_s/Δ_f of different walls comparable

It is obvious that the ratio of shear to flexural displacements also depends on the geometry of a wall. Hines *et al.* [2004] chose the shear span ratio as a parameter for making the ratio Δ_s/Δ_f of different walls comparable. Within this study the ratio of height to plastic hinge length (instead of the wall length) is chosen as the parameter for normalising the Δ_s/Δ_f -ratios. The choice of the parameter H/L_{ph} is based on the following considerations: If one assumes (i) that the flexural deformation is solely caused by the plastic rotation in the plastic hinge and (ii) that the shear deformations are also concentrated in the plastic hinge region (with an average shear strain γ) one can write the ratio Δ_s/Δ_f as follows:

$$\frac{\Delta_s}{\Delta_f} = \frac{\gamma \cdot L_{ph}}{\theta_p \cdot H} = \frac{\gamma}{\theta_p} \cdot \frac{L_{ph}}{H} \quad (5.3)$$

where γ is the shear strain and θ_p the plastic rotation within the plastic hinge zone. The first factor γ/θ_p reflects the dependence of shear strains on flexural strains – this is the ratio for which we would like to gather experimental information – while the second factor L_{ph}/H represents the geometry of the test unit. From the experimental data, the ratios Δ_s/Δ_f were

determined. Hence, in order to make these ratios comparable for walls of different geometries, Δ_s/Δ_f has to be multiplied by H/L_{ph} . It is evident that the parameter for normalisation is strongly dependent on the assumptions made but this approach seems a satisfactory compromise between simplicity and accurateness and is therefore considered as suitable for this empirical study.

5.1.3 Effect of shear stresses on shear deformations

One of the factors controlling the shear deformations are certainly the shear stresses. Using again the walls of Phase I of the PCA test serie as an example one can see that at $\Delta_{top} = 2$ in the ratios Δ_s/Δ_f fall into two groups: R1, R2, B1 and B3 have a ratio of $\Delta_s/\Delta_f = 0.15 - 0.33$ and B2, B5, F1 a ratio of $\Delta_s/\Delta_f = 0.45 - 0.47$. The key difference between the groups appears to be the nominal shear stress which is defined as:

$$\tau = \frac{V_n}{l_w \cdot t_w} \quad (5.4)$$

For the first group this varies between 0.57 and 1.37MPa whereas for the second group the values fall between 3.58 and 4.25MPa. Thus, the shear demand seems to be one of the factors controlling the ratio Δ_s/Δ_f .

Figure 5.3a shows the standardised ratio Δ_s/Δ_f as a function of the nominal shear stress τ . A weak trend of Δ_s/Δ_f with τ is recognisable. However, there are a large number of specimens that deviate significantly from the general trend. Two of these outliers are associated with the East flanges of TUA and TUB at Position E when the ratio Δ_s/Δ_f is negative. Possible reasons for the negative ratios were discussed in Section 4.4.2; these two ratios will not be included in the following discussion since it seems beyond the limits of a simple empirical model to capture the aspect of the complex behaviour of U-shaped walls that led to the negative ratios. Another group of specimens that produce data points outside the bulk data are three specimens by Hines *et al.* [2004]. These three specimens had more than the double shear reinforcement ratio than the other specimens of Hines' test series. To account for the fact that the shear deformations will be dependent on the ratio of shear demand to shear capacity the shear stress is normalised by the nominal shear stress capacity v_n [ACI Committee 318, 2002]:

$$v_n = \frac{\sqrt{f'_c}}{6} + \rho_h f_{yh} \quad (5.5)$$

where f'_c is the cylinder strength of the test unit, ρ_h the shear reinforcement ratio and f_{yh} the yield strength of the horizontal reinforcement. For walls that are under net tension the shear stress capacity v_n is reduced to [ACI Committee 318, 2002]:

$$v_n = \frac{\sqrt{f'_c}}{6} \left(1 + \frac{P}{A_g \cdot 3.45\text{MPa}}\right) + \rho_h f_{yh} \geq \rho_h f_{yh} \quad (5.6)$$

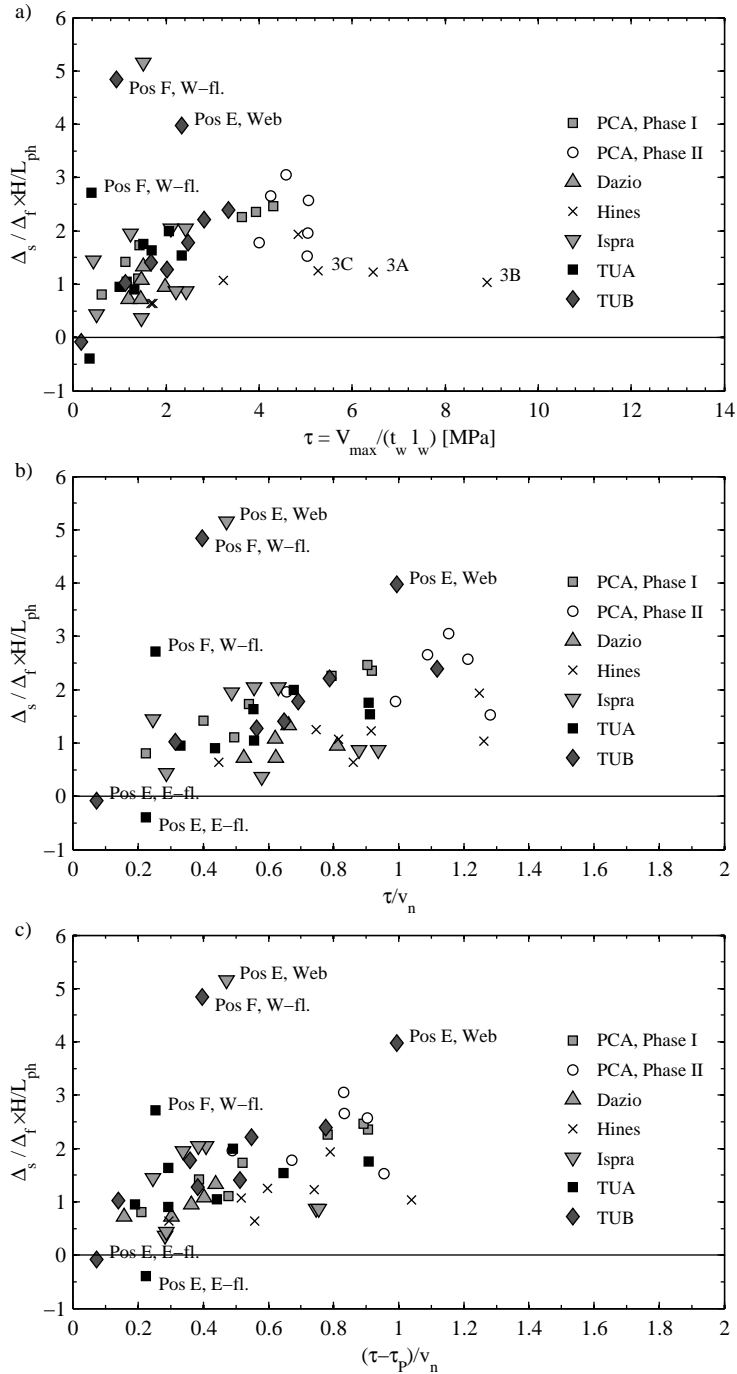


Figure 5.3. Shear deformations: The ratio Δ_s / Δ_f as a function of three different shear stress parameters: τ (a), τ/v_n (b) and $(\tau - \tau_p)/v_n$ (c).

where P is the axial force, which is defined as negative for tension. For rectangular or near rectangular walls the section is rarely subjected to large net tension forces; exceptions might occur if two walls are connected by deep coupling beams. For non-planar walls such as U-shaped walls, individual rectangular wall sections, i.e. the web or the flanges, might be subjected to large net axial forces depending on the direction of loading. For these wall sections the nominal shear stress capacity was computed according to Equation 5.6. In the code the effective shear area is defined as the web width times the distance from the extreme compression fibre to the centroid of the longitudinal reinforcement in tension [ACI Committee 318, 2002]. However, it was found that using this more elaborate definition of the shear area did not improve the correlation of τ/v_n to Δ_s/Δ_f . The nominal shear stress is therefore defined as described in Equation 5.4.

Figure 5.3b shows that normalising the shear stress demand by the shear stress capacity v_n improves slightly the correlation with the normalised ratio Δ_s/Δ_f . Note that Hines' empirical equation used a similar stress parameter, which was described by the variable $\alpha = \frac{V}{V_s} + \frac{V}{V_{sc}}$ (Equation 2.39). This parameter was not adopted here since it is believed that the ratio of shear demand to the diagonal tension shear capacity V_s has a stronger effect on the shear deformations than the ratio of shear demand to the diagonal compression shear capacity V_{sc} . It is believed that for most walls the diagonal compression strut is a relatively stiff member in the idealised shear truss mechanism (Figure 5.2a) compared to the shear reinforcement. Therefore only the shear capacity due to the shear reinforcement and the concrete friction component are considered when computing the shear stress capacity v_n , which is used to normalise the shear demand τ .

According to the modified UCSD model for the shear capacity of RC walls, the shear stress is transferred via three principal mechanisms [Kowalsky and Priestley, 2000], i.e. the steel truss mechanism, the concrete shear resisting mechanism, and an inclined compression strut due to the axial load. The latter of the three mechanisms seems to be the stiffest mechanism and it is therefore assumed that shear forces transmitted by the inclined compression strut do not contribute significantly to shear deformations. The shear capacity due to the inclined compression strut is V_p and the associated shear stress $\tau_p = V_p/(l_w \cdot t_w)$; for wall sections under net tension V_p is zero. Figure 5.3c shows the standardised ratio Δ_s/Δ_f as a function of $(\tau - \tau_p)/v_n$. The variability is slightly reduced with respect to Figure 5.3b. However, there are still four data points that lie above the general trend; these outliers are data points of TUA, TUB and IspraXY representing wall sections that had been under net tension while carrying a significant shear force (i.e. the web at Position E and the West flange at Position F).

5.1.4 Effect of axial strains: Coupling of shear and flexural deformations

In Section 5.1.1 it was shown that the shear strains are dependent on the mean axial strains, which can be caused by a moment and an axial force. In typical structural walls the mean axial strains are chiefly caused by flexural deformations; to improve the readability they will therefore be called flexural strains in the following. The objective of this section is to identify a parameter that describes the state of flexural strains and that is correlated with the standardised ratio Δ_s/Δ_f . Three different parameters will be discussed in the following.

a) Parameter as a function of the compression zone depth.

Equation 5.2 showed that the shear strain is related to the average flexural strain. A parameter which could identify whether the average flexural strain is relatively large or small is the normalised compression zone depth c/l_w . The compression zone depth can be determined from section analysis. Section analyses were carried out for the 29 walls within the database. The compression zone depth was determined at the point of the nominal moment, i.e. when the maximum steel strain reached 1.5%. Details on the section analyses of the walls included in the database can be found in Appendix A. Note that for the wall sections of TUA, TUB and IspraXY that are under large net tension forces the compression zone depth is zero.

Figure 5.4 illustrates the effect of the compression zone depth on the mean axial strain ε_m : For the same curvature, i.e. for the same flexural deformation, a large compression zone depth leads to a small medium axial strain and vice versa. It is expected that the larger c/l_w the smaller the Δ_s/Δ_f -ratio; to reach a positive correlation the Δ_s/Δ_f -ratios are plotted against the parameter $(1 - c/l_w)$ instead of c/l_w (Figure 5.5a). Contrary to expectations there is only a very weak correlation between $1 - c/l_w$ and Δ_s/Δ_f . The scatter is so large that the parameter c/l_w seems hardly suitable as exclusive parameter in an empirical approach for estimating Δ_s/Δ_f .

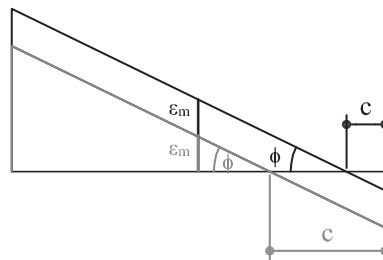


Figure 5.4. Effect of compression zone depth c on the mean axial strain ε_m .

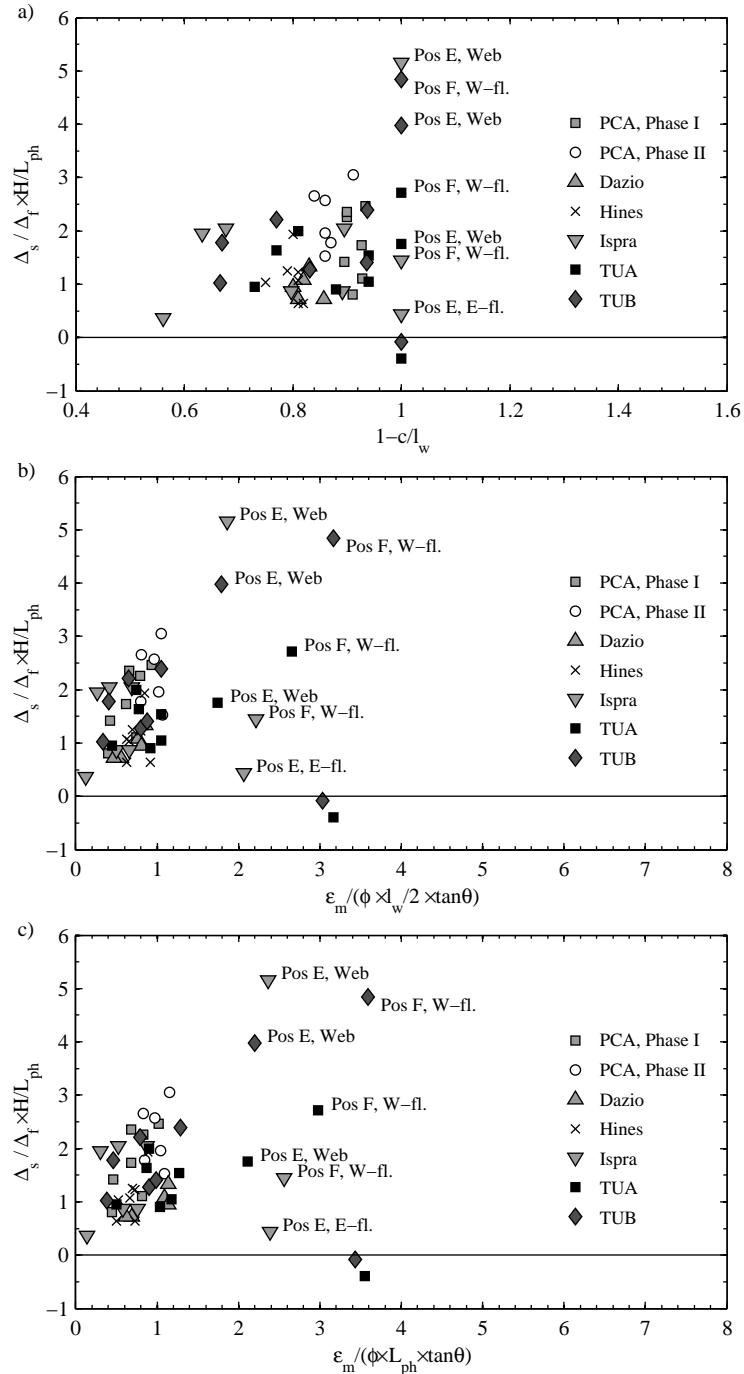


Figure 5.5. Shear deformations: The ratio Δ_s / Δ_f as a function of three different flexural strain parameters: $1 - c/l_w$ (a), $\varepsilon_m / (\tan\theta \cdot \varphi \cdot l_w / 2)$ (b) and $\varepsilon_m / (\tan\theta \cdot \varphi \cdot L_{ph})$ (c).

b) Parameter as a function of the mean axial strain - Approach 1.

To account for the effect of flexural strains on shear strains a second alternative parameter was considered; it is the first term of Equation 5.2. The mean axial strain was taken as the strain at the centre line from section analyses when the maximum steel strain is $\varepsilon_s = 1.5\%$ (point of nominal moment). The cracking angle θ was taken from observations, i.e. the actual cracking angle was used. The mean axial strain itself is, however, not a meaningful parameter since two walls of different length subjected to the same curvature would have different axial strains at the centre line. The objective of this parameter should be to distinguish between "normal" rectangular walls that have a compression zone at one end and wall sections of for example U-shaped walls for which the entire wall section is in tension. It is therefore suggested to normalise the mean axial strain by the fictive flexural strain at the centre line assuming the compression zone depth is zero, i.e. by $\varphi \cdot l_w/2$. Figure 5.5b shows Δ_s/Δ_f as a function of the parameter $\varepsilon_m/(\tan\theta \cdot \varphi \cdot l_w/2)$. The bulk of the data is concentrated in the first quarter of the plot, close to the origin. Within this bulk there is no clear trend recognisable. However, the sections of the test units TUA, TUB and IspraXY that are under net tension are not part of the bulk of the data but lie to the right of the bulk.

For sections with a compression zone this second parameter (ε_m) is of course related to the first parameter (c) since there is a direct relationship between c and ε_m/φ :

$$c = \frac{l_w}{2} - \frac{\varepsilon_m}{\varphi} \quad (5.7)$$

Hence, the difference between the two parameters is more eminent for wall sections that do not have a compression zone: Whereas the parameter c/l_w is limited to values between 0 and 1, the parameter ε_m/φ allows to define "negative" compression zones. It is therefore possible to differentiate more strongly between wall sections with and without compression zone. The overall correlation between the parameter $\varepsilon_m/(\tan\theta \cdot \varphi \cdot l_w/2)$ and the normalised ratio Δ_s/Δ_f is, however, still fairly poor.

c) Parameter as a function of the mean axial strain - Approach 2.

The third parameter used to characterise the effect of the flexural strain on the shear strain is very similar to the second one. Instead of normalising the mean axial strain by $\varphi \cdot l_w/2$ the mean axial strain is normalised by $\varphi \cdot L_{ph}$. Using the same simple model as in Section 5.1.2 (Equation 5.3) and assuming that the shear strain γ can be expressed by the first term of Equation 5.2 leads to the following expression of the Δ_s/Δ_f -ratio:

$$\frac{\Delta_s}{\Delta_f} = \frac{\varepsilon_m}{\tan\theta} \frac{L_{ph}}{\varphi L_{ph} H} = \frac{\varepsilon_m}{\tan\theta \varphi L_{ph}} \cdot \frac{L_{ph}}{H} \quad (5.8)$$

The second factor in the rearranged form of Equation 5.8 is used to standardise the ratio Δ_s/Δ_f whereas the first factor will be investigated as the third parameter characterising the

effect of flexural strain on shear strain. It is very similar to the second parameter, only that half the wall length $l_w/2$ has been replaced by the plastic hinge length L_{ph} . The similarity is also reflected in Figure 5.5c which is only marginally different from Figure 5.5b.

d) Choice of the parameter characterising the effect of the flexural strains on the shear strains.

None of the three discussed parameters for characterising the influence of the flexural strains on the shear strains shows a distinguished correlation with Δ_s/Δ_f over the entire range of explored x -values (Figure 5.5). Hence, none of these parameter is suited to serve as the single parameter in an empirical relationship of Δ_s/Δ_f . However, they might be used in conjunction with the stress parameter $(\tau - \tau_P)/v_n$, which was derived in the previous section. The joint use of the stress and a strain parameter for predicting the ratio Δ_s/Δ_f will be investigated in the following section.

5.1.5 An empirical relationship for the ratio Δ_s/Δ_f

In the two previous sections it was shown that the ratio of shear to flexural displacement depends on the shear stress demand to capacity ratio as well as on the axial strains within the section. Among the investigated stress parameters the parameter $(\tau - \tau_P)/v_n$ was most suitable (Section 5.1.3). On the strain side, three different parameters were investigated (Section 5.1.4); none of the three parameters was clearly superior to the other two and hence all three are tested in combination with the stress parameter. The results are shown in Figure 5.6. The overall best agreement is achieved for the third strain parameter, i.e. $\varepsilon_m/(\varphi \cdot L_{ph} \cdot \tan\theta)$ (Figure 5.6c). Without question, the scatter of the standardised Δ_s/Δ_f -ratios is still relatively large. However, with this empirical approach all data points fit into the same general trend (excluding the two negative ratios for TUA and TUB). To found the empirical relationship on a more sound basis additional data points for x -values between 1.0 and 2.0 would be required, but for the time being the following empirical estimate for the ratio Δ_s/Δ_f is suggested:

$$\frac{\Delta_s}{\Delta_f} = \left(1 + 1.5 \cdot \frac{\tau - \tau_P}{v_n} \cdot \frac{\varepsilon_m}{\varphi \cdot L_{ph} \cdot \tan\theta}\right) \frac{L_{ph}}{H} \quad (5.9)$$

The proposed linear equation does not pass through the origin. This implies that shear deformations are also present in walls in which – according to the UCSD model – the entire shear force is transmitted by the inclined compression strut, which transfers the axial load from the top of the wall to the base. The second factor $\varepsilon_m/(\varphi \cdot L_{ph} \cdot \tan\theta)$ is normally larger than zero since the compression zone depth is in almost all cases smaller than half the wall length.

Figure 5.7a shows the comparison of the predicted and the experimentally derived ratio of shear to flexural displacements. The plot clearly demonstrates the correlation between the two

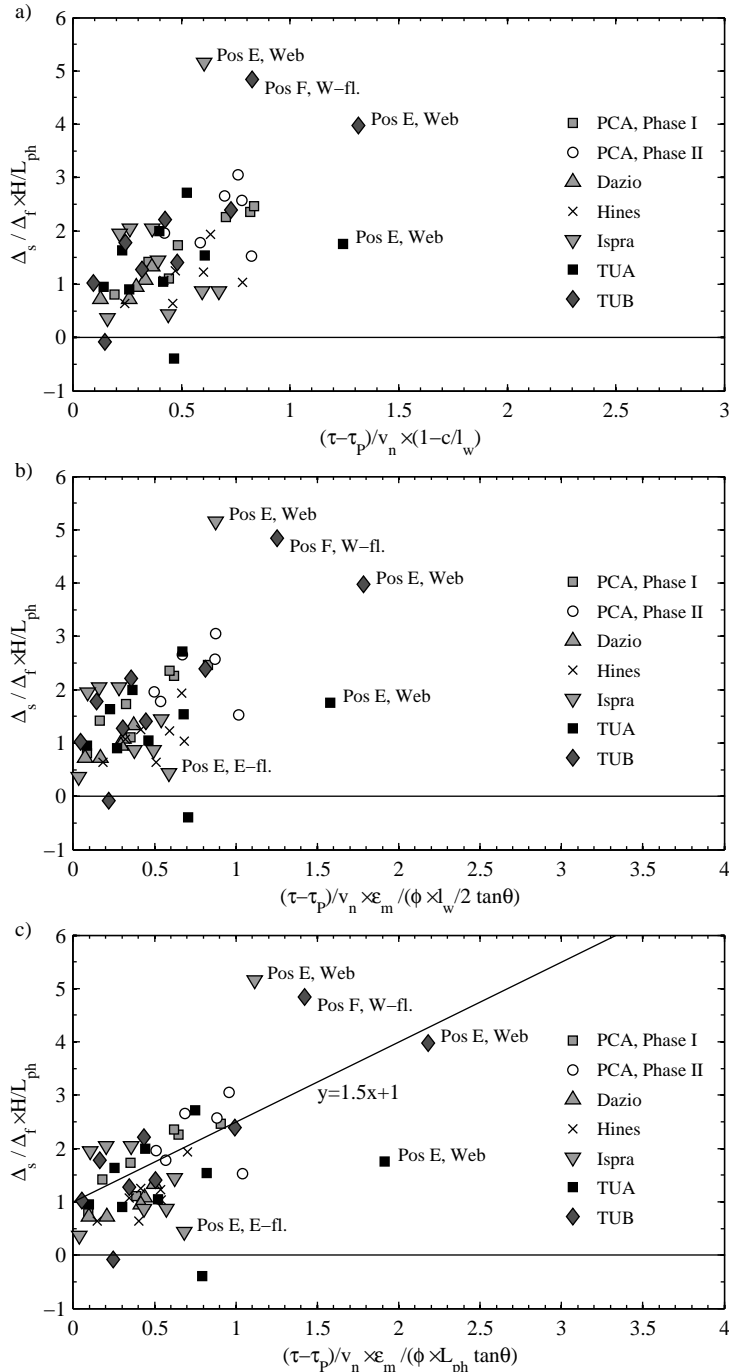


Figure 5.6. Shear deformations: The ratio Δ_s / Δ_f as a function of the stress parameter $(\tau - \tau_P) / v_n$ and three different flexural strain parameters: $1 - c / l_w$ (a), $\varepsilon_m / (\tan\theta \cdot \varphi \cdot l_w / 2)$ (b) and $\varepsilon_m / (\tan\theta \cdot \varphi \cdot L_{ph})$ (c).

variables but also highlights the scatter involved in predicting the shear deformations. Nevertheless, if the entire range of the investigated dataset is considered, the new empirical approach yields better results than the two existing approaches, which were discussed in Section 4.4.3 (Figure 5.7b). In this comparison these three approaches are of course rated unequally since the new empirical equation was derived from exactly the same dataset that was used for the comparison while the equation by Hines *et al.* [2004] were derived only from a number of data points within the dataset and the approach by Priestley *et al.* [2007] had not been calibrated at all with the dataset.

In Table 5.1 the Δ_s/Δ_f -ratios predicted by the new empirical equations are compared with the experimentally determined ratios. The comparison shows that in particular the smaller Δ_s/Δ_f -ratios of TUA (e.g. at Positions C and D) are typically overestimated by a considerable margin. It is also noteworthy that the predicted ratios for TUA and TUB are relatively similar although the shear stresses are fairly different for the two test units. This is because the shear reinforcement is the same for the two test units; hence the difference in the shear capacity results solely from the concrete contribution which amounts – dependent on the considered direction of loading – to a maximum of 48% and 34% of the shear capacity of TUA and TUB, respectively.

Table 5.1. TUA and TUB: Comparison of the experimentally determined and predicted Δ_s/Δ_f -ratios for the different wall sections (predicted ratios were estimated with Equation 5.9).

		TUA			TUB		
		Exp.	Predicted	Error	Exp.	Predicted	Error
Pos. A, B	Web	0.25	0.36	46%	0.38	0.39	3%
Pos. C	Flanges	0.14	0.23	61%	0.20	0.24	20%
Pos. D	Flanges	0.17	0.28	69%	0.22	0.28	27%
Pos. E	Web	0.28	0.62	121%	0.63	0.68	8%
	West flange	0.26	0.22	-15%	0.28	0.20	-29%
	East flange	-0.06	-	-	-0.01	-	-
Pos. F	Web	0.32	0.27	-16%	0.35	0.26	-26%
	West flange	0.43	0.34	-21%	0.76	0.49	-36%
	East flange	0.15	0.18	20%	0.16	0.17	6%

If the estimate of Δ_s/Δ_f is used for design purposes an estimate of the cracking angle θ is required. Attempts to estimate the cracking angles for TUA and TUB assuming the shear reinforcement has yielded led to poor results. A first indication of the cracking angle might be obtained from Figure 5.8, which shows the observed cracking angles as a function of the stress parameter $(\tau - \tau_p)/v_n$, which is already known during the design stage. The figure indicates

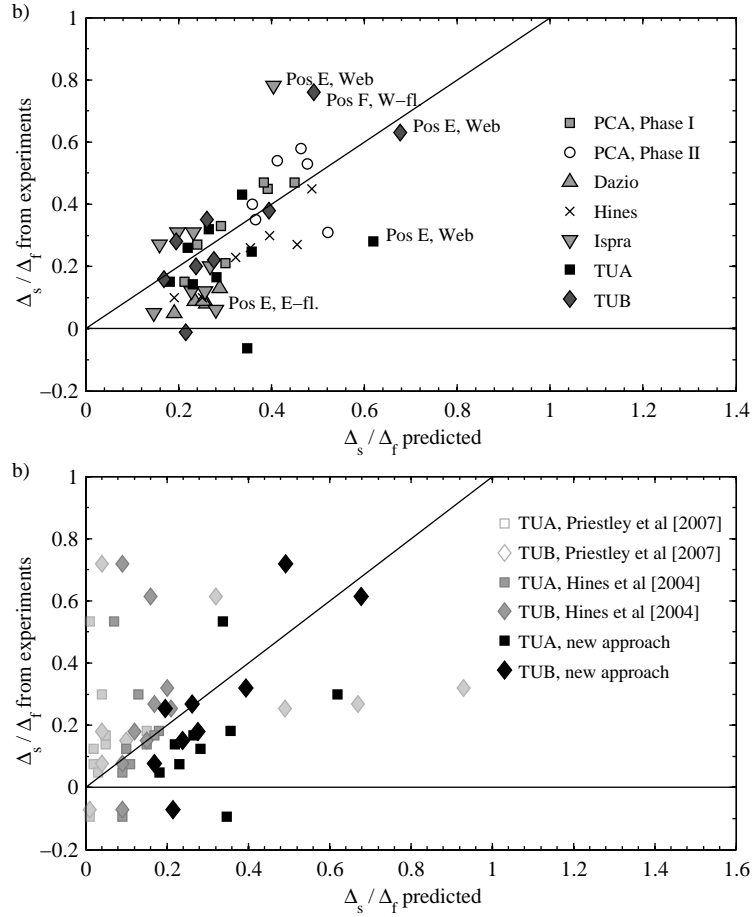


Figure 5.7. Prediction of the shear deformations: Using Equation 5.9 for the entire dataset (a) and comparison of the predictions by Priestley *et al.* [2007], Hines *et al.* [2004] and Equation 5.9 for TUA and TUB (b).

that the cracking angle θ measured in degrees against the wall axis can be estimated as:

$$\theta = 50 - 12.5 \cdot \frac{\tau - \tau_p}{v_n} \quad (5.10)$$

As alternative, an angle of $\theta = 45^\circ$ might be assumed; Figure 5.9 shows that for $\theta = 45^\circ$ the correlation between the predicted and experimentally determined Δ_s / Δ_f -ratios is almost as good as if the observed cracking angle is used. When deriving the empirical model the maximum measured shear force V_{max} was used. When the equation is used for design purposes, this force needs to be estimated by numerical models. For ductile flexural walls with rectangular or near-rectangular cross-section good estimates can be obtained from section analysis assuming plane sections remaining plane. For non-planar walls such as U-shaped walls and depending

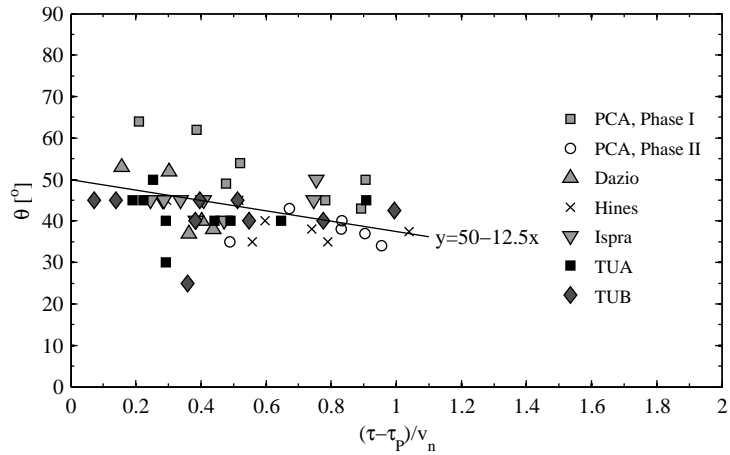


Figure 5.8. Cracking angle θ as a function of the shear stress ratio $(\tau - \tau_P)/v_n$.

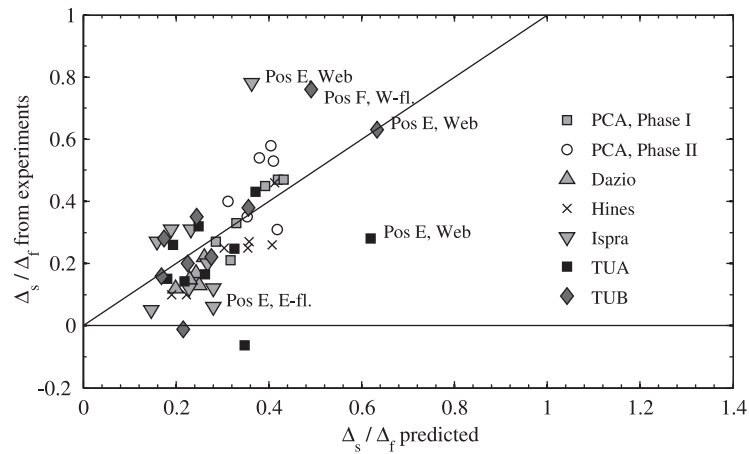


Figure 5.9. Prediction of the shear deformation with Equation 5.9 assuming $\theta = 45^\circ$.

on the direction of loading more elaborate models might be required as will be discussed in detail in Chapter 6.

5.2 Numerical modelling of shear displacements

The objective of this section is to evaluate two softwares regarding their capability of modelling shear displacements. The two chosen programs are VecTor2 [Wong and Vecchio, 2002] and Response2000 [Bentz, 2001]. Both programs were developed at the University of Toronto

and are based on the modified compression field theory (MCFT). The MCFT is a well-known theory on the stress-strain behaviour of cracked RC panels under a 2D stress state. It is believed that this theory is one of the most suitable theories for assessing the shear deformations of RC elements because it unifies shear and axial strain demands in a physical model.

The work in this section is restricted to a preliminary investigation into the topic of numerical modelling of shear deformations. If one or both of the two programs proves to yield good estimates of shear deformations, they could be used for adding data points to the plots in the previous section where experimental results are missing or for computing directly the shear deformations of a specific wall. For the moment, however, the two programs are limited to the analysis of simple symmetric wall sections that are loaded along their symmetry axes. A 3D version of VecTor is under development but pre- and post-processors are not yet available for 3D models.

Before the two programs are evaluated, the MCFT is briefly introduced in Section 5.2.1. Since the setup and analysis of finite element models in VecTor2 is relatively elaborate, the VecTor2-program is discussed on the basis of the analysis results for one rectangular and one barbelled wall, which were tested under cyclic loading (Section 5.2.2). The detailed results obtained from the analysis are used to compare different methods of evaluating shear deformations. In addition, the shear deformations under cyclic and monotonic loading is compared. In Response2000 which is a section analysis program that can consider monotonic loading only, new models are setup fairly quickly and the analysis time never exceeds a minute. Hence, in addition to the two walls that were analysed with VecTor2, all other rectangular, barbelled and flanged walls included in the database in Appendix A are considered and the results are discussed in Section 5.2.3. Conclusions regarding the success of computing the ratio of shear to flexural displacements from the results of the finite element analysis are drawn on in Section 5.2.4.

5.2.1 Introduction to the Modified Compression Field Theory

The MCFT was developed by Vecchio and Collins [1986]. It is a numerical model based on first principle mechanics that describes the stress-strain characteristics of RC in its cracked state. By subdividing a plane RC member into small elements with constant thickness and uniform axial and shear stresses along their edges, it is possible to derive the force-displacement characteristics of the structural member. The MCFT consists of four main modules: (i) the average strains of a small cracked RC element and their rotation into the principle directions, (ii) the equilibrium equations for the small element, (iii) the stress-strain relationships for concrete and reinforcement, and (iv) considerations of the local stresses that are transmitted across

a crack. In the following these four modules will be briefly introduced without presenting any equations.

Figure 5.10a shows the small membrane element with uniform axial stresses and shear stresses. The deformed shape of the element due to this stress state is shown in Figure 5.10b. For a cracked RC element the strains can be written in terms of either the element coordinate axes x and y or the strains can be decomposed into principal strains (Figure 5.10d). This is best visualised by means of a Mohr's circle (Figure 5.10c), which has already been introduced in Section 5.1.1. The strains shown in Figures 5.10c and d are average strains; however, due to the discrete cracks the strain state is not uniform over the element.

The stresses within a RC panel element (Figure 5.10a) are resisted by the concrete and the reinforcement. While it is assumed that the reinforcing bars can only resist axial forces, the concrete is subjected to axial stresses and shear stresses, which are decomposed into principal stresses parallel and perpendicular to the cracks. To link the strains and stresses in reinforcement and concrete, it is necessary to formulate average stress-average strain relationships for these two materials. The relationships for the average stress-strain state can be different to stress-strain relationships for the local material behaviour. For the reinforcement a classical elasto-plastic material model is assumed. For the concrete the average stress-average strain relationships are formulated in the two principal directions. It is assumed that these coincide for the stresses and strains and are therefore parallel and perpendicular to the cracks. The novelty for the average stress - average strain relationship along the principal compressive axis is the dependence on the transverse tensile strain: the larger the transverse tensile strain, the smaller the compressive stress capacity.

In a last step the local stresses across the crack are considered. At a crack the concrete tensile stresses are zero and therefore the stresses in the reinforcing bars will be larger. Hence, it is necessary to check that the capacity of the reinforcing bars is not exceeded. The local stress

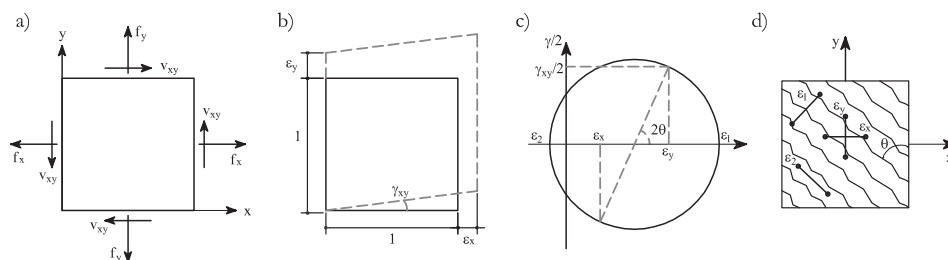


Figure 5.10. MCFT: Loading (a), deformation (b), Mohr's circle of average strains (c) and average strains in the cracked element (d); figures from Vecchio and Collins [1986].

also accounts for aggregate interlock across a crack. Aggregate interlock allows to transmit shear stresses across the crack although in an average sense the crack corresponds to a principal direction. The magnitude of the shear stresses that can be transmitted across the crack will depend on the crack width, the aggregate size and the concrete strength.

5.2.2 VecTor2: A shell element analysis program based on the MCFT

VecTor2 is a two-dimensional nonlinear finite element program for RC membrane elements [Wong and Vecchio, 2002], which is based on the MCFT. It has a substantial library of inelastic reinforcing steel and in particular concrete material models for both monotonic and cyclic loading. The program is delivered with the pre-processor "Formworks" and the post-processor "Augustus", which allow an easy handling of the input data and of the results. Within this case study the program VecTor2 is used to analyse the Wall WSH₃ that was tested by Dazio *et al.* [1999] and the walls B₃ and B₄ that were tested by Oesterle *et al.* [1976]. The wall WSH₃ was selected as an example of a capacity-designed wall since all the experimental data are available in electronic format and the experiment is very well documented. Among the six test units tested by Dazio *et al.* [1999] WSH₃ was the one with the largest ratio of shear to flexural displacements (Section A.3). The test units B₃ and B₄ were selected as examples of walls that were not capacity designed. The two test units have the same reinforcement layout but were subjected to different loading schemes: While specimen B₃ was subjected to cyclic loading, specimen B₄ was loaded monotonically. This wall configuration was chosen because it allows to study the impact of cyclic loading on shear displacements and to assess the capability of the program VecTor2 to account for the difference between monotonic and cyclic loading.

a) Analysis of test unit WSH₃.

Finite element model of WSH₃

The cross section of the test unit and the principle instrumentation are shown in Figure 5.11a and b. The test unit WSH₃ was modelled using plane membrane elements; the finite element mesh is shown in Figure 5.11c. The wall was divided into three areas with different properties; these are the boundary element of the wall, the web of the wall and the load stub. These three areas were assigned different RC properties and wall thicknesses. The longitudinal and horizontal reinforcement ratios as well as the compressive and tensile strength of the concrete are shown in Figure 5.11c. The load stub of the physical test unit was post-tensioned and hence cracking was very limited within this regions. To simplify matters in the numerical model, the load stub was assigned no reinforcement but a large concrete tensile strength; hence it remained uncracked during the analyses.

From the library of material models the following were selected (details on these models can be found in Wong and Vecchio [2002]): The concrete back-bone curve is assembled of Hognested's

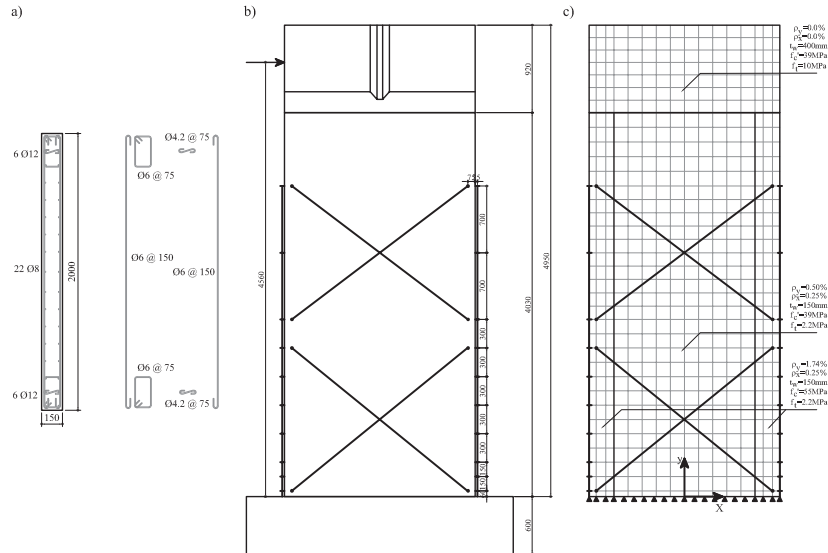


Figure 5.11. WSH3: Cross section (a), instrumentation (b) and finite element mesh and virtual instruments in VecTor2 (c).

parabola for pre-peak response and the Popovics/Mander model for the post-peak response. Compression softening was modelled by Vecchio's 1992-A model. Tension stiffening was also included and was modelled using the modified Bentz approach. Cracking of the concrete was determined on the basis of Mohr's circle for stresses. The hysteretic response of the concrete was modelled using Palermo's model from 2002. The crack width check used as reference length 20% of the aggregate size. The reinforcement was modelled as smeared reinforcement; the cyclic behaviour follows the hysteresis rule by Seckin, which includes the Bauschinger effect. By using smeared reinforcement, buckling of the reinforcement bars could not be included in the model. Although the physical wall had failed after buckling of the longitudinal reinforcing bars (see Appendix A.3) this approach was preferred over the discrete modelling approach for reinforcing bars since it tends to lead to more stable analysis results and reduces the analysis time.

In order to compare the numerical and experimental results the mesh of the wall was generated in such a way that a node was placed at every position of an instrument that had been mounted on the wall WSH3 (Figure 5.11b). Using the displacements of these nodes, it was possible to compute the numerical equivalent to the measurement of an instrument mounted on the physical wall [Hines *et al.*, 2002a]. From the results of these "virtual instruments" flexural and shear deformations were computed applying the same procedures as to experimental

measurements. In this way the possibility could be eliminated that differences between the numerical and experimental results originated from differences in the procedures for evaluating the shear and flexural deformations.

Pushover analysis of WSH₃

In a first step the wall was subjected to a centric constant axial load ($P = 686\text{kN}$) and an increasing top displacement at $h = 4.56\text{m}$. Figure 5.12 shows that the numerical model reflects the force capacity of the physical test unit very well. Note that the ultimate displacement of the numerical model was not determined from strain limits but the analysis was stopped at the displacement corresponding to $\mu_{\Delta} = 6.0$ since the focus of this case study is set on the numerical modelling of shear displacements and not on determining the ultimate displacement capacity. In a 2D model in which the wall is subdivided into a number of elements along its length there are different possibilities of calculating the shear displacement at the top of the wall. On one hand, there are the experimental approaches, i.e. the shear displacements can be computed from the "measurements" of the virtual instruments in the same manner as it has been done for the experiments. On the other hand, the shear displacement can be computed from the shear strains of the elements. The aim of this section is to compare these two approaches in order to draw conclusions on their comparability.

The experimental approaches for computing the shear displacements were explained in Section 4.4.1. In this section three different approaches were distinguished: the original method,

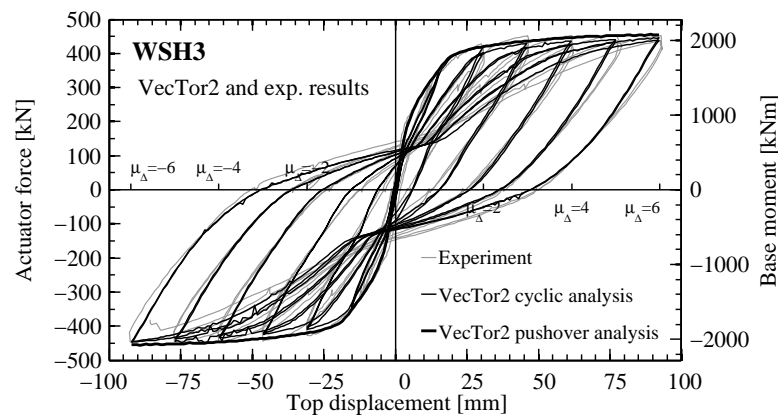


Figure 5.12. WSH₃: Comparison of results of cyclic and pushover analyses with VecTor2 to experimental force-displacement hysteresses.

Hiraishi's method and the indirect method. The latter two demand that the flexural deformations can be determined. The flexural deformations were computed from the virtual instruments along the wall edges following the method described in Section 4.4.1.

The second set of shear displacements were computed from the shear strains of the finite elements. When computing the shear displacements at $h = 4.56\text{m}$ from the shear strains of the elements it is necessary to average the shear strains over each section along the wall length and then to integrate these average shear strains over the wall height. For computing the average of the shear strains over the wall section different approaches exist:

- The average shear strain γ_{xy} of a section is computed as the average of the element shear strains within the section weighted by the lengths of the element. In the following this shear strain will be referred to as γ_m .
- Alternatively the average shear strain can be computed from principles of virtual work (Bentz, private communication, 2007). The average shear strain is therefore defined as

$$\gamma_{VW} = \frac{\sum_{i=1}^N \tau_i \cdot \gamma_i \cdot l_{el,i}}{\sum_{i=1}^N \tau_i \cdot l_{el,i}} \quad (5.11)$$

where N is the number of elements per row, τ_i the shear stress within element i , γ_i the shear strain of element i and $l_{el,i}$ its length.

- Bentz, who developed in collaboration with Collins the program Response2000, argued that taking the average of the shear strain over the entire section might overemphasise the zero shear strain at the edges of the wall (Bentz, private communication, 2007). He therefore computed the average shear strain of the section as the average of the shear strain within the central 45% of the wall length¹. This definition is included here in order to provide a context for the discussion in Section 5.2.3 of the results obtained with Response2000. The average shear strain computed with this approach will be labelled $\gamma_{m,0.45}$

Once the average shear strains are determined for each section the shear displacements at the top is obtained by integrating the average shear strains over the height. Figure 5.13a and c show the displacements due to shear and flexural deformations. In Figure 5.13a the shear displacements were computed from the measurements of the virtual instruments whereas in

¹In our email correspondence, Bentz wrote that he computed it over the central two thirds or three quarters of the wall length. However, when computing the average shear strain for a number of shear strain profiles obtained from Response2000 results, it was found that the average shear strain is probably computed over only 45% of the wall length.

Figure 5.13b the shear displacements were computed from shear strains of the finite elements. The best fit between the sum of shear and flexural deformations ($\Delta_s + \Delta_f$) and the actual top displacement was obtained for Hiraishi's method of evaluating the virtual instruments and the average shear strain γ_m .

Figure 5.13b and d show the ratios of shear to flexural deformations. It is noteworthy that the shear displacements according to the original method led to Δ_s/Δ_f -ratios, which remained constant for $\Delta_{top} > 20\text{mm}$. For all other methods of evaluating the shear displacements the ratio dropped off until $\Delta_{top} \cong 40\text{mm}$ before it remained approximately constant. Hiraishi's method and the indirect method led to relatively similar results; they also compare well to the ratios based on shear displacements computed from shear strains of the finite elements (possibly with exception of the virtual work approach which leads to slightly lower ratios). For the wall section analysed here the approximate method by Bentz ($\gamma_{m,0.45}$) coincided almost exactly with the simple average strain γ_m . Bentz' concern, that the zero shear strains at the wall edges might be overemphasised by γ_m , seems therefore not justified in the considered case but the situation might be different for walls with larger shear deformations. From these comparisons one can conclude that the two experimental methods that were identified as suitable in Section 4.4.1 (Hiraishi's method and the indirect method) lead to similar estimates of the shear displacements as computing the shear displacements from shear strains of finite elements. Of course, this conclusion was drawn from the analysis of a single wall configuration. To generalise it, a larger set of walls should be studied, in particular walls with larger shear deformations should be included.

Figure 5.13e shows the comparison between the numerical and experimental results of the Δ_s/Δ_f -ratios. For all three methods of evaluating shear displacements that are included in the figure (indirect, original and Hiraishi's method) the experimentally determined ratios of Δ_s/Δ_f are larger than the numerically determined ratios. In particular the indirect method applied to the experimental data led to Δ_s/Δ_f -ratios that were significantly larger than any of the other ratios. The large variability among the experimental results renders it difficult to compare the experimental and numerical results in detail. One can, however, observe that for both experimental and numerical measurements the Δ_s/Δ_f -ratios evaluated according to the original method tend to remain constant with increasing top displacements whereas the Δ_s/Δ_f -ratios evaluated according to Hiraishi's method or the indirect tend to slightly drop off.

Cyclic analysis of WSH3

In the previous section it was shown that the numerical results led to slightly smaller ratios of shear to flexural displacements than the experimental results. A possible reason for the

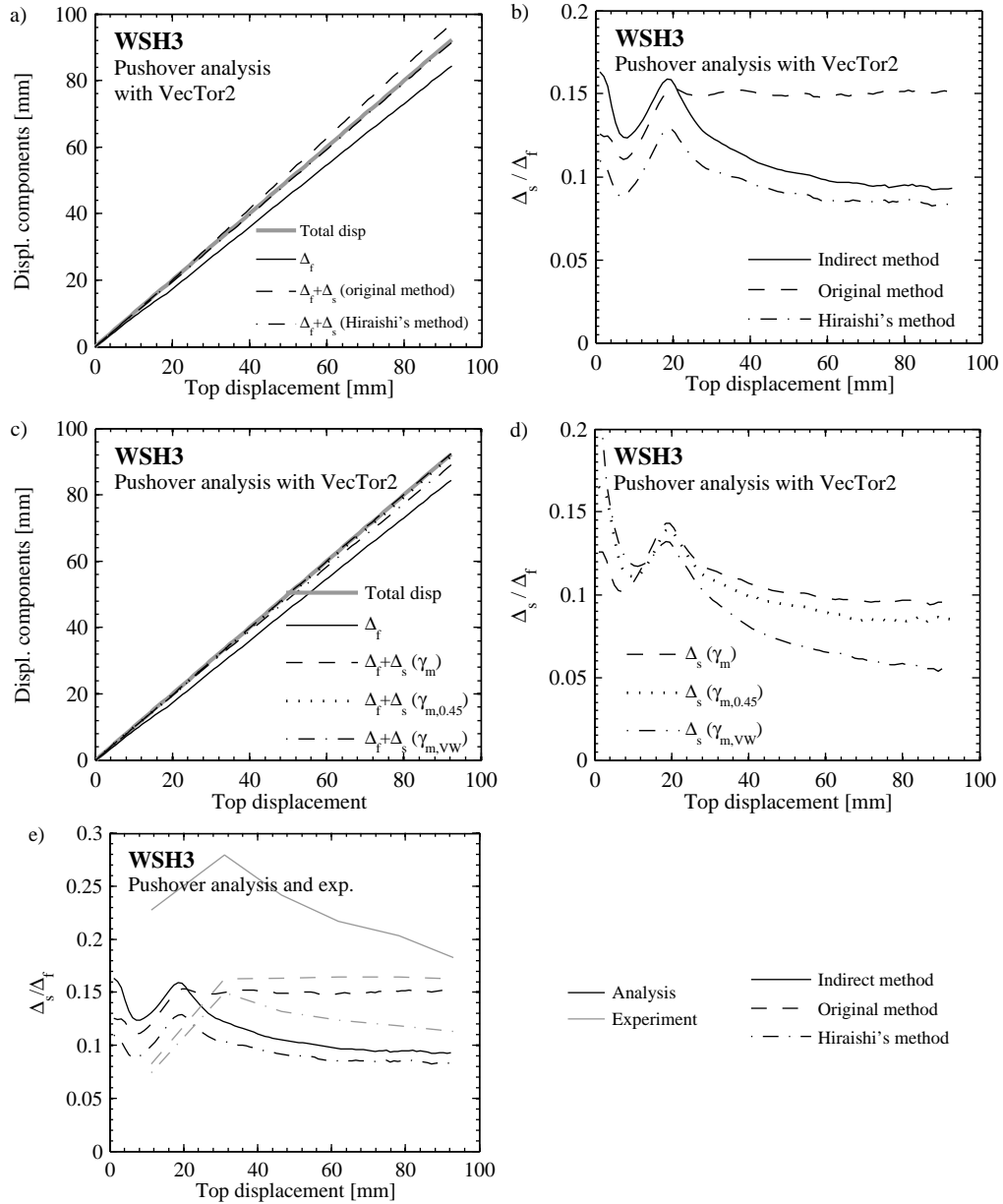


Figure 5.13. WSH₃ (cyclic loading), VecTor₂ (pushover analysis): Displacement components (a+c) and ratio of shear to flexural displacements (b+d) for shear displacements computed from virtual instruments (first row) and element shear strains (second row); (e) comparison of experimental and numerical ratios of shear to flexural displacements.

discrepancy between numerical and experimental results could be the type of loading: While the analysis was conducted as pushover analysis the physical test units were subjected to cyclic loading with cycles of increasing amplitude. Hence we need to investigate whether cyclic loading tends to increase the shear displacements. For this purpose the different contributions to shear strains which were described in Equation 5.2 are considered once again. These were the contributions due to the mean axial strain ε_m , the horizontal strain ε_h and the strain in the compression diagonal ε_d . To ease the reading Equation 5.2 is repeated here:

$$\gamma = \frac{\varepsilon_m}{2\tan\theta} + \varepsilon_h \cdot \tan\theta - \frac{2\varepsilon_d}{\sin 2\theta}$$

The mean axial strain ε_m is chiefly caused by flexural deformations; hence any variation in ε_m will have similar effects on the magnitude of the shear and flexural deformations and will therefore not affect the ratio Δ_s/Δ_f . Whether the horizontal strain ε_h will be larger for cyclic loading than for monotonic loading depends on the strain level in the shear reinforcement. If the shear reinforcement remains elastic, i.e. if the wall has been capacity designed, the strains in the horizontal reinforcement remain relatively small and therefore the difference between monotonic and cyclic loading will be small. If the shear reinforcement yields, positive plastic strains will accumulate and grow with the number of cycles since independent of the direction of the top displacement the shear reinforcement is always under tension. Hence, in this case, the shear deformations will be larger if the wall is loaded cyclically than monotonically. The last term in Equation 5.2 describes the effect of the strains in the compression diagonal ε_d on the shear strains. The strains in the concrete compression diagonal will be larger for cyclic loading than for monotonic loading since the compression struts tend to soften under cyclic loading. The ratio of E-moduli of concrete under cyclic and monotonic loading are approximately 0.6 – 0.7². For typical walls, however, the concrete compressive strains are quite small when compared to the mean axial strains and their effects on the total shear strains are probably not very large.

To sum up, considerations on the basis of Equation 5.2 show that shear displacements will be larger for cyclic loading than for monotonic loading if the shear reinforcement yields. In addition to the accumulation of plastic strains in the shear reinforcement, the softening of the compression strut under cyclic loading might also contribute to this effect. For capacity designed walls, however, the difference between the ratio of shear to flexural displacement for cyclic and monotonic loading should be small. The wall WSH₃ was capacity designed and

²Priestley *et al.* [2007] suggested to use a modular ratio of $n = 10$ when computing shear displacements for cyclically loaded walls or columns. Typical modular ratios for monotonic loading are $n = 6 - 7$. Therefore the ratio of E-moduli under cyclic and monotonic loading was estimated as 0.6 – 0.7.

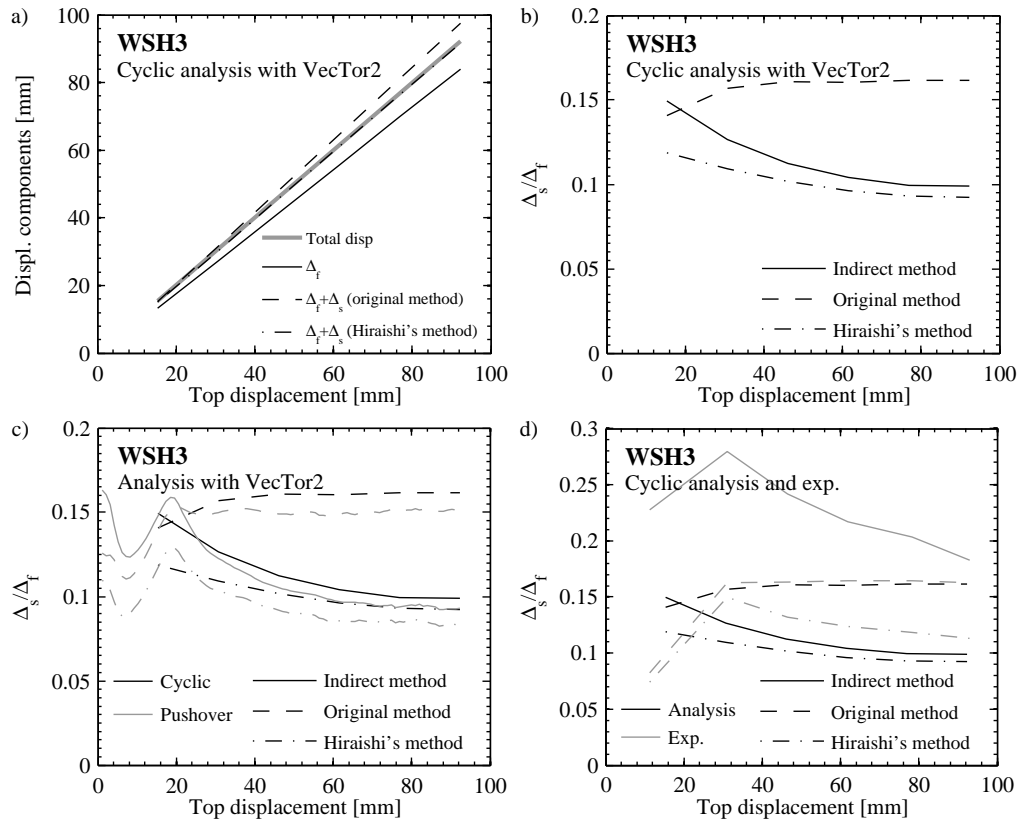


Figure 5.14. WSH₃, VecTor₂ analysis: Displacement components (a) and ratio of shear to flexural displacements (b) for cyclic analysis; comparison of Δ_s/Δ_f -ratios from pushover analysis and cyclic analysis (c) and comparison of Δ_s/Δ_f -ratios from cyclic analysis to experimentally determined ratios (d).

hence it is expected that the ratio of shear to flexural displacements is similar for monotonic and cyclic loading. This is confirmed by a cyclic analysis of the VecTor₂ model of WSH₃. Figure 5.12 shows the good agreement of the numerical and experimental force-displacement hysteresses. The comparison of the ratios of shear to flexural displacements obtained for monotonic and cyclic loading are shown in Figure 5.14c. The ratios obtained for cyclic loading are indeed slightly larger than those for monotonic loading but the difference is so small that it cannot be considered relevant for design purposes. Hence, for design purposes the shear displacements of capacity designed walls could also be estimated on the basis of a pushover analysis. The objective of the following section is to study walls under monotonic and cyclic loading which have not been capacity designed.

b) Analysis of test units B₃ and B₄.

Among the PCA walls tested during Phase I, two specimens (B₃ and B₄) had the same cross section and the same reinforcement layout. Specimen B₄ was tested under monotonic loading whereas B₃ was subjected to cyclic loading; the latter was also included in the discussion in Section 5.1.1. Specimen B₃ failed due to fracture of longitudinal reinforcing bars; from $\Delta_{top} > 4$ in onwards until failure it was subjected to significant crushing and grinding of the web concrete. It is supposed that this led to the increase in the Δ_s/Δ_f -ratios for top displacements greater than 4in as shown in Figure 5.1. Specimen B₄ failed also due to fracture of longitudinal reinforcing bars. However, in contrast to specimen B₃ crushing of the web concrete was not observed for specimen B₄. It is therefore expected that the ratio of shear to flexural displacements is larger for specimen B₃ than B₄ in particular for $\Delta_{top} > 4$ in. This is confirmed by Figure 5.15b, which shows the comparison of the experimentally and numerically determined ratios of shear to flexural displacements for specimens B₃ and B₄. Whereas the Δ_s/Δ_f -ratios of B₃ increased continuously for $\Delta_{top} > 4$ in, the ratios of B₄ were approximately constant for all imposed top displacements. This finding holds for both experimentally and numerically determined Δ_s/Δ_f -ratios. The comparison of the two specimens therefore shows, that the ratios of shear to flexural displacements are of similar magnitude for cyclic and monotonic loading as long as the shear transfer mechanism does not degrade significantly (i.e. no yielding of the horizontal reinforcement and no crushing or grinding of the web concrete). If the shear transfer mechanism degrades, shear deformations constitute a larger part of the total displacements when the wall is subjected to cyclic loading than to monotonic loading. VecTor2 is hence capable of reflecting the difference between monotonic and cyclic loading on the ratio of shear to flexural deformations. However, VecTor2 predicts smaller ratios than those derived from experimental evidence. Figure 5.15a shows that the numerical model overestimated the loading stiffness. Possible reasons for the difference between numerical and experimental results are of course not only related to the numerical model but could also be related to biased experimental measurements.

5.2.3 Response2000: A section analysis program based on the MCFT

The second program whose capabilities of computing shear displacements were assessed was Response2000. Response2000 is a section analysis program for RC members subjected to axial force, moment and shear [Bentz, 2000]. It is primarily based on a publication by Vecchio and Collins [1988] that outlined the procedure for section analysis of RC beams based on the MCFT. According to this procedure the beam is considered as a number of concrete and reinforcement layers. These layers are analysed individually but strain compatibility and equilibrium requirements are satisfied. For the strain compatibility the assumption of plane sections

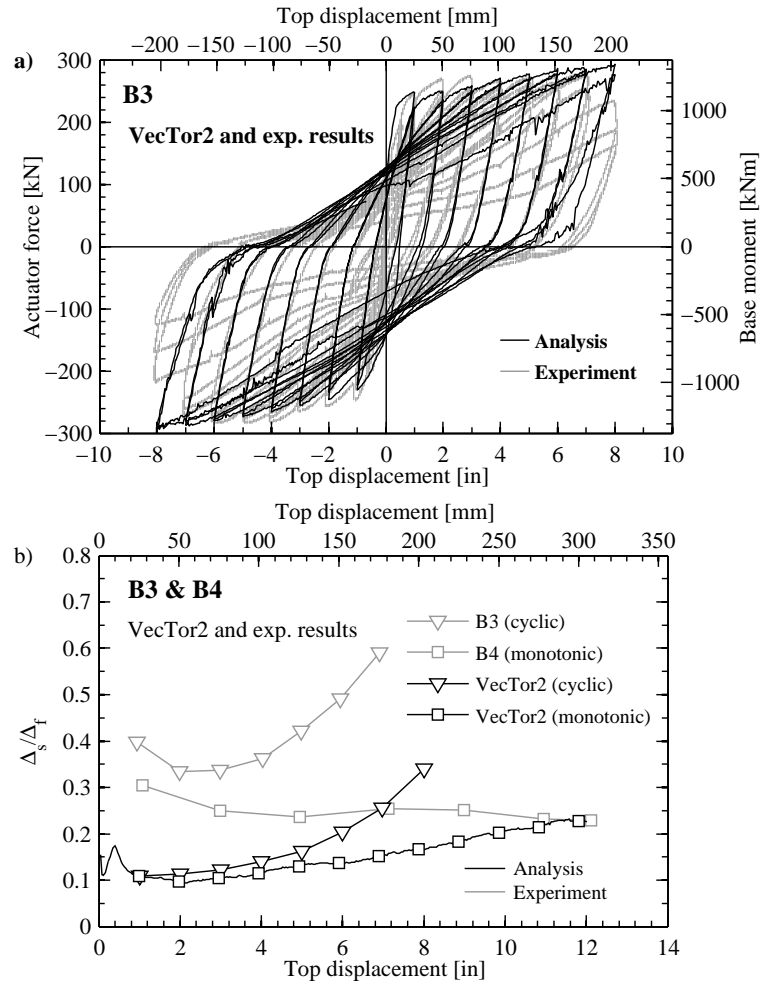


Figure 5.15. Test Units B3 and B4: Comparison of numerical and experimental force-displacement hysteretic curves of test unit B3 (a); comparison of numerically and experimentally determined ratios of shear to flexural deformations for specimens B3 and B4, which were identical in their configuration but were subjected to cyclic and monotonic loading, respectively (b).

remaining plane is made. Equilibrium requirements are split into two aspects: First, the sum of the stresses of all layers must be in equilibrium with the global axial force, bending moment and shear force. Second, the shear stress variation over the depth of the concrete section is derived by analysing a second section of the beam which is at a small distance (approximately one sixth of the beam depth) from the first section. Bentz [2000] improved the approach by reducing the distance of the two sections to zero and using the derivative of the stiffness matrix. The shear force is then computed by integrating the shear stresses over the section.

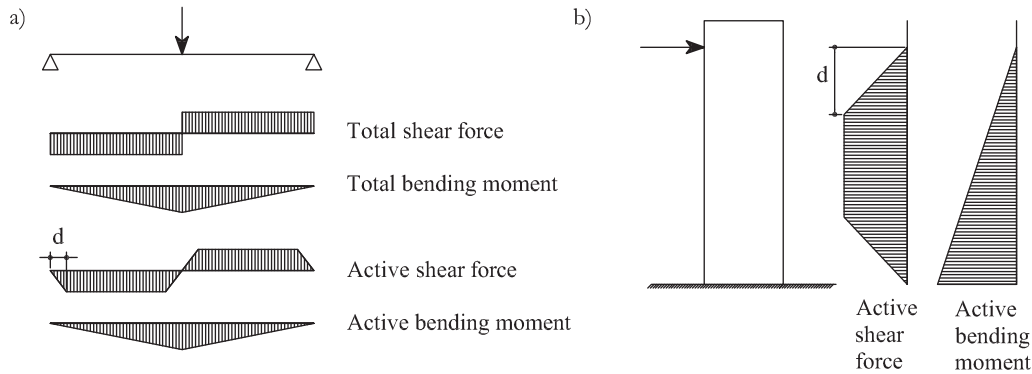


Figure 5.16. Response2000: Clipping of the active shear forces in Response2000 for a simply supported beam (a) and a cantilever wall (b).

Since Response2000 is actually a section analysis program, it computes the member response by integrating over the deformations of several sections. To do so, assumptions on the load transfer mechanism in the support regions are required. Bentz [2000] proposed that "within a distance d from a point load and d from a support there are other support mechanisms that mean the entire load is not supported in a sectional mode". He names direct strut action and clamping from the load and the support as mechanisms which can enhance the capacity of the member in these regions. To account for these other mechanisms Bentz clipped the shear force diagram at distance d from a load or a support. He introduced a linear transition from zero shear at the section of the support or load to the actual shear force at the section at distance d (Figure 5.16). Both the capacity check as well as the computation of the shear deformations are based on the clipped shear force diagram; the bending moment diagram remains unaltered. The assumed value for d could not be found neither in his thesis [Bentz, 2000] nor in the manual to Response2000 [Bentz, 2001] but shear displacements obtained from the Response2000 analysis of uncracked members suggest that d is taken as $0.85l_w$. For beams the length of the clipped regions diminishes with respect to the total beam length (Figure 5.16a). Hence, it is expected that for beams the effect of the clipping on the computation of the total shear displacements is relative small. For cantilever walls, however, the length of the clipped regions to the overall length can be large. For a cantilever wall with a shear span ratio of 3.0, for example, only 43% of the wall height lie outside the clipped regions (Figure 5.16b), whereas for a wall with a shear span ratio of 2.0 this ratio reduces even to 15%. Hence, in the latter case the shear displacements of 85% of the wall length are computed on the basis of the approximate clipped shear force profile. Experimental evidence has shown that the major part of the shear displacement of RC cantilever walls occurs in the plastic hinge region. With Response2000, however, shear displacements in the plastic hinge region (which lies within the clipped region)

are only computed in an approximate way. This is no criticism on Response2000 but any program based on section analysis will have to make some assumptions on the behaviour in the plastic hinge zones. A further approximation of the computation of the shear deformations in Response2000 relates to the computation of the average shear strain of a section. In Section 5.2.2 it was discussed that Response2000 computes the average shear strain of a section as the average of the shear strains within the central 45% of the wall length (this average shear strain was called $\gamma_{m,0.45}$). From the comparison of different values of γ it was found that – at least for the wall WSH₃ that is considered here – the approach of computing the average shear strain that is adopted in Response2000 yields very similar results to other methods.

Analysis of test unit WSH₃

In the following the wall WSH₃ is analysed using the program Response2000 and the results are compared to the experimental data as well as the results obtained from the VecTor2 pushover analysis. Figure 5.17 shows the comparison of the force-displacement envelope obtained with Response2000 to the experimentally determined force-displacement hysteresis. The agreement of the predicted force capacity is remarkably good. Response2000 underestimates, however, the displacement capacity by about a quarter (flexural displacements due to strain penetration into the foundation are included).

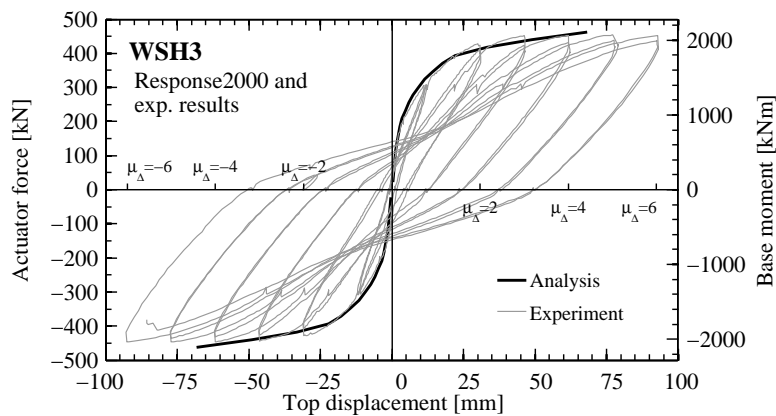


Figure 5.17. Test Unit WSH₃: Comparison of Response2000 analysis results to the experimental force-displacement hysteresis.

Figure 5.18 shows the comparison of the ratios of shear to flexural displacements obtained from Response2000, VecTor2 and the experiment. For the VecTor2 analysis the shear displacement based on $\gamma_{m,0.45}$ is shown; the shear displacements obtained from Response2000 and VecTor2 were therefore evaluated according to the same method. The shear to flexural

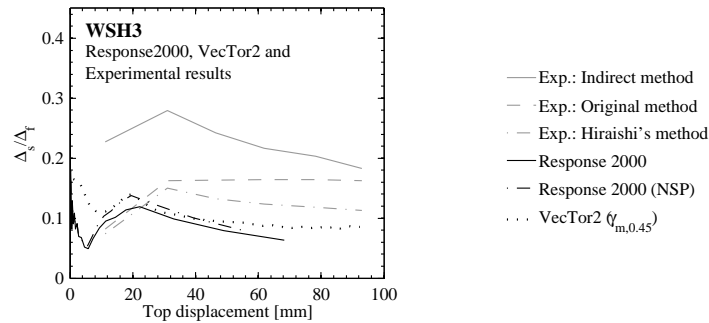


Figure 5.18. Test Unit WSH3, Response2000 and VecTor2 analyses: Ratio of shear to flexural displacements obtained experimentally and numerically. For the Response2000 analysis the flexural displacements were computed once with (label 'Response2000') and once without accounting for strain penetration into the foundation (label 'Response2000 (NSP)').

displacements from Response2000 are computed twice; once including flexural displacements due to strain penetration into the foundation and once neglecting such displacements. In VecTor2 the reinforcement was modelled as smeared and hence the base rotation due to strain penetration into the foundation was not captured. The Response2000 analysis results for which strain penetration was not considered agreed remarkably well with the VecTor2 results. It is, however, also noteworthy that the ratio of shear to flexural displacements obtained from Response2000 analysis dropped continuously and did not level off for larger displacement ductilities as the results from the VecTor2 analysis and experimental results did. As noted previously for the results of the VecTor2 analysis, the numerically determined ratios tend to be smaller than the experimentally determined ratios. Only for $\mu_{\Delta} < 2.0$ equal the numerical ratios the experimental ratios according to the original method and the method by Hiraishi.

Analysis of the rectangular, barbelled and flanged walls in the database

The fact that Response2000 analysis tends to lead to smaller ratios of shear to flexural displacements than what is obtained from experiments was also confirmed when a larger set of walls was considered. Figure 5.19 shows the comparison of the numerical and experimental ratios for the PCA walls of Phase I and II [Oesterle *et al.*, 1976, 1979] and the walls tested by Dazio *et al.* [1999] and Hines *et al.* [1999, 2002b]. The computation of the experimental ratios was outlined in Appendix A. The ratios from the Response2000 analysis are average ratios for top displacement between twice the experimentally determined yield displacement and the displacement at which the analysis stopped because a strain limit was exceeded. For a number of specimens the Response2000 analysis stopped before twice the yield displacement was attained and hence these data points were not included in Figure 5.19; the omitted specimens were: B6, B7, B9 and F2 from PCA, Phase II and Hines' test units 2B and 3B. For all specimens the

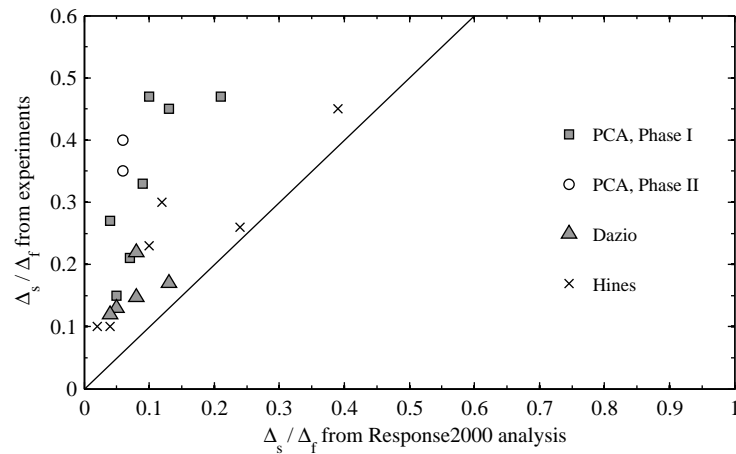


Figure 5.19. Comparison of ratios of shear to flexural displacements obtained from experiments and Response2000 analysis.

Response2000 analysis predicted a smaller Δ_s / Δ_f -ratios than obtained from the experimental results. In average the numerical ratios were about 50% smaller than the experimental ratios.

5.2.4 Discussion of the numerical results

The two programs that were assessed regarding their capability of computing shear displacements were VecTor2 and Response2000. Both programs are based on the modified compression field theory but VecTor2 is a two-dimensional finite element program and Response2000 a section analysis program. VecTor2 allows analysing structural walls along their symmetry axis for imposed displacements that can be either monotonically increasing or quasi-static cyclic with increasing amplitudes. Two wall configurations were analysed for monotonic and cyclic loading; the two configurations corresponded to Dazio's wall WSH₃ and Oesterle's wall B₃. The two test units differed regarding the evolution of shear displacements with ductility demand: For test unit WSH₃ the ratio of shear to flexural displacements was fairly stable for the entire ductility range whereas it increased with increasing top displacements for B₃. It is assumed that the increase of the ratio of shear displacements was associated with the degradation of the web concrete. A test unit of the same configuration as unit B₃ was tested under monotonic loading and this wall B₄ showed a stable ratio of shear to flexural displacements. Hence, the test units B₃ and B₄ were used to assess whether VecTor2 is capable of capturing the difference in behaviour between monotonic and cyclic loading. The findings from the VecTor2 analysis were as follows:

- For WSH₃, which shear deformations were limited, VecTor2 predicted the ratio of shear to flexural displacements fairly accurately (considering the significant variation of the experimentally determined ratios depending on the method of evaluation). For test units B₃ and B₄, which were not capacity designed, the experimentally determined Δ_s/Δ_f -ratios were relatively large. For these test units VecTor2 underestimated the shear deformations. It did, however, capture the difference between the behaviour of the wall under monotonic and cyclic loading.
- Two fundamentally different methods of evaluating the shear displacements of numerical models were compared. The first group of methods used virtual instruments to compute shear displacement in the same way as they are computed for experimental measurements. The second group of methods were based on the shear strains of the finite elements. The two methods were compared for the analysis of WSH₃. It showed that all results with the exception of the original method led to similar ratios. The original method led to ratios of shear to flexural displacements which were larger than the ratios obtained from the other methods.

To summarise, VecTor2 is suited to predict shear displacements of walls for which the shear displacements constitute a relatively small portion of the total displacements (test unit WSH₃). For walls in which shear deformations contribute significantly to the total wall deformation the shear displacements were underestimated (test units B₃ and B₄) although the general shear behaviour such as the increase in shear displacements for cyclic loading were well captured. The sources for this discrepancy should be investigated further.

Since Response2000 is a section analysis program it is required to integrate the results of the section analysis over the member length in order to determine the member response. As a consequence, Response2000 cannot compute rigorously the shear deformations in regions in which load transfer mechanisms such as direct strut actions contribute significantly to the shear capacity (e.g. plastic hinge zones). In these regions assumptions regarding the distribution of the shear forces on the different load transfer mechanisms have to be made and shear deformations can only be estimated in an approximate manner. Since a large portion of the shear deformations of the considered structural walls originated from deformations in the plastic hinge zone this is a significant short-coming when predicting the ratio of shear to flexural displacements. All rectangular, barbelled and flanged walls included in the database were modelled with Response2000. For all walls were the ratios of shear to flexural displacements computed with Response2000 smaller than the ratios determined from the experimental results. It is therefore concluded that for structural walls Response2000 is not very well suited for the assessment of shear deformations. The shear force capacity of a structural wall, however, can be very well assessed with Response2000 since it is typically smallest at a section at

some distance to the support for which direct strut actions no longer contribute to the shear capacity. For these sections Response2000 is well suited for assessing the shear behaviour.

5.3 Summary and conclusions

The objective of this chapter was to identify methods that have the capability of estimating the ratio of shear to flexural deformations of RC structural walls. The problem was approached in two different ways: First, it was attempted to develop an empirical relationship for the ratio of shear to flexural deformations (Δ_s/Δ_f). Second, analyses with two computer programs were carried out in order to assess their capability of modelling the shear deformations. To develop the empirical equation and to validate the analysis results, a small database of quasi-static cyclic tests of structural walls was set up.

When developing an empirical relationship for the ratio of Δ_s/Δ_f it was sought to identify parameters that are related to shear displacements. The parameters were first classified into stress and strain parameters and of each group one parameter was chosen that seemed to lead to the best correlation with the experimental data. These two parameters were then linked in an empirical relationship for the ratio of Δ_s/Δ_f . However, despite the choice of the best fitting parameters, the correlation between the predicted and observed ratios of shear to flexural displacements is relatively weak. Part of the variability can be certainly linked to deficiencies of the empirical model but some variability is most likely also associated with uncertainties related to the experimentally determined shear displacements. Sources of these uncertainties can be the choice of the method for evaluating shear displacements, the subdivision of measurements (i.e. the location of the devices on the test unit) and the quality of the data. Although the herein developed empirical equation is certainly not the last word on the subject of shear displacements of structural walls, it will be used in Chapter 6 when carrying out plastic hinge and wide-column analysis of TUA and TUB. It should be noted that this empirical approach for estimating the Δ_s/Δ_f -ratios is only applicable to walls whose shear transfer mechanism is not degrading significantly under cyclic loading. For walls whose shear reinforcement is yielding or whose concrete compression struts are softening considerably, the evolution of shear displacements with top displacements is strongly dependent on the loading history. For these walls the ratio of shear to flexural displacements is typically not constant over the ductility range and hence the developed empirical equation cannot be applied.

In a second phase the capability of the computer programs VecTor2 and Response2000 of predicting shear displacements was assessed. The two programs were chosen because both are based on the modified compression field theory. The scope of the assessment of the two programs was that of a preliminary investigation. The purpose of the study was to assess the suitability of the two programs for estimating the ratio of shear to flexural displacements for

structural walls. If the programs have this capability, they could be used for either adding data points in the regions of the empirical study where data points are missing or for predicting directly the ratio of shear to flexural displacements for a particular wall configuration. Note that for the moment the latter is limited to walls which are loaded along the symmetry axis. From the analysis results it was concluded that Response2000, which is a section analysis programs, is not suited for estimating the ratio Δ_s/Δ_f for structural walls with shear span ratios as small as 2.0 since the load transfer mechanism in the plastic hinge region cannot be accounted for properly. The program VecTor2 led to promising results although for one of the two analysed wall configurations it underestimated the ratio Δ_s/Δ_f considerably. A more detailed study is required to detect possible causes; this should also include a reassessment of the accuracy of the experimentally determined ratios Δ_s/Δ_f .

6. NUMERICAL MODELS OF TUA AND TUB

In Chapter 2 four different types of structural analysis models of U-shaped walls were reviewed. These were the plastic hinge model, the stick model, the wide-column model and shell element models. The objective of this chapter is (i) to apply two of these models to Test Units A and B, (ii) to compare the predicted behaviour to the experimental results, and (iii) to formulate modelling guidelines for these two types of models when applied to U-shaped walls that respond under lateral loading in the inelastic range. The two chosen models are the plastic hinge model (Section 6.1) and the wide-column model (Section 6.2). The plastic hinge model was selected for the sake of its simplicity and its ability of estimating displacement capacities on the basis of empirical quantities (see also Chapter 4). The wide-column model was chosen because unlike a stick model it represents the U-shaped wall as a three-dimensional structure while it is still relatively simple and easy to set up when compared to shell or solid element models. The chapter concludes with a comparison of the merits and drawbacks of the two types of models (Section 6.3).

6.1 Plastic hinge analysis of TUA and TUB

The plastic hinge analysis (PHA) consists of two analysis steps: First, a moment-curvature relationship of the considered cross section is derived (Section 6.1.1). In a second step this moment-curvature relationship is transformed into a force-displacement relationship (Section 6.1.2). One of the key functions of the PHA is the estimation of displacement capacities. Based on the quantities studied in Chapter 4 and estimates for the ratio of shear to flexural displacements (Chapter 5) the displacement capacities of TUA and TUB for the different directions of loading are computed and the main sources for discrepancies between experimental and numerical results are identified. In the last section (Section 6.1.3) the differences between the predicted and observed moments for bending in the diagonal direction are investigated in more detail.

6.1.1 Moment-curvature relationships

The moment-curvature analyses of the open wall sections were carried out using the zero-length fibre element of the program "Opensees" [Mazzoni *et al.*, 2005]. The U-shaped sections were subdivided into approximately 260 concrete and reinforcement fibres. The concrete area was grouped into different zones depending on the degree of confinement. The material behaviour of the concrete fibres was modelled using the stress-strain relationship by Mander *et al.* [1988b] model. The approach by Mander *et al.* [1988b] was also used for estimating the strength and strain capacity of confined concrete regions. Mander's approach is known to underestimate the actual strain capacity (Section 2.5.1); for the computation of the moment-curvature relationship the concrete strain capacity was hence increased by a factor of 1.3, which is the lower limit of the factors suggested by Priestley *et al.* [2007]. For an increase in strain capacity of the confined concrete by 30%, the ultimate curvature for all directions of loading was controlled by the maximum reinforcement strain. The reinforcement behaviour was modelled using the Giuffr -Menegotto-Pinto model [Menegotto and Pinto, 1973] with the default parameters in Opensees. Example of stress-strain relationships for reinforcement and confined concrete are shown in Figure 6.1.

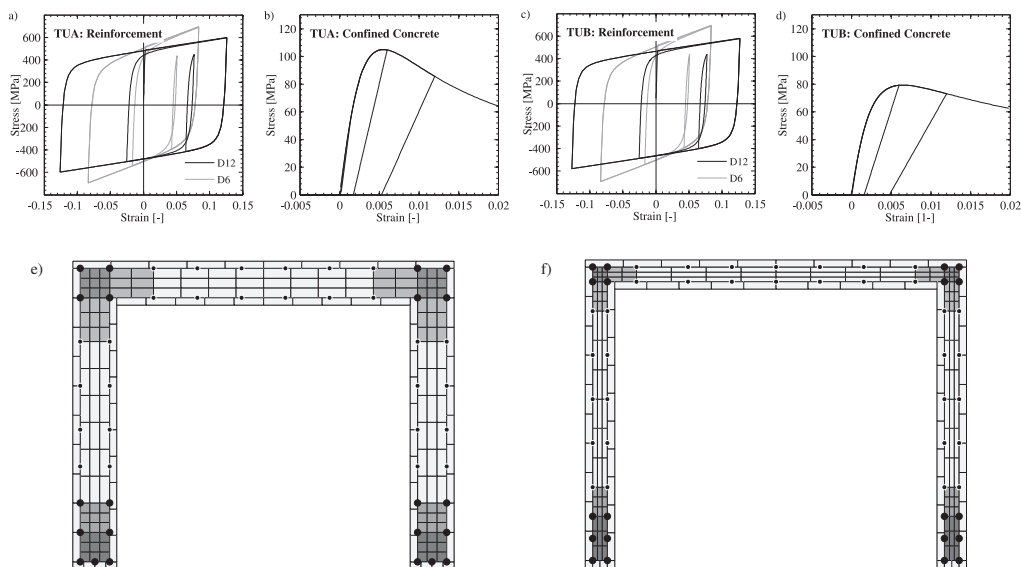


Figure 6.1. TUA and TUB: Material models for section analysis (a-d, as an example for the concrete materials the stress-strain curves for the flange ends are shown) and the subdivision of the sections into concrete and reinforcement fibres (e and f, the different shades of grey indicate the areas with different concrete properties).

Figures 6.2a and b show the moment-curvature relationships of TUA and TUB for the five different directions of loading. The analyses were carried out neglecting any tensile strength of the concrete. All curvatures and moments were plotted as positive values. For each direction of loading, the ultimate curvature was determined as the curvature that first exceeded half the strain capacity of the D12 reinforcing bars (Table 3.2); judging from the experimentally determined strain values at failure, this criteria was found to be the most appropriate (Section 4.2). The monotonically increasing curves show that crushing of the confined concrete did not occur prior to reaching the ultimate strain capacity of the reinforcing bars. Had the strain capacity of the concrete been based on Mander's approach neglecting the amplification factor suggested by Priestley *et al.* [2007] this would have not been the case for Direction E of TUB: a sudden drop in the moment capacity at about $\varphi = 0.04\text{m}^{-1}$ indicated that the confined concrete at the flange end that was in compression had reached its strain capacity.

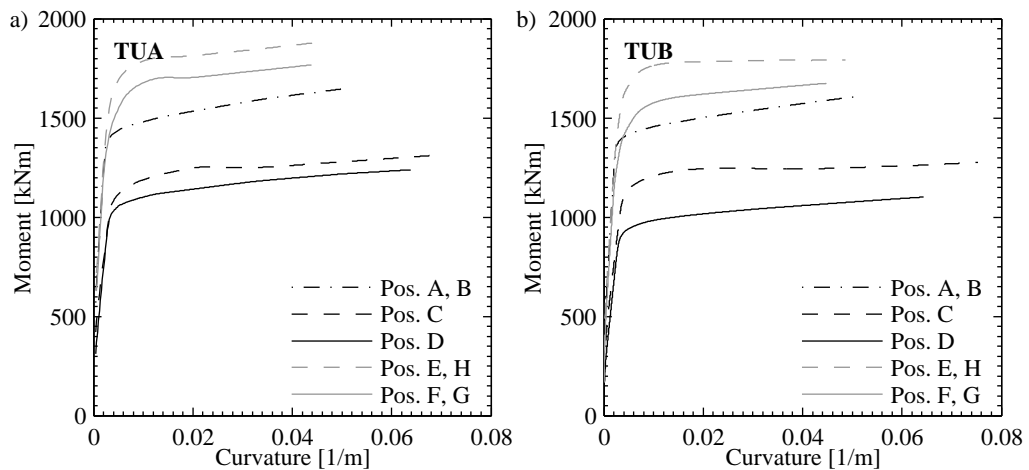


Figure 6.2. TUA and TUB: Moment-curvature relationships for the five different directions of loading that were examined during the experimental testing.

An important quantity when transforming the moment-curvature relationship into a force-displacement relationship is the nominal yield curvature, which is the threshold between the elastic and the inelastic deformation. The nominal yield curvature is computed according to Equation 4.2:

$$\varphi_y = \varphi'_y \frac{M_n}{M'_y}$$

where φ'_y is the curvature at first yield and M_n/M'_y the ratio of nominal to first yield moment. In the following paragraphs the first yield curvatures and ratios of nominal to first yield moment obtained from the moment-curvature analyses are compared to experimentally

determined values. Differences between the experimental and numerical values and possible reasons are identified and discussed:

First yield curvature For the moment-curvature analysis the curvature at first yield φ'_y was determined as the curvature for which one of the corner D12 bars first exceeded a strain of f_y/E_s . In Table 6.1 the values of φ'_y from the analysis are compared with the experimentally derived yield curvatures (Section 4.1). In all cases the section analysis underestimated the experimental curvature at first yield. There are a number of possible explanations: To determine the instant of first yield in the experiments, the strains over a height interval of 200mm were averaged (Section 4.1). The onset of yielding was determined as the instant when the average strains first reached the yield strain of the reinforcement. Hence, at this moment, the reinforcing bars would have already yielded in cracks and, therefore, it is likely that the experimental curvatures at first yield were biased high. A further discrepancy was introduced accidentally by evaluating the experimental yield strains on the basis of the measured E_s -moduli (195GPa and 192GPa for the D12 bars of TUA and TUB, respectively). The section analyses were, however, carried out assuming $E_s = 200$ GPa. Hence, the experimentally determined first yield curvatures were slightly overestimated.

Ratio of nominal to first yield moment (M_n/M'_y) For both experimental and numerical results the first yield moment was defined as the moment at the instant of the first yield curvature. For the moment-curvature analysis the nominal moment capacities were defined as the moment for which one of the corner D12 bars first exceeded a strain of 1.5%. For the experimental results, the nominal moment capacities were computed as average of the peak moments of cycles with $\mu_\Delta \geq 2.0$. The fact that, for the experimental data, the first yield curvatures were overestimated, was also reflected in M_n/M'_y -ratios which were lower than the numerically derived ratios (Table 6.2). The most significant difference between TUA and TUB concerned the experimental ratios M_n/M'_y at Positions E and F. While for TUB the ratios were about the same as for the other directions of loading they were significantly larger for TUA. It was not possible to identify the exact cause for this observation. It is, however, possible that different crack spacings contributed to this effect. For bending of TUA in the diagonal direction only very few cracks opened up initially. The deformation was concentrated in few cracks close to the base and therefore the first yield moment was relatively low. This led in return to a large ratio of M_n/M'_y . For the principal directions of loading the crack distribution during the initial cycles was slightly more even but it is not certain whether the crack pattern alone qualifies as an explanation.

The discrepancy between the nominal yield curvatures φ_y obtained from experiments and analyses will be the product of the discrepancies of the first yield curvature φ'_y and the ratio M_n/M'_y (Table 6.3¹). In some cases the error in the prediction of the first yield curvature and the ratio M_n/M'_y were of opposite sign and therefore the nominal yield curvature was predicted relatively accurately (TUA: Positions D and F, TUB: Positions: D, E and F). Even if the errors did not cancel out the overall agreement between numerical and experimental nominal yield curvatures is quite satisfactory; errors of 20% seem acceptable.

Table 6.1. Comparison of the curvatures at first yield obtained from experiments and moment-curvature analysis.

	TUA			TUB		
	Exp. [1/km]	Analysis [1/km]	Difference [%]	Exp. [1/km]	Analysis [1/km]	Difference [%]
Position A, B	2.70	2.40	-11	2.30	2.22	-3
Position C	3.47	3.20	-8	4.40	3.38	-23
Position D	3.10	2.80	-10	3.16	2.72	-14
Position E	2.30	2.22	-3	2.73	2.09	-23
Position F	2.43	2.23	-8	2.36	1.95	-17

Table 6.2. Comparison of ratios M_n/M'_y obtained from experiments and moment-curvature analysis.

	TUA			TUB		
	Exp. [-]	Analysis [-]	Difference [%]	Exp. [-]	Analysis [-]	Difference [%]
Position A, B	1.23	1.11	-10	1.20	1.13	-6
Position C	1.21	1.21	1	1.18	1.20	2
Position D	1.09	1.21	11	1.12	1.21	8
Position E	1.38	1.34	-3	1.11	1.40	26
Position F	1.23	1.33	8	1.16	1.43	23

The moment-curvature analysis results that were shown in Figure 6.2 were carried out in a displacement-controlled mode. That means that for example for the diagonal direction the sections were forced to have neutral axes perpendicular to the diagonal of the section. It is believed that this reflects best the imposed displacement in the diagonal direction during the experimental testing. As an alternative to the displacement-controlled analysis the pushover

¹Note that the same results but in terms of the proportionality constant K_1 rather than the actual curvature were presented in Table 4.1 in the columns "TUA Exp." and "TUB Exp.".

Table 6.3. Comparison of nominal yield curvatures from experiments and moment-curvature analysis.

	TUA			TUB		
	Exp. [1/km]	Analysis [1/km]	Difference [%]	Exp. [1/km]	Analysis [1/km]	Difference [%]
Position A, B	3.32	2.66	-20	2.76	2.51	-9
Position C	4.16	3.87	-7	5.19	4.06	-22
Position D	3.38	3.39	-0	3.54	3.29	-7
Position E	3.17	2.97	-6	3.03	2.93	-3
Position F	2.99	2.97	-1	2.74	2.79	2

analysis could be conducted in a force-controlled mode for which the resultant moment is perpendicular to the diagonal. Even if it is believed that the displacement-controlled mode is more appropriate, the results of the moment-curvature analysis in the force-controlled mode are included here. Figures 6.3a and b show the moment-curvature relationships in the diagonal direction for the two types of moment-curvature analysis. The plots show that the type of analysis has relatively little influence on the moment capacities although the orientation of the neutral axes (Figures 6.3c and d) differs considerably.

6.1.2 Force-displacement relationships

In this section the PHA method is applied to TUA and TUB. Details on the moment-curvature analysis were given in the previous section (Section 6.1.1). The discussion of the force-displacement relationship is divided into a section on the elastic branch (Section 6.1.2b) and a section on the inelastic branch of the pushover curve (Section 6.1.2c). To transform the curvatures into displacements estimates on the contribution of the shear displacements are required; these are derived in Section 6.1.2a according to the empirical approach developed in Chapter 5.

a) Shear deformations.

For the following plastic hinge calculations the ratio of shear to flexural displacements is estimated according to the newly developed empirical equation which was presented in Section 5.1.5 (Equation 5.9). The predicted Δ_s/Δ_f -ratios for TUA and TUB were given in Table 5.1. Since the walls are capacity designed, it is assumed that the ratio of shear to flexural displacements remains approximately constant over the entire range of the displacement demand. When the sections are analysed for diagonal bending the Δ_s/Δ_f -ratios of the web and the two flanges need to be reduced to a single ratio of the shear displacements to the flexural displacements. As an estimate the Δ_s/Δ_f -ratios of the flanges and the web are

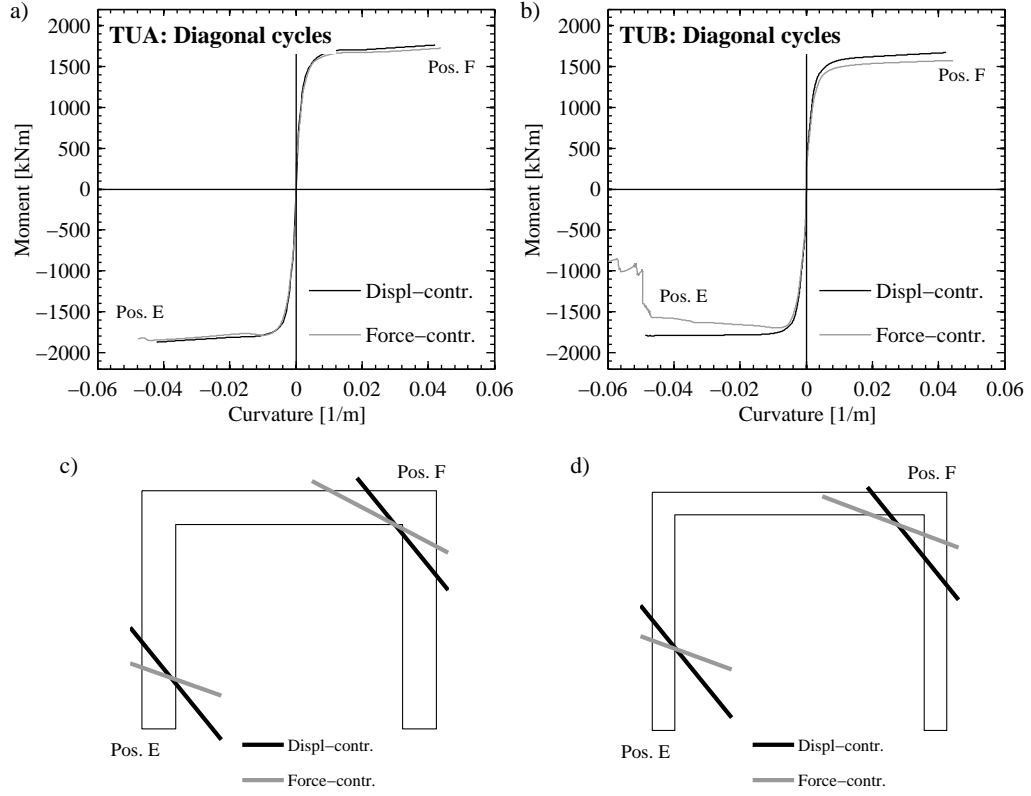
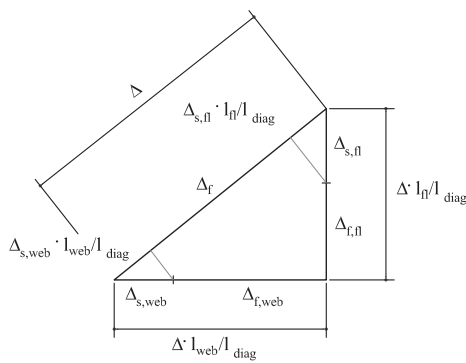


Figure 6.3. TUA and TUB: Moment-curvature relationships for bending in the diagonal direction for displacement- and force-controlled pushover analysis (a,b) and orientation of the neutral axes for the two types of analyses (c,d).

combined as follows:



$$\alpha = \left(\frac{\Delta_s}{\Delta_f} \right)_{web} ; \quad \Delta_{s,web} = \Delta \frac{\alpha}{1 + \alpha} \frac{l_{web}}{l_{diag}}$$

$$\beta = \left(\frac{\Delta_s}{\Delta_f} \right)_{fl} ; \quad \Delta_{s,fl} = \Delta \frac{\beta}{1 + \beta} \frac{l_{fl}}{l_{diag}}$$

$$\Delta_s = \Delta_{s,web} + \Delta_{s,fl}$$

$$x = \frac{\alpha}{1 + \alpha} \left(\frac{l_{web}}{l_{diag}} \right)^2 + \frac{\beta}{1 + \beta} \left(\frac{l_{fl}}{l_{diag}} \right)^2$$

$$\left(\frac{\Delta_s}{\Delta_f} \right)_{diag} = \frac{x}{1 - x} \quad (6.1)$$

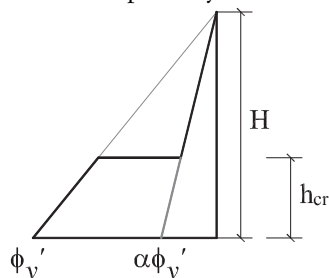
The ratio Δ_s/Δ_f for the flanges is approximated by the ratio of the West flange at Position E since the West flange carries the largest part of the load in the direction of the flanges. At Position F, the forces applied to the two flanges are of similar magnitude and hence Δ_s/Δ_f is computed as the average ratio of the East and West flange. The following $(\frac{\Delta_s}{\Delta_f})_{diag}$ ratios result: TUA: Position E: 0.44, Position F: 0.26; TUB: Position E: 0.45, Position F: 0.28.

b) Yield displacements.

Nominal yield displacements are used to express the displacement demand or capacity in terms of displacement ductility and are in this regard an important design parameter. Commonly, the estimates for the nominal yield displacements are based on the assumption of a linear curvature profile with a nominal yield base curvature that is derived from section analysis (Section 2.1.1). A linear curvature profile tends to overestimate the flexural displacements in the upper part of the wall and the discrepancy is commonly assigned to account for shear displacements and flexural displacements due to strain penetration into the foundation. In the following, this simple approach is replaced by a more complex approach that attempts to break down the nominal yield displacement into its actual components; these are (i) flexural deformation due to bending of the wall, (ii) deformations due to strain penetration into the foundation and (iii) shear deformations. The nominal yield displacement is hence predicted using an equation that differs from the equation by Hines (Equation 2.4) only with regard to the factor κ :

$$\Delta_y = \varphi'_y \frac{M_n}{M'_y} \cdot \left(\frac{\kappa}{3} H^2 + L_{spp} H \right) \cdot \left(1 + \frac{\Delta_s}{\Delta_f} \right) \quad (6.2)$$

The factor κ is a newly introduced reduction factor that accounts for the fact that at yield the wall is typically not cracked over its entire height but cracks concentrate in its lower part whereas upper parts might still be uncracked. Calculations on the basis of a linear curvature profile – corresponding to a constant stiffness along the wall height – might therefore overestimate the flexural displacement at first yield. To determine the flexural displacement at first yield it might be more appropriate to assume a curvature profile of a wall whose bottom part is cracked and whose upper part is uncracked. For the same base curvature φ'_y the top displacement of the partially cracked wall can be expressed as the ratio κ of the fully cracked wall:



$$\kappa = \alpha + (1 - \alpha) \cdot \left(\frac{h_{cr}^3}{H^3} - \frac{3h_{cr}^2}{H^2} + \frac{3h_{cr}}{H} \right) \quad (6.3)$$

where α is the ratio of the cracked to the uncracked flexural wall stiffness (EI''/EI'). The

stiffness of the uncracked wall section EI^I was taken as the gross sectional stiffness and the stiffness of the cracked section EI^II was computed as M'_y/φ'_y . The height h_{cr} up to which the wall is cracked was determined as the larger value of the wall length and the height at which the moment equals the cracking moment M_{cr} ; the wall length was used as a lower bound for h_{cr} in order to account for the effect of inclined shear cracks. The cracking moment M_{cr} is determined from moment-curvature analysis including the tensile strength of the concrete.

Table 6.4 benchmarks the analytical flexural displacements of a partially cracked and a fully cracked wall against the flexural displacements obtained from integrating the experimentally determined curvature profile at first yield. In order to draw conclusions regarding the best assumptions on the curvature profile, both analytical flexural displacements (partially and fully cracked) were evaluated for the experimentally determined base curvature. Hence, the analytical and experimental cases differ only regarding the curvature profile whereas the base curvature is in all three cases the same. For almost all directions of loading (exceptions are Position A and D of TUB) the displacement on the basis of the partially cracked profile approximates the experimentally determined flexural displacement at first yield better than the displacement on the basis of the fully cracked profile. Assuming a partially cracked wall seems therefore the most suitable approximation when the flexural displacements at first yield are determined.

Table 6.4. Comparison of the experimental and analytical flexural top displacements at first yield (excluding the displacement due to strain penetration into the foundation); the analytical displacements were computed for the experimentally determined base curvature.

	TUA			TUB		
	Curv. profile integrated	Fully cracked	Partially cracked	Curv. profile integrated	Fully cracked	Partially cracked
	[mm]	[mm]	[mm]	[mm]	[mm]	[mm]
Position A, B	5.9	10.1	8.0	8.1	8.6	6.9
Position C	6.7	10.1	7.8	10.0	12.8	10.0
Position D	8.5	9.0	8.0	9.0	9.2	8.5
Position E	4.6	6.7	6.1	6.7	7.9	7.4
Position F	6.3	7.0	6.7	6.4	6.8	6.7

Having evaluated different possible sources of discrepancies between experimental and analytical results (i.e. first yield curvature, ratio M_n/M'_y , curvature profile and ratio of shear to flexural displacements), the nominal yield displacements of TUA and TUB were computed.

The results are summarised in Table 6.5 and compared to the experimentally determined nominal yield displacements. For clarification the main assumptions for the computation of the nominal yield displacements are repeated here:

- The curvature at first yield φ'_y and the ratio M_n/M'_y were obtained from section analysis with $f_t = 0$ MPa.
- The wall remained uncracked in the upper part and hence the factor κ was introduced. The factor κ describes the flexural displacement ratio of a partially cracked to a fully cracked wall. It was derived from a section analysis with $f_t > 0$ MPa.
- The yield penetration length L_{syy} was estimated as $0.011d_b f_y$ which is the approximate mean value of the observed values (Section 4.3). The strain penetration length was smaller than what is typically observed because the foundation was prestressed horizontally.
- The ratios of shear displacement to flexural displacement Δ_s/Δ_f were estimated following the new empirical equation developed in Section 5.1.

Table 6.5. Comparison of the nominal yield displacements obtained from the experiments and from the section analysis.

	TUA			TUB		
	Exp. [mm]	Analysis [mm]	Difference [%]	Exp. [mm]	Analysis [mm]	Difference [%]
Position A, B	10.4	11.5	10	13.5	11.2	-17
Position C	9.8	11.6	19	12.7	12.3	-3
Position D	13.0	12.1	-7	15.0	12.1	-19
Position E, H	8.8	12.3	40	12.7	13.3	5
Position F, G	10.5	11.1	5	12.1	10.2	-15

The discrepancy between analytical and experimental values vary strongly between the different directions and test units. The largest error is obtained for Position E of TUA. It was chiefly caused by overestimating the flexural displacement despite introducing the factor κ . In other cases, e.g. the yield displacement of TUB at Position C, the small error of just 3% must not stimulate the impression of a "perfect" match between analysis and experiment but the small error was caused by the lucky combination of over- and underestimating different components of the yield displacement. Hence, the question poses whether the obtained estimates of the nominal yield displacement are any better than those obtained from the simple estimate according to Equation 2.2 (see first paragraph of this section). In Figure 6.4 the results from

both approaches are plotted against the experimentally obtained nominal yield curvatures. For TUA the agreement with the experimental values is indeed of similar kind: While the simple approach (linear curvature profile) tends to underestimate the experimentally determined yield displacements, the here introduced more elaborate approach generally overestimates the nominal yield displacements. For TUB, however, the agreement is improved if the components are predicted one-by-one. This can be mainly traced back to the curvature profile at first yield which itself is in some cases already close to the linear profile, therefore reducing the margin which could account for displacements due to shear deformation and strain penetration. The simple approach hence underestimates the actual nominal yield displacements. One may therefore conclude that the simple approach yields in satisfactory results if the wall section at first yield is not excessively cracked and if the shear deformations are not larger than for typical rectangular walls. If one of the two conditions is not fulfilled the simple approach tends to underestimate the actual yield displacements.

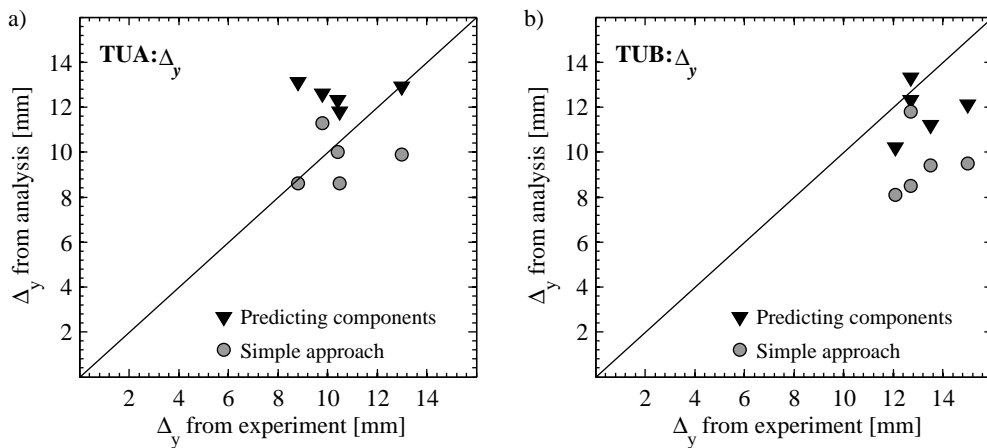


Figure 6.4. TUA and TUB: Comparison of the analytically with the experimentally obtained nominal yield displacements. Two types of different analytical approaches are included in the plot: (i) predicting the single components of the yield displacements and combining these according to Equation 6.2 and (ii) estimating the total displacement from a linear curvature profile (Equation 2.5).

c) Displacement capacities.

Once the nominal yield displacement is determined, the inelastic part of the force-displacement relationship can be readily determined (Equation 2.6). The following assumptions were made:

- The plastic hinge lengths were estimated according to Equation 2.12 which seems – from comparison to experimentally derived plastic hinge lengths – suitable for assessment tasks such as the prediction of test results. Note, however, that the component of the plastic hinge length that accounts for strain penetration into the foundation was reduced to half the value in Equation 2.12 since the foundation was prestressed horizontally (see Section 4.3.3). The corresponding plastic hinge lengths for TUA and TUB were summarised in the column $L_{ph3,mod}^*$ in Table 4.4.
- For all directions of loading the displacement capacity was determined as the capacity for which the strain of a D12 reinforcing bar first reaches $0.5\varepsilon_{su}$. Note that this is not absolutely correct since the limit of $0.5\varepsilon_{su}$ in fact applies to the total excursion strain and not to the tensile strain alone (Section 2.5). However, in PHA it is difficult to combine compressive and tensile strains. Since the compressive strains are typically small the resulting error is acceptable. Displacement limits dictated by the strain or strength capacity of the concrete were not critical for computing the force-displacement relationship; limits on the displacement capacity due to web crushing are discussed towards the end of this section.
- The ratio of the shear to flexural displacements is assumed to be the same as at the onset of yielding (Section 6.1.2a). They were estimated using the new empirical equation presented in Section 5.1.

The force-displacement relationships which are based on the aforementioned assumptions will be referred to as "assessment" curves since the objective was to remove any conservatism in the prediction and to aim for expected values. In design, the objective is different in the respect that one is interested in conservative estimates instead of mean estimates of the expected displacement capacity. A standard procedure for estimating the design displacement capacity with the PHA method is based on the following assumptions:

- The plastic hinge length is estimated as the maximum of the two equations for the plastic hinge length that are given in Paulay and Priestley [1992] (L_{ph1} and L_{ph2} in Table 4.4).
- The displacement capacity is limited to the displacement for which the maximum tensile strain reaches $0.6\varepsilon_{su}$. For ductile reinforcing bars the strain capacity is often estimated as 10%. The ultimate displacement is hence linked to a maximum steel strain of 6% (note that this yields in approximately the same strain limit as for the assessment curves since $0.5\varepsilon_{su}$ equates to 6.3% and 6.4% for TUA and TUB, respectively).
- The shear displacements are typically accounted for by a nominal factor of 1.15 [Dazio, 2000], i.e. the ratio of shear to flexural displacements is estimated as 0.15.

Figures 6.5 (TUA) and 6.6 (TUB) show the envelopes resulting from the "assessment" and "design" PHA in comparison to the experimental force-displacement hysteresses. Cycles of the sweeping motions were omitted since it is not possible to carry out PHA for bi-directional loading histories.

Computing displacement capacities using design estimates for plastic hinge length and shear displacements yields ultimate displacements that are all smaller than the actually achieved displacements. Hence, the experiments confirmed that the design equations yield safe estimates of displacement capacities not only for rectangular but also for U-shaped walls. Apart from the direction in that failure occurred it is not possible to quantify how close the actual displacement capacities were approached. This is one of the disadvantages of subjecting a single test unit to a bi-directional loading history instead of testing several specimens of the same wall configurations under different directions of loading.

The following discussion focuses on the assessment case since test results for U-shaped walls have not been compared to PHA results before and therefore it seems more appropriate to focus on the prediction of expected values of displacement capacities rather than conservative estimates. It is then possible to reduce these predicted capacities in order to introduce a safety margin for design purposes. This can be done by either reducing the plastic hinge length (as it has been done in the past) or by reducing the strain limit.

TUA failed at Position F during the cycles at $\mu_{\Delta} = 8.0$. While the maximum imposed displacement corresponds quite well to the predicted displacement capacity, the first rupture of a D12 bar occurred much earlier (i.e. when passing $\mu_{\Delta} \cong 6.0$ during the $\mu_{\Delta} = 8.0$ cycle). According to Park [1988] the displacement capacity should be defined as "that post-peak deformation when load has reduced by a small specified amount, or when the reinforcement fractures or buckles, whichever occurs first". In the study here, buckling of reinforcement was not considered as criterion for the definition of the ultimate displacement capacity. The PHA overestimated the displacement capacity in the Direction F since fracture of the bars occurred for displacements smaller than the derived ultimate displacement capacity. However, the displacement at which failure occurred might have been also influenced by strain demands in preceding cycles. In particular the large tensile strains in the D12 reinforcing bars at the flange ends when loading to Position D at $\mu_{\Delta} = 8.0$ (Table 4.2) might have reduced the displacement capacity when loading in Direction F.

At Position E the predicted displacement capacity exceeds the imposed displacement demand. This finding is in-line with the observation that at this position only two further D6 bars had ruptured but none of the D12 bars. Nevertheless, the predicted displacement capacity would

have probably slightly exceeded the true experimental capacity had the wall been pushed further in this direction. Based on the strain limit for bar buckling by Restrepo (Section 2.5.2), the PHA predicts that onset of buckling occurs at $\Delta \approx 63\text{mm}$ which is about the displacement imposed at $\mu_\Delta = 7.0$. However, buckling had already been observed at Position E during the cycle at $\mu_\Delta = 6.0$. Hence, for Position E, it is likely that also the displacement capacity associated with bar fracture was slightly overestimated by the assessment curve.

TUB failed at the end of the sweeping motion with $\mu_\Delta = 6.0$ (Position B) due to web crushing. Hence, the reinforcement strain limits do not really apply when determining the displacement capacity of TUB. However, from the degree of buckling of the D12 bars in the flange ends it was assumed that the bars would have ruptured soon had the loading been continued (most likely at Position E or F during cycles at $\mu_\Delta = 8.0$). Whether the compressive strain capacity of the concrete would have soon set a limit to the displacement capacity when loading in Direction E is difficult to extrapolate from the experimental evidence. At Position E at $\mu_\Delta = 6.0$ the flange end was in clear distress due to a slight outward movement of the flange end but not due to excessive axial compression. The former effect can not be captured by moment-curvature analysis. Moreover, determining displacement capacities on the basis of ultimate compressive strains is most often related to large uncertainties; this is for two reasons: First, estimates of the strain capacity of concrete are not as dependable as those for reinforcing bars. One reason for this is that equations for the compressive strain capacity of concrete have been derived for pure axial instead of combined axial-flexural loading (Section 4.2.1). Second, empirical equations of plastic hinge length were typically calibrated to yield good estimates of the displacement capacity if the reinforcing bar strain capacity was critical. In conjunction with compressive strain limits of the concrete the displacement capacity estimates are less reliable (Section 2.1.3b).

The limit on the displacement capacity due to crushing of the compression diagonal in the web are included in Figure 6.7; shear capacities were computed according to the approaches by Oesterle *et al.* [1984] and Paulay and Priestley [1992], which were summarised in Section 2.5.3. According to Paulay and Priestley [1992] web crushing would have occurred already at $\mu_\Delta \approx 3.0$. However, one needs to keep in mind that the equation by Paulay and Priestley [1992] is explicitly intended for design and not for assessment purposes and it therefore seems natural that it underestimates the actual capacity. The equation by Oesterle *et al.* [1984] was calibrated with experimental data. The prediction by Oesterle *et al.* [1984] comes very close to the force at which web crushing occurred although Hines and Seible [2004] claimed that for walls with boundary elements the approach by Oesterle *et al.* [1984] yielded conservative results. The reduced web thickness near the SE corner where web crushing finally occurred (t_w was reduced to $\sim 3\text{cm}$ in some parts of the web, Section 3.5.2) renders it difficult to judge on the

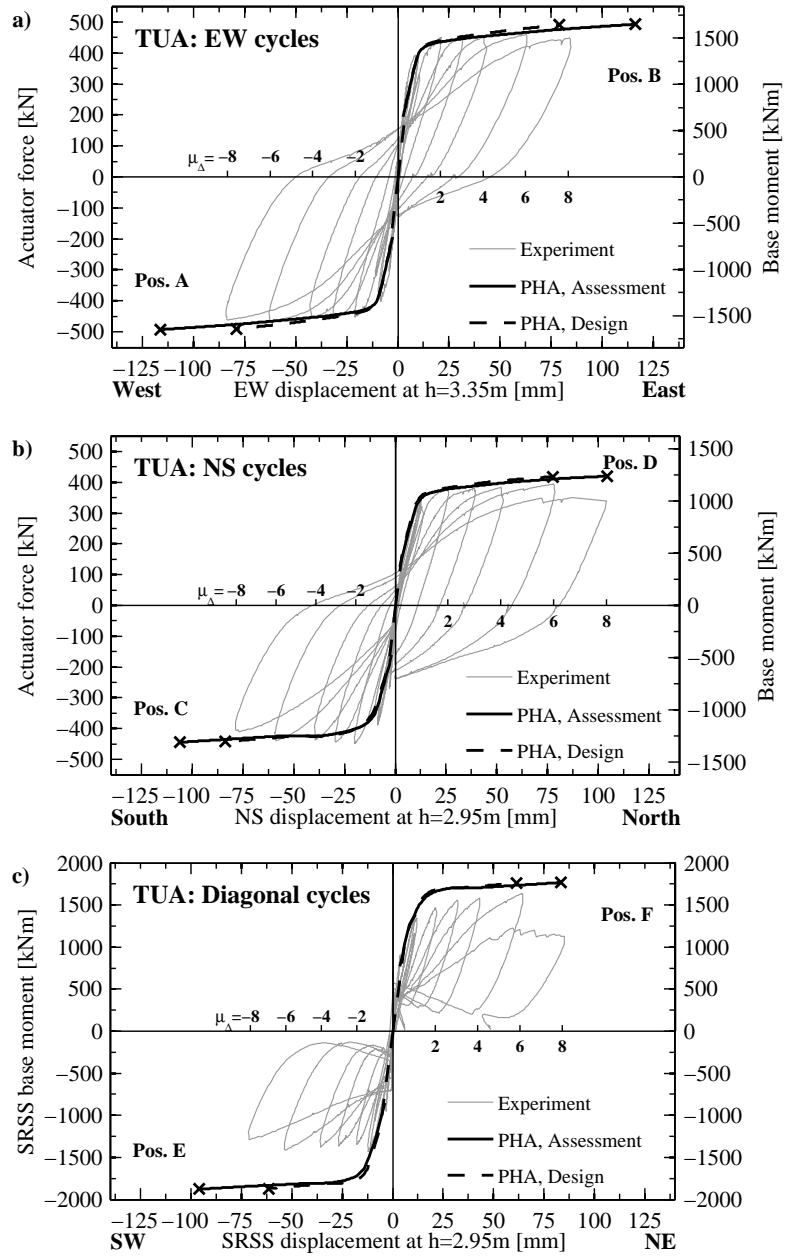


Figure 6.5. TUA: Comparison of results of pushover analyses to experimental force-displacement hysteretic behavior for loading parallel to the web (a), the flanges (b) and in the diagonal direction (c).

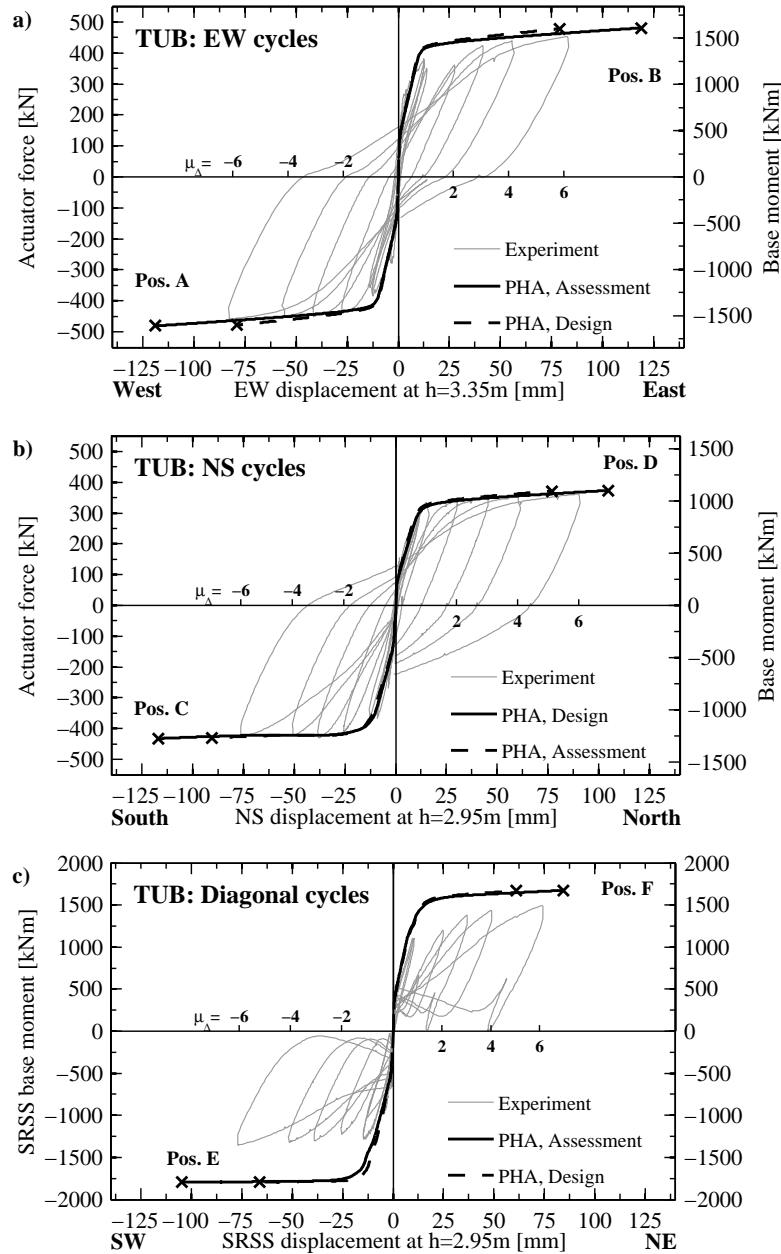


Figure 6.6. TUB: Comparison of results of pushover analyses to experimental force-displacement hysteresses for loading parallel to the web (a), the flanges (b) and in the diagonal direction (c).

accurateness of the predicting equations since the actual web crushing capacity would have been reduced by the extensive spalling of the unconfined concrete (Section 2.5.3).

6.1.3 Moment capacities

The main discrepancy between the predicted force-displacement curves and the experimentally determined hysteresses, which were shown in Figures 6.5 (TUA) and 6.6 (TUB), does not concern the displacement capacities but the moment capacities: At Position E and F for both TUA and TUB the predicted moment capacities exceed the actual observed moments considerably. The predicted moment-capacities in the diagonal directions are larger than in any of the principal directions. Decomposing the predicted moments at Position E and F into the components parallel to the principal axes shows that these are almost as large as for bending in the principal directions. For TUA, at the nominal yield point, the NS-moment component at Position E corresponds to 88% of M_n at Position C and the EW-moment component to 95% of M_n at Position A; at Position F the nominal moment is composed of 85% of M_n at Position D and of 93% of M_n at Position B. For TUB, the ratios are very similar: at Position E the nominal moment is composed of 84% of M_n at Position C and 98% of M_n at Position A whereas at Position F the nominal moment is composed of 82% of M_n at Position D and 92% of the M_n at Position B. This is also illustrated in Figure 6.8, which shows the first yield and nominal moments for all directions of loading.

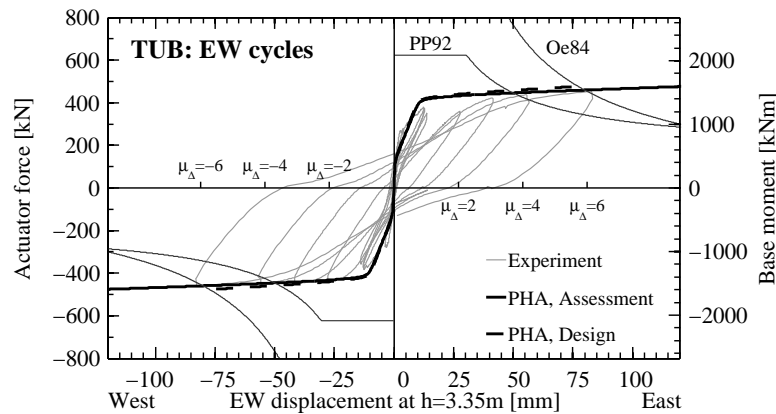


Figure 6.7. TUB, EW cycle: Comparison of results of pushover analyses to experimental force-displacement hysteresses including the capacity curves for web crushing (Legend: Oe84=Oesterle *et al.* [1984], PP92=Paulay and Priestley [1992]).

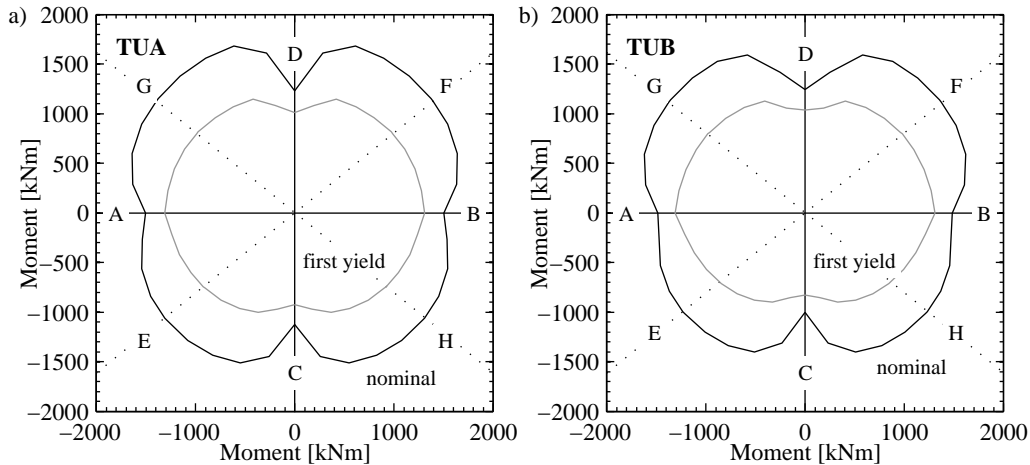


Figure 6.8. TUA and TUB: First yield and nominal yield moments for all directions of loading.

The main difference between the experimental and numerical moment capacities for displacements towards Position E resulted from the moment capacities M_{EW} , for which the experimental value reached only about two thirds of the numerical value (Table 6.6). At Position F, the difference between the experimental and numerical values was less at Position E. The remaining difference resulted chiefly from the moment M_{NS} that was smaller for the experiments than the moment obtained from the section analyses. One of the key objectives of the wide-column analysis presented in Section 6.2 is to identify possible reasons for these differences.

Table 6.6. Comparison of maximum moments at Positions E and F obtained from the experiments and the section analysis.

	Experiment			Analysis		
	M_{EW} [kNm]	M_{NS} [kNm]	M_{SRSS} [kNm]	M_{EW} [kNm]	M_{NS} [kNm]	M_{SRSS} [kNm]
TUA						
Position E	1030	970	1415	1500	1140	1880
Position F	1440	770	1640	1440	1020	1770
TUB						
Position E	1050	860	1360	1480	1010	1790
Position F	1340	671	1497	1440	880	1690

M_{EW} Moment due to forces in the EW direction

M_{NS} Moment due to forces in the NS direction

M_{SRSS} Moment resulting from the vectorial addition of M_{EW} and M_{NS}

6.1.4 Summary of findings from plastic hinge analysis

The findings from the PHA of TUA and TUB concern both strength and displacement aspects:

Strength capacity: For bending parallel to the flanges and the web the strength capacity can be predicted as accurately as for rectangular walls. For bending in the diagonal direction, in particular when one flange end is in compression (Position E), the moments are grossly overestimated. The analysis of the wide-column models in the following section will explain this discrepancy.

Yield displacement: The yield displacements were estimated using a simple approach that uses only the yield curvature and a more elaborate approach that attempts to predict the displacement components at yield due to flexure, base rotation and shear. For TUA both approaches achieved a similar match with the experimental results. For TUB, the elaborate approach yielded slightly better results. On a whole, the match between analytically and experimentally determined yield displacements was mediocre: The analytical results deviated up to 20–40% in both directions from the experimental results. However, the discrepancy is not alone related to deficiencies in the analytical models but also to uncertainties when determining the experimental yield displacements.

Displacement capacity: A design and an assessment approach were distinguished when the ultimate displacement capacity of the U-shaped walls for different directions of loading was predicted. For all directions of loading the design approach predicted displacement capacities smaller than the maximum displacements reached during the testing. This is inline with the intention of the design approach, which leaves a safety margin between the predicted and the actual displacement capacity. On the contrary, the assessment approach was able to yield reasonable, yet in most cases probably slightly too large, estimates of the actual displacement capacities. The displacement capacities were determined on the basis of a maximum tensile strain of $0.5\varepsilon_{st}$, which – from comparison to experimental results – seemed to predict the measured ultimate total strain excursion fairly well. It is, however, difficult to draw exact conclusions since the test units could only fail in one direction; for the other four directions of loading a displacement capacity could not be determined. This is certainly one of the drawbacks when testing a single unit under a bi-directional loading history instead of testing several units under cyclic loading in different directions.

6.2 Wide-column models

In the course of the literature research on wide-column models (WCMs) it was found that there is a lack of reports on the properties and the performance of WCMs with inelastic properties (Section 2.3.5). The objective of this section is therefore to model TUA and TUB with WCMs and to compare the numerical and experimental force-displacement hysteresses. When building a WCM of a U-shaped wall the engineer needs to take decisions regarding the following modelling parameters:

- Subdivision of the U-shaped section into planar wall sections.
- Vertical spacing of the horizontal links.
- Number of vertical elements representing the planar wall sections between horizontal links (a wall section between two horizontal links is typically subdivided into a number of column elements).
- Properties of the links.
- Properties of the vertical elements: In the study here the axial and flexural properties were defined via a fibre section. The shear and torsional stiffness of these elements had to be defined independently.

Existing modelling guidelines for WCMs are based on studies of elastic systems. The objective of the following study is to test the sensitivity of analysis results of WCMs with inelastic properties to these modelling parameters and to identify appropriate choices of the modelling parameters for such models. The section is divided into two parts: In a first step (Section 6.2.1) reference WCMs for TUA and TUB are defined. Where such exist, the choice of the modelling parameters follows the recommendations for elastic models which were found in the literature. These models of TUA and TUB are also referred to as WCMs with state-of-the-art properties. In a second step, the sensitivity of the analysis results to the five key modelling assumptions, which were listed above, is tested. The sensitivity study is divided into three sections: The first concerns the geometry of the WCM, the second the shear and torsional properties of the vertical members and the last the properties of the horizontal links. Recommendations of the choice of the modelling parameters are based on the sensitivity of the analysis results and the appropriateness of the modelling assumptions for a RC sections undergoing large inelastic deformations. In the final section the modelling recommendation are summarised and applied to TUA and TUB showing the goodness of fit between the numerical and experimental results.

All WCMs of TUA and TUB that are presented in the following sections were analysed using the program Opensees [Mazzoni *et al.*, 2005]; that is the same program that has also been used

for the section analyses required for the plastic hinge models in Section 6.1. Although the element library of Opensees comprises a wide range of special elements and force-displacement hysteresis rules only standard element types and rules are used since the objective of this study is to develop a WCM that could be analysed with any standard engineering software packages which offers nonlinear fibre elements. The properties of the reinforcing steel and concrete were identical to those used in the PHA (Section 6.1.1). Only the limits on the concrete strains were omitted; the stress-strain relationship of the concrete was hence defined according to the curve by Mander *et al.* [1988b] but no ultimate strain was defined for which the stress level would suddenly drop to zero. The reason for this modification was twofold: First, concrete crushing had not been observed during the experiment. It is also generally acknowledged (Sections 2.5.1 and 4.2.1) that the strain capacity predicted according to the mechanical model by Mander *et al.* [1988b] tend to be too low if the member is subjected to axial load and flexure. Second, and most importantly, the strains at the integration points of the elements are strongly dependent on the formulation of the elements and the element length. It will be shown that without accounting for the element length and the element formulation, the strains at the integration points are of little meaning and cannot be employed directly for determining limit states of the structural element.

6.2.1 Description of the reference WCM for TUA and TUB

This section describes the reference WCM for TUA and TUB which is assigned state-of-the-art properties. Figure 6.9 shows the layout of the reference WCM for TUA and TUB. The WCM is a frame model with vertical and horizontal elements. Five different types of frame elements are distinguished:

- Wall elements: The column elements representing the web and flange sections between the wall base and the lower edge of the collar. The bottom wall elements were assumed to be fully fixed at the wall base.
- Collar elements: Column elements within the collar.
- Wall links: Horizontal links within the wall. The links within the flanges join the flange elements and the corners. The links within the web join the web elements and the corners.
- Collar links: Horizontal links within the collar.
- The small elements joining the links of the walls and collar at the lower edge of the collar ($h = 2.72\text{m}$) were modelled as rigid in both shear and flexure.

The designation "vertical elements" is used when both wall and collar elements are meant.

The collar elements were offset towards the outside by 75mm and 50mm for TUA and TUB respectively (see isometric views of TUA and TUB in Figure 3.3) since the vertical elements were always placed at the centre line of the wall sections they were representing. Figure 6.9d shows a close-up of the collar of the WCM. The four horizontal links within the collar were at heights of $h = 2.72\text{m}$ (lower edge of collar), $h = 2.95\text{m}$ (height of actuators in the NS direction), $h = 3.35\text{m}$ (height of actuator in the EW direction) and $h = 3.56\text{m}$ (top edge of collar). The actuators were represented by zero-length spring elements (Figure 6.9d). When the WCM was analysed for imposed top displacements, the displacements were imposed on the free end nodes of the actuator springs. The spring elements were rigid in the line of action of the actuators and were used to measure the applied forces which corresponded to the actuator forces.

In the following paragraphs only the reference model for TUA is described in depth; the reference WCM for TUB was built along the same lines with only small adaptations where required by the different geometry of the cross section. The paragraphs follow the sequence of the modelling parameters which were given in the introduction to the section on WCMs (i.e. subdivision of the U-shaped section, vertical spacing of the horizontal links, number of vertical elements between links, properties of the links and properties of the vertical elements).

a) Subdivision of the section.

For the reference WCM of TUA the section was subdivided into three rectangular sections, i.e. the web and the two flanges. The corner areas were half attributed to the web section and half to the flange sections (Figure 6.9b). Since most structural analysis programs only allow the definition of reinforcing bars within the rectangular concrete sections, the inner corner bar was attributed to both the web and the flange section whereas the outer bar was not assigned to any section; the total reinforcement area was therefore modelled correctly. The web section was 1.15m long and 0.15m wide while the flange section was 0.975m long and 0.15m wide. Figure 6.9c shows the in-plan location of the vertical elements representing the web and the flange sections. The wall sections were modelled as fibre sections because of their ability to capture the axial elongation at the centroid and the axial force-bending moment interaction of RC sections; this was considered important since the axial load on the individual wall sections will change greatly throughout the bidirectional loading history to which TUA and TUB were subjected during the testing. The discretisation of the sections (Figure 6.9b) was kept similar to the discretisation of the U-shaped section for the PHA (Figure 6.1) only that the section was divided into planar web and flange sections.

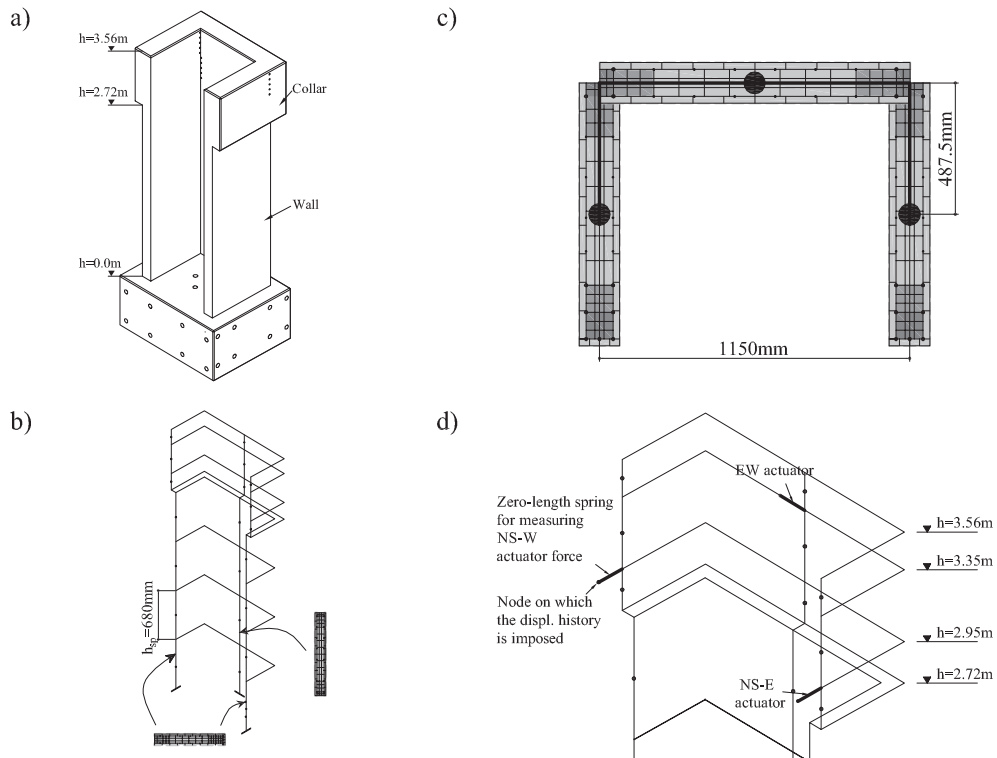


Figure 6.9. WCM: Isometric view (a), wide-column model (b), fibre cross sections of TUA (c) and details of collar of WCM where the lateral displacements are imposed (d).

b) Spacing of the horizontal links.

While the spacing of the horizontal links within the collar was basically dictated by the geometry of the collar and the location of the lines of action of the actuators, the spacing of the horizontal links within the wall region (i.e. between $h = 0 - 2.72\text{m}$) could be chosen more freely. Stafford-Smith and Girgis [1986] suggested to limit the link spacing to about one fifth of the overall wall height (Section 2.3.3) which corresponds for TUA and TUB to a link spacing of 590mm and 670mm for the NS and EW direction, respectively. For the reference WCM it was decided to place the links at $h_{sp} = 680\text{mm}$ intervals dividing the wall into four parts of equal height (Figure 6.9c).

c) Number of vertical elements between links.

The vertical elements of the reference WCM were modelled by means of two-nodes, displacement-based beam elements with two Gauss-Legendre integration points along their length [Mazzoni *et al.*, 2005]. Two beam elements between consecutive links were used. Hence, the length of every beam element in the wall was $l = 0.5h_{sp} = 340\text{mm}$; the length of

the collar elements varied since the spacing of the links was not constant. A beam length of $l = 0.5h_{sp}$ also required that additional nodes at mid-height between the links were introduced (Figure 6.9b).

d) Shear and torsional properties of the vertical elements.

By assigning a fibre section to the wall elements only the axial and flexural properties were defined. The other flexibilities (i.e. shear and torsion) were decoupled from the axial and flexural properties. The nonlinear displacement-based element implemented in Opensees is rigid in shear and flexible in torsion. To account for shear flexibility of the wall elements zero-length spring elements were introduced at the nodes at midheight between the links. These zero-length springs were assigned stiffnesses in the two horizontal translational degrees of freedom; all other degrees of freedoms of the two nodes were slaved. The stiffnesses of the springs represented the in- and out-of-plane shear stiffness of the two wall elements above and below the spring. For the reference WCM of TUA and TUB the spring properties were computed to represent the shear stiffness of uncracked sections:

$$k_s = \frac{G_c A_{sb}}{h_{sp}} \quad (6.4)$$

where the shear area A_{sb} was taken as $0.8A_g$.

While the displacement-based element in Opensees has no shear flexibility, it has a torsional flexibility. For the reference WCM of TUA the torsional stiffness of the web and flange sections was computed as the torsional stiffness of a slender rectangular, homogenous section with elastic properties:

$$GK = G_c \cdot \frac{l_w \cdot t_w^3}{3} \quad (6.5)$$

e) Link properties.

As suggested by Reynouard and Fardis [2001] the links were assigned infinite flexure and shear stiffnesses. Only the torsional degree of freedom was given the flexibility (Equation 2.19) corresponding to an elastic, uncracked section. Hence, out of the aforementioned four types of elements of the WCM (wall and collar elements, wall and collar links) only the wall elements were assigned inelastic properties for the coupled axial and flexural behaviour. The shear and torsional stiffness of these elements as well as all properties of the other element types were assigned elastic properties.

f) Load cases and results.

During the testing TUA and TUB were subjected to an axial load and imposed lateral displacements. In the experiments the axial load was applied near the centre of the gross section; in addition the selfweight of the test unit and the weight of any equipment mounted onto the

wall contributed to the axial load. The resultant axial force at the wall base was 780kN for both TUA and TUB. In the WCM the axial load was modelled as three point loads which were applied at the top nodes of the collar elements; the selfweight of elements was not modelled. For TUA, the load applied to one flange was $P = 265\text{kN}$ and the force applied to the web $P = 250\text{kN}$ (TUB: flange: 257kN, web: 266kN). The total axial force was hence $P = 780\text{kN}$, which corresponded to the axial load at the base of the physical test units. Note that the axial loads were not distributed according to the cross section areas of the web and flanges. The proportion of the axial load applied to the web and flanges was computed to yield a resultant axial load at the centroid of the wall section but the forces were applied to the collar nodes, which did not align with the wall nodes.

The WCMs of TUA and TUB were analysed for two types of loading: In a first step pushover analyses in the five directions of loading were carried out (for the description of the directions see Section 3.3). In a second step, the models were analysed for the entire loading history which had been applied to TUA and TUB (excluding those instants of the loading history when a small twist was applied to the wall head). For both the pushover and the full load path analysis the displacements were imposed at the free end nodes of the zero-length elements representing the actuators.

As an example for the obtained analysis results Figure 6.10 shows the forces of the wall elements at Position A during the EW cycles with $\mu_{\Delta} = 4.0$.

Figures 6.11 and 6.12 show the comparison of the analysis and the experimental results. The results are compared in terms of the hysteresis loops for the cycles in the EW, NS and diagonal directions and in terms of the loops of the actuator forces during the cycles at $\mu_{\Delta} = 4.0$. While the WCMs predict the moment capacity for cycles in the EW and NS directions fairly well, they overestimate the capacity in the diagonal direction – in particular at Position E – considerably. The analysis results for both TUA and TUB are characterised by a too large loading and unloading stiffness for all directions of loading. The same observation was made for the PHA which was presented in Section 6.1. As for the PHA the moment capacity in the diagonal direction was overestimated by the WCM with state-of-the-art properties. The numerical and experimental results differed also significantly with respect to the actuator forces (plots d-f). One of the objectives of the sensitivity analysis which is presented in Sections 6.2.2 to 6.2.4 will be to identify possible modelling parameters that could account for these discrepancies.

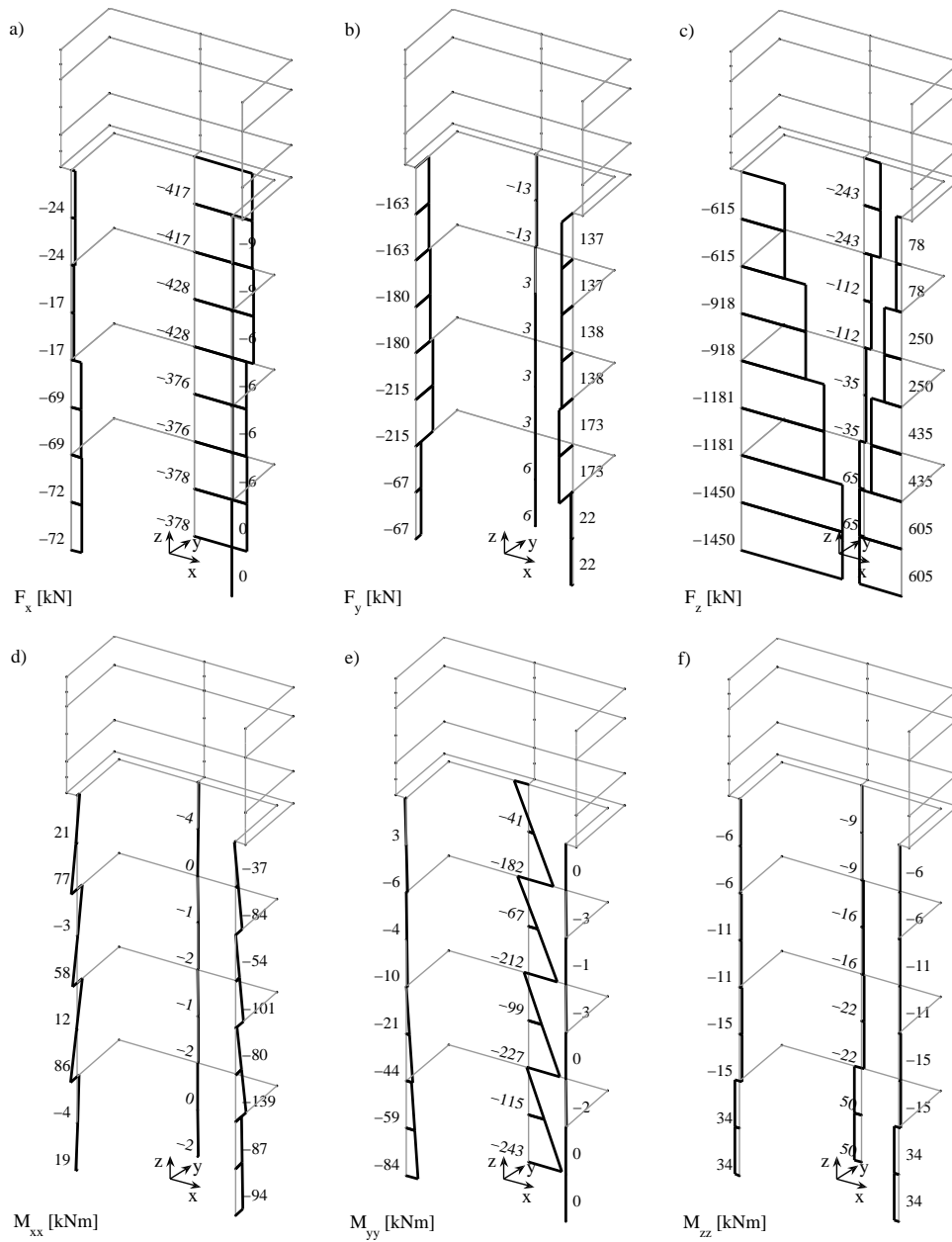


Figure 6.10. TUA, WCM: Internal forces at Position A at $\mu_{\Delta} = 4.0$; the forces are given in the global coordinate system.

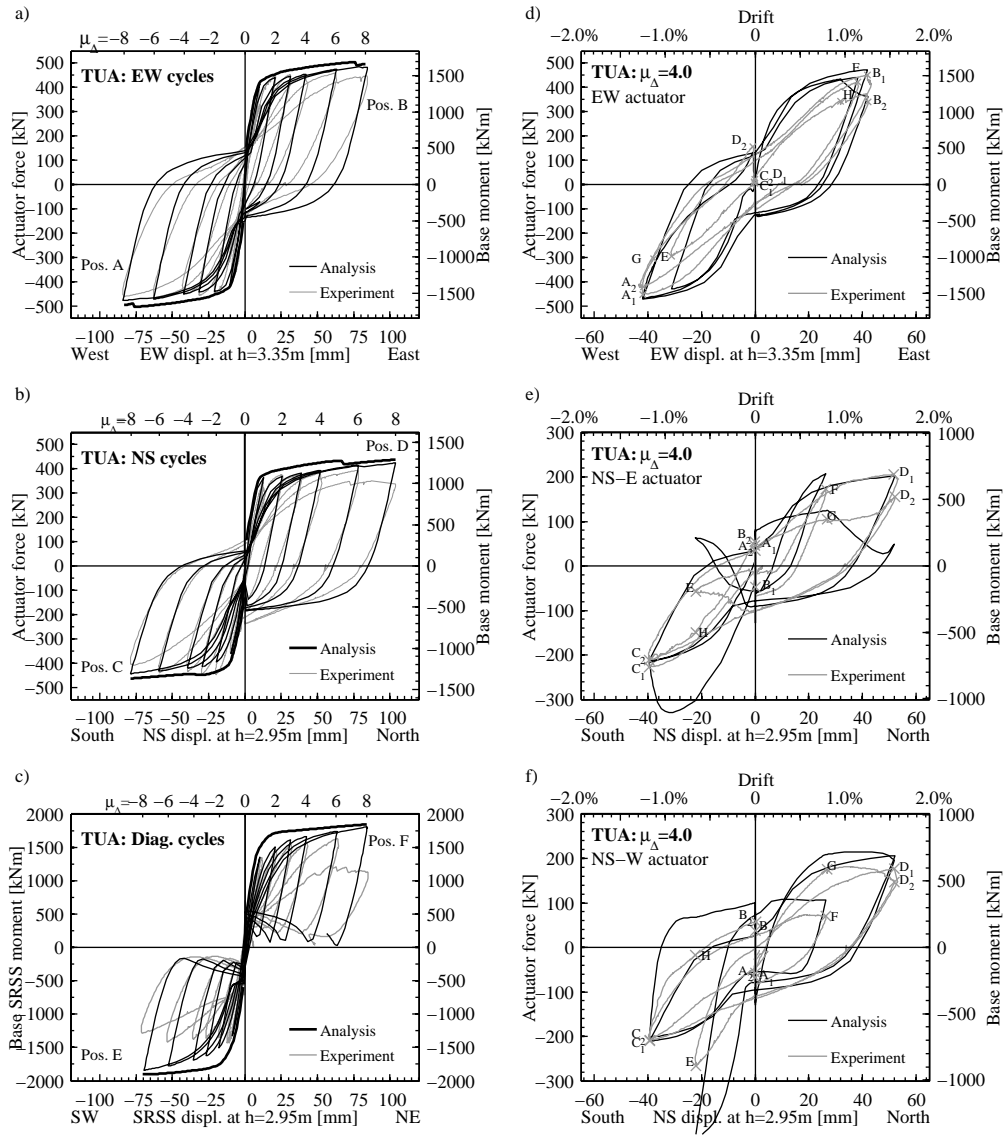


Figure 6.11. TUA, WCM with state-of-the-art properties: Comparison of analysis and experimental results for cycles in the EW, NS and diagonal directions (a-c, also included are the results of the pushover analyses of the WCM) and comparison of actuator forces obtained from analysis and experiment during the cycles of $\mu_{\Delta} = 4.0$ (d-f).

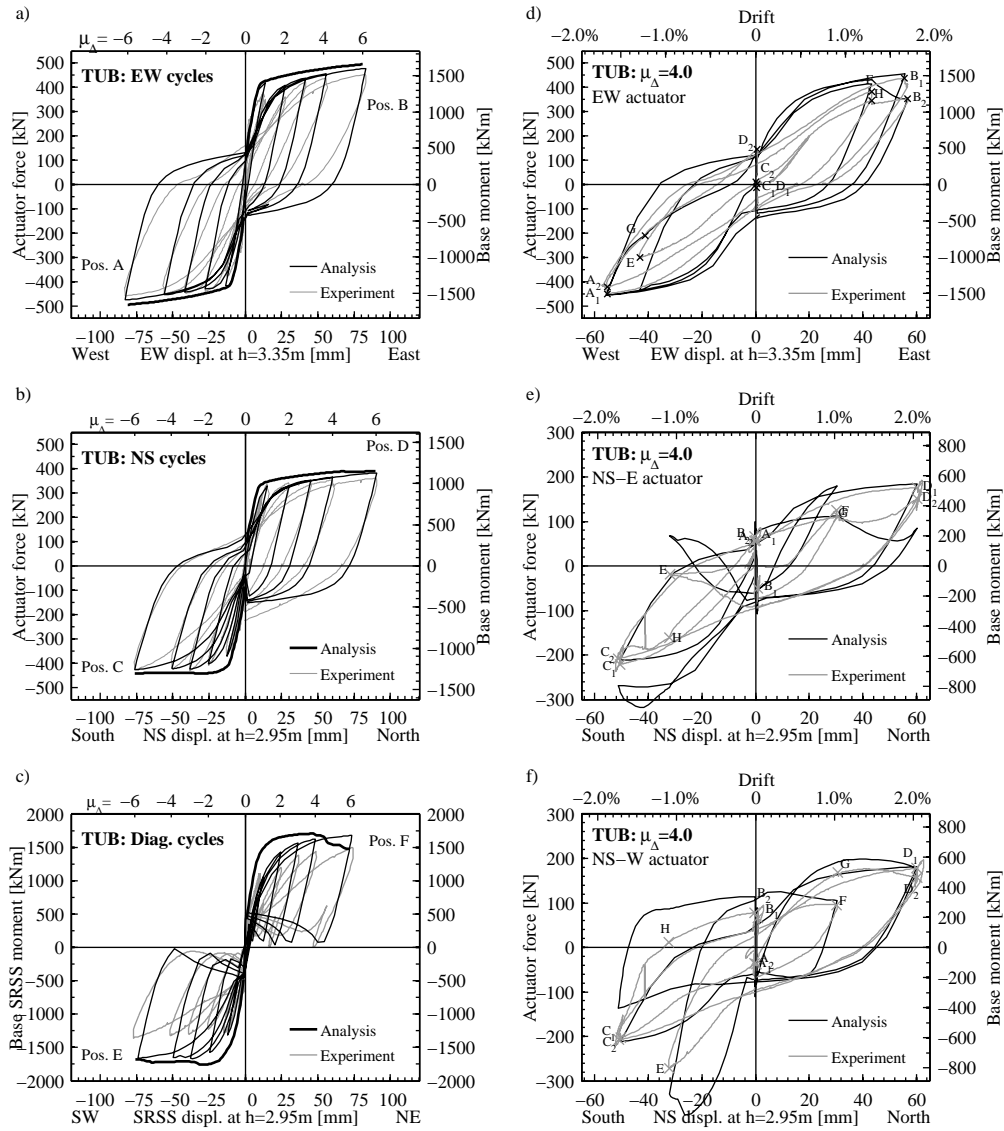


Figure 6.12. TUB, WCM with state-of-the-art properties: Comparison of analysis and experimental results for cycles in the EW, NS and diagonal directions (a-c, also included are the results of the pushover analyses of the WCM) and comparison of actuator forces obtained from analysis and experiment during the cycles of $\mu_{\Delta} = 4.0$ (d-f).

6.2.2 Sensitivity of the WCM analysis to the geometry of the model

Based on the reference models for TUA and TUB, which were described and analysed in the previous section, the sensitivity of the analysis results to different modelling assumptions is tested. The first decisions required when building a WCM of a structure concern the geometry of the model. The geometry of the model is characterised by three principal parameters, i.e. (i) the subdivision of the non-planar wall section into rectangular sections, (ii) the spacing of the horizontal links and (iii) the number of vertical wall elements connecting the horizontal links. The literature on these issues is very scarce. The objective of this section is therefore to investigate the sensitivity of analysis results with respect to the three aforementioned geometrical parameters. The study is limited to TUA. It is, however, assumed that the conclusions can be expanded to TUB since the configuration of the two walls is very similar. When further experimental evidence is available, the study should be broadened to include these wall configurations, in particular if E-shaped walls or more irregular configurations were tested.

a) Subdivision of non-planar wall sections.

The wide-column analogy requires the subdivision of non-planar wall sections into planar subsections, which can typically be undertaken in different ways. Figure 6.13 shows three possible division schemes for a U-shaped wall that differ regarding the allocation of the corner areas to the web and flange sections:

- Scheme A: The web element includes the corner areas whereas the flange elements end before the corner area.
- Scheme B: Scheme B is similar to Scheme A but the corner area is attributed to the flange elements instead of the web element.
- Scheme C: The corner area is split between the flange and the web elements. The corner bar is not assigned to any element², in return the bar near the inner edge is covered by both web and flange element. The horizontal links join where the web and flange elements meet.

Assuming the links are perfectly rigid, the gross section properties of Scheme A and B equal the properties of the U-shaped wall section. Scheme C models the gross area correctly while the centre of mass is slightly further away from the web than for the gross section; the moments of

²In Opensees it is possible to define reinforcing bars outside the concrete section. Opensees also allows to define non-rectangular concrete sections; it would hence be possible to divide the section along the connection of the inner and the outer corners. In most structural analysis programs reinforcing bars cannot be defined outside the concrete section, which in turn has to be rectangular. Therefore, only such sections are used in the study presented here.

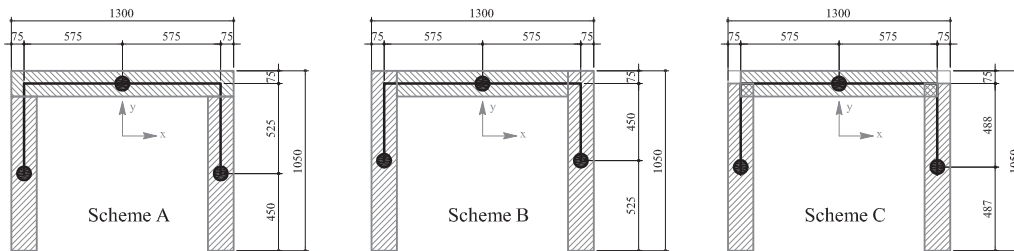


Figure 6.13. TUA: Different schemes for subdividing the U-shaped section into planar wall sections (all dimensions are in millimetres).

inertia about the x - and the y -axes are slightly smaller than those of the gross section (1%). The differences are, however, so small that they are hardly of significance in seismic engineering, in particular if the structure is expected to respond in the inelastic range.

Figure 6.14 shows the comparison of the pushover curves of the three models for the EW direction (plot a) and for Direction F (plot b). The difference between the three models is relatively small. For pushover analyses in the EW direction the response of the model with the subdivision "Scheme C" laid in between the responses of the other two models. When the WCM was analysed for a displacement in the diagonal direction towards Position F the model with the subdivision "Scheme C" resulted in slightly smaller moments than the other two models because the missing corner piece caused a small reduction of the lever arm. This became less significant for larger displacements when the other two models lost part of their cover concrete at the corner.

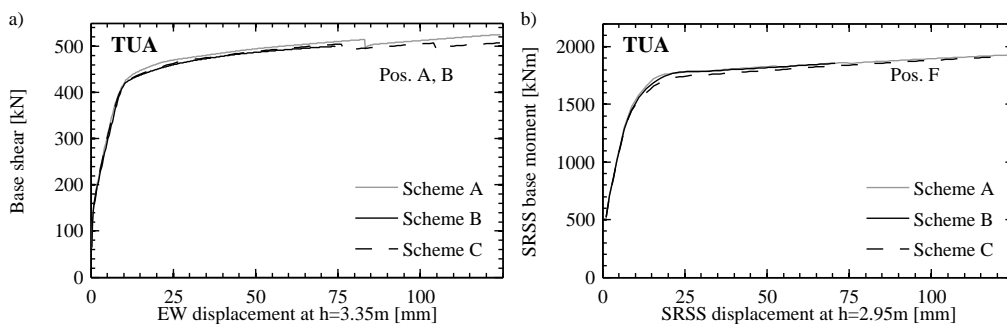


Figure 6.14. TUA: Influence of the subdivision of the section on the pushover curves in the EW direction (a) and in the Direction F (b).

Figure 6.15 displays selected results for the three models when analysed for the entire loading history to which TUA was subjected. As examples, the hysteresis curves for displacements in the diagonal direction (plot a) and the force applied by the NS-W actuator during the cycles at $\mu_{\Delta} = 4.0$ were selected. Out of the six graphs which were shown in Figure 6.11 the results displayed in these two plots proved to be the most sensitive to the modelling assumptions. The comparison of the three models with respect of their cyclic response showed that – as for the uni-directional loading – the differences were fairly small between the three models. The model "Scheme C" led again in most cases to moments or forces that were in between those of the other two models. Hence, this subdivision scheme seems suitable if the WCM is analysed for different directions of loading.

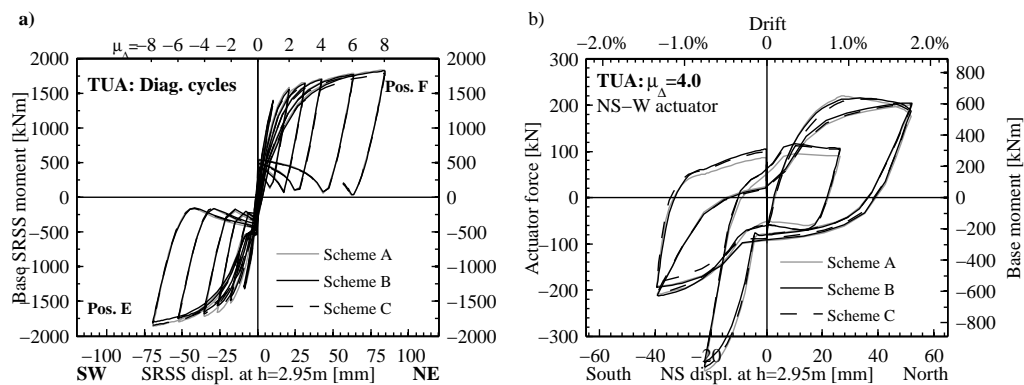


Figure 6.15. TUA: Influence of the subdivision of the section on the hysteresis curves for the diagonal cycles (a) and the force of the NS-W actuator for cycles with $\mu_{\Delta} = 4.0$ (b).

b) Spacing of the horizontal links.

The horizontal links connect the vertical elements, which represent the planar wall sections. When a WCM is setup, it is common practice to set the link spacing equal to the storey height (e.g. Xenidis and Avramidis [1999]). From a modelling point of view a larger link spacing is preferable since it reduces the number of elements in the model. However, the spacing of the links directly influences the behaviour of the WCM in two respects: First, at the location of the links compatibility of the axial elongation and the rotation of the wall elements representing different wall sections is enforced. Second, it was shown in Section 2.3.3 that the spacing of the horizontal link also influences the parasitic bending moments which occur as a consequence of the transmission of shear forces from the links to the wall elements. The larger the spacing of the links the larger the parasitic bending moments introduced into the wall elements. Stafford-Smith and Girgis [1986] suggested to limit the link spacing to one fifth of the overall wall height in order to control the deformations due to parasitic bending moments.

The objective of this section is to investigate the effect of the link spacing on the general behaviour of WCMs with inelastic properties. For this purpose three WCMs of TUA with different link spacings were built. The first model had a link spacing of 1360mm, which corresponded at full scale to 2720mm, i.e. 80% of the storey height of the reference building for TUA and TUB. This model served as a proxy for WCMs with link spacings equal to the storey height. In the second model the link spacing was reduced to 680mm, which corresponded roughly to the one fifth of the wall height suggested by Stafford-Smith and Girgis [1986], and in the third to 453mm. Figure 6.16 shows the element layout of the three WCMs.

As a first example, the behaviour of the WCMs for loading in the EW direction is compared (Positions A and B). Figure 6.17a shows the pushover curves for the three models. Before the onset of yielding the stiffness of the model is larger for smaller links spacings. The difference is caused by the parasitic bending moments, which reduce the stiffness of the WCM. With increasing link spacing the parasitic bending moments and also the deformations due to these moments increase. The difference between the three models is, however, relatively small and it seems irrelevant for seismic engineering concerns for which the elastic stiffness of a system responding in the inelastic range is normally not of great importance.

The moment capacities of the three models were fairly similar. Differences can be partly attributed to different heights of the first integration points above the base and different strains and hence stresses at this point (in particular due to the post-yield stiffness of the reinforcing steel). The three models were built with displacement-based elements with two integration points per element. Between two successive links (or the base and the first link) each wall section was represented by two elements. The elements were integrated using the integration

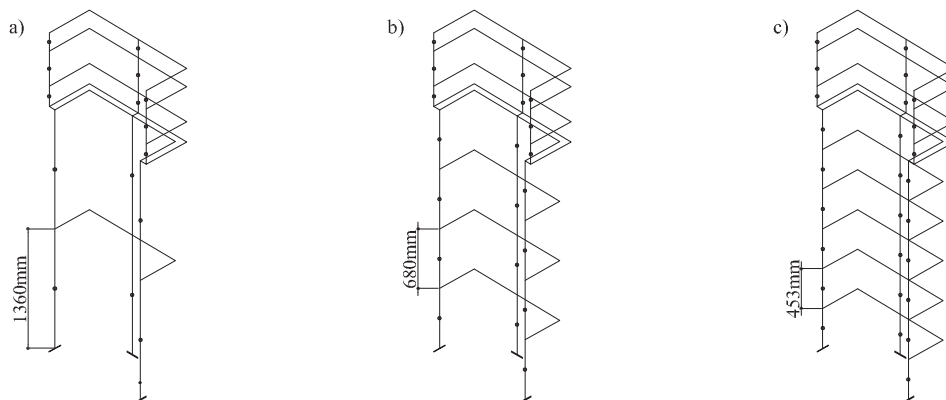


Figure 6.16. TUA: Wide-column models with link spacings of 1360mm (a), 680mm(b) and 453mm (c).

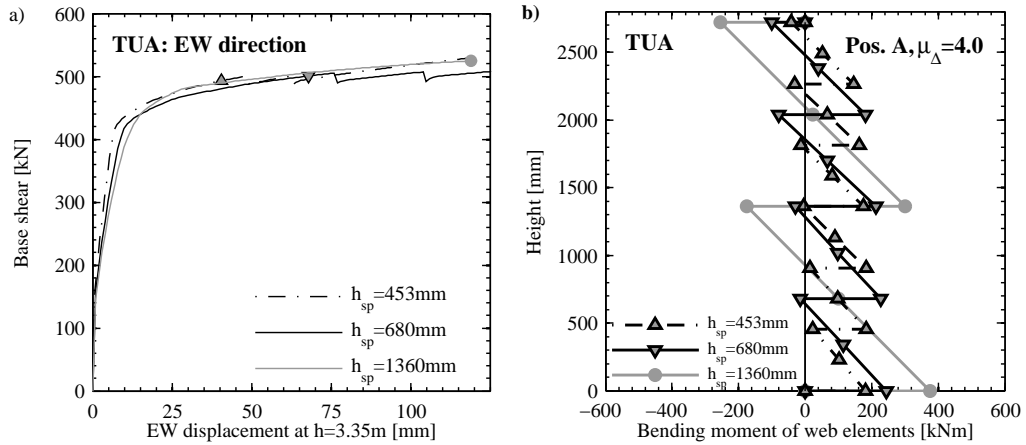


Figure 6.17. TUA: Influence of the spacing of the horizontal links on the pushover curves (a) and the moment distribution (b); as an example the pushover curves for loading in the EW direction (Positions A and B) and the moments in the web at Position A at $\mu_{\Delta} = 4.0$ are plotted.

rule by Gauss-Legendre. The first integration point above the base was hence at $h = 143mm$, $h = 71mm$ and $h = 48mm$ for the model with $h_{sp} = 1360mm$, $h_{sp} = 680mm$ and $h_{sp} = 453mm$, respectively. The fact that the lowest integration point is at a certain distance to the wall base reduces the effective lever arm. The effective lever arm was hence smallest for the model with the largest link spacing and hence the base shear capacity of this model tends to be slightly larger.

The element length also affected the strain distribution over the height of the model. The ultimate displacements derived from the tensile strain limit $0.5\varepsilon_{su}$ in the outermost steel fibre are included as small marks along the pushover curves in Figure 6.17a. The derived displacements are very different for the three models. The dependence of the fibre strains on the element length is a general shortcoming of inelastic beam elements and applies to both displacement-based and force-based elements [Coleman and Spacone, 2001]. Without adaption of the strains to account for the element length, the strains extracted at the integration points of the beams are basically meaningless to the engineer and should not be used for determining displacement limits.

Figure 6.17b shows the bending moments of the wall elements representing the web at Position A. These moments are plotted to illustrate the effect of the link spacings on the moment distribution over the height. The horizontal jumps in the moment profile were caused by the parasitic bending moments that were introduced by the horizontal links. The comparison of

the three curves confirm that the larger the link spacing the larger the parasitic bending moments. If the jagged appearance of the moment profiles is smoothed out the moment profiles of the three models are very similar. Hence, the parasitic bending moments affect the moments at the locations where the wall elements are connected to the links but at mid-height between the links they are fairly independent of the link spacing. This observation does not quite hold near the base where the elements yield.

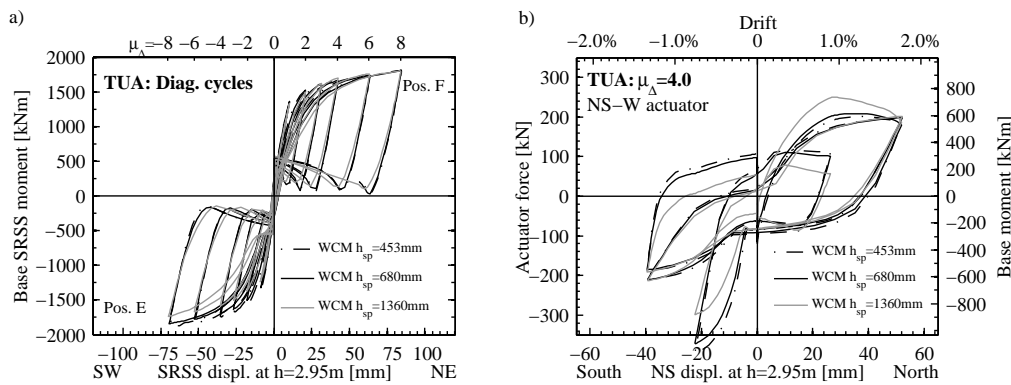


Figure 6.18. TUA: Influence of the spacing of the horizontal links on the hysterese curves for the diagonal cycles (a) and the force of the NS-W actuator for cycles with $\mu_{\Delta} = 4.0$ (b).

For uni-directional loading it was shown that the difference in stiffness and strength between the three models is relatively small; for cyclic loading, however, the difference between the three models was more predominant. Figure 6.18 shows selected results for the three WCMs when analysed for the entire loading history to which TUA was subjected. As an example the hysteresis curves for displacements in the diagonal direction (plot a) and the actuator force during the cycles of ductility (plot b) are shown. While there was a relatively large difference in the hysteresis curves for the WCMs with $h_{sp} = 1360\text{mm}$ and $h_{sp} = 680\text{mm}$, the difference between the WCMs with $h_{sp} = 680\text{mm}$ and $h_{sp} = 453\text{mm}$ was significantly smaller. For the following analyses the model with $h_{sp} = 680\text{mm}$ was chosen because it combines the merits of few elements with a good accuracy (using the WCM with the smallest link spacing $h_{sp} = 453\text{mm}$ as a benchmark). As shown before, the link spacing of 680mm is only slightly larger than one fifth of the wall height, which is the criteria suggested by Stafford-Smith and Girgis [1986]. For TUA and TUB it also corresponds to about 50% of the longer wall length ($l_{web} = 1300\text{mm}$). For elastic homogenous elements the wall length was – next to the link spacing – the second geometric parameter that affected the apparent shear flexibility due to the parasitic bending moments (see Equation 2.19). It is suggested that both dimensions of the wall, i.e. the wall height and the wall length, should be considered when selecting a link spacing.

c) Number of elements between links.

Once the spacing of the links has been decided on, the engineer needs to select the number of elements between the horizontal links. In the simplest solution two horizontal links would be connected with one vertical element for each wall section. However, if displacement-based elements are used – which are the standard type elements in most element libraries – this is not appropriate. Most commonly, cubic Hermitian interpolation functions are used as shape functions for displacement-based beams. For these elements the curvature is linear along beam elements (note that the curvature is not continuous across nodes). If the curvature variation along one element varies strongly nonlinearly those elements lead to wrong solutions. This is illustrated using the example of the WCM for TUA. In the reference model, nodes at intermediate heights between the links were introduced and the vertical element length was hence $l_{el} = h_{sp}/2$. Results from the reference model are compared with the results of WCMs with $l_{el} = h_{sp}$ (one element between consecutive links) and $l_{el} = h_{sp}/3$ (three elements between consecutive links).

Figures 6.19a and b show the pushover curves and the moment distribution in the web for TUA for cycles in the EW direction for a horizontal link spacing of $h_{sp} = 680\text{mm}$. The different curves represent models with one, two and three elements between the horizontal links. The moment capacity for one displacement-based element was significantly greater than for two or three elements whereas the difference between models with two and three displacement-based elements between links was relatively small. Also included in the figure are the results of the analysis of a model with force-based elements (dashed line). Force-based elements are elements where the interpolation functions describe the force-distribution along the element; based on the stress state the flexibility matrix is derived and the element deformations computed [Taucer *et al.*, 1991]. For the model with force-based elements one element between horizontal links was sufficient since force-based elements are capable of reflecting the nonlinear strain distribution along the element. Comparing the results of the force-based elements to the displacement-based elements shows that the difference between the two types is smallest if at least two elements between links were used for the model with displacement-based elements. It is not clear what caused the difference between the displacement-based models with two or three elements between links and the force-based model. For a link spacing of $h = 1360\text{mm}$, for example, these two types of model yielded approximately the same results regarding the pushover curves. The small markers in Figure 6.19a illustrate again the displacement capacities determined from the strains at the first integration point above the wall base. The significant differences between the models underline the finding from the previous section that in its original form, the strains measured at the integration points are hardly

suitable for determining the displacement capacity of the wall since they are strongly dependent on the element formulation and the element length. The sensitivity of the cyclic analysis results to the number of elements was not larger than for monotonic results (Figure 6.20).

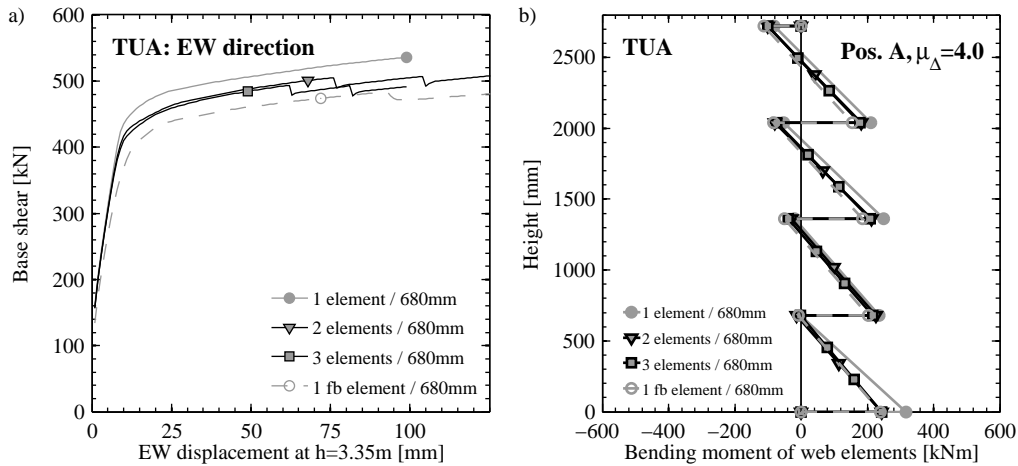


Figure 6.19. TUA, $h_{sp} = 680\text{mm}$: Influence of the number of elements between horizontal links on the pushover curves (a) and the moment distribution (b); as an example the pushover curves for loading in the EW direction (Positions A and B) and the moments in the web at Position A at $\mu_{\Delta} = 4.0$ are plotted (fb=force-based element formulation).

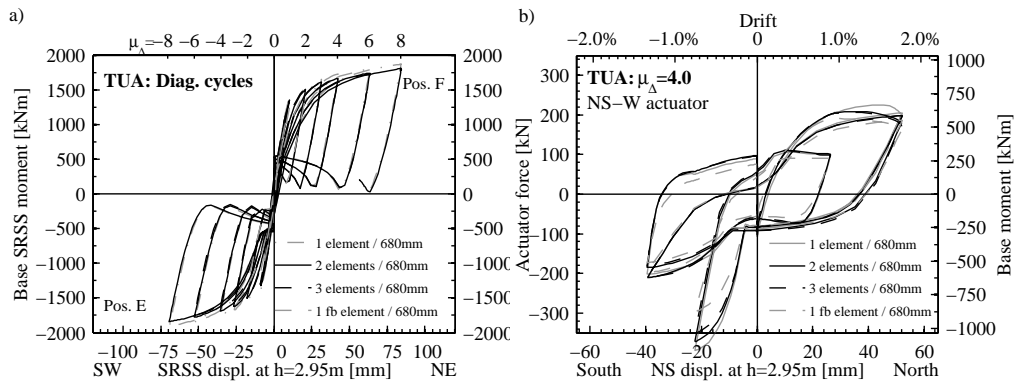


Figure 6.20. TUA: Influence of the number of elements between horizontal links on the hysteresis curves for the diagonal cycles (a) and the force of the NS-W actuator for cycles with $\mu_{\Delta} = 4.0$ (b).

It is therefore suggested, either to use force-based elements and connect the horizontal links with a single continuous element or to use two displacement-based elements instead and add an additional node at midheight between the links. Hence, the number of degrees of freedoms of

the model with displacement-based elements is larger than the number of degrees of freedoms of a model with force-based elements. However, the solution algorithm for the force-based elements is considerably more elaborate than the solution algorithm for the displacement-based elements and it is therefore often quite difficult to achieve convergence of models with force-based elements. In addition, most common engineering softwares do not offer the choice between different nonlinear beam elements but have only the displacement-based element implemented. Hence, in most engineering studies a WCM with two displacement-based elements between consecutive links ($l_{el} = h_{sp}/2$) will be most suitable.

6.2.3 Shear and torsional stiffness of wall elements

In this part of this study the sensitivity of the analysis results to the in-plane and out-of-plane shear stiffness and the torsional stiffness of the wall elements is examined. The axial and flexural properties of the vertical elements were defined by means of fibre sections since this is the most suitable method for modelling the interaction of the axial and the flexural capacities of RC members. The remaining flexibilities, i.e. the in- and out-of-plane shear flexibility and the torsional flexibility, are decoupled from the axial and flexural properties. In most structural analysis programs the shear and torsional stiffness of beam elements are constant and cannot be assigned nonlinear and inelastic properties. The focus of this section is therefore on the choice of appropriate equivalent elastic stiffness estimates.

a) Equivalent elastic shear stiffness of wall sections undergoing inelastic flexural displacements.

In the reference WCMs of TUA and TUB with state-of-the-art properties the shear stiffness of the web and flanges was based on the properties of a homogenous, elastic section. Though this is still a common modelling assumption it is certainly too stiff if a cracked RC section is considered. It has been shown in previous chapters (Section 2.6, Chapter 5) that the shear stiffness of a RC wall is not constant but reduces simultaneously to the flexural stiffness. Moreover, the shear stiffness also varies with the axial load level on the wall section. Ideally, one would therefore update the shear stiffness of the web and flanges of a U-shaped wall over the course of an analysis as a function of the axial load on the wall section and of the peak lateral displacements. In most structural analysis programs – including the program Opensees – it is, however, at present not possible to update the element properties during the analysis. The engineer therefore faces the difficulty of selecting a single shear stiffness that best represents the shear stiffness over the entire loading history.

If the ratio of shear to flexural displacements Δ_s/Δ_f of a wall section is known or can at least be estimated the shear displacements at the ductility level μ_Δ can be computed as follows:

$$\alpha = \frac{\Delta_s}{\Delta_f} \rightarrow \Delta_s = \Delta_{top} \cdot \frac{\alpha}{1 + \alpha} \text{ with } \Delta_{top} = \mu_{\Delta} \cdot \Delta_y \quad (6.6)$$

During the experiment only the actuator forces were measured whereas the base shear forces could not be measured. However, it seems reasonable to assume that for most directions of loading the proportion of the lateral load which is carried as out-of-plane shear force was relatively small. Hence the base shear forces of the wall sections can in a first approximation be estimated as the actuator forces applied to the particular wall sections. To be explicit, the base shear force of the web can be estimated as the EW actuator force, the base shear of the West and East flange as the NS-W and NS-E actuators respectively. If the shear force F_n acting on the section is known, the shear stiffness k_s can then be simply computed as:

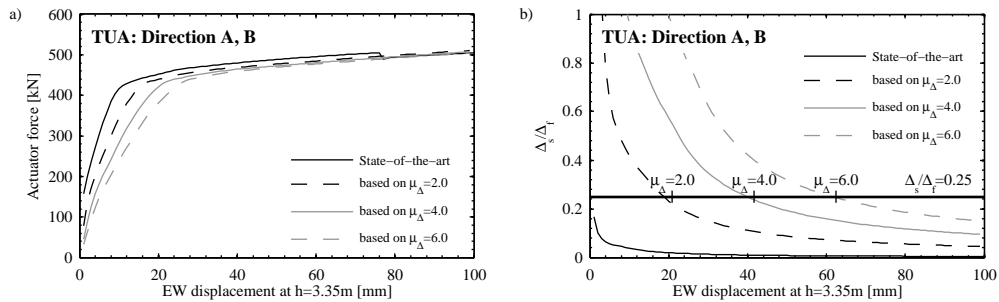
$$k_s = \frac{F_n}{\Delta_s} \quad (6.7)$$

To exclude the uncertainty associated with the prediction of the ratio Δ_s/Δ_f the shear stiffnesses k_s were at first computed for the experimentally determined ratios Δ_s/Δ_f , which were summarised in Table 4.5 (Δ_{s2}/Δ_f). At a later stage (Section 6.2.5), when recommendations on the modelling of U-shaped walls have been formulated, the analyses are rerun using stiffness estimates that were obtained from the empirical equation derived in Chapter 5 (Equation 5.9). Table 6.7 summarises the equivalent elastic shear stiffnesses of the test units for different ductilities and the corresponding ratio of the gross shear stiffness based on $0.8A_gG_c$. The given shear stiffness values are global stiffnesses of the test units, i.e. the ratio of total base shear in either the EW or NS direction divided by the top displacement.

Figure 6.21a illustrates for TUA the difference in shear deformation if the shear stiffness is computed for $\mu_{\Delta} = 2.0, 4.0$ and 6.0 . The smaller the shear stiffness (i.e. the larger the displacement ductility for which the equivalent elastic shear stiffness was computed), the smaller the total stiffness of the wall. The lateral force capacity of the model is not affected by the shear stiffness of the wall sections. Since the shear stiffness is set constant, the ratio of shear to flexural displacements varies during the analysis. This is shown in Figure 6.21b, which displays the variation of the Δ_s/Δ_f -ratios as a function of the top displacement. Also included in the figure are the couples of top displacements and Δ_s/Δ_f -ratios for which the equivalent stiffnesses were computed. The black horizontal line in Figure 6.21b represents the average experimentally determined ratio $\Delta_s/\Delta_f = 0.25$, which was approximately constant over the tested ductility range. In the following the equivalent elastic shear stiffness for TUA and TUB will be computed as equivalent elastic stiffnesses for $\mu_{\Delta} = 4.0$ since $\mu_{\Delta} = 4.0$ lies approximately in the middle of the imposed ductilities on TUA and TUB; for TUA and TUB the maximum imposed displacement ductilities were $\mu_{\Delta} = 8.0$ and $\mu_{\Delta} = 6.0$, respectively.

Table 6.7. Equivalent elastic shear stiffnesses of TUA and TUB in the EW and NS directions for different ductilities levels.

	$\mu_{\Delta} = 2.0$		$\mu_{\Delta} = 4.0$		$\mu_{\Delta} = 6.0$	
	$K_{s,\mu_{\Delta}=2.0}$ [kN/mm]	$\frac{K_{s,\mu_{\Delta}=2.0}}{K_{s,g}}$ [-]	$K_{s,\mu_{\Delta}=4.0}$ [kN/mm]	$\frac{K_{s,\mu_{\Delta}=4.0}}{K_{s,g}}$ [-]	$K_{s,\mu_{\Delta}=6.0}$ [kN/mm]	$\frac{K_{s,\mu_{\Delta}=6.0}}{K_{s,g}}$ [-]
TUA						
Pos. A, B (EW)	110	0.12	55	0.06	37	0.04
Pos. C (NS)	175	0.11	88	0.06	58	0.04
Pos. D (NS)	97	0.06	49	0.03	32	0.02
Mean C, D (NS)	136	0.09	68	0.04	45	0.03
TUB						
Pos. A, B (EW)	59	0.11	30	0.05	20	0.04
Pos. C (NS)	99	0.11	50	0.06	33	0.04
Pos. D (NS)	59	0.07	29	0.03	20	0.02
Mean C, D (NS)	79	0.09	40	0.04	26	0.03

**Figure 6.21.** TUA, Direction A, B: WCMs with different shear stiffnesses (stiffness of uncracked section and equivalent linear-elastic stiffnesses for different ductility levels); pushover curves in the EW direction (a) and ratio of shear to flexural displacements (b).

When loading to Position E the shear stiffnesses of the two flanges was very different (Table 4.5). The East flange, which was under tension, had a very small shear stiffness while the West flange, whose flange end was in compression, was fairly stiff. The stiffness of the East flange could not be computed from the experimental results since its experimentally determined ratio of Δ_s/Δ_f was negative; it was therefore arbitrarily assumed that the stiffness of the East flange was one tenth of the stiffness of the West flange. Figure 6.22a shows the effect of the unequal and reduced shear stiffnesses on the pushover curve for diagonal displacements towards Position E. As for loading in the EW direction the reduced shear stiffness affected mainly the loading stiffness whereas the moment capacity remained the same. The line with markers in the plots shows the SRSS moments at Positions E, which were attained during the

test at the different ductility levels. The greatest difference between the two WCMs is, however, noticed when the individual actuator forces are compared: Figure 6.22b shows the three actuator forces for the two models as well as the actuator forces attained at Positions E during the experiment. While in the reference WCM with state-of-the-art properties the stiffnesses of the two flanges were the same they were different in the model with cracked section properties. This caused a reduction of the force couple required to restrain the wall from rotating since the shear centre moved towards the stiffer West flange. As a consequence, the signs of the West and East NS actuators were the same which reflects the observations during the test. The figure also confirms that the difference between the experimentally attained moments at Position E and the pushover curve in the diagonal direction are mainly caused by a difference in the shear force in the web (Section 6.1.3).

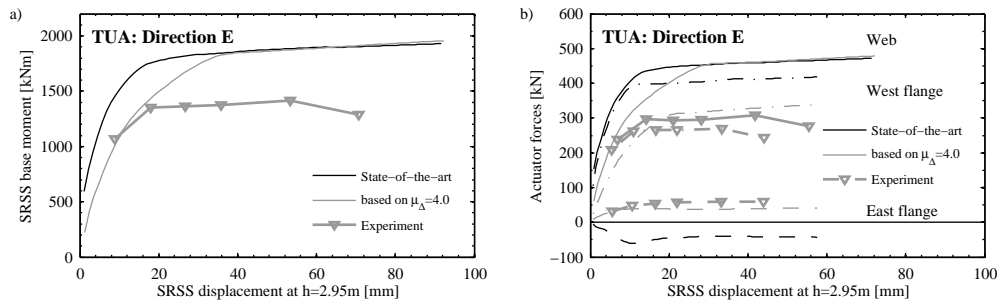


Figure 6.22. TUA, Direction E: WCMs with different shear stiffnesses (stiffness of uncracked section and equivalent linear-elastic stiffnesses for $\mu_{\Delta} = 4.0$); pushover curves for displacement in the diagonal direction towards Position E (a) and actuator forces (b).

By means of the examples of pushover analyses for the Directions A and E it was shown that the shear stiffness assigned to the web and flange elements affected the stiffness of the total system as well as the distribution of the base shear between the two flanges; the ultimate moment capacity for uni-directional loading of the system was not affected by the shear stiffnesses of the wall section. In a next step the effect of the shear stiffness on the cyclic behaviour is examined. When analysing the wall with a bi-directional loading history, the approximate nature of the equivalent elastic shear stiffnesses is even stronger since a constant stiffness cannot account for the variation of stiffness with the direction of loading. Hence in addition to the previously discussed short-coming that a constant shear stiffness cannot reflect the decreasing shear stiffness with increasing flexural displacements which was observed from the experiments a further approximation has to be introduced by neglecting the dependence of the shear stiffness on the direction of loading. It was found that estimating the equivalent elastic shear stiffness of the web and the flanges from the Δ_s/Δ_f -ratios obtained for the principal directions of loading yielded the best results. That means that for the web the shear stiffness was computed from

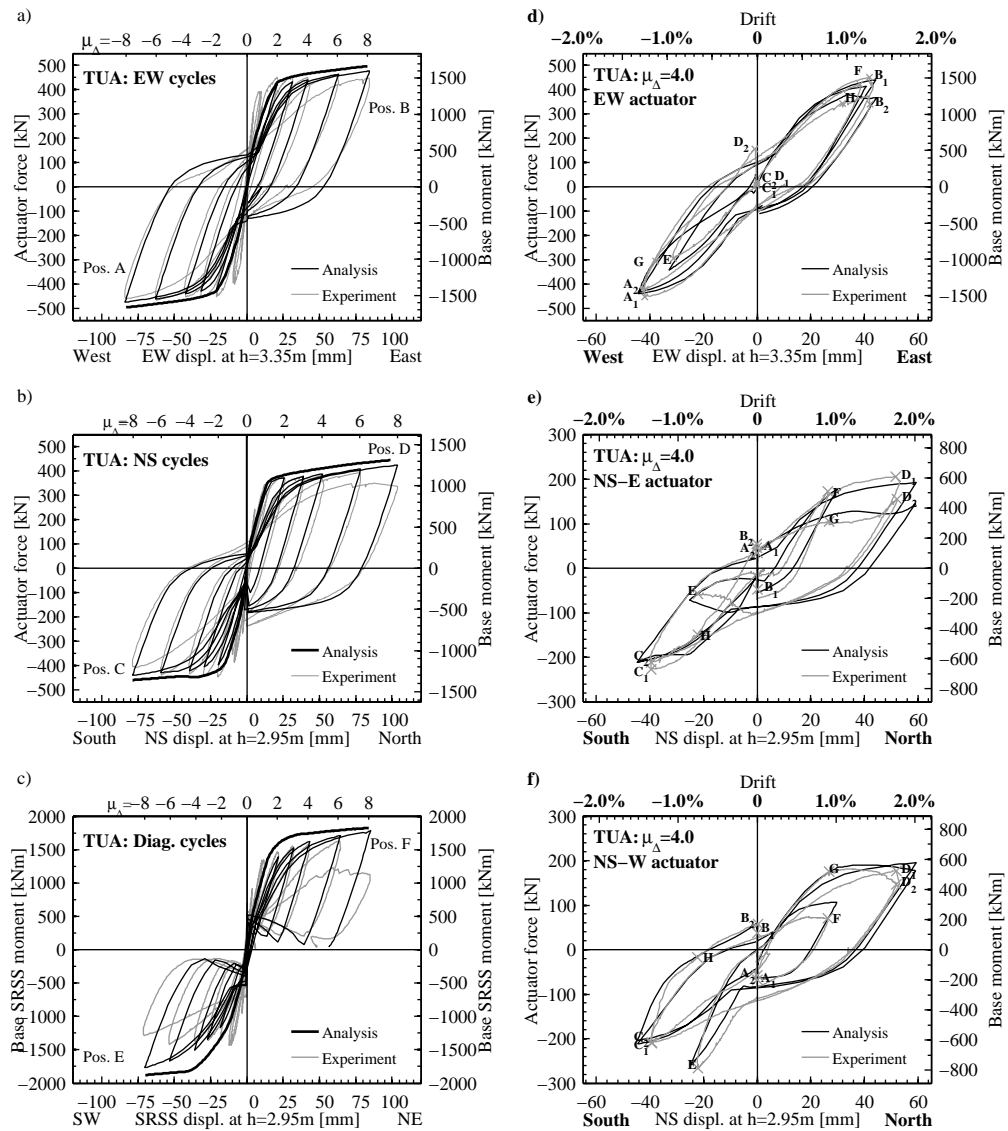


Figure 6.23. TUA, WCM with improved shear stiffness of wall elements: Comparison of analysis and experimental results for cycles in the EW, NS and diagonal directions (a-c); comparison of actuator forces obtained from analysis and experiment during the cycles at $\mu_{\Delta} = 4.0$ (d-f).

the Δ_s/Δ_f -ratio at Positions A and B while the shear stiffness of the flanges was computed as average of the shear stiffness corresponding to the Δ_s/Δ_f -ratios at Positions C and D. All other properties of the model correspond to those of the reference WCM. Figure 6.23 shows the hystereses of TUA for displacements in the EW, NS and diagonal directions (plots a-c) and the actuator forces during the cycles of ductility level 4.0. The same plots but for the reference model with state-of-the-art properties were shown in Figure 6.11. Comparing the figures for the different WCMs shows that replacing the shear stiffness representing uncracked sections by shear stiffnesses representing cracked sections at $\mu_\Delta = 4.0$ improves the match between the numerical and experimental results significantly. It is, however, important to note that assuming a constant equivalent elastic stiffness which was computed for $\mu_\Delta = 4.0$ overestimated the shear deformations at small displacements considerably; as a consequence the stiffness of the test unit for small displacements was significantly underestimated. The contrary was the case for displacements with $\mu_\Delta > 4.0$: For these displacement demands the shear stiffness – and therefore also the total stiffness – of the test unit was overestimated.

b) Distribution of shear stiffnesses over the height.

So far the shear stiffness of the wall elements was modelled as constant over the height (with exception of the collar elements, which in all WCMs were assigned shear stiffnesses based on uncracked section properties). In the experiments, however, the shear deformations were unequally distributed over the wall height: most of the shear deformation took place in the zone undergoing plastic deformation. About 65 – 85% of the shear deformations at peak displacements occurred in the lowest of the three panels ($h = 50 - 850\text{mm}$) over which the shear deformations were measured while the shear deformations within the upper two panels were fairly small (see Section 3.3). In order to investigate the sensitivity of the analysis results to the assumptions on the distribution of the shear stiffness over the height of the wall the WCM of TUA is modified such that 50% of the shear flexibility was assigned to the elements below the first horizontal link ($h = 0 - 680\text{mm}$) and 50% to the elements above ($h = 680 - 2720\text{mm}$); the shear deformations of the collar are negligible. Figure 6.24 shows as an example the hysteresis loops in the diagonal direction and the NS-W actuator force at $\mu_\Delta = 4.0$. The difference between the results for the two WCMs is extremely small and can be neglected for engineering purposes because the relative stiffnesses of flanges and web were the same for the two models. Note that, although the distribution of the shear stiffness was not an important parameter for the analyses conducted here, a reasonable distribution should be chosen when the WCM of a U-shaped wall is part of a larger model representing an entire building. Forces due to interaction with other structural elements might be sensitive to the shear stiffness distribution over the height of the wall.

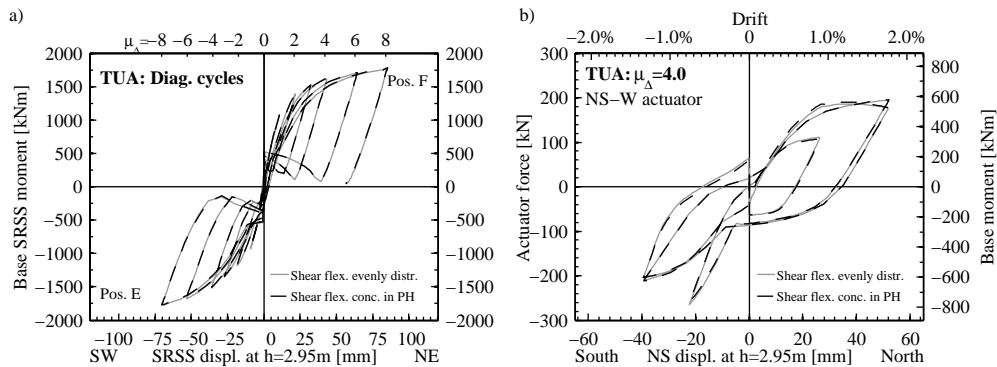


Figure 6.24. TUA: Influence of the distribution of the shear flexibility over the wall height (shear flexibility evenly distributed between $h = 0 - 2.72\text{m}$ and shear flexibility concentrated in the plastic hinge zone) on the hysteresis curves for the diagonal cycles (a) and the force in the NS-W actuator for cycles with $\mu_{\Delta} = 4.0$.

c) Out-of-plane shear stiffnesses.

In the state-of-the-art model, the in-plane and out-of-plane shear stiffnesses of the wall sections (web and flanges) were of the same magnitude whereas for the updated model with cracked section properties the out-of-plane shear stiffness of the wall sections was assumed as small and was modelled as one percent of the in-plane stiffness of the wall section. Both assumptions represent extreme situations. The actual out-of-plane stiffness of cracked wall sections cannot be determined from experimental results since out-of-plane deformations were not measured during the testing. Moreover, the portion of the forces carried as out-of-plane forces by the different wall sections could also not be determined from the experimental results since the only forces measured during the testing were the actuator forces. Hence, making some relatively arbitrary assumptions regarding the out-of-plane shear stiffness of the wall elements seems inevitable.

For design purposes, it is recommended to set the out-of-plane shear stiffness to zero (or a very low value). Out-of-plane shear forces are typically not accounted for in design; setting the out-of-plane shear stiffness to zero ensures that all lateral forces are carried as in-plane shear forces and are therefore considered in the design process. For assessment purposes or the modelling of experiments more realistic assumptions could be required if the results proved sensitive to these assumptions. Based on the observations during testing it is assumed that out-of-plane forces played a role in the load transfer mechanism of TUA and TUB. For example, when loading to Position E or H, only the flange end was in compression. Apart from the shear forces that were transmitted by concrete interlocking and dowel action along the open part of

the base crack, the shear forces had to be transmitted in the compression zone from the wall to the foundation. As a consequence, some portion of the shear force component parallel to the web was probably transmitted as out-of-plane shear force in the flange in compression.

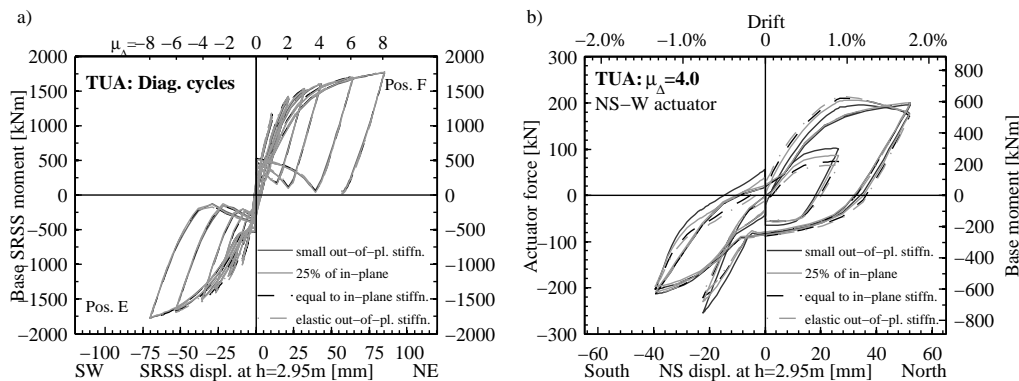


Figure 6.25. TUA: Influence of the out-of-plane shear stiffness of the wall elements on the hysterese curves for the diagonal cycles (a) and the force of the NS-W actuator for cycles with $\mu_{\Delta} = 4.0$ (b).

Figure 6.25 shows the sensitivity of the cyclic response to the out-of-plane stiffness of wall elements. The WCM of TUA was analysed for four different values of out-of-plane shear stiffnesses: In the first case, the out-of-plane stiffnesses were very small (i.e. 1% of the in-plane stiffness). In the second case, the out-of-plane stiffnesses of the wall elements were reduced to 25% of the in-plane stiffnesses to account for cracking of the wall. In the third case, the out-of-plane and the in-plane shear stiffnesses were equal and in the fourth case, the out-of-plane stiffnesses were much larger than the in-plane stiffness. In this case the out-of-plane stiffnesses were set to the elastic shear stiffnesses of the wall sections. For all four cases the in-plane and out-of-plane shear stiffness of the collar elements were based on the properties of an elastic, homogenous section since due to lateral prestress the collar remained largely uncracked. The in-plane stiffness of the wall elements was the equivalent elastic stiffness computed from the shear deformations in the principal directions at $\mu_{\Delta} = 4.0$. Figure 6.25a and b show selected results of the cyclic analyses of the three models with different out-of-plane stiffnesses. The results showed that varying the out-of-plane stiffness had almost no effect on the global hysteretic response (Figure 6.25a) and the effect on the force distribution between the NS-W and NS-E actuator was relatively small (Figure 6.25b). There was little difference between case two (out-of-plane stiffnesses were 25% of the in-plane stiffnesses) to four (out-of-plane stiffnesses were set to the elastic shear stiffnesses). It is believed that in these cases the maximum shear forces that could be carried as out-of-plane shear forces were limited by the out-of-plane bending capacity of the wall. The out-of-plane bending capacity was accounted for in the fibre

sections, which had in-plane and out-of-plane dimensions. In the first case, for which the out-of-plane shear stiffnesses were very small, the out-of-plane bending capacity of the wall could probably not be reached because the wall sections were too soft in out-of-plane shear. Among the investigated cases approximating the out-of-plane shear stiffness as 25% of the in-plane shear stiffness seems most reasonable and hence this estimate will be used for the following calculations.

To conclude, for design purposes it was argued that it is most likely on the safe side to neglect any out-of-plane stiffness of the wall elements. In this way, all shear forces are transmitted as in-plane shear forces in the model and will therefore be considered in the design of the wall sections. For assessment purposes, out-of-plane shear stiffnesses might be included in the model although it was shown that it had almost no effect on the global hysterese. Only the internal force distribution was affected. It could also be shown that the magnitude of the out-of-plane shear stiffness was of secondary importance since the out-of-plane shear forces were limited by the out-of-plane bending capacity of the wall section and are therefore always relatively small.

d) Torsional flexibility of wall elements.

During the experiment the wall head was restraint from rotating. Only at Positions O, A, B, C and D during the cycles with $\mu_{\Delta} = 1.0$ and 4.0 a small rotation was applied to the wall head in order to determine the rotational stiffness of the wall (see Section 3.3). These rotations, however, were not included in the previous WCM analyses since the torsional stiffness of the walls will be the topic of a future study (the limits to the scope of the study presented here were described in Section 1.2).

Figure 6.26 shows the comparison of the hysterese curves for the diagonal direction (plot a) and the force in the NS-W actuator for wall sections with rotational stiffnesses of uncracked sections and for wall sections with reduced rotational stiffnesses to account for the effect of cracking. For TUA the ratio of the rotational stiffness of the cracked to the uncracked section was estimated as 2.5%, which corresponds approximately to the ratio of the shear stiffnesses of the cracked to the uncracked section (the shear stiffness of the cracked section was based on the shear deformations in the principal directions at $\mu_{\Delta} = 4.0$). The plots show that the results of analyses for which the wall head is restraint from twisting are not sensitive to the torsional stiffness of the wall elements.

The torsional stiffness of the vertical elements becomes, however, more important if the wall is also subjected to rotation instead of pure translational movements. To demonstrate the effect a pushover analysis in the Direction D was carried out until a top displacement of $\Delta_{top} =$

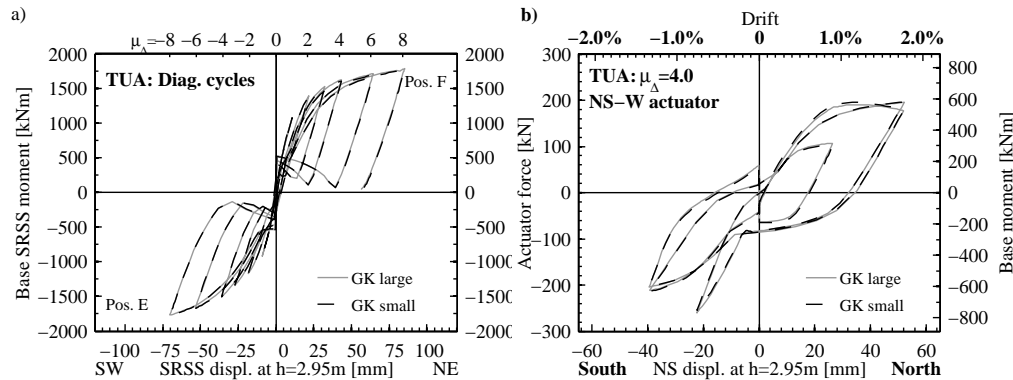


Figure 6.26. TUA: Influence of the torsional stiffness of the wall and collar elements on the hysteresis curves for the diagonal cycles (a) and the force of the NS-W actuator for cycles with $\mu_{\Delta} = 4.0$ (b). The term "large GK" refers to the torsional stiffness of uncracked, homogenous sections and "small GK" refers to the rotational stiffness of cracked sections (as an approximation the torsional stiffness was reduced by the same ratio as the shear stiffness).

52mm ($\mu_{\Delta} = 4.0$) was reached. The wall head was then subjected to a torsional moment of $\pm 100 \text{ kNm}^3$. Figure 6.27a shows the resulting actuator forces NS-W and NS-E for the two WCMs with different rotational stiffnesses of the vertical elements. In Figure 6.27b the applied torsional moment is plotted against the wall head rotation. Reducing the torsional stiffnesses of the wall elements to 2.5% of their original values reduced the torsional stiffness of the WCM to about 30% of the original stiffness. If the WCM is subjected to a load history involving torsion it is hence necessary to develop appropriate estimates of the torsional stiffness of wall elements and to test the sensitivity of the analysis results to the assumptions made. Note that the results shown here are only the results of a preliminary investigation into the modelling of the rotational stiffness of U-shaped walls, the results have not yet been validated against experimental data for the rotational stiffness, which has been gathered during the experimental testing of TUA and TUB.

6.2.4 Link properties

The reference models of TUA and TUB featured links that were rigid for all sectional forces but for torsion. The torsional stiffness of the links was computed based on thin-walled section theory according to Equation 2.19. In this section the sensitivity of the analysis results to the torsional and to the shear stiffness of the links is discussed.

³Note that during the experimental testing at $\mu_{\Delta} = 4.0$ the test unit was subjected to a smaller torsional moment. The torsional moment of $\pm 100 \text{ kNm}$ was used for illustrational purposes in this analysis.

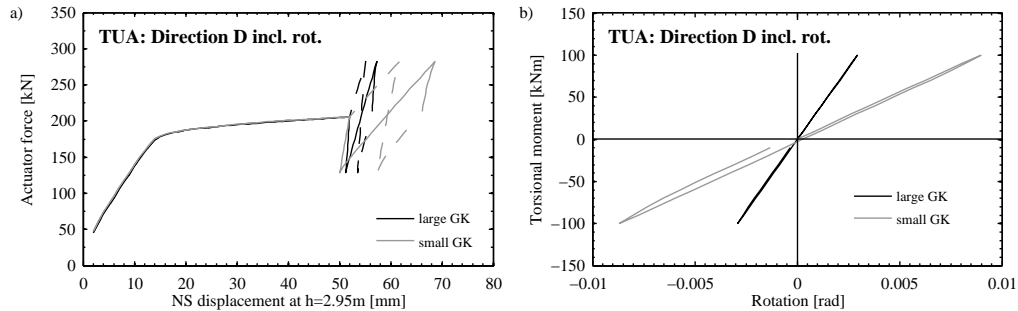


Figure 6.27. TUA: Influence of the torsional stiffness of the wall and collar elements on the actuator forces (a) and the torsional stiffness (b) when the WCM is first subjected to a translation in the Direction D and then to a rotation of the wall head.

a) Torsional stiffness of the links.

Up to now the links were modelled as rigid except for the torsional flexibility which was assigned the properties of an elastic, uncracked section (Equation 2.19, Section 6.2.1). The horizontal links were assigned this torsional flexibility in order to account for the warping of the section. Reynouard and Fardis [2001] stated that "in this way the beam elements are allowed to bend relatively independently of each other". To investigate the effect of the torsional stiffness of the links on the analysis results, five different models with decreasing stiffness were considered: In the first model (labelled as "rigid") the links were assumed to be rigid also in torsion. In the second model ("Avramidis") following the suggestion by Avramidis [1991] and Xenidis *et al.* [1993], only the web links were given a torsional flexibility corresponding to the stiffness of the elastic section (Equation 2.19) while the flange links were modelled as rigid. In the third model (" GK_{el} ") the link properties correspond to those of the reference model. In the fourth model (" $0.25GK_{el}$ ") the torsional stiffness of all wall links was reduced to account for the effect of cracking of the concrete and yielding of the longitudinal reinforcement on the warping stiffness of the U-shaped section. In the fifth model ("pinned") the torsional stiffness of all wall links was set to zero by introducing torsional pins at their ends. During the testing the collar remained elastic and largely uncracked, the stiffness of the collar links was hence not reduced. It is believed that this also reflects the situation in a real building in which the upper storeys remain largely uncracked. While the geometry of these five models is the same as for the reference model with state-of-the-art properties (Section 6.2.1), the shear properties of the vertical wall elements have been updated according to the recommendations formulated in the previous section (Section 6.2.3).

Figure 6.28a shows the effect of the torsional stiffness of the horizontal links on the pushover curves in the Direction E. While there was a significant difference between modelling the links as rigid and assigning them the flexibility of an elastic homogenous member, the difference

between the latter case and increased flexibility up to the pinned connection was relatively minor. This finding is confirmed when the actuator forces for the pushover analysis in the Direction E (Figure 6.28b) or cyclic analysis results (Figure 6.29) are considered. Figure 6.29a shows that the maximum reached capacity during the diagonal cycles was larger for the WCM with rigid links than for the WCMs with pinned or flexible links. Hence, assigning the links a rotational flexibility influences the loading and unloading stiffness of the U-shaped wall and as a consequence also the maximum reached capacity during the diagonal cycles.

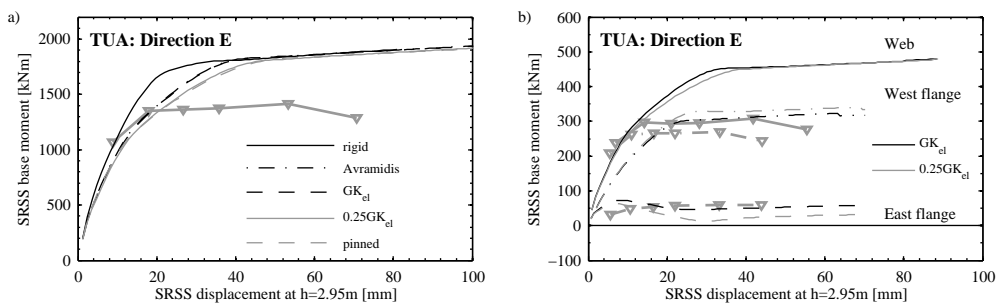


Figure 6.28. TUA, Direction E: WCMs with different torsional stiffnesses of the horizontal links: Pushover curves for displacement in the diagonal direction towards Position E (a) and actuator forces (b).

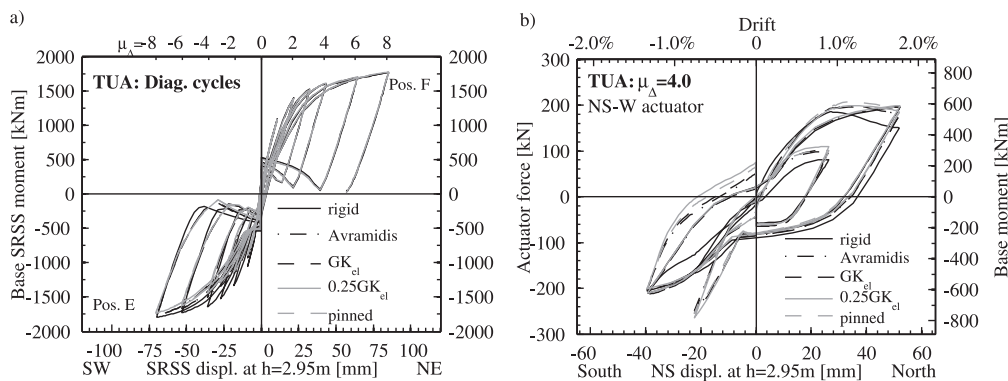


Figure 6.29. TUA: Influence of the torsional stiffnesses of the horizontal links on the hysteresis curves for the diagonal cycles (a) and the force of the NS-W actuator for cycles with $\mu_{\Delta} = 4.0$ (b).

b) Shear flexibility of the links.

In order to account for the shear deformations resulting from the vertical in-plane shear stresses transmitted from the web to one flange along the corners, the links were also assigned

an in-plane shear flexibility. This is normally not done in WCMs because of the strain compatibility issues discussed in the following. The shear flexibility of the wall links was estimated on the basis of the analogous truss model proposed by Park and Paulay [1975] assuming that the shear deformations concentrate in the regions with small diameter vertical reinforcement outside the boundary elements. Alternatively, the shear stiffness of the elastic, homogenous link section could be reduced by the same factor as the in-plane shear stiffness of the wall elements (for TUA and TUB at $\mu_{\Delta} = 4.0$ these two approaches yielded very similar results). The shear flexibility of the collar links was computed based on the properties of the elastic and uncracked gross concrete sections. As a consequence, these links were almost rigid in shear.

Figure 6.30 compares two models, one with links that are rigid in shear and one with links that are flexible in shear. The first model corresponds to the model "0.25GK_{el}" of the previous section while in the second model the links were also assigned a shear flexibility. The links were modelled as elastic beam elements which have – as the nonlinear displacement-based elements – only a torsional but no shear flexibility in Opensees. The shear flexibility of the links was hence modelled by zero-length spring elements that were placed at the corners and at the centres of the flange sections. The spring elements were assigned an elastic translational stiffness in the vertical direction; all other degrees of freedom of their two end nodes were slaved. The results in Figure 6.30a show that introducing a shear flexibility to the links brings the analysis results in terms of the hysteresis curve in the diagonal direction closer to the experimental results. The reduction in the moment capacity at Position E results mainly from a smaller EW shear force, the actuator force in the NS-W direction, for example, is hardly affected by the shear flexibility of the links (Figure 6.30b).

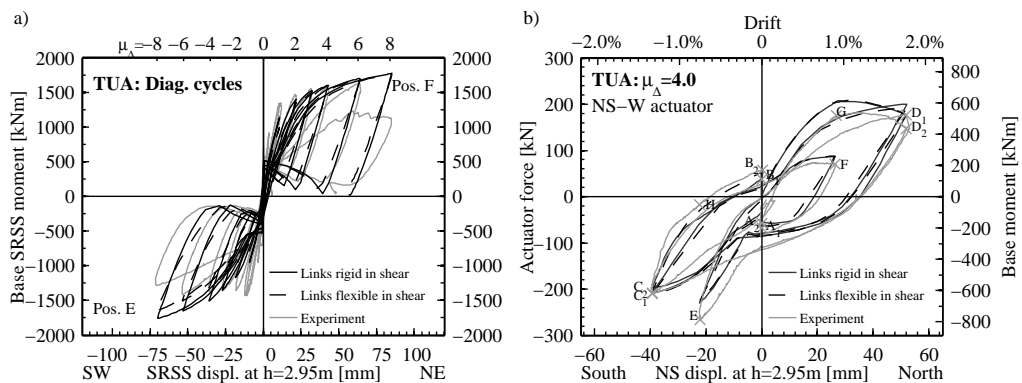


Figure 6.30. TUA: Influence of the shear flexibility of the horizontal links on the hysteresis curves for the diagonal cycles (a) and the force of the NS-W actuator for cycles with $\mu_{\Delta} = 4.0$ (b).

In the reference WCM the rectangular sections that make up the U-shaped section remain plane while the U-shaped wall section as a whole does not remain plane due to the torsional flexibility of the links. This modelling assumption was supported by Demec measurements (Whitmore gauge measurements) taken on the inner faces of the web and flanges of TUA and TUB during testing. As an example, Figure 6.31 shows the vertical strain profiles obtained from the Demec measurements at Position E in the $\mu_{\Delta} = 3.0$ cycles. Since the crack spacing was of the same magnitude as the length over which average strains were measured the strain profiles appear slightly erratic but the results suggest that the assumption of linear profiles over individual wall sections (i.e. one flange or the web) is reasonable. The dashed lines in Figure 6.31 are best fit linear profiles over the individual wall sections. Assigning a shear flexibility to the links in the WCM leads to a discrepancy of the longitudinal strains of the web and flange sections at the corner, which was not observed during the tests. However, the analysis of elastic non-planar walls for which the ratio of shear to flexural deformations Δ_s/Δ_f was in the order of those encountered for TUA and TUB (see Section 4.4.1) indicated, that the links should be assigned shear flexibilities in order to model the overall stiffness of the wall correctly. This conclusion was drawn when comparing the results from elastic WCMs to elastic shell element models. In the latter the deviation from the assumption of rectangular sections remaining plane increased with decreasing shear stiffness of the walls. However, for shear stiffnesses corresponding to Δ_s/Δ_f -ratios up to about 0.5, this deviation was small and could therefore be compatible with the jagged strain profiles obtained from the Demec measurements. It is believed that in WCMs, the shear flexibility of the links compensates for the stiffening effects resulting from the assumption that the individual web and flange sections remain plane. That in WCMs the shear flexibility of the links leads to a strain incompatibility at the corners is an acceptable drawback since it was already shown in Section 6.2.2 that strains extracted at the integration points of the wall elements are not suitable to determine performance limits. Moreover, it was shown in Figure 6.30 that introducing the shear flexibility of the links improves the match of the numerical results with the experimental evidence considerably.

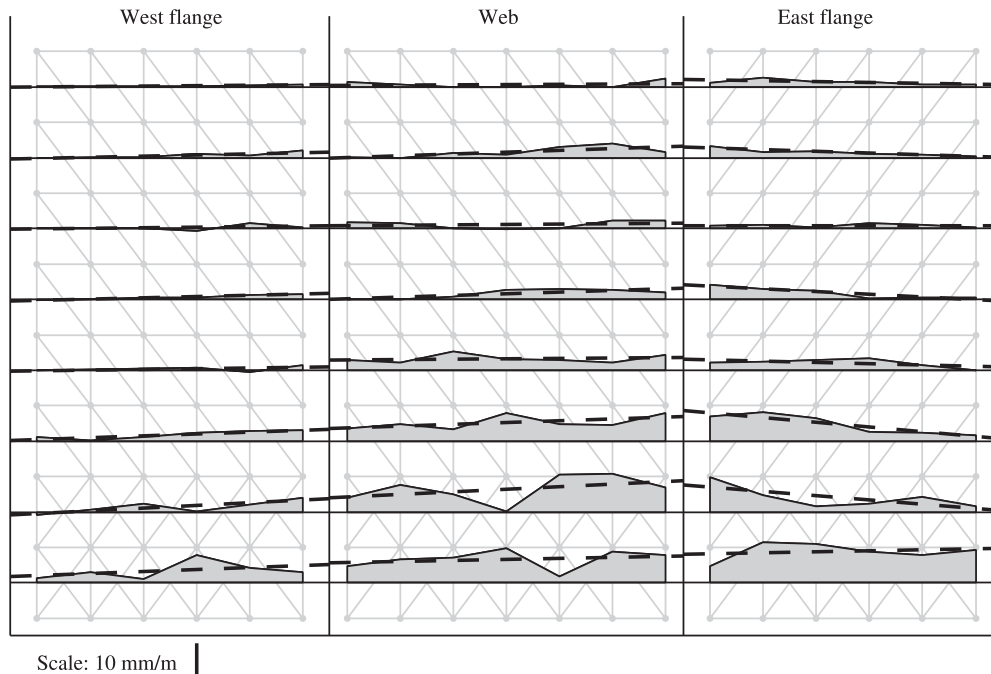


Figure 6.31. TUA: Vertical strain profile of TUA at Position E with $\mu_{\Delta} = 3.0$ (at Position E the West flange end was in compression). The grey lines represent the grid of the Demec measurements, the grey shaded areas the vertical strains and the dashed black lines the best fit linear strain profiles over one wall section.

6.2.5 Summary of findings and recommendations for properties of WCMs of U-shaped walls

The objective of Section 6.2 was to deduce guidelines for properties of WCMs of U-shaped walls. The following is a summary of the findings of the sensitivity analysis of a WCM for TUA, which were presented in Sections 6.2.2 to 6.2.4. Only wide column models with displacement-based beam elements as vertical elements to which fibre sections were assigned are addressed. This type of element was chosen for two reasons: First, the displacement-based formulation is the most commonly implemented beam element formulation in structural analysis programs. Second, fibre sections allow capturing the interaction of the axial and flexural capacity. This was considered important since the axial load on the web and flange sections varied significantly during the loading of TUA and TUB.

Subdivision of the section: Three different schemes of subdividing the U-shaped section into rectangular sections were investigated. For Scheme C the corners were half attributed to the web section and half to the flange sections. Since most structural analysis

programs only allow the definition of reinforcing bars within the concrete section, the inner corner bar was attributed to both the web and the flange section while the outer corner bar was not assigned to any section; the total reinforcement area was therefore modelled correctly. This subdivision scheme was chosen because it led for most directions of loading to intermediate results between the other two schemes and hence seemed most suitable for a WCM that was analysed for different directions of loading.

Spacing of the horizontal links: The spacing of the horizontal links affects the magnitude of the parasitic bending moments and hence also the apparent shear stiffness. It was found that the effect was more pronounced during the unloading phase of cyclic loading than during monotonic loading. Stafford-Smith and Girgis [1986] suggested to limit the link spacing to about one fifth of the total wall height. Setting the link spacing equal to the storey height, which is often done when the U-shaped wall is modelled as part of an entire building, might lead to a softer structure than intended. In a secondary way the horizontal link spacing also affects the length of the vertical elements and hence the height of the integration point closest to the base. If the first integration point is at some distance to the wall base the lateral load capacity might be overestimated. Instead of altering the link spacing a larger number of elements between the links might be chosen (see the following point).

Number of elements between links: Connecting two horizontal links with a single vertical element would be the simplest solution. One should, however, refrain from it in regions undergoing significant inelastic deformations, since standard displacement-based elements are not capable of capturing large nonlinear curvature variations. Hence, at least two elements having each an element length of $h_{sp}/2$ should be used for connecting two consecutive horizontal links. For the case of TUA with $h_{sp} = 680\text{mm}$ it was found that the difference between using two or three elements between consecutive links was small. To keep the model simple the links were connected with two elements.

In-plane shear stiffness of the vertical elements: When assigning shear and torsional stiffnesses to vertical wall elements, regions undergoing inelastic deformations and regions that remain largely uncracked and elastic should be distinguished. The following summary refers to the wall elements that are expected to undergo inelastic deformations. In reality, the shear and torsional stiffness of a web or flange section is dependent on the state of cracking and the axial and flexural strains. This varies during the course of the loading. In most structural analysis programs shear and flexural stiffnesses need, however, to be assigned constant values that cannot be updated during the loading history. The objective of this part of the study was therefore to test the sensitivity of the results to different assumptions and to propose an appropriate constant value, which could be used for TUA and TUB when analysed for the entire loading history. It was

shown that based on the Δ_s/Δ_f -ratios, which were gained from the experimental results, in-plane shear stiffness estimates could be derived. If the WCMs were analysed for the entire bi-directional loading history, the shear stiffnesses were best derived from the Δ_s/Δ_f -ratios for the principal directions of loading at $\mu_\Delta = 4.0$ which represents an intermediate ductility level. Consequently, for smaller displacement demands the shear stiffnesses were underestimated while for larger displacement demands they were overestimated. For the analysis of the isolated U-shaped wall it did little matter whether the shear flexibility was distributed constantly over the wall height or whether the shear flexibility was concentrated within the plastic hinge zone. If the U-shaped wall is part of a larger structure, the distribution of the shear flexibility should reflect the distribution of the expected inelastic deformations.

Out-of-plane shear stiffness of the vertical elements: The out-of-plane shear stiffness of the wall sections undergoing inelastic deformations is even more difficult to estimate than the in-plane shear stiffness since no out-of-plane deformation quantities were measured, which could help in deducing a stiffness. The sensitivity analysis showed, however, that the magnitude of the out-of-plane shear stiffness was not that important (as long as some stiffness was assigned) since the shear force was limited by the out-of-plane bending capacity. Depending on the ratio of wall length to wall width of the considered section, the out-of-plane stiffness could be estimated as a fraction of the in-plane stiffness (e.g. 25%). If the U-shaped wall is analysed to derive design forces (rather than for assessment of an existing structure or modelling of a test unit) the out-of-plane shear stiffness might be set to zero. In this way, all shear forces are carried as in-plane shear forces and are therefore included in the design process.

Torsional stiffness of the vertical elements: The torsional stiffness of the vertical elements was not the focus of this study since the WCM were only analysed for translational deformations; this type of loading was not sensitive to the assumed torsional stiffnesses of the vertical elements. Without having it yet verified by experimental results, it is recommended that the torsional stiffness is reduced to allow for the inelastic deformations. As a first estimate the torsional stiffness might be reduced by a similar ratio as the in-plane shear stiffness.

Link properties: As recommended by Reynouard and Fardis [2001] the links were assigned a torsional flexibility in order to allow warping of the section. Reynouard and Fardis [2001] suggested to use the elastic torsional stiffness of the links $GK = G_c \cdot h_{sp}/3 \cdot t^3$. Reducing the torsional stiffness of the links further had relatively little effect on the analysis results, while the difference in analysis results between flexible and rigid links was considerable. Hence, it is suggested to use either the properties suggested by Reynouard and Fardis [2001] for all links or to reduce this stiffness a little further

in regions where inelastic deformations of the wall sections are expected to reduce the warping stiffness of the section. Unlike all previous studies of which we are aware, it is also proposed to assign an in-plane shear flexibility to the links. This shear flexibility is introduced to account for deformations in the physical test unit, which were caused by vertical shear stresses transmitted from the web to one flange along the corners. Assigning the horizontal links such shear flexibility caused a discontinuity in the strain profile at the corners. Considering that the WCM is in all cases only a very simple approximation of the real physical test unit, it was judged that this is acceptable. The shear stiffness of the wall links could be either estimated on the basis of the truss model developed by Park and Paulay [1975] or the shear stiffness of the elastic, uncracked section could be reduced by the same amount as the shear stiffness of the vertical wall elements.

Shifting from values for the in-plane shear stiffness of the vertical wall elements representing elastic, uncracked sections to values that account for the effect of the inelastic deformation had the largest effect on the force-displacement hystereses. Also the introduction of a shear flexibility to the horizontal links had a significant effect; this was in particular noticeable for the moment hysteresis in the diagonal direction. These two modifications to the reference models with state-of-the-art properties brought the numerical results in terms of the unloading stiffness, the force distribution between the East and West actuator and most importantly the maximum reached moments for loading in the diagonal direction fairly close to the experimentally determined values. Modifying the torsional stiffness of the links had the same effect, i.e. a reduction of the stiffness of the system, but to a far smaller extent. From a modelling point of view it is therefore important to find appropriate estimates for the in-plane shear stiffness of the wall elements.

The analysis has also shown that the maximum capacity reached for the pushover analysis was not affected by the choice of the modelling parameters that were discussed in this section; the pushover analysis always reached the same moment capacity. Hence, one can conclude that the moment capacity that was reached during the testing of TUA and TUB for displacements in the diagonal direction were not the ultimate moment capacities but that the loading in the diagonal direction was in fact always stopped before the ultimate capacities were reached, since the system was much softer than expected due to the large shear deformations.

Up to now the in-plane shear stiffnesses of the wall elements were computed from the experimentally determined Δ_s/Δ_f -ratios. This was done to reduce the number of factors that introduce an uncertainty in the comparison of the numerical results from the WCM and the experimental results. In Chapter 5 an empirical equation for the prediction of the ratio

of shear to flexural deformations was developed. Although the predicted Δ_s/Δ_f -ratios (Table 5.1) were in particular for TUA in some cases too large this hardly affected the results of the WCM analyses. Figures 6.32 and 6.33 show the force-displacement hysteresses for cycles in the EW, NS and diagonal directions and the actuator forces during the cycles at $\mu_\Delta = 4.0$. For the global hysteresses there is almost no difference between the WCMs whose shear stiffnesses were based on the predicted and experimentally determined Δ_s/Δ_f -ratios. There is a slight difference for the actuator forces between the two models; it is, however, relatively small. Hence, it seems that the models were not very sensitive to the chosen shear stiffnesses as long as the stiffness was in the right ballpark. For TUA both WCMs tend to be a little too soft when the maximum reached moment during the diagonal cycle at $\mu_\Delta = 4.0$ as well as the NS-W and NS-E actuator forces are considered. For the experimental Δ_s/Δ_f -ratios the shear displacement was determined according to the indirect method. Compared to the other two methods the indirect method led to the largest ratios of shear to flexural deformations. It is therefore possible that the shear flexibility of the wall elements was slightly overestimated. For TUB, the difference between the three methods was less significant. On the whole, however, the agreement between the experimental results and the numerical predictions is rather satisfactory and much improved when compared to the results obtained from the reference models with state-of-the-art properties (Figures 6.11 and 6.12).

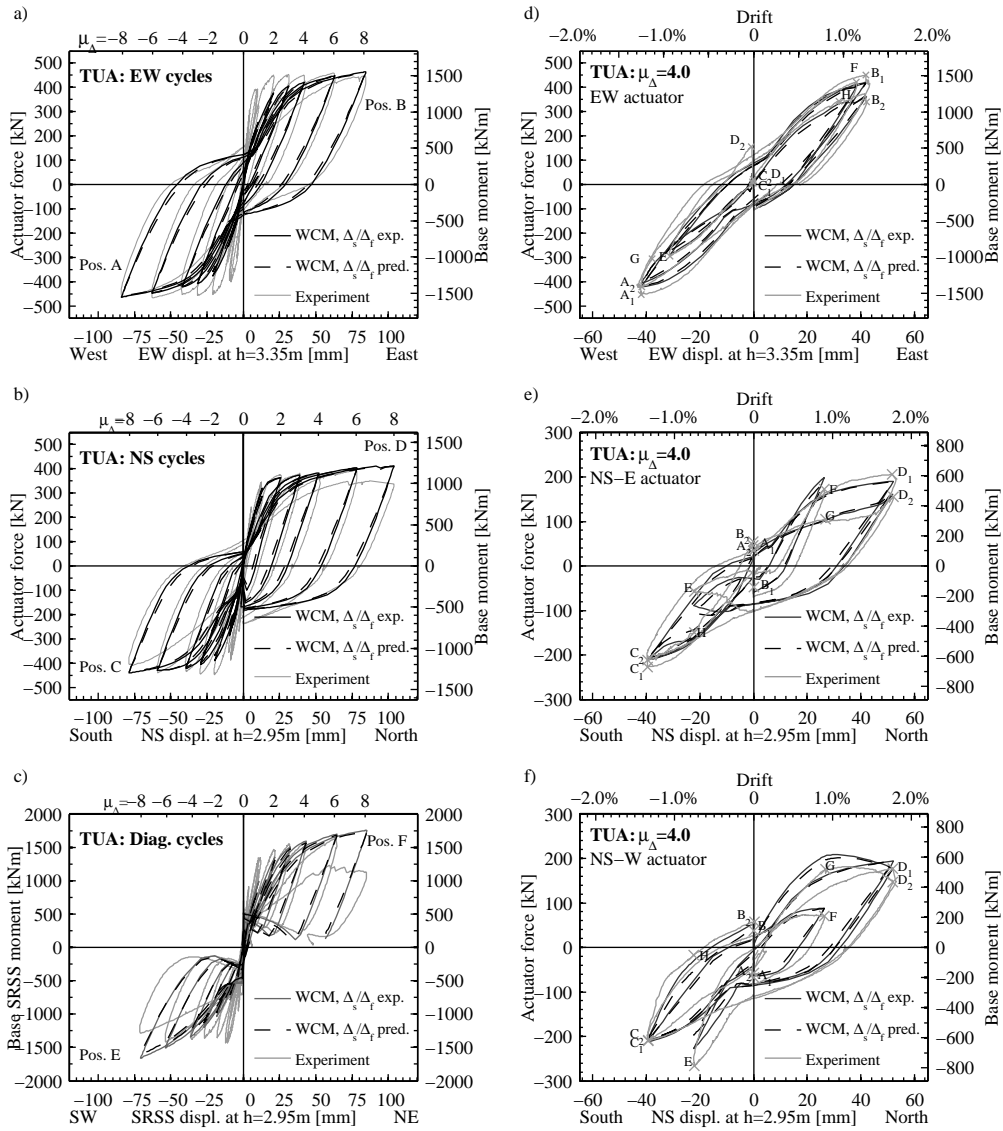


Figure 6.32. TUA, final WCM with in-plane shear stiffnesses derived from experimentally determined and predicted Δ_s/Δ_t -ratios: Comparison of analysis and experimental results for cycles in the EW, NS and diagonal directions (a-c); comparison of actuator forces obtained from analysis and experiment during the cycles of $\mu_\Delta = 4.0$ (d-f).

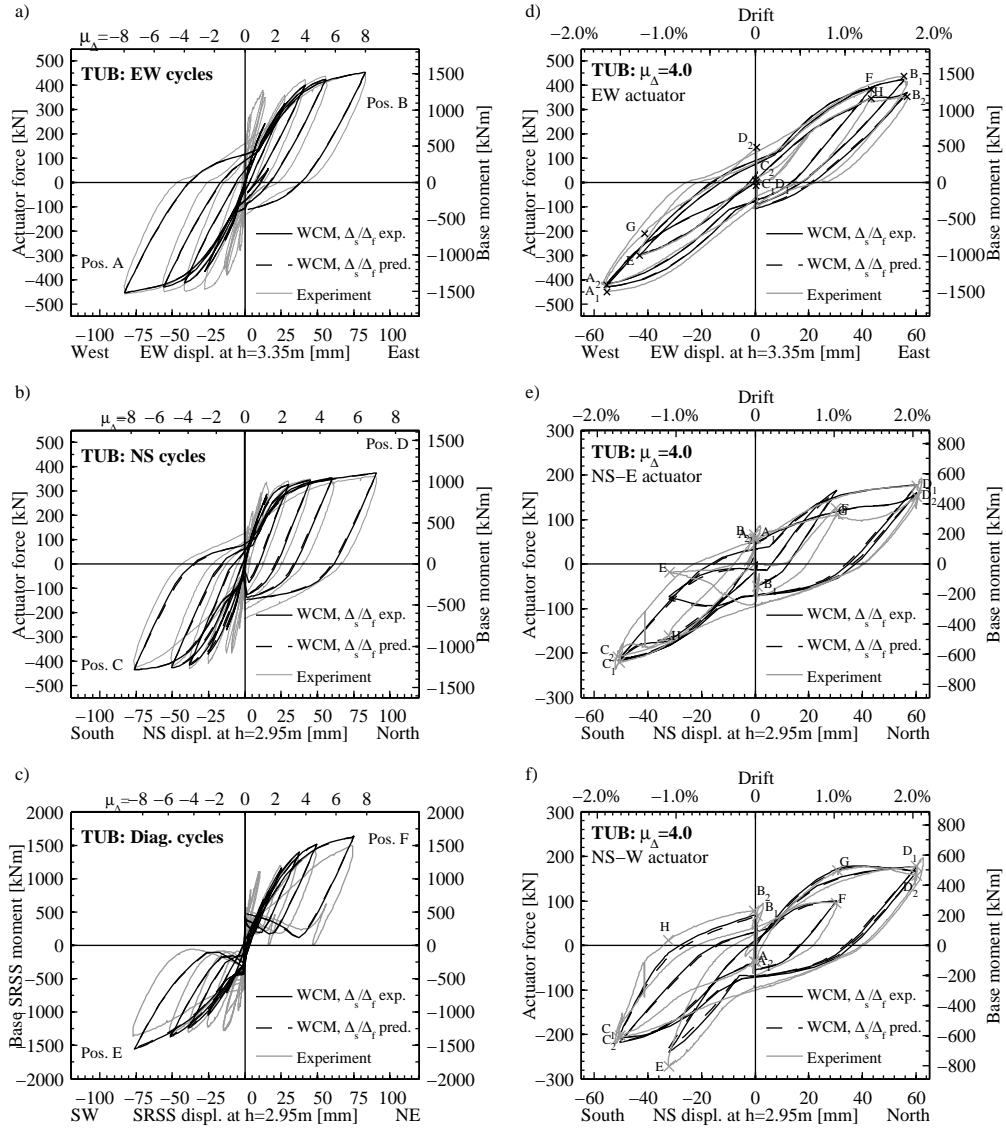


Figure 6.33. TUB, final WCM with in-plane shear stiffnesses derived from experimentally determined and predicted Δ_s/Δ_f -ratios: Comparison of analysis and experimental results for cycles in the EW, NS and diagonal directions (a-c); comparison of actuator forces obtained from analysis and experiment during the cycles of $\mu_{\Delta} = 4.0$ (d-f).

6.3 Discussion of results from plastic hinge and wide-column models and outlook on future research

The objective of this chapter was to apply the plastic hinge and the wide-column model to TUA and TUB and to compare the analysis results to the experimental results. The results showed that the plastic hinge model was well suited to predict displacement capacities. However, the pushover curves for loading in the diagonal direction that were derived by means of plastic hinge analysis resulted in much larger moment capacities than were actually attained during the experiments. Here, the limits of the capabilities of plastic hinge model were reached because the reasons for the difference laid in the difference of cyclic and monotonic loading. This could be shown when wide-column models were analysed. Due to shear flexibilities, which were relatively large when compared to those of rectangular walls, the loading and reloading stiffness was reduced and hence the maximum moment capacity in the diagonal direction was probably never reached. The comparison of the global forces and deformations obtained from wide-column analysis to the experimental results proved that the wide-column analogy is a powerful tool when analysing 3D structures. It is the simplest of the 3D models (shell and solid elements models being others) yet it is also the most convenient for the design engineer since it allows the direct extraction of section forces and moments. A novelty of the proposed wide-column models is the introduction of a shear flexibility of the links. This proved to be the final step that was required to achieve a good match between the numerical and experimental results. In contrast to the plastic hinge model the wide-column model was not ideally suited to determine displacement limits. The strains that can be extracted at integration points of elements were strongly dependent on the element length and it would therefore be required to use different measures such as the average rotation over the plastic hinge length (Yazgan, 2007, personal communication) to determine displacement capacities from wide-column analyses.

The evaluation of the different types of models and hence the choice of the modelling parameters for the wide-column models was based on the experimental results for TUA and TUB. Validating against two experiments can only be a start but cannot result in final conclusions. It is therefore important that more experimental results on the cyclic behaviour of U-shaped walls (or walls with other non-planar sections) become available.

7. ACCOUNTING FOR TORSIONAL RESPONSE IN DDBD

7.1 Introduction

The objective of this thesis is to contribute to the seismic design of RC buildings with U-shaped walls (Section 1.2). While in the previous chapters the seismic behaviour of isolated U-shaped walls has been examined, this chapter will provide a missing piece to the conceptual design of the entire building rather than the design and analysis of a single structural member. A key characteristic of buildings with U-shaped walls is their plan-asymmetry. In many buildings the U-shaped wall is placed at the perimeter of the plan layout in order to create large open floor areas. Since the U-shaped wall is typically stiffer and stronger than other structural elements, the building is in most cases asymmetric regarding the stiffness and strength distribution over the plan area. As a result the structure will not only translate but will also twist when subjected to seismic excitation. This was illustrated in Figure 1.2 of the introduction to this report. Figure 1.2 showed a building in which a U-shaped wall and three rectangular walls are the lateral strength providing elements. During an earthquake, the lateral resistance provided by the U-shaped wall and other walls are different, resulting in a twist of the structure. The most important consequence of the twist is the increase in displacement demand on some structural components [Paulay, 1997].

Torsional provisions in codes are predominantly based on elastic considerations. Paulay [1997] pointed out that such provisions are hardly suitable to describe the torsional behaviour of structures that are expected to respond in the inelastic range. The study presented here follows Paulay's argumentation and the torsional response of inelastic rather than linear elastic systems will be examined. While most design codes still focus on force rather than displacement demands, a number of displacement oriented design approaches have been developed over the last two decades. Such design approaches allow the engineer to estimate displacement demands on structural components and thus protect these components from excessive deformations that would lead to unacceptable damage. One of the most completely developed approaches is the direct displacement-based design (DDBD) approach, which has been developed by Priestley and his co-workers [Priestley, 2000; Priestley and Kowalsky, 2000; Priestley

et al., 2007]. In its current form, this design approach can be applied to any kind of MDoF system that is symmetric in-plan but not to in-plan asymmetric buildings. Therefore, next to examining the torsional response of inelastic systems, the second objective of this chapter is to develop a simple method that allows to account for additional displacement demand due to twist within the framework of DDBD.

While the focus of this project is on buildings with U-shaped walls, the following study on the torsional response is based on buildings with rectangular RC walls. This was done to simplify and generalise the parametric study on the response of in-plan asymmetric buildings. It is believed that for the preliminary stages of conceptual design, when the displacement demand on the structural elements is estimated, the U-shaped wall can be idealised as two rectangular walls since in most cases the torsional stiffness of the U-shaped wall is relatively small compared with the rotational stiffness of the entire structure. This applies, for example, to the system in Figure 1.2. The lever arm between the walls at the perimeter of the slab is considerably larger than the lever arm between the two flanges of the U-shaped wall and therefore the torsional stiffness and strength of the entire building is much larger than that of the U-shaped wall. The error introduced by neglecting the torsional stiffness of the U-shaped wall is relatively small and hence acceptable during the conceptual design stage. When verifying the design by means of nonlinear time history analysis, the U-shaped wall can then be modelled as a three dimensional structure that also possesses a torsional stiffness. The wide-column analogy, which was applied to TUA and TUB in Chapter 6, seems suitable for this purpose. However, at present, its capabilities of reflecting the correct torsional stiffness of the U-shaped walls has not been examined; this will be the topic of a future study.

If the torsional stiffness of the U-shaped wall is not negligible when compared with the torsional stiffness of the entire system, the simplification of representing the U-shaped wall as two rectangular walls is not acceptable. An extreme case of such a building is shown in Figure 7.1: In this building the entire lateral resistance is provided by the core wall; all other vertical structural elements carry only gravity loads. In such a case, the torsional resistance of the U-shaped wall should be considered when designing the structure. Also considered should be the location of the shear centre of the U-shaped wall, which varies depending on the degree of damage to the structural wall [Pégon *et al.*, 2000a]. Since the torsional stiffness and the location of the shear centre have not yet been addressed, structures whose predominant torsional resistance results from the U-shaped wall are excluded from the following design approach.



Figure 7.1. Photo of a RC structure with flat slabs and gravity columns and a very eccentric core structure, which is the only member providing lateral strength (photo by the courtesy of H. Bachmann).

7.1.1 Objectives of this chapter and limitations to the study

The objective of this study is twofold: First, it is aimed to characterise the seismic response of in-plan asymmetric building systems that respond in the inelastic range. The seismic response is characterised in terms of the displacement demands on structural elements. The second and principal objective is to develop for such systems a simple approach for estimating the displacement demand on the centre of mass and the structural elements. This approach can then be used in conjunction with DDBD for designing in-plan asymmetric structures. The study is limited to the class of "regular asymmetric systems", which was defined by Hejal and Chopra [1989]. The characteristics of such systems are:

- The vertical resisting elements must be arranged on an orthogonal grid.
- The centres of mass of all the floors must line up vertically.
- The ratio of rotational inertia to mass must be constant over the height of the structure.
- The stiffness matrices of all lateral load resisting elements must be mutually proportional over the height of the wall.

The example structures used in this study are all simple wall-type structures that are regular in elevation. Note that due to the last requirement for regular asymmetric walls, a mixed frame-wall structure is strictly speaking not a regular asymmetric system because the stiffness matrices of walls and frames do not vary in the same way over the height of the structure [Hejal and Chopra, 1989]. Both, uni-directional and bi-directional input will be considered for the

nonlinear time-history analysis. For the uni-directional analysis, artificially generated spectra will be used. The bi-directional analysis are carried out using the two horizontal components of real records.

7.1.2 Layout of this chapter

The section following this introduction gives a short summary of the principles of DDBD and then focuses on previous studies on torsional response of in-plan asymmetric structures (Section 7.2). The analysis method and earthquake records used for this study are presented in Section 7.3. The results of the parametric study on 2D asymmetric systems are presented in Section 7.4. Based on these results a method for estimating the displacement demand on 2D asymmetric systems is developed; with this tool it is possible to extend the DDBD approach to in-plan asymmetric structures (Section 7.5). In the last section (Section 7.6), the key findings from this study on the torsional response of inelastic systems are summarised and suggestions for future research made.

7.2 Literature review on DDBD and torsional response of in-plan asymmetric structures

The aim of this study is to extend the DDBD approach to structures that are asymmetric in plan. To set the study in context, a brief overview of the principles behind DDBD are given (Section 7.2.1). The main part of the literature review section focuses on previous studies on torsional response of in-plan asymmetric structures. This part is subdivided into four sections:

- An overview on research activities regarding torsional response (Section 7.2.2).
- 2D models for in-plan asymmetric structures and the definition of relevant terms (Section 7.2.3).
- Results of previous studies on the response of 2D models of in-plan asymmetric structures (Section 7.2.4).
- Different design approaches considering the torsional response of in-plan asymmetric structures (Section 7.2.5).

7.2.1 Direct displacement-based design

The DDBD approach characterises a multi-degree of freedom system by a substitute linear single-degree of freedom system. The substitute system is characterised by the secant stiffness at the design displacement of the structure and a viscous damping value accounting for the

combined effects of elastic and hysteretic energy dissipation in the nonlinear multi-degree of freedom system [Priestley and Kowalsky, 2000]. The design displacement corresponds to the maximum displacement that leads to acceptable displacement and drift demands. With some fundamental knowledge of the hysteretic characteristics of the main structural elements, the effective viscous damping can be estimated and the effective period at peak displacement can be obtained from elastic response spectra for different levels of damping. Knowing the effective period and the design displacement, the required strength can be readily obtained. To reduce the multi-degree of freedom system to a single degree of freedom system, assumptions regarding the displaced shape over the height of the structure at maximum displacement are required. Appropriate shape functions have been developed for a number of structural systems such as structural wall type and frame type buildings. The shape functions are dependent on the displacement profile of the structure at yield and the inelastic mechanism the structure is expected to develop.

The DDBD approach is an instrument that allows the engineer to design structures focusing on displacement rather than force demands. The effectiveness of this design approach has been proven in a number of studies considering different types of structures (e.g. Priestley and Amaris [2002]; Pettinga and Priestley [2005]; Sullivan *et al.* [2006]). However, in its current form, the design approach is limited to structures that only translate and do not twist when subjected to seismic excitation. While earthquakes produce also a rotational component of motion, this is typically assumed to be negligible and it is therefore not considered in seismic design. Hence, structures that can be addressed by means of DDBD in its current form are structures that are symmetric in plan. For this type of structures the translational components of seismic excitation do not cause the structure to twist and hence produce a constant displacement demand over one floor level.

If the system is asymmetric in plan and torsional response is expected to occur under seismic loading, the displacement demand on elements at one particular floor level is no longer uniform. To reduce the multi-degree of freedom system to a single degree of freedom system, it has been shown that it is sufficient to estimate the displacement demand at the centre of mass at each storey level [Castillo, 2004]. However, to assess the structural performance, not only the displacement demand at the centre of mass but also at the locations of the structural elements needs to be addressed. This will be the main focus of the study presented in this chapter.

7.2.2 Selected studies describing the torsional response of buildings

The torsional response of buildings when subjected to seismic excitation has been the focus of a number of research groups for many years. Different approaches have been taken with the

objective of understanding and describing the torsional response of buildings. The research approaches of the last 30 years can be broadly grouped into five categories:

Torsional response of elastic systems: In particular in the early years most researchers focused on the torsional response of elastic systems. The objectives were chiefly the derivation of modal properties of different in-plan asymmetric buildings and estimation of peak displacements and forces using response spectrum analysis. Some key references for this direction of research are: Kan and Chopra [1977], Rutenberg *et al.* [1978] and Hejal and Chopra [1989]. A more recent study by Lopez *et al.* [2000] proposed a method for estimating the maximum response of in-plan symmetric and asymmetric elastic structures when subjected to multi-component earthquakes using different rules for combining the response of several modes.

Base-shear torque surface: De la Llera and Chopra [1995] introduced the base-shear torque surface (BST-surface), which is a failure surface for an asymmetric in-plan 2D system. The method is based on static considerations and failure is defined as the formation of a mechanism. The BST-surface is an interesting concept for visualising the interaction of base shear and torque capacity. From a seismic design point of view, however, it has a number of short comings: First, it does not address base shear and torque demands but solely the structure's capacity. Second, it does not address the displacement demand on the structure under seismic excitation. Finally, the definition of failure that is applied for the BST-surface is unsuitable for dynamic considerations in which a mechanism is allowed to form as long as the displacement capacity of the structure is not exceeded. The concept of the BST-surface has also been studied and extended by a number of other researchers, e.g. Rutenberg and De Stefano [1997a], Kilar and Fajfar [1999] and Sommer [2000].

Pushover analysis of asymmetric buildings: Several uni-directional pushover analysis methods for in-plan symmetric buildings have been developed in the past and have in some cases also been implemented in seismic design codes. These pushover methods can not be applied to buildings that are asymmetric in plan. A number of researchers hence developed extensions of pushover analysis tools for in-plan asymmetric structures, which can be implemented in structural analysis programs. Different approaches were for example proposed by Kilar and Fajfar [1997], Tso and Moghadam [1997], Chopra and Goel [2004] and Fajfar *et al.* [2005]. The main drawback of static pushover methods (apart from the modal pushover methods) consists in the difficulty of properly accounting for the effect of rotational inertia, which is, however, crucial for the rotational response of elastic and inelastic systems (see Section 7.2.3).

nonlinear time history analysis of asymmetric buildings: Since the computer power became sufficient large to carry out inelastic analysis of buildings, nonlinear time-history analyses have been carried out for many different configurations of asymmetric buildings. Simple in-plan 2D systems have often been used to identify key parameters influencing the torsional response. Results of two selected studies [Sommer, 2000; Castillo, 2004] are presented in detail in Section 7.2.4. More complex models of 3D structures that are asymmetric in-plan have also been studied but due to the large number of parameters involved in 3D models, such analyses are often restrained to case studies.

Design-oriented studies: Paulay developed design approaches for different torsional systems (see Section 7.2.5), which were purely displacement-oriented [1996; 1997; 1999; 2001]. Unlike other researchers, he focused on the mechanisms of the system that could develop when subjected to torsional response. He pointed out that rotations are not of primary concern when assessing the performance of an in-plan asymmetric system that is asymmetric in plan and suggested that displacement or drift demands on structural and non-structural components should be addressed directly. His earlier studies were later complemented by nonlinear time-history analyses of simple 2D models by his student Castillo [2004]. Castillo's work is described in detail in Section 7.2.4. Sommer [2000] and Trombetti *et al.* [2002] both developed methods for estimating the rotational response of asymmetric 2D systems based on the torsional response of elastic systems, the method of the latter is also known as the "alpha"-method. While Trombetti *et al.* [2002] considered the ratio of maximum translation to maximum rotation of the elastic system under free vibration, Sommer [2000] considered maximum translation and rotation of an elastic system under seismic excitation. The application of these approaches to inelastic systems is based on the assumption that rotations of inelastic systems are always smaller than rotations of their elastic counterparts. Both approaches neglect that maximum translation and maximum rotation do not occur at the same instant. Sommer's [2000] approach will be described in more detail in Section 7.2.5.

More comprehensive reviews of the past and ongoing research activities on the torsional response of in-plan asymmetric structures including extensive reference lists can be found in the following publications: Rutenberg [1992], Rutenberg and De Stefano [1997b], Rutenberg [2002] and De Stefano and Pintucchi [2006].

7.2.3 Simple 2D models and the definition of terms relevant to torsional response

In order to carry out parametric studies, it is beneficial to reduce the number of degrees of freedoms of the model. Regular asymmetric 3D systems, which were defined in Section 7.1.1,

can be approximated by 2D systems. In such 2D systems the lateral strength providing structural elements (e.g. walls or frames) are represented by a spring that is characterised by the deformations of the structural element at the effective height and its base shear capacity. The springs are connected to the CoM by rigid links assuming the deformability of the slabs are small. The storey masses are reduced to an effective mass, which is lumped at the centre of mass. To account for the fact that the mass in reality is distributed over the floor area, it is also assigned an effective rotational inertia. Such a 2D model has three degrees of freedom, i.e. two horizontal, translational degrees of freedom and one rotational degree of freedom about the vertical axis. Many parametric studies on in-plan asymmetric structures have been based on such 2D systems. In the following sections, the classes of torsionally restrained and torsionally unrestrained 2D systems are introduced (Section 7.2.3a) and the characteristic properties of such systems are defined (Section 7.2.3b).

a) Torsionally restrained and torsionally unrestrained systems.

The classification of in-plan asymmetric structures into torsionally restrained (TR) and torsionally unrestrained (TU) was introduced by Paulay [1996]. Figure 7.2 shows plan layouts of simple TR and TU systems. The mass of the system is distributed over the floor area; the location of the centre of mass coincides in the examples with the geometric centre of the slab but this is not mandatory. The lateral strength is provided by RC walls. Their out-of plane stiffness and strength is not considered in the following. The main characteristics of the two types of systems are discussed in depth by Castillo [2004]. For completeness, they are repeated here in brevity.

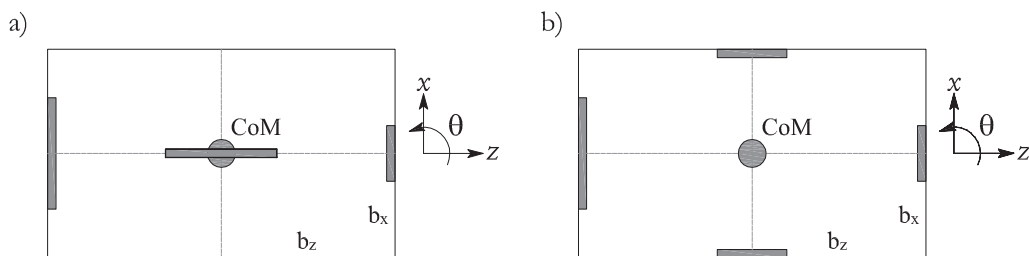


Figure 7.2. Torsionally unrestrained and torsionally restrained systems: Examples of systems that are for excitation in the x direction classified as TU system (a) and TR system (b).

Figure 7.2a shows an example of a TU system that is asymmetric for excitation in the x direction. Such systems are characterised by the absence of a wall couple in the z direction, which would provide a rotational restraint. When the 2D system from Figure 7.2a is subjected to

seismic excitation in the z direction the resistance is provided by the single wall through the centre of mass. For this direction of excitation the system is symmetric and hence this direction is not considered in the following. For excitation in the x direction the lateral resistance is provided by the two walls at the perimeter of the slab. The walls have unequal lengths and hence their yield displacements, which are inversely proportional to the wall length, will also be different. If the reinforcement ratios of the walls are similar, the strength and stiffness will be greater for the long wall than for the short wall. In the following the edge of the slab with the long wall is referred to as "stiff edge" and that with the short wall as "soft edge". If the entire mass of the system would be concentrated at the centre of mass, i.e. if the system had no rotational inertia, the reaction forces in the long and short wall due to seismic excitation in the x direction would always be equal. Figure 7.3a shows the displacement profile of the system one would obtain for zero rotational inertia: The long and strong wall would remain elastic and its deformation would be small. The short and soft wall would yield and be subjected to large displacement demands. In reality, however, there will always be some rotational inertia associated with the distributed mass of the slab and the mass of the walls at the perimeter of the slab. When the slab rotates, a torsional moment due to the rotational inertia is created and the forces in the two walls are no longer equal. As a consequence, the difference in displacement demand on the long and short wall is typically reduced and in most cases both walls respond in the nonlinear range. Once the two elements have reached their inelastic state, there are no further structural elements, which restrain the rotation of the system. At this stage, only the rotational inertia limits the rotation of the slab. The difference in behaviour between TU systems with and without rotational inertia underlines the fact that torsion cannot be looked upon as a static problem; consideration of the rotational inertia is very important in understanding the dynamic behaviour of in-plan asymmetric systems.

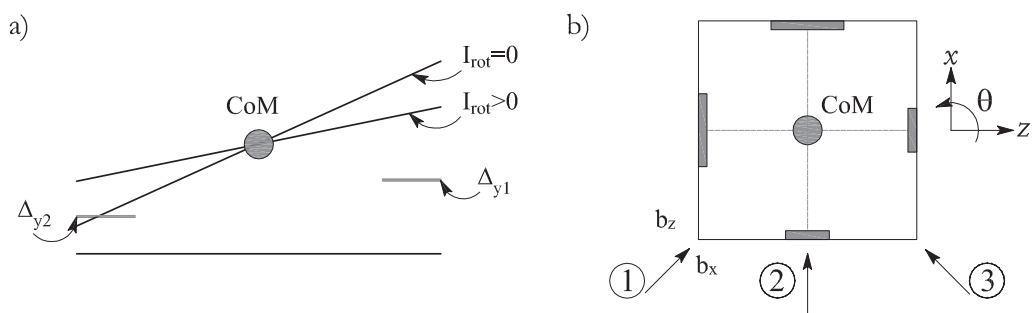


Figure 7.3. Maximum displacement profiles if rotational inertia is considered or neglected (a) and example of a system for which the definition of TR or TU is dependent on the direction of excitation (b): Direction 1: TU, direction 2: TR, direction 3: The system is symmetric.

A sketch of a TR system is shown in Figure 7.3b. In contrast to the TU system, the resistance in the z direction is provided by two walls at the perimeter of the slab rather than a single wall passing through the centre of mass. Hence, if the system is subjected to rotation, the wall elements in the z direction contribute to the rotational resistance. For the hypothetical case of uni-directional excitation in the x direction, the two walls in the direction of excitation are expected to yield. The walls in the z direction will in most cases remain elastic and will provide resistance to rotation. As a consequence, the rotations of a torsionally restrained system will be much smaller than the rotations of a torsionally unrestrained system. Due to the effects of the rotational inertia, maximum displacement demands on the stiff and soft edge and maximum rotation do not occur simultaneously during seismic excitation. In the following, the focus is set on the displacement demand on structural elements and not on the maximum system rotation since the structural displacement demands are the important design quantities [Paulay, 1996]. Sommer [2000] rightly pointed out that the classification of asymmetric systems into torsionally restrained and unrestrained systems is dependent on the considered direction of excitation (Figure 7.3b). In the case of a square slab with identical walls on either side of the slab, for example, the system would be classified as torsionally restrained when excited parallel to the orientation of the walls and as torsionally unrestrained when excited along the diagonals of the floor. In general terms, a system will always be torsionally unrestrained when excited parallel to its principal directions of strength. It will be torsionally unrestrained in more than two directions if the structural components in x or z direction cannot sustain a moment. However, the labelling of torsionally restrained and unrestrained systems as introduced by Paulay [1996] helps to distinguish between preferable and less favourable wall layouts of systems that are asymmetric in plan and therefore this classification is also adopted in this study.

b) Definition of terms.

In this section, all terms relevant for the following discussion of the design of structural walls and the torsional response of asymmetric systems are introduced. The list includes definition of component properties and system properties. If the same quantity is defined for components as well as for the system (e.g. the yield displacement), system properties are marked with the subscript "s" while component properties (i.e. wall properties) carry a number as a subscript.

Effective height and effective mass of a structural wall system

To reduce a MDoF system to a substitute SDoF system the effective properties of the system have to be computed. The effective properties are a function of displacement profile over height. In DDBD, the effective properties are computed based on the displaced shape at the

design point, i.e. the maximum displacement. The effective mass of a system is defined as:

$$m_{eff} = \frac{(\sum \Delta_j \cdot m_j)^2}{\sum \Delta_j^2 \cdot m_j} \quad (7.1)$$

where Δ_j is the design displacement at storey j and m_j is the storey mass. The effective height of a system is defined as:

$$h_{eff} = \frac{\sum \Delta_j \cdot m_j}{m_{eff}} \quad (7.2)$$

Stiffness and yield displacement of one structural wall

The lateral load bearing components of the analysed systems are structural walls. The mean nominal yield curvature φ_y of a structural wall is a function of the wall length l_w and the yield strain ε_{sy} of the longitudinal reinforcement (Section 2.1.2). For rectangular walls the coefficient K_1 is often assumed as 2.0:

$$\varphi_y = 2 \frac{\varepsilon_{sy}}{l_w} \quad (7.3)$$

Based on the classical beam theory the flexural stiffness after cracking of the component can be computed as:

$$EI = \frac{M_n}{\varphi_y} \quad (7.4)$$

where M_n is the moment capacity at nominal yield. The nominal base shear capacity V_n is the ratio of the nominal moment M_n and the effective height H . Typically, during the conceptual design stage, the nominal yield displacement of a wall is estimated assuming a linear curvature variation over the height of the wall (for a discussion of this issue see Section 2.1.1 and 6.1.2). The nominal yield displacement Δ_y at the effective height H can be expressed as a function of the total height h_n of the wall:

$$\Delta_y = \varphi_y H^2 \cdot \left(\frac{1}{2} - \frac{H}{6h_n} \right) \quad (7.5)$$

From the nominal base shear capacity V_n and the yield displacement Δ_y of a wall the equivalent wall stiffness k is defined as:

$$k = \frac{V_n}{\Delta_y} \quad (7.6)$$

System yield displacement and uncoupled translational period

The yield displacement of the system is defined as the translational displacement only, i.e. when computing the system yield displacement, it is assumed that the system is restrained

against rotation. The system yield displacement Δ_{ys} is the ratio of translational system strength and system stiffness in one particular direction (i.e. the x or the z direction):

$$\Delta_{ys} = \frac{\sum V_{ni}}{\sum k_i} = \frac{\sum V_{ni}}{\sum V_{ni}/\Delta_{yi}} \quad (7.7)$$

where the subscript i stands for the i -th wall contributing to the strength in the considered direction. The uncoupled translational period in one particular direction is defined as

$$T_0 = 2\pi \sqrt{\frac{m_{eff}}{\sum k_i}} \quad (7.8)$$

Centre of mass, rotational inertia and radius of gyration of mass

The origin of the coordinate system with axes x and z in the plane of the slab is defined at the centre of mass (CoM). The mass M is the mass contributing to the horizontal inertia of the system. The rotational inertia I_{rot} depends on the distribution of the mass over the slab. For a uniform mass distribution, the rotational inertia of a rectangular slab is:

$$I_{rot} = \frac{M}{12}(b_x^2 + b_z^2) \quad (7.9)$$

where b_x and b_z are the horizontal dimensions of the slab (Figure 7.2). The radius of gyration of mass r_m is defined as:

$$r_m = \sqrt{\frac{I_{rot}}{M}} \quad (7.10)$$

Castillo [2004] introduced a reference parameter for the rotational inertia that is the radius of gyration of mass of a square slab with equal area and uniformly distributed mass:

$$r_0 = \sqrt{\frac{b_x b_z}{6}} \quad (7.11)$$

The ratio of r_m/r_0 gives a good indication by how much the rotational inertia of a slab deviates from the reference square slab with uniform mass distribution.

Translational system stiffness and centre of stiffness

The system translational stiffness in one direction is the sum of the stiffness of all components providing resistance in this direction:

$$K_x = \sum k_{xi} \quad \text{and} \quad K_z = \sum k_{zi} \quad (7.12)$$

The distance of the centre of stiffness from the CoM is computed as:

$$e_{rz} = \frac{\sum k_{xi} z_i}{K_x} \quad \text{and} \quad e_{rx} = \frac{\sum k_{zi} x_i}{K_z} \quad (7.13)$$

x_i and z_i are the lever arm of the component i from the CoM and k_{xi} , k_{zi} the component stiffnesses in the x and z directions. The position of the centre of stiffness is annotated with "CR".

System strength and centre of strength

The system strength and the strength eccentricity are defined in analogy to the translational system stiffness and stiffness eccentricity. The system strength in the x and z directions is defined as:

$$V_{nxs} = \sum V_{nxi} \quad \text{and} \quad V_{nzs} = \sum V_{nzi} \quad (7.14)$$

The coordinates of the centre of strength in the x and z directions are:

$$e_{vz} = \frac{\sum V_{nxi} \cdot z_i}{V_{nxs}} \quad \text{and} \quad e_{vx} = \frac{\sum V_{nzi} \cdot x_i}{V_{nzs}} \quad (7.15)$$

The position of the centre of strength is annotated with "CV".

Radius of gyration of stiffness

The square of the radius of gyration of stiffness is the ratio of rotational and translational stiffness of the elements in one principal direction [Castillo, 2004]. The rotational stiffness $K_{rot,x}$ of elements acting in the x direction and the radius of gyration of stiffness r_{rx} in the x direction are:

$$K_{rot,x} = \sum k_{xi} \cdot (z_i - e_{rz})^2 \quad \text{and} \quad r_{rx} = \sqrt{\frac{K_{rot,x}}{K_x}} \quad (7.16)$$

For the z direction:

$$K_{rot,z} = \sum k_{zi} \cdot (x_i - e_{rx})^2 \quad \text{and} \quad r_{rz} = \sqrt{\frac{K_{rot,z}}{K_z}} \quad (7.17)$$

Radius of gyration of strength

The radius of gyration of strength is defined similar to the radius of gyration of stiffness. For the x and z directions:

$$V_{rot,x} = \sum V_{nxi} \cdot (z_i - e_{vz})^2 \quad \text{and} \quad r_{vx} = \sqrt{\frac{V_{rot,x}}{V_{nx}}} \quad (7.18)$$

$$V_{rot,z} = \sum V_{nzi} \cdot (x_i - e_{vx})^2 \quad \text{and} \quad r_{vz} = \sqrt{\frac{V_{rot,z}}{V_{nz}}} \quad (7.19)$$

Rotational stiffness

The rotational stiffness is computed either about the centre of mass or about the centre of

stiffness. If the system is rotated about the centre of mass the sum of the forces in the x and z directions for a pure rotation is non-zero. The rotational stiffness about the centre of mass is

$$K_{rot,CoM} = \sum k_{xi}z_i^2 + \sum k_{zi}x_i^2 \quad (7.20)$$

By definition the sum of the forces in the x and z directions is zero for rotation about the centre of stiffness. The rotational stiffness about the centre of stiffness is

$$K_{rot} = K_{rot,x} + K_{rot,z} = K_{rot,CoM} - K_x e_{rz}^2 - K_z e_{rx}^2 \quad (7.21)$$

The rotational stiffness about the centre of mass is therefore always greater than the rotational stiffness about the centre of stiffness.

Definition of additional terms

Stiff edge and soft edge: The term stiff edge refers to the edge with the long wall, which is usually stronger and stiffer than the soft edge with the short wall (Figure 7.2).

Nominal rotation: From the profile with the maximum absolute displacement demand on the edges and the centre of mass a nominal rotation can be computed, which links the maximum edge displacement to the maximum centre of mass displacement. In general the nominal rotation will be different for the stiff edge and the soft edge. The nominal rotation is only a concept to describe the maximum displacement demand on the edges and is not a quantity that can be directly observed; the actual maximum rotation will always be greater than the nominal rotation. The concept of nominal rotations was introduced by Castillo [2004].

Skew attack: Skew attack refers to analysis in which a uni-directional excitation is not applied parallel to the x or z axis but at varying angles. Skew attack is not equivalent to bi-directional excitation in which the two horizontal components of one ground motion are applied in perpendicular directions.

7.2.4 Previous studies on torsional response of 2D models

Out of the studies on asymmetric 2D systems, which have been conducted in the past, the results of the two most comprehensive ones are presented in the following. These two studies are part of the Ph.D. theses by Sommer [2000] and Castillo [2004]. A large number of earlier studies were based on the erroneous assumption that stiffness and strength of a cracked RC member are independent rather than directly proportional; Paulay [2001] and Rutenberg [2002] warned that the conclusions drawn from these studies should therefore be treated with

caution. Castillo first published results on TU systems in Castillo *et al.* [2001, 2002]. In the following, however, reference will only be made to his Ph.D. thesis [Castillo, 2004], which contains all results of his parametric study including those presented in the earlier two publications. Within the scope of his Ph.D. thesis, Castillo [2004] analysed 2D systems similar to the ones shown in Figure 7.2. For the analyses, he used the inelastic dynamic analysis program "Ruaumoko" [Carr, 2004]. Castillo analysed TU and TR systems with strength and stiffness eccentricities in one horizontal direction. He also studied systems with more than four elements; as the other systems these multi-element systems had strength and stiffness eccentricities in only one horizontal direction. Most analyses were carried out applying a single component of motion in the x direction (Figure 7.2). However, Castillo also included analyses of TR systems subjected to skew attack. Bi-directional excitation was not considered.

Castillo applied the elasto-plastic hysteretic rule to elements in TU systems. He conducted a sensitivity study comparing results for the elasto-plastic model, a bi-linear model with post-yield stiffness, the modified Takeda model and the Al-Bermani model, in which the transition from the elastic to the post-yield stiffness is gradual. Based on the results of this sensitivity study Castillo concluded that displacement demands on the structural elements are not sensitive to the hysteresis model. It is not clearly stated, which hysteretic model was used for the analysis of TR systems but most likely Castillo concluded in analogy to the TU systems that the choice of the hysteretic model had little influence on the analysis results and therefore used also elements with an elasto-plastic behaviour.

For the time-history analysis of the 2D systems, Castillo used two real earthquake records and an artificial record that was obtained from modifying the El Centro record to match the New Zealand loading standard design spectrum for intermediate soils. This spectrum has a spectral displacement of 0.25m at $T = 2$ s for 5% damping. All records consisted of a single horizontal component only. In his thesis, Castillo plotted the spectra only for periods smaller than 2s but overdamped elastic spectra ($\zeta = 5 - 40\%$) and inelastic spectra for displacement ductilities of up to $\mu_{\Delta} = 5.0$ were also shown. From a DDBD point of view, response spectra of elastic systems with longer periods would have been of particular interest since a typical uncoupled translatory period of an elastic TR system in Castillo's study is $T_{el} = 1.3$ s and a typical design displacement ductility $\mu_{\Delta} = 5.35$. Hence, the effective period at the design point for which the spectral displacement is of interest is about $T_{eff} = T_{el}\sqrt{\mu_{\Delta}} \cong 3$ s.

Some years before Castillo commenced his studies on torsion, Sommer [2000] had carried out a similar parametric study on asymmetric 2D systems. Since he doubted the appropriateness of the classification of in-plan asymmetric buildings into TR and TU systems (see Section 7.2.3a), he did not distinguish between the two types but the systems he analysed covered TR and TU

systems as defined by Paulay. The scope of Sommer's parametric study on 2D systems was similar to Castillo's study. In addition to the systems studied by Castillo, Sommer also included systems with eccentricities in both horizontal directions rather than only one. Nevertheless, Sommer limited his study to analyses with uni-directional excitation. As Castillo he designed the systems for an approximate system ductility of 5.0. The hysteretic behaviour of the walls was modelled as elasto-plastic with a smooth transition from the elastic to the plastic state. The systems were analysed using the finite element program ABAQUS. For the time-history analyses Sommer used six artificial records, which all matched the design spectrum in the Swiss Code SIA 160 [1989] for medium stiff soil. The displacement spectrum had no corner period but increased linearly up to 5s. For 5% damping the spectral displacement at 5s was 0.2m. The seismic displacement demand was therefore less than half as onerous as the demand imposed by the records in Castillo's study. The duration of the records varied between 10 and 12s, the peak ground acceleration of all records was 0.16g. The nonlinear time-history analyses were carried out using 5% tangent stiffness and mass proportional Rayleigh damping in the first and third mode.

Although the range of systems that Sommer considered was slightly greater than the range of systems analysed by Castillo, Castillo's thesis is used as the main reference since in particular his design recommendations (Section 7.2.5) give the framework to the study presented here. Castillo's and Sommer's main findings on TR systems are summarised in the following paragraphs. To improve the readability, no reference is given if the finding results from Castillo's study. Additional findings by Sommer are marked with a reference to Sommer's Ph.D. thesis [Sommer, 2000].

a) Rotations and mass rotational inertia.

- Rotations are not a suitable measure for the behaviour of asymmetric structures because in general the maximum rotation and the maximum displacement demand on the CoM do not occur at the same instant. Instead, the displacement demand on the structural elements should be addressed directly (see also Paulay [1997]).
- Unlike static considerations would suggest (Section 7.2.3a), the stiff wall of TU systems generally reaches a post-yield state provided the rotational inertia is greater than zero. Thus, it is important to consider the rotational inertia when studying the torsional response of in-plan asymmetric systems.
- The mass rotational inertia of the diaphragm restricts system rotations caused by strength and stiffness eccentricities. Rotations are further reduced in case of TR systems where transverse elements provide a torsional restraint.

- The response of TR systems is fairly insensitive to the magnitude of the rotational inertia if the structure is excited parallel to a principal axis (i.e. parallel to the walls in the x or z direction).
- Sommer [2000] found that the displacement demand on the soft edge for $I_{rot} > 0$ was only slightly larger than the displacement demand on the soft edge for $I_{rot} = 0$. For the stiff edge the displacement demand was larger for $I_{rot} > 0$ than for $I_{rot} = 0$ since in the first case the stiff wall reached the inelastic state while in the latter it remained elastic.

b) Displacement demand and translatory mass.

- The displacement demand on the CoM can be predicted by an equivalent SDoF system. The equivalent SDoF should be assigned the effective translatory mass of the system and the total lateral stiffness (K_x and K_z).
- The accuracy of the equivalent SDoF model reduces with increasing ratio of the wall lengths of the long and the short wall as well as for very stiff systems (uncoupled translatory period $T_0 < 0.7s$).
- Mass eccentricity is not having an effect on the torsional response. The mass eccentricity is defined as the distance between the geometric centre of the slab and the CoM.

c) Stiffness and strength eccentricity.

- Stiffness eccentricity plays a minor role when assessing the torsional behaviour of ductile systems. Independent of the stiffness eccentricity, the displacement demand on CoM, stiff and soft edge is approximately the same if the strength eccentricity is zero. It should be noted that Castillo only considered seismic intensities that led to relative large displacement ductility demands ($\mu_{\Delta} \cong 5.0$).
- Strength eccentricity is acceptable provided it results from strength in excess of the one required for zero strength eccentricity. This is one of Castillo's most important findings and it is also reflected in his design guidelines. According to these, strength eccentricity must always be coupled to an increase in base shear capacity if the displacement demand on the stiff and soft edge is not to be larger than for zero strength eccentricity.
- Sommer [2000] examined the effect of stiffness and strength eccentricity regarding the displacement *ductility* demand and not (as Castillo did) regarding the displacement demand on the elements. To obtain similar displacement ductilities in the elements on the soft and stiff edge Sommer [2000] found that the position of the centre of strength

should be between the centre of stiffness and the centre of mass. This seems convenient since it is the typical position of the centre of strength if the elements have similar reinforcement and axial load ratios. Hence, most of the existing buildings would have been designed to result in similar ductility demands on the stiff and soft edge. However, for design purposes it seems more convenient to address the displacement demand directly rather than aiming for equal displacement ductilities. For example, if drift limits govern the design, the limiting displacement ductility demands will be different for long and short walls.

d) Transverse elements (TR systems).

- Changes in strength and stiffness of the transverse elements do not significantly affect the displacement demand on the elements parallel to the direction of excitation. Note, however, that Castillo only considered uni-directional excitation and hence the transverse elements always remained elastic.

e) Multi-element systems.

- Multi-elements systems are systems in which more than two elements provide lateral stiffness and strength in one direction.
- Castillo found that multi-element systems can be represented by a two-element system with similar stiffness, capacity and corresponding eccentricities. For this reason, only systems with a maximum of two walls in each direction will be considered in this study.

f) Skew attack.

- For skew attack the systems were excited at angles to the principal directions (i.e. in the x and the z direction). The principal directions refer to the directions parallel to the elements. The magnitude of the excitation remained unchanged.
- Due to yielding of the transverse elements torque and rotations increased significantly for skew attack. As a consequence, the displacement demand on the stiff edge was in some cases larger for skew attack than for excitation in longitudinal direction. However, the maximum displacement demand on the elements was bounded by the displacement of a zero-strength eccentricity system excited along its principal direction. (note: only systems with uni-directional eccentricities were studied). Castillo's results confirmed Sommer's findings [Sommer, 2000] for systems with uni-directional eccentricity if the excitation was applied in longitudinal directions. Sommer had also studied systems

with bi-directional eccentricity, for which he found that the demand was maximum for the direction that maximised the strength eccentricity. Note that both Castillo and Sommer considered only uni-directional excitation.

7.2.5 Different design approaches for estimating the torsional response

Paulay [2001] was the first to point out that most of the earlier studies were based on the erroneous assumption that stiffness is independent of strength. He also pointed out that the elastic properties of a structural system – on which most codified provisions for torsional response were (and still are) based – are fairly irrelevant when considering the torsional response of an inelastic system. He proposed to consider the strength eccentricity e_v rather than the stiffness eccentricity e_r when assessing the in-plan irregularity of a system that is expected to respond in the nonlinear range. As a direct consequence, he suggested to aim for zero strength eccentricity when designing systems that are irregular in plan [Paulay, 1999].

Myslimaj and Tso [2002] carried out a study on the torsional response of 2D systems with the objective of identifying a criterion for the strength distribution that minimises torsional effects. Their study is based on the correct relations between element strength, stiffness and yield displacement. Unlike Paulay [1999], Myslimaj and Tso suggested that neither the stiffness nor the strength eccentricity is the most relevant measure for the irregularity of a system since during strong ground shaking a system passes through a number of stages in which none, all or some of the walls will have yielded. By means of a parametric study, they found that the rotational response was smallest for systems for which the centre of strength was located on the opposite side of the centre of mass as the centre of stiffness (Figure 7.4a). They named this type of strength distribution "balanced CV-CR location criterion". The rotational response was measured as the cumulative rotational energy of the system. It is, however, questionable whether the magnitude of rotational energy is relevant when designing a structure. It is believed that Paulay's and Castillo's design philosophy of directly addressing the displacement demand on structural elements is more appropriate. The strength distribution criterion suggested by Myslimaj and Tso leads for structures like the one shown in Figure 7.4a to the result that the short wall must be given a larger moment capacity than the long wall. As a consequence the reinforcement content of the short wall will be significantly higher than the reinforcement content of the long wall. It is questionable whether such a design approach is feasible. The design approach might be more feasible if there is a larger number of short walls along the soft edge than long walls along the stiff edge (Figure 7.4b).

Sommer [2000] derived a design method for regular asymmetric buildings (Section 7.1.1). The method is based on a force-based design approach but addresses also the displacement demand on structural elements due to the combined translational and rotational response of

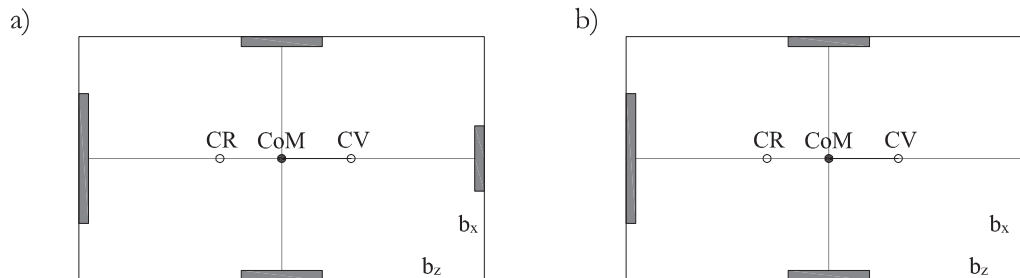


Figure 7.4. "Balanced CV-CR location criterion" according to Myslimaj and Tso [2002] for the TR system (a) and wall layout for which it might be feasible to satisfy this criterion without excessive reinforcement ratios in the short walls (b).

the system. The design method is based on Sommer's findings from linear and non-linear time-history analyses of 2D systems. Selected results of this studied were presented in Section 7.2.4. From these analyses Sommer found that the rotation of elastic systems tended to be larger than the rotation of the corresponding inelastic systems. For design purposes, Sommer therefore approximated the rotation of the inelastic system by the rotation of the elastic system. Sommer based his design recommendations on the response of planar 2D systems with three degrees of freedoms. Using response spectrum analysis he combined for each of the two horizontal axes the two contributing modes using the CQC method assuming that the frequencies of both modes lie within the constant velocity range of the spectrum (i.e. in the range where spectral displacements increase linearly with period). From the combined modal displacements Sommer derived a dynamic eccentricity e_{dyn} . This eccentricity is defined as the eccentricity with respect to the CoM at which the static design force needs to be applied to result in the estimated maximum rotation. When a force is applied at the distance e_{dyn} to the CoM, the resulting displaced shape of the elastic system is hence similar to the combined modal displacements (i.e. the CoM displacement and the rotation scale by the same factor). The displacement demand on the soft edge is computed by multiplying the displaced shape with the displacement at the CoM. Since, according to Sommer, the rotation of the elastic system is an upper bound to the rotation of the inelastic system, this method would yield in non-conservative estimates of the displacement demand on the stiff edge.

One of Castillo's [2004] central observations concerned the displacement demand on the soft edge (see also Section 7.2.4c): He found that the displacement demand on neither the soft edge nor the stiff edge increased with strength eccentricity if the strength eccentricity e_v resulted from an increase in strength with respect to the required strength for $e_v = 0$. At $e_v = 0$, the strength was distributed between the walls to satisfy static equilibrium. Castillo defined an excess strength ratio λ_i , which is the ratio of the actual strength of a wall to the required

strength of this wall when $e_v = 0$:

$$\lambda_i = \frac{V_{ni}}{V_{0i}} \quad (7.22)$$

where V_{0i} is the strength of wall i required when $e_v = 0$ and V_{ni} the actual assigned element strength. If the CoM is at midspan between Wall 1 and 2, V_{01} and V_{02} are equal. Based on the key finding that the displacement demand on the soft edge does not increase if the strength eccentricity results from excess strength Castillo suggested the following displacement oriented design procedure:

- First, the displacement capacity of each structural element is determined.
- It is then assumed that for zero strength eccentricity the displacement demands on CoM, stiff and soft edge are equal. The displacement demand of the system at zero strength eccentricity is limited to the displacement demand of the element with the smallest displacement capacity.
- The system strength required can be obtained by means of an equivalent SDoF approach (e.g. DDBD). The properties of the equivalent SDoF system are the translatory system properties for suppressed rotation (Section 7.2.3b). A strength eccentricity may be introduced to the system only if it results from one or several elements having strength in excess of the strength required for zero strength eccentricity. In this case, the displacement demand on any structural element will not be larger than for zero strength eccentricity.

Castillo's design approach is very appealing since it is simple and addresses the displacement demand on the structural elements of the stiff and soft edge directly. It will therefore be taken as the starting point for the study on 2D systems in Section 7.4.

7.3 Analysis method applied in this study and earthquake records for dynamic analyses

Within the scope of this study nonlinear time-history analyses of simple 2D models were carried out. The 2D models were similar to those used in the studies by Sommer [2000] and Castillo [2004] but apart from the uni-directional excitation with records that have linearly increasing displacements spectra also analyses with records with a constant spectral displacement range and analyses with bi-directional excitation were carried out. Some of the analyses in this study overlap with analyses by Sommer [2000] and Castillo [2004]. This redundancy was intended for two reasons: First, to validate the models used in this study and second, to give a more complete picture regarding the key parameters controlling the torsional response

of in-plan asymmetric systems. From the results of the parametric studies of 2D systems, semi-empirical equations are derived in Section 7.5 that can be used to estimate the displacement demand at the stiff and soft edge of the structure as a function of the displacement demand at the centre of mass. These equations can be employed to extend the DDBD approach to buildings that are asymmetric in-plan.

As Sommer's and Castillo's studies, most of the following parametric studies will be carried out considering one component of the horizontal ground motion only. This is of course a simplification but with this approach it is easier to identify the parameters controlling the torsional response. At a later stage, the models were analysed for bi-directional input motion from recorded accelerograms. Three different sets of records are used for the analysis of the 2D systems:

- Set A: Set A contains five artificial accelerograms with a single horizontal component only. The displacement spectra increase linearly to about 4s, which is the upper limit of the period range of interest.
- Set B: As Set A, Set B consists of five artificial accelerograms with a single horizontal component. The corner period of displacement spectra of the records in Set B is, however, only 2s. For longer periods the spectral displacement is approximately constant.
- Set C: Set C contains 20 real accelerograms with both horizontal components.

7.3.1 Design spectrum and artificial accelerograms with a corner period of $T_D = 4\text{s}$ (Set A)

The 2D systems were designed for a displacement spectrum with spectral displacement of $S_{d,5\%} = 0.6\text{m}$ at $T_D = 4\text{s}$. The five artificial accelerograms of Set A were generated by Priestley and Amaris [2002] using the program Simqke [Carr, 2003]; Priestley and Amaris used the accelerograms in their study on cantilever walls. The duration of all accelerograms was 25s. The five accelerograms matched in average the design spectrum up to the corner period T_D . Beyond the corner period the average spectrum of the accelerograms increased almost linearly with period whereas the target spectrum was level. However, periods greater than $T_D = 4\text{s}$ were of minor concern in the parametric study carried out here since the effective periods of the examined systems were smaller than 4s. The response of higher damped SDoF systems were approximately spectrum compatible if the target spectrum is adjusted according to the formula in the meanwhile superseded version of EC8 [CEN, 1994]:

$$S_{d,\xi} = S_{d,5\%} \sqrt{\frac{7}{2 + \xi}} \quad (7.23)$$

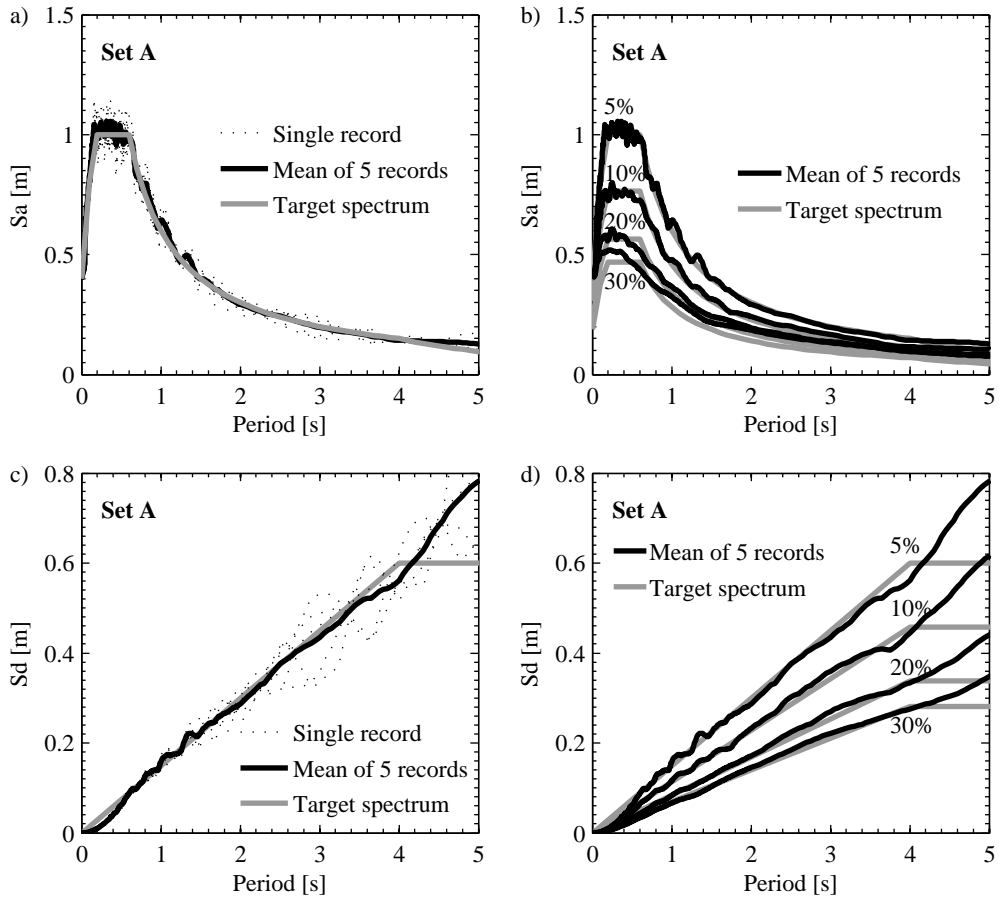


Figure 7.5. Acceleration and displacement spectra for the five artificial records of Set A.

The acceleration and displacement spectra are shown in Figure 7.5. The accelerograms of Set A are used for the analyses in Section 7.4.2 to 7.4.6.

7.3.2 Artificial accelerograms with a corner period of $T_D = 2\text{s}$ (Set B)

To investigate the behaviour of structural systems with effective periods longer than the corner period of the displacement spectrum, a second set of artificial accelerograms was generated using the program Simqke [Carr, 2003]. The duration of all accelerograms was again 25s. The corner period of the target displacement spectrum was reduced to 2s and when selecting the accelerograms care was taken that the displacement spectra of the accelerograms was in deed

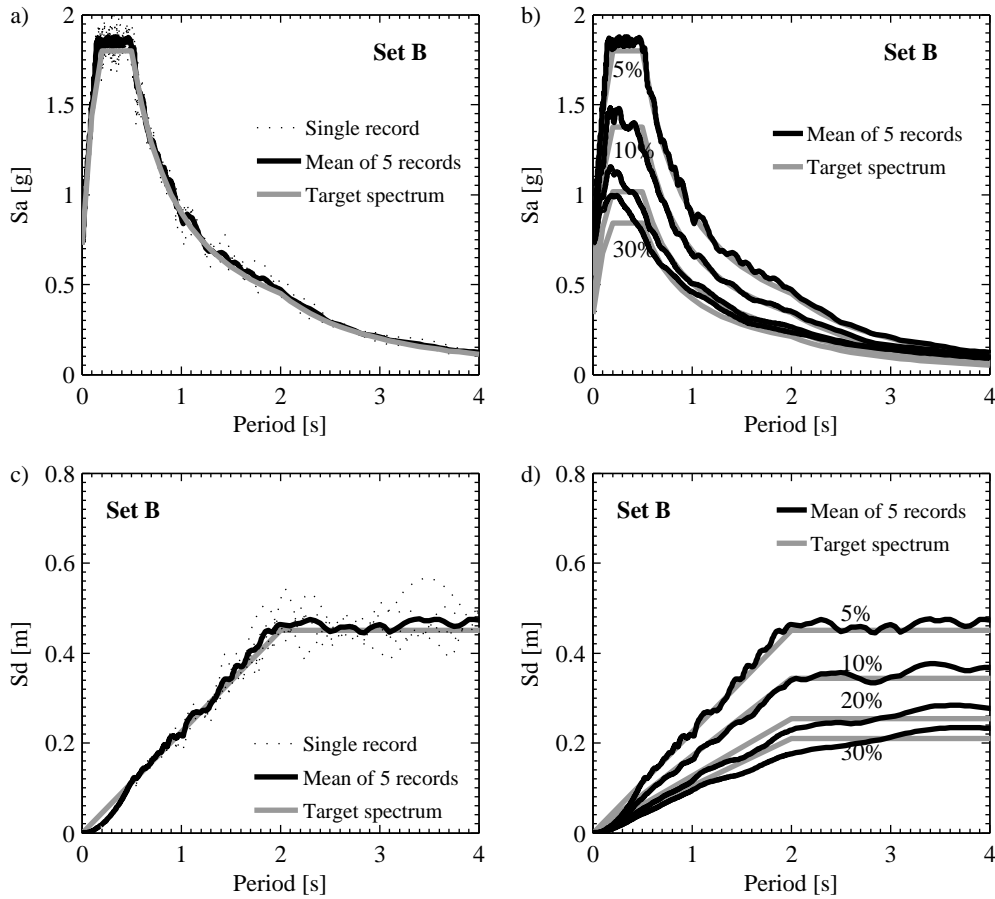


Figure 7.6. Acceleration and displacement spectra for the five artificial records of Set B.

level for periods greater than the corner period $T_D = 2$ s. The average of the five accelerograms has a spectral displacement of about 0.45 m for $T_D = 2$ s and $\xi = 5\%$. The acceleration and displacement spectra for the accelerograms of Set B are shown in Figure 7.6. The accelerograms were used for the analyses in Section 7.4.5.

7.3.3 Real records for bi-direction analysis (Set C)

Set C contains twenty ground motions consisting each of the two horizontal translational components. The ground motions were selected from the NGA-database [PEER, 2005] to match the shape of the geometric mean displacement target spectrum. The records were then

scaled by factors between 0.83 and 5.88 in order to achieve a good match of the absolute ordinates; the two components of one record were scaled by the same factor. The geometric mean $S_{d,GM}$ of the two horizontal spectral displacements $S_{d,x}$ and $S_{d,y}$ at the period T_i is defined as

$$S_{d,GM}(T_i) = \sqrt{S_{d,x}(T_i) \cdot S_{d,z}(T_i)} \quad (7.24)$$

The geometric mean of the spectral accelerations is defined accordingly. Figure 7.7 shows the geometric mean acceleration (plots a and b) and displacement (plots c and d) spectra. The displacement spectra of the individual components for 5% damping are shown in Figures 7.7e and f. The records are used for the analyses presented in Section 7.4.7.

7.4 Torsional response of 2D systems

The aim of the parametric study is to identify the key parameters that affect the displacement demand on the structural elements of an in-plan asymmetric systems (see Section 7.3). The investigated parameters are the following:

- Strength eccentricity (Section 7.4.2)
- Rotational inertia (Section 7.4.3)
- Seismic intensity (Section 7.4.4)
- Spectral shape (Section 7.4.5)
- Skew attack (Section 7.4.6)
- Second horizontal component of ground motion (Section 7.4.7)

Both TR and TU systems are covered. However, the focus is set on TR systems since the conceptual design of new buildings should aim for layouts of the lateral strength providing system that correspond to TR systems. TU systems are therefore only treated within the first three sections (Sections 7.4.2 to 7.4.4), which examine the effect of system properties on the torsional response. In the last three sections (Sections 7.4.5 to 7.4.6), in which the effect of the seismic input is investigated, only TR systems were analysed. In the next section the properties of the investigated systems are summarised. The results of the parametric study will be presented in the then following sections and are summarised at the end of this chapter.

7.4.1 TR and TU 2D systems for parametric study

The parametric studies on TR and TU systems are based on an 8-storey RC wall structure (Figure 7.8a). The height of the building is 24m; the building has a storey mass of $M = 309t$

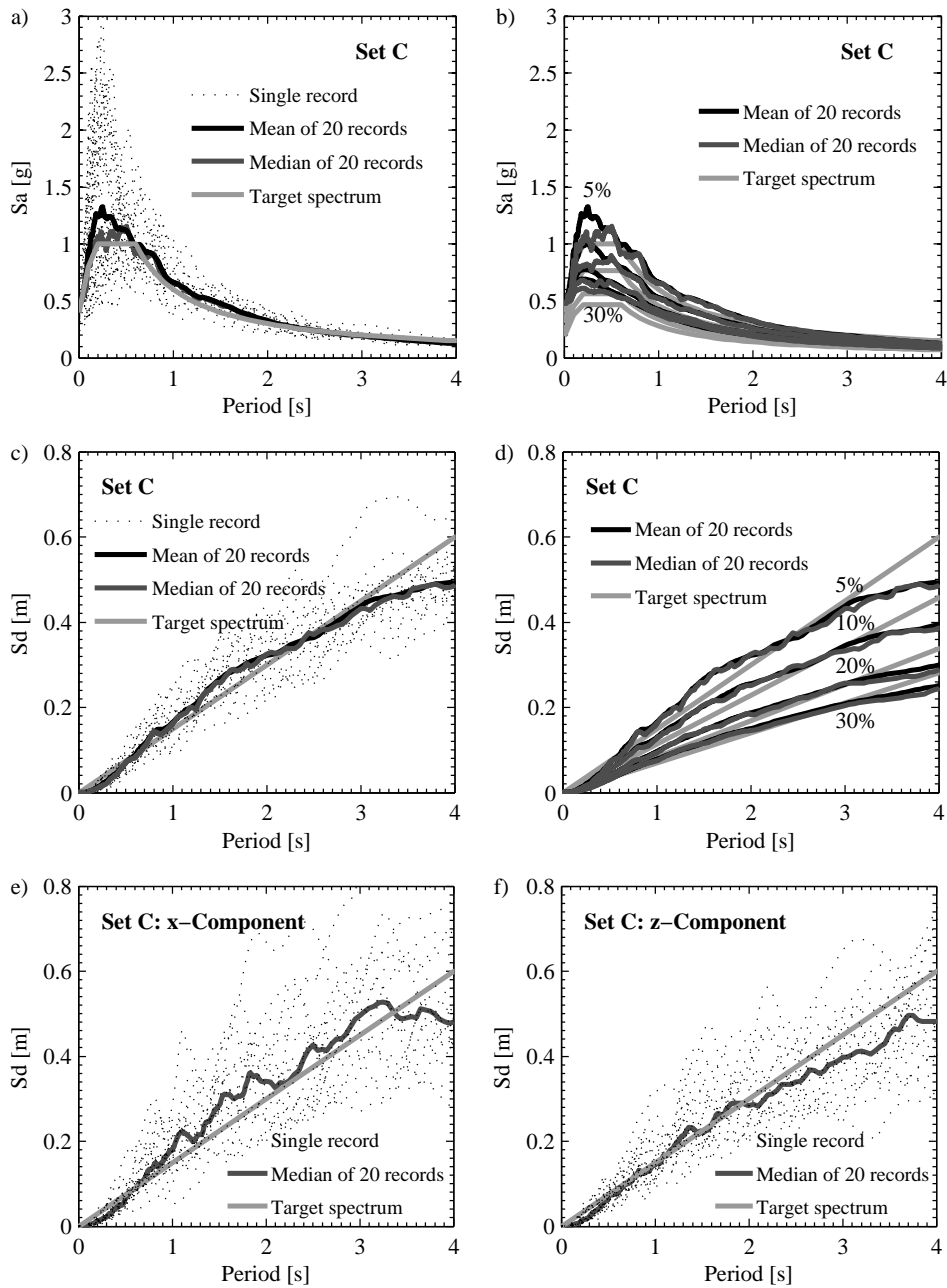


Figure 7.7. Acceleration (a and b), and displacement spectra (c-f) for the 20 artificial records of Set C. Plots a-d show the geometric mean of the spectral acceleration and the spectral displacement respectively. Plots e and f show the displacement spectra for the horizontal ground motion components in x and z direction.

and a rotational inertia per storey of $I_{rot} = 23200\text{tm}^2$. The floor diaphragms are assumed to be rigid in plane; the floor dimensions are 25m x 15m.

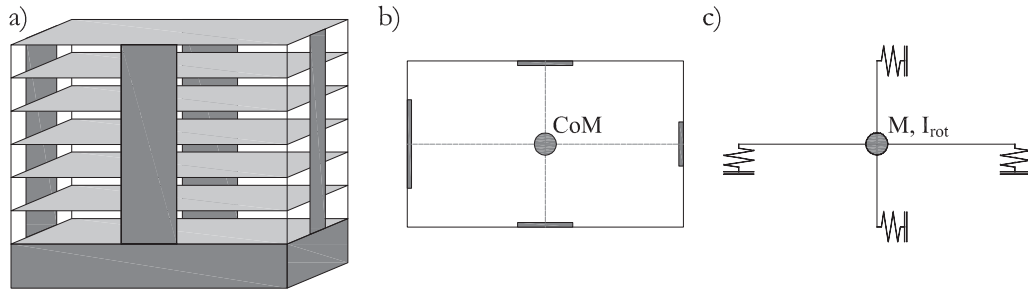


Figure 7.8. Approximation of a 3D system by a 2D system with springs and lumped mass: Example of a 3D wall-type structure (a), plan view of the asymmetric system (b), 2D system with springs and lumped mass (c).

As outlined in Section 7.2.3, regular asymmetric 3D systems can be approximated by horizontal 2D systems. The force-displacement relationship of each structural wall was represented by a bi-linear spring (Figure 7.8c). The structural walls were represented by their effective properties, i.e. the flexibilities at the effective height ($h_{eff} = 17.8\text{m}$) and the base shear forces. The effective mass ($m_{eff} = 1788\text{t}$) was lumped at the centre of mass. It was assumed that the ratio of effective rotational inertia to storey inertia and effective mass to storey mass were equal. The effective rotational inertia was therefore $I_{rot,eff} = 1.36 \cdot 10^5\text{tm}^2$.

The plan layout of the TR and TU building and the 2D representation of the building with springs are shown in Figures 7.9 and 7.10. Both systems have four walls, which are labelled with numbers from 1 to 4. The longitudinal walls are 8m and 4m long. In the following the 8m wall is labelled as "Wall 1", the shorter wall as "Wall 2". The transverse Walls 3 and 4 have the same dimensions ($l_w = 5.0\text{m}$) and strengths. The "longitudinal direction" is the direction parallel to Wall 1 and 2 (x direction) while the "transverse direction" is the direction parallel to Wall 3 and 4 (z direction).

Using the DDBD method the walls were designed for a maximum drift of 2%. The design spectrum has a spectral displacement of $S_{d,5\%} = 0.6\text{m}$ at 4s (Section 7.3.1). For critical damping ratios greater than 5% the spectral displacements were adjusted according to Equation 7.23. To limit the displacement of the transverse walls (Walls 3 and 4) to 2% drift, the walls required each a nominal moment capacity of 17400kNm assuming a post-elastic stiffness ratio $r_F = 0.05$. The nominal base shear of each transverse wall equated to $V_n = 977\text{kN}$. Using Equation 7.5 the yield displacement at the effective height was 0.107m. The plastic hinge length L_{ph} was computed for all walls as the maximum of the following two equations [Paulay

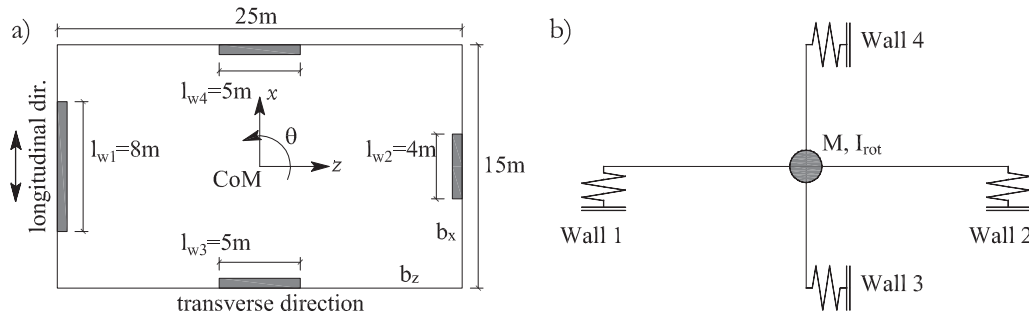


Figure 7.9. TR system for parametric study: Plan layout of floor system (a) and 2D representation of the structure with springs and lumped mass (b).

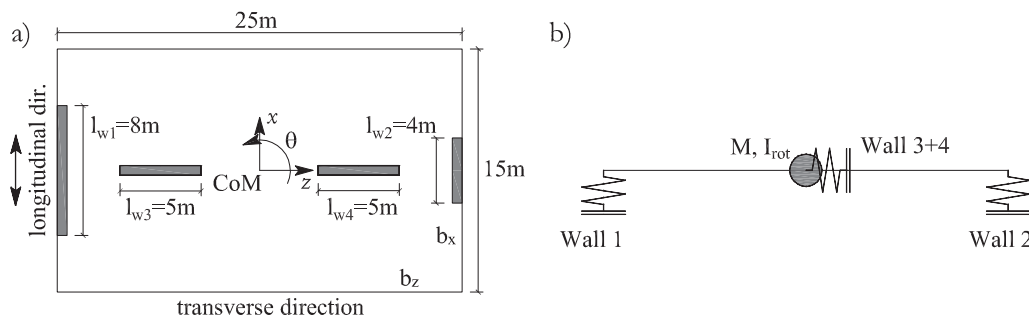


Figure 7.10. TU system for parametric study: Plan layout of floor system (a) and 2D representation of the structure with springs and lumped mass (b).

and Priestley, 1992]:

$$\begin{aligned} L_{pb} &= 0.2l_w + 0.03h_n \\ L_{pb} &= 0.054h_n + 0.022f_y d_b \end{aligned} \quad (7.25)$$

where l_w is the wall length in metre, h_n the entire height of the building in metre, f_y the yield strength in MPa of the main vertical bars and d_b the diameter of the main vertical bars in millimetres.

In the longitudinal direction, Wall 1 and 2 were designed for zero strength eccentricity. Following Castillo's observations (Section 7.2.5), nominal rotations were small if the strength eccentricity diminished and hence the displacement demand on the long and short wall are expected to be approximately equal. For the same displacement, the drift of a shorter, free-standing wall is greater than the drift of a longer free-standing wall. It is assumed that the displacement profiles of the two walls can be approximated by those of free-standing walls

neglecting the effect of any forces transmitted by the floor diaphragms on the displacement profiles.

Limiting the drift of the short wall to 2% and designing the system for zero strength eccentricity yields in nominal moment capacities of $M_n = 16690\text{kNm}$ ($V_n = 937\text{kN}$) for both the long and the short wall (Wall 1 and 2). At maximum displacement the two walls reach not the same moment since the curvature ductilities at the maximum displacement differ by about a factor of two ($\mu_{\varphi 1} > \mu_{\varphi 2}$). The strength eccentricity at the maximum displacement was approximately $1.0\text{m} = 0.04b_z$. The design displacement of 0.253m corresponded for the long wall (Wall 1) to a displacement ductility of $\mu_{\Delta 2} = 3.82$ and for the short wall (Wall 2) to a displacement ductility of $\mu_{\Delta 1} = 1.85$. The properties of the transverse walls and the longitudinal walls when designed for zero strength eccentricity are summarised in Table 7.1; the system properties are given in Table 7.2. The hysteretic behaviour of the walls was modelled by means of the modified Takeda rule with the unloading stiffness parameter $\alpha = 0.5$ and the reloading stiffness parameter $\beta = 0.0$.

Table 7.1. 2D parametric study on TR systems: Properties of the walls when designed for zero strength eccentricity.

	l_w [m]	t_w [m]	I_{pb} [m]	Δ_y [m]	Δ_d [m]	μ_{Δ} [-]	k_i [kN/m]	V_n [kN]	r_F [-]
Wall 1	8.0	0.20	2.32	0.066	0.253	3.82	14160	937	0.05
Wall 2	4.0	0.30	1.52	0.136	0.253	1.85	6890	937	0.05
Wall 3+4	5.0	0.20	1.72	0.107	0.267	2.49	9120	977	0.05

t_w Wall thickness
 r_F Post-elastic stiffness ratio

Table 7.2. 2D parametric study on TR systems: Properties of the system when designed for zero strength eccentricity.

	$V_{n,s}$ [kN]	K [kN/m]	$\Delta_{y,s}$ [m]	Δ_d [m]	$\mu_{\Delta,s}$ [-]
longitudinal direction (x)	1874	21050	0.089	0.253	2.84
transverse direction (z)	1954	18240	0.107	0.267	2.49

The first two natural periods of the 2D system with three degrees of freedom were about 1.97s , the third natural period was 1.09s . The first mode shape consisted of a translational component in the x direction and a rotational component. The second mode shape was a

pure translation in the z direction. The third mode shape was predominately a rotational movement with some translation in the x direction. The nonlinear time-history analyses of the 2D systems were carried out using the structural analysis program "Ruaumoko3D" [Carr, 2004], which was also used by Castillo [2004] for his parametric study on 2D systems. The analyses were performed with tangent-stiffness proportional Rayleigh damping with 5% damping for the second mode.

7.4.2 Strength eccentricity

To investigate the effect of strength eccentricity on the displacement demand on the stiff and soft edge, the strength of the stiff edge was successively increased. The TR and TU systems that were described in Section 7.4.1 had zero strength eccentricity. By increasing the strength of the long wall, the strength eccentricity e_v increased and the centre of strength CV moved towards the longer wall. The same applied to the stiffness eccentricity and the centre of stiffness CR since stiffness is directly related to strength (Equation 7.4). The increase in strength of Wall 1 corresponded to excess strength factors λ_1 between 1.1 – 1.8. The strength of Wall 2, 3 and 4 remained unaltered (i.e. $\lambda_i = 1.0$). The properties of the nine systems corresponding to $\lambda_1 = 1.0 – 1.8$ are given in Table 7.3. Figure 7.11 shows the strength and stiffness eccentricity and the total base shear capacity in the z direction as a function of λ_1 . Note that the values of λ_1 on the x axis are increasing from the right to the left since CV and CR in Figures 7.9 and 7.10 move to the left towards Wall 1. This convention is also applied in all following figures that show the strength eccentricity ratio e_{vz}/b_z on the x axis.

Table 7.3. 2D systems with different strength eccentricities.

Strength Ecc.		Wall 1		Wall 2		Wall 3+4		System	
λ_1	e_{vz}/b_z	V_{n1}	k_1	V_{n2}	k_2	$V_{n3,4}$	$k_{3,4}$	V_{nxs}	V_{nzs}
		[kN]	[kN/m]	[kN]	[kN/m]	[kN]	[kN/m]	[kN]	[kN]
1.0	0.000	937	14160	937	6890	977	9120	1870	1950
1.1	-0.024	1030	15570	937	6890	977	9120	1970	1950
1.2	-0.046	1130	16990	937	6890	977	9120	2060	1950
1.3	-0.065	1220	18400	937	6890	977	9120	2160	1950
1.4	-0.083	1310	19820	937	6890	977	9120	2250	1950
1.5	-0.100	1410	21240	937	6890	977	9120	2340	1950
1.6	-0.115	1500	22650	937	6890	977	9120	2440	1950
1.7	-0.130	1590	24070	937	6890	977	9120	2530	1950
1.8	-0.143	1690	25480	937	6890	977	9120	2620	1950

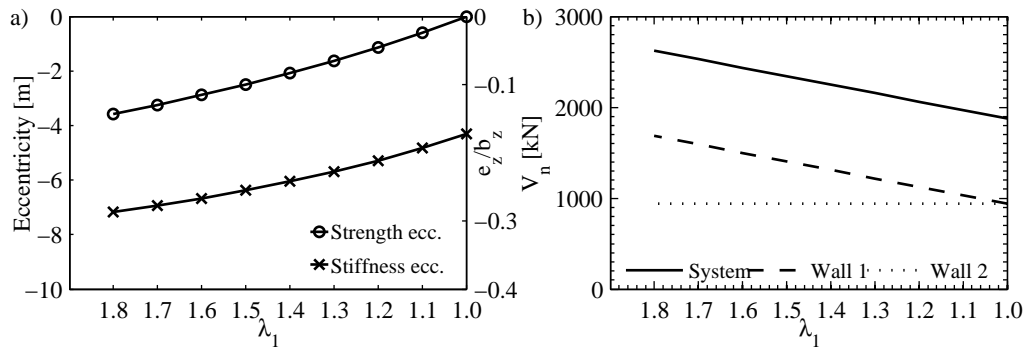


Figure 7.11. 2D systems with strength eccentricity: stiffness and strength eccentricity (a) and element and system strength (b) as a function of the excess strength ratio λ_1 .

Figure 7.12a shows the variation of the displacement demand on the CoM, the stiff edge (Wall 1) and the soft edge (Wall 2) for the different strength eccentricity ratios e_{vz}/b_z . Plotted are only the average results of the five time-history analyses. The average was here defined as the average of the absolute maximum displacements, i.e. the sign of the displacement demands was omitted. The results confirmed the following findings by Castillo [2004]: First, the displacement demand on the CoM and the stiff edge reduced with increasing strength eccentricity (the strength eccentricity is plotted as negative values to make the figure compatible with the sketch of the 2D system in Figure 7.9). Note that this is chiefly caused by the increase in system strength with increasing strength eccentricity ratio (Table 7.3). Second, the displacement demand on the soft edge remained fairly constant for the range of strength eccentricities that were investigated. Contrary to Castillo's finding, the displacement demands on the CoM, stiff and soft edge at zero strength eccentricity were not exactly equal. At zero strength eccentricity the stiffness eccentricity was -4.32m , which corresponded to $e_{rz}/b_z = -0.17$. Hence, it appears that the stiffness eccentricity had some influence on the displacement demand. Castillo analysed mainly systems that were subjected to larger displacement ductility demands than the ductility demands applied in this study. It appears that the influence of the stiffness eccentricity on the displacement demands on the structural elements is larger for smaller displacement ductilities than for larger displacement ductilities. This will be further investigated in Section 7.4.4.

Figure 7.12b shows the maximum and the nominal rotation. A definition of the nominal rotation was given in Section 7.2.3b. The maximum rotation is the maximum rotation of the in-plane rigid system that occurred over the course of the earthquake. The nominal rotation was about 20 – 25% smaller than the maximum rotation.

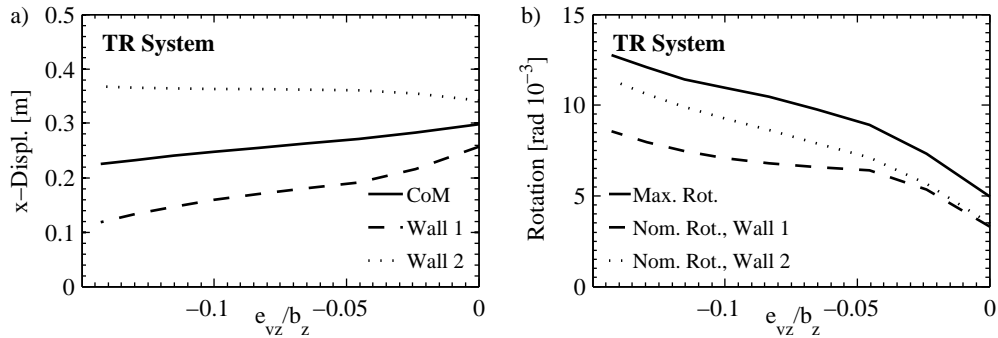


Figure 7.12. TR system: Displacement demand on CoM, stiff and soft edge (a) and maximum and nominal rotation (b) for different strength eccentricity ratios e_{vz}/b_z .

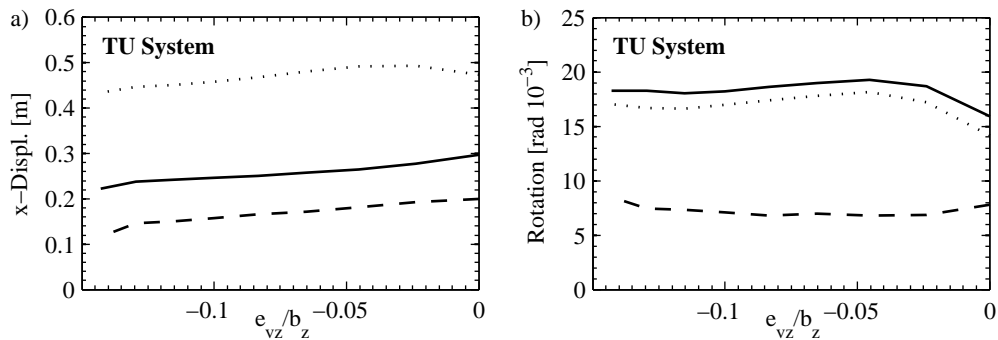


Figure 7.13. TU system: Displacement demand on CoM (solid line), stiff edge (dashed line) and soft edge (dotted line) (a) and maximum and nominal rotation for different strength eccentricity ratios e_{vz}/b_z (b).

Figure 7.13 contains the same information as Figure 7.12 but this time for the TU system instead of the TR system. The layout of the TU system was shown in Figure 7.10. The element properties were the same as for the TR system (Table 7.3). Comparing the displacement demands for the TU system to those of the TR system, it becomes obvious that the loss of the torsional restraint affected in particular the displacement demand on the soft edge (Wall 2): For $e_{vz} = 0$ it increased from about 0.34m to about 0.47m. The displacement demand on the stiff edge was slightly reduced for small strength eccentricities while the displacement demand on the CoM was about the same for TR and TU systems. The maximum and nominal rotations (Figure 7.13b) were almost independent of the strength eccentricity. This is a fundamental difference between TU and TR systems; for the latter both maximum and nominal rotations increased with strength eccentricity (Figure 7.12b).

In Figures 7.14 and 7.15 the displacement demands on the TR and TU systems with inelastic elements are compared with the displacement demands for the equivalent elastic systems. For the TR system, the difference in displacement demands between the elastic and the inelastic model was not very significant if the strength eccentricity was larger than $e_{vz}/b_z \geq 0.07$. The small difference is probably related to the only very brief excursions of Wall 1 into the inelastic range. For $e_{vz}/b_z = 0.0$, the displacement ductility demand on Wall 1 is about $\mu_{\Delta 1} = 3.9$ while for $e_{vz}/b_z = 0.07$ the displacement ductility demand on Wall 1 is reduced to about $\mu_{\Delta 1} = 2.7$. The nominal and maximum rotations of the TR system were generally greater for the elastic than for the inelastic model. This confirms Sommer's [2000] finding that approximating the rotation demand of the inelastic system by the rotation demand of the elastic system is generally a conservative assumption. However, for $e_{vz}/b_z = 0.14$ the maximum rotation is just about larger for the inelastic than for the elastic system. Hence, it is possible, that for extreme eccentricities Sommer's assumption no longer holds. Such systems with extreme strength and stiffness eccentricities are, however, not the subject of this study because very uneven plan layouts should generally be avoided.

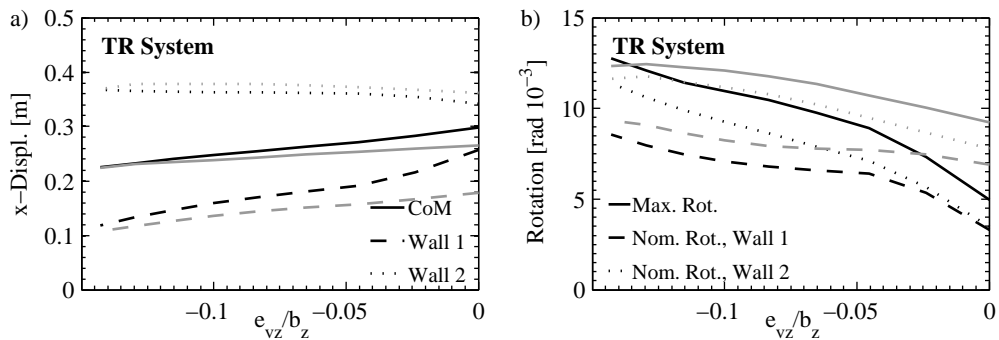


Figure 7.14. TR system: Comparison of displacement (a) and rotation (b) demand for elastic (grey lines) and inelastic (black lines) systems.

For TU systems the difference in displacement demands between the elastic and the inelastic system is generally larger than for TR systems. When the elastic system is taken as a proxy of the inelastic system, it significantly underestimates the displacement demand on the soft edge and the nominal and maximum rotation. Hence, for TU systems Sommer's approximation is not valid. His design approach should be limited to newly designed buildings that correspond to TR systems with only medium-sized eccentricities ($e_{vz}/b_z < 0.15$). The elastic model also underestimated to a lesser extent the displacement demand on the CoM and the stiff edge.

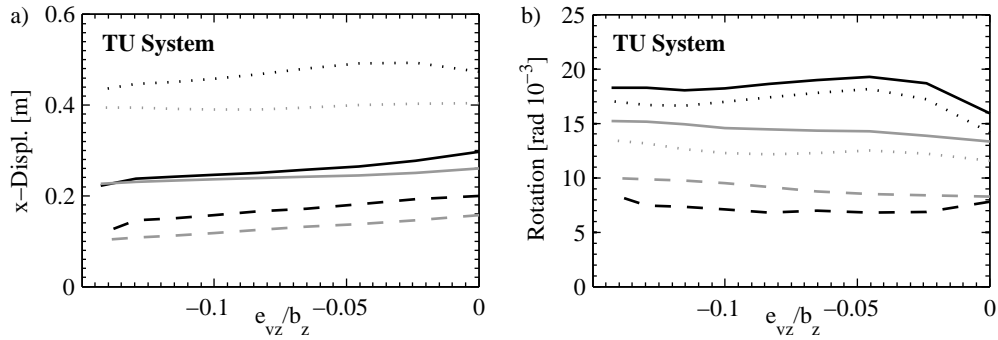


Figure 7.15. TU system: Comparison of displacement (a) and rotation (b) demand for elastic (grey lines) and inelastic (black lines) systems. For the legend the reader is referred to Figure 7.14.

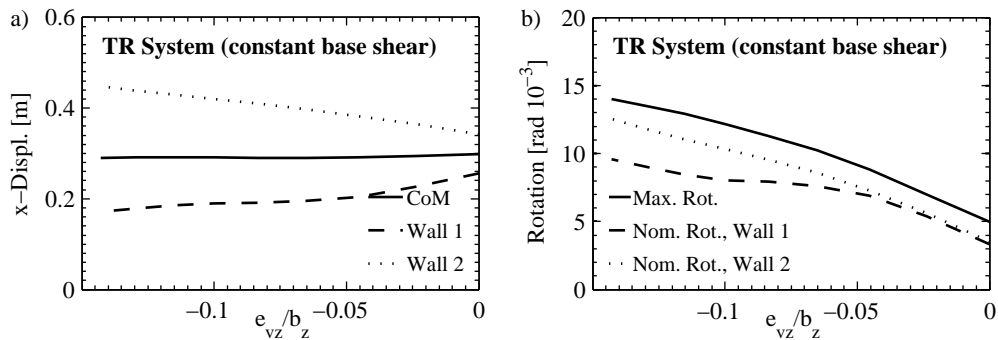


Figure 7.16. TR systems with constant base shear: Displacement demand on CoM (solid line), stiff edge (dashed line) and soft edge (dotted line) (a) and maximum and nominal rotation for different values of e_{vz}/b_z (b).

To stress the effect of the rule that – in order to protect the soft edge from excessive displacement demands – strength eccentricity should result from element strength in excess of the strength required at $e_v = 0$, analysis results of systems are presented for which this rule was *not* observed. For this purpose a set of TR systems were analysed with strength eccentricities between $0.0 - 0.14e_{vz}/b_z$. The layout of the systems and the properties of Wall 3 and 4 are identical to the systems analysed previously (Figure 7.9, Table 7.3). However, the increase in strength of Wall 1 was compensated by a decrease in strength of Wall 2 so that the base shear remained constant for all strength eccentricities ($V_{ms} = 1870kN$). The stiffnesses of Wall 1 and 2 were adjusted accordingly. Figure 7.16a shows the displacement demand on the CoM and the stiff and soft edge. The displacement demand on the CoM was relatively independent of the strength eccentricity. This confirms the finding by Castillo [2004] that the CoM displacement

can be estimated assuming a pure translational movement of the mass. The nominal rotations of the stiff and soft edge (Figure 7.16b) increased with strength eccentricity; this was also observed for the former analyses of TR systems for which the strength eccentricity resulted from excess strength (Figure 7.12b). Unlike in the latter cases, the displacement demand on the soft edge increased with strength eccentricity since the CoM displacement was approximately the same for all analysed strength eccentricities.

7.4.3 Effect of the rotational inertia

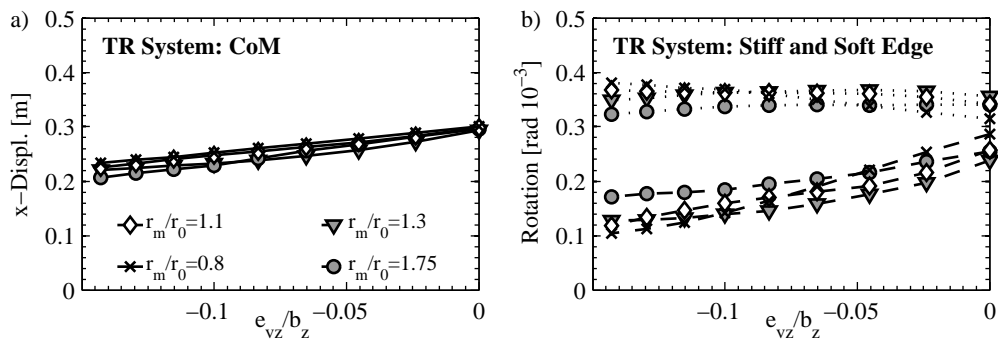
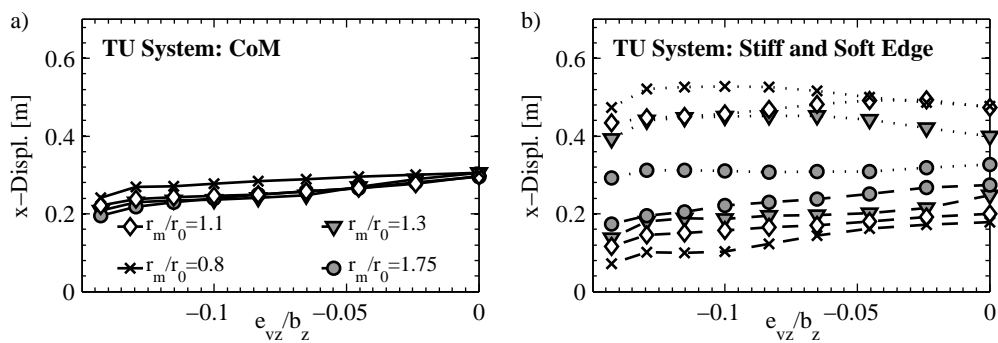
In the previous analyses the translatory mass of the 2D system was 1788t and the rotational inertia $I_{rot} = 1.36 \cdot 10^5 \text{tm}^2$. Hence, the radius of gyration of mass was $r_m = 8.72\text{m}$. The reference radius r_0 , which corresponds to the radius of gyration of mass of a square slab with the same area and uniformly distributed mass (Equation 7.11), was 7.91m. The previous analyses had thus a ratio of $r_m/r_0 = 1.1$. In this section the rotational inertia will be altered to yield r_m/r_0 ratios of 0.8, 1.3, 1.5 and 1.75. The mass and rotational inertia of the 2D systems as well as the resulting r_v/r_m ratios are given in Table 7.4.

Figures 7.17 and 7.18 show the effect of the rotational inertia on the displacement demand on the CoM and the stiff and soft edges for the TU and the TR systems, respectively. Castillo [2004] had noted that – as long as the rotational inertia is larger than zero – the magnitude of the rotational inertia has only a negligible effect on the displacement demands of the structural elements for excitation parallel to a principal axis. This was not quite confirmed with this parametric study: The displacement at the CoM was indeed relatively independent of the rotational inertia but the displacement demand on the edges varied with rotational inertia. The variation was particularly significant for the TU systems in which no transverse elements were present that could restrain the rotation. For TU systems the trends in displacement demand on the stiff and soft edge were relatively clear: The greater the rotational inertia, the smaller was the nominal rotation. As a consequence, for an increasing rotational inertia, the displacement demand on the soft edge reduced while the displacement demand on the stiff edge increased.

For the TR systems the trends with rotational inertia in displacement demands on the stiff and soft edges were less clear (Figure 7.17). For $e_{vz} = 0$, for example, the r_m/r_0 ratio of 1.3 led to the greatest displacement demand on the soft edge. The displacement demand for the same strength eccentricity and a r_m/r_0 ratio of 0.8 was about 20% smaller. For $e_{vz}/b_z = -0.14$, the trends in displacement demand with rotational inertia were again the same as for the TU system; the dependence of the displacement demand on the rotational inertia was, however, considerably weaker. The variable relationship between displacement demand and rotational inertia was probably caused by the interplay of rotational restraint and rotational energy,

Table 7.4. 2D systems with different rotational inertias.

	M [t]	I_{rot} [tm ²]	$\lambda_1 = 1.0$ r_{vx}/r_m	$\lambda_1 = 1.8$ r_{vx}/r_m	$\lambda_1 = 1.0 - 1.8$ r_{vz}/r_m
$r_m/r_0 = 1.1$	1788	$1.36 \cdot 10^5$	1.44	1.60	0.86
$r_m/r_0 = 0.8$	1788	$0.72 \cdot 10^5$	1.98	2.21	1.19
$r_m/r_0 = 1.3$	1788	$1.89 \cdot 10^5$	1.22	1.36	0.73
$r_m/r_0 = 1.75$	1788	$3.42 \cdot 10^5$	0.90	1.01	0.54

Figure 7.17. TR system: Comparison of displacement demands on CoM (a) and stiff and soft edges (b) for different values of rotational inertia expressed in terms of r_m/r_0 -ratios.Figure 7.18. TU system: Comparison of displacement demands on CoM (a) and stiff and soft edges (b) for different values of rotational inertia expressed in terms of r_m/r_0 -ratios.

which were both related to the transverse elements and the rotational inertia. Note that the difference between TR and TU systems manifests itself also when the boundary case of zero rotational inertia is considered: In a TR system with zero rotational inertia both longitudinal elements could still reach the inelastic state because the transverse elements can establish moment equilibrium. This is different to the TU systems, in which the absence of rotational inertia would imply that the stronger element would have to remain elastic (Section 7.2.3a). For an infinitely large rotational inertia the rotation of both TR and TU systems would be fully restrained and not rotate at all.

From the results of the analyses it can be concluded that the effect of the rotational inertia on the displacement demand of TR systems is relatively small for typical values of rotational inertia. Hence, it seems feasible to neglect the influence of the rotational inertia when designing a TR structure using displacement-based design principles.

7.4.4 Different seismic intensities

To investigate the effect of the seismic intensity on the displacement demand, the five artificial records were scaled up and down by 50%. The original records are referred to as records of 100% intensity, the newly scaled records have hence intensities of 50% and 150%, respectively. The TR and TU systems as described in Section 7.4.1 were again used when investigating the effect of seismic intensity. The left hand column of the plots in Figure 7.19 shows the displacement demand on the CoM, Wall 1 and Wall 2 while the ductility demands are shown by the plots in the right hand column. Note that, according to Equation 7.7, the system yield displacement is not independent of λ_1 . The system yield displacement reduced from $\Delta_{ys} = 0.089\text{m}$ for $\lambda_1 = 1.0$ ($e_{vz}/b_z = 0.0$) to $\Delta_{ys} = 0.081\text{m}$ for $\lambda_1 = 1.8$ ($e_{vz}/b_z = -0.14$).

Independently of the intensity, the overall trends were the same: The displacement demand on the CoM and the stiff edge reduced with increasing strength eccentricity that was coupled to an increase in strength of Wall 1 whereas the displacement demand on the soft edge remained fairly independent of the strength eccentricity. For 150% intensity, there was a slight increase in displacement demand on the soft edge with strength eccentricity, which was probably caused by the fact that the displacement demand on the CoM did not decrease at the same rate for strength eccentricities greater than $0.02e_{vz}/b_z$ as for smaller strength eccentricities. For 50% intensity the behaviour of the system was almost elastic and the trends that have been observed for inelastic behaviour were also confirmed for this range of demand. At zero strength eccentricity, the displacement demands on the system, Wall 1 and Wall 2 were similar but the displacement ductilities differed significantly (Figure 7.19). Wall 1 and Wall 2 were subjected to approximately equal ductility demands at $e_{vz}/b_z \cong -0.07$ and $e_{vz}/b_z \cong -0.09$ for 100% and 150% intensity, respectively. This observation coincided with the finding by

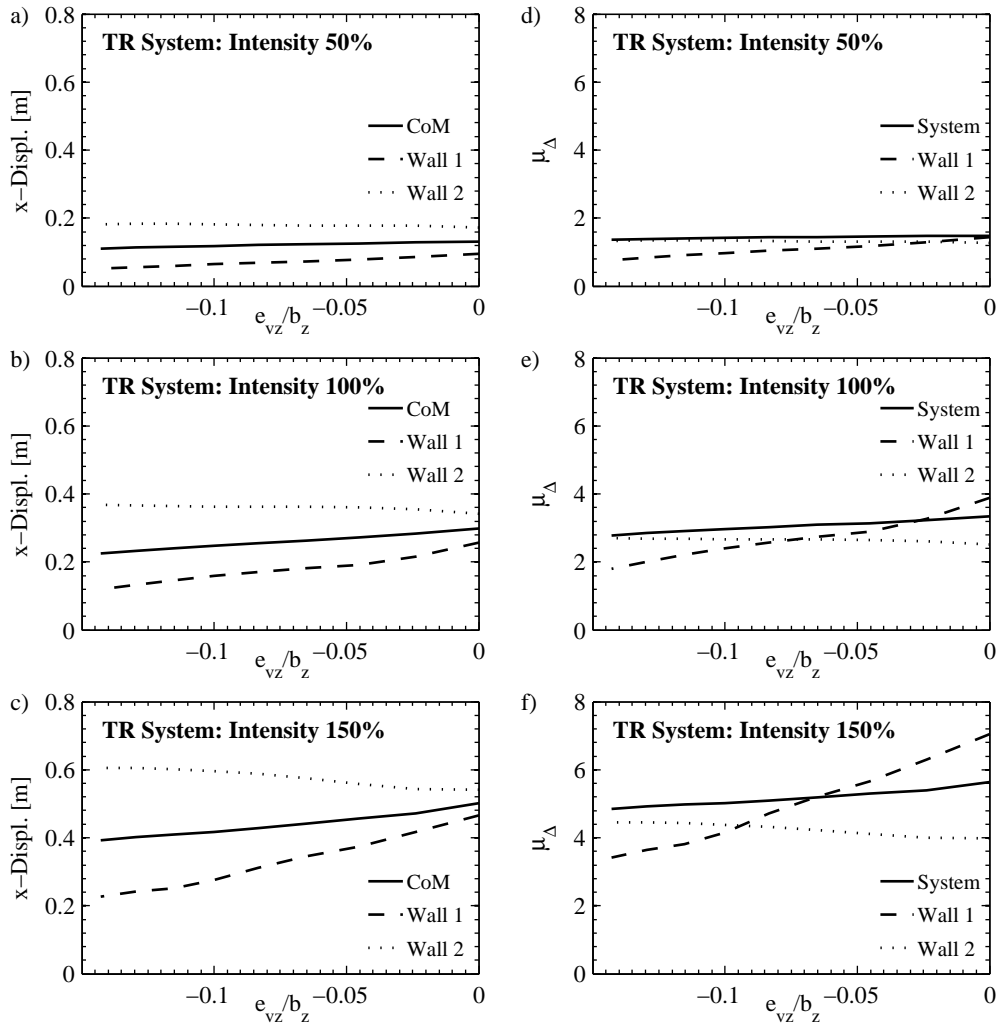


Figure 7.19. TR system: Comparison of displacement (a-c) and ductility (d-f) demands on CoM and stiff and soft edges for different seismic intensities.

Sommer [2000] who noted that ductility demands on the walls were approximately equal if some strength eccentricity was present. For TU systems (Figure 7.20d-f) the eccentricities that resulted in approximately the same ductility demand on the two walls were smaller than for TR systems.

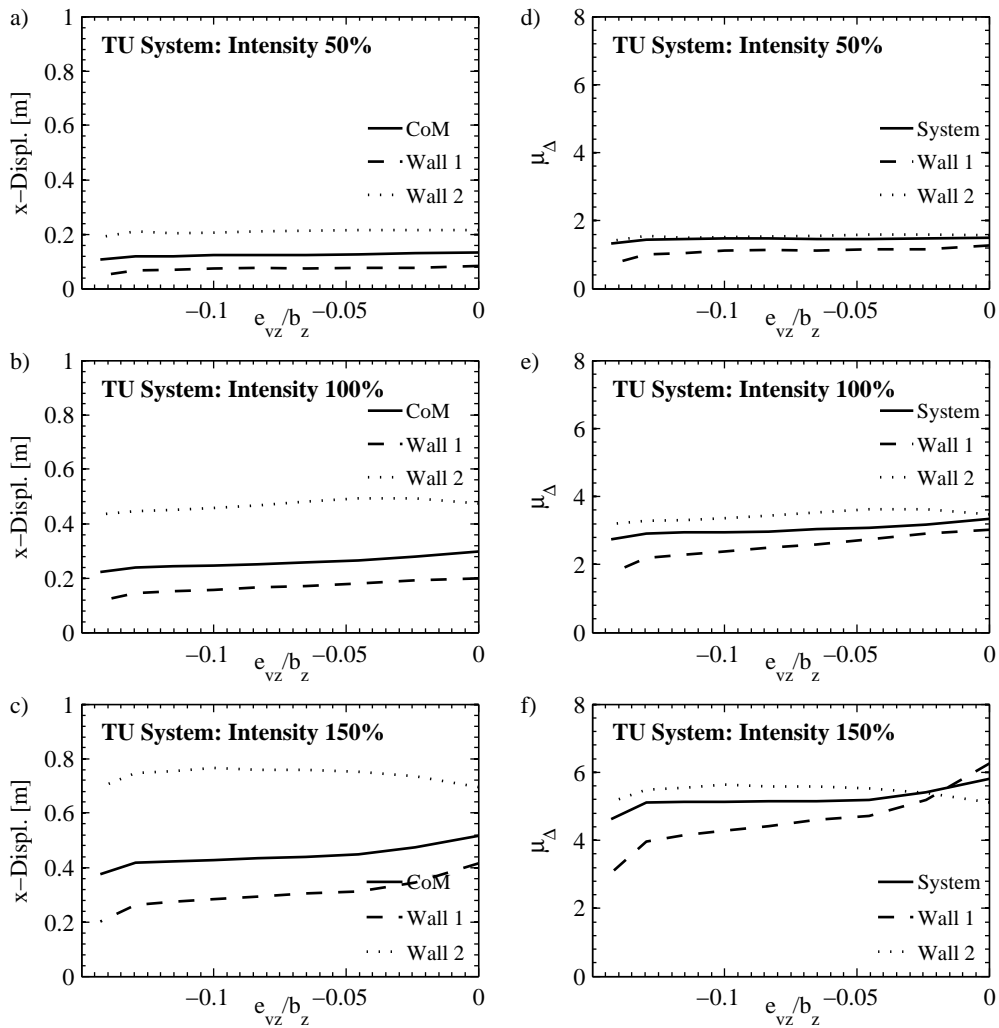


Figure 7.20. TU system: Comparison of displacement (a-c) and ductility (d-f) demands on CoM and stiff and soft edges for different seismic intensities.

It is interesting to note that for the TR system with zero strength eccentricity the difference in displacement demand between the CoM and the structural elements was almost independent of the seismic intensity (Table 7.5). Since the strength eccentricity was zero, the difference in displacement demands must have been controlled by the stiffness eccentricity, which was caused by the fact that one wall was twice as long as the other (Figure 7.11). For the TU system, however, the difference in displacement demand on the CoM and Wall 1 or 2 ($\Delta_i - \Delta_{CoM}$) at zero strength eccentricity varied with intensity (Table 7.6).

Table 7.5. TR system: Displacement demands at zero strength eccentricity for different seismic intensities.

Intensity	System		Wall 1			Wall 2		
	μ_{Δ_s} [-]	Δ_{CoM} [m]	Δ_1 [m]	$\Delta_1 - \Delta_{CoM}$ [m]	$\frac{\Delta_1 - \Delta_{CoM}}{\Delta_{CoM}}$ [-]	Δ_2 [m]	$\Delta_2 - \Delta_{CoM}$ [m]	$\frac{\Delta_2 - \Delta_{CoM}}{\Delta_{CoM}}$ [-]
50%	1.48	0.13	0.10	-0.04	-28%	0.17	0.04	30%
100%	3.35	0.30	0.26	-0.04	-14%	0.34	0.04	15%
150%	5.63	0.50	0.47	-0.04	-7%	0.54	0.04	8%

Table 7.6. TU system: Displacement demands at zero strength eccentricity for different seismic intensities.

Intensity	System		Wall 1			Wall 2		
	μ_{Δ_s} [-]	Δ_{CoM} [m]	Δ_1 [m]	$\Delta_1 - \Delta_{CoM}$ [m]	$\frac{\Delta_1 - \Delta_{CoM}}{\Delta_{CoM}}$ [-]	Δ_2 [m]	$\Delta_2 - \Delta_{CoM}$ [m]	$\frac{\Delta_2 - \Delta_{CoM}}{\Delta_{CoM}}$ [-]
50%	1.50	0.13	0.08	-0.05	-37%	0.21	0.08	60%
100%	3.34	0.30	0.20	-0.10	-59%	0.47	0.18	59%
150%	5.81	0.52	0.41	-0.10	-20%	0.69	0.18	34%

The findings regarding the effect of seismic intensity on the displacement demand on the CoM and the stiff and soft edge can be summarised as follows:

- The general trends in displacement demands on the CoM and the stiff and soft edge were very similar for low, medium and high ductility. More specifically, the displacement demand on the soft edge remained approximately constant with increasing strength eccentricity (providing the strength eccentricity resulted from excess element strength [Castillo, 2004]). The displacement demand on the CoM reduced with increase

in strength eccentricity since the total shear capacity increased. The displacement demand on the stiff edge also decreased with strength eccentricity since its capacity increased and the lever arm to the centre of strength reduced. These findings applied to both TR and TU systems.

- The displacement ductility demands on Wall 1 and 2 were not equal for zero strength eccentricity since the two walls had different lengths. The larger the seismic intensity, the larger was the strength eccentricity for which the seismic demand yielded approximately equal ductility demands on the two walls. The strength eccentricities, for which Wall 1 and 2 were subjected to equal ductility demands, were larger for TR than for TU systems.
- For TR systems, the difference in displacement demand at zero strength eccentricity between the CoM and the two walls was approximately independent of the seismic intensity. Since the strength eccentricity was zero, this difference must have been controlled by the stiffness eccentricity.

7.4.5 Long-period structures ($T_{eff} > T_D$)

The averaged displacement spectra of the artificial records that were employed in the previous sections increased linear with period (Figure 7.5). The corner period of the design spectrum at 4s was not reflected in the average of the spectra of the artificial accelerograms but the spectral displacement kept increasing linearly for periods longer than 4s. For records that have a displacement spectrum with a constant spectral displacement range, the displacement demand on systems with effective period longer than the corner period is insensitive to a change in effective stiffness. For such systems, it is expected that an increase in system base shear capacity does not alter the displacement demand on the CoM significantly (as long as the effective periods remains longer than the corner period). However, if the increase in base shear capacity goes along with an increase in strength eccentricity – as an increase in the parameter λ_1 implies – the moment due to strength eccentricity increases. Therefore, the nominal rotations, i.e. the difference in the edge displacements and the CoM, increases too. Hence, assuming a constant CoM displacement, the displacement demand on Wall 2 (soft edge) is expected to increase with strength eccentricity. In this situation, Wall 2 is no longer protected if the strength capacity of Wall 1 is increased as it was the case for spectral shapes that increase linearly with period.

To prove the above point, time-history analyses of the TR systems described in Section 7.4.1 were carried out using the five artificial accelerograms of Set B (Section 7.3.2). The corner period of these records was approximately 2s. The uncoupled translational period (Equation 7.8) of the system for an excitation in the x direction was $T_0 = 1.83s$ for $\lambda_1 = 1.0$ and

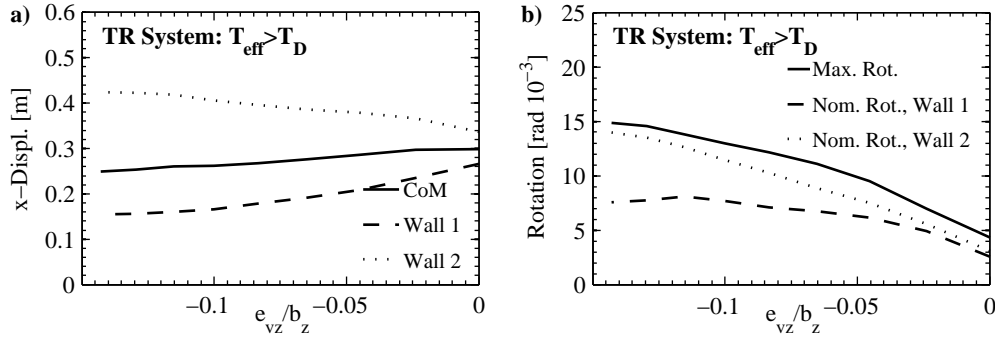


Figure 7.21. TR systems analysed for skew attack with uni-directional strength and stiffness eccentricity (a) and bi-directional strength and stiffness eccentricity (b).

$T_0 = 1.48\text{s}$ for $\lambda_1 = 1.8$. Hence, for displacement ductilities $\mu_{\Delta_s} \geq \sim 2.0$ the effective period $T_{eff} = T_0 \cdot \sqrt{\mu_{\Delta_s}}$ of all systems should be larger than the corner period $T_D = 2.0\text{s}$.

Figure 7.21a shows the displacement demand on the CoM and the stiff and soft edge. The results confirmed the expectation that the displacement demand on the soft edge increases with strength eccentricity while the displacement demand on the CoM remains approximately constant. The system ductility demand varied between $\mu_{\Delta_s} = 3.8 - 4.0$. The effective periods were therefore between $\sim 2.9 - 3.7\text{s}$. The maximum rotation and the nominal rotations for Wall 1 and 2 are shown in Figure 7.21b. The rotations followed very similar trends as the rotations of systems with $T_{eff} < T_D$ (Figure 7.12). However, the increase in rotation with strength eccentricity was not compensated by a decrease in CoM displacement. Therefore, the rule that the soft edge displacement is independent of strength eccentricity provided the strength eccentricity results from excess strength [Castillo, 2004] does not apply to systems with effective periods longer than the corner period of the displacement spectrum.

7.4.6 TR systems with uni- and bi-directional strength and stiffness eccentricities under skew attack

In this section the effect of the direction of the input component on the displacement demand on the structural elements is investigated. The analyses were carried out with a single horizontal component of excitation for which the angle α with respect to the system axes was altered (skew attack). For this purpose, two different sets of TR systems were analysed: The first set contained the TR systems that have been already studied in previous sections; the key properties of these systems were given in Table 7.3. The second set of systems were systems with bi-directional strength and stiffness eccentricities. For these systems, Wall 4 was assigned

the properties of Wall 1 and Wall 3 the properties of Wall 2. Figure 7.22b shows the position of the centre of strength (CV) and the centre of stiffness (CR) for $\lambda_1 = \lambda_4 = 1.8$ (and $\lambda_2 = \lambda_3 = 1.0$). Both, the centre of strength and the centre of stiffness, lie on the diagonal of the diaphragm because Wall 1 and 4 and Wall 2 and 3 have identical properties. To limit the number of analysis, only three different systems were considered for both the set with uni- and bi-directional eccentricities. These three systems corresponded to excess strength factors of 1.0, 1.4 and 1.8. The respective strength eccentricity ratios were $e_v/b = 0.0, 0.08$ and 0.14 and the stiffness eccentricity ratios are $e_r/b = 0.17, 0.24$ and 0.29 .

The systems with uni-directional eccentricity were symmetric about the z axis. It was hence sufficient to analyse these systems for values of the angle α , which defines the orientation of the single ground motion component with respect to the system axes (Figure 7.22), between 0° and 90° . The angle $\alpha = 0^\circ$ corresponds to the z direction, $\alpha = 90^\circ$ to the x direction. The systems with bi-directional eccentricity were no longer symmetric and hence the input component was applied at angles between 0° and 180° . Angles of $\alpha = 31^\circ$ and $\alpha = 149^\circ$ corresponded to the diagonals of the $25\text{m} \times 15\text{m}$ diaphragm.

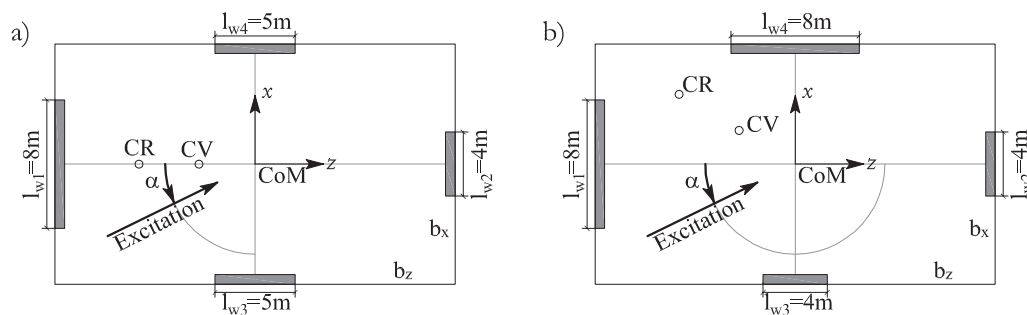


Figure 7.22. TR systems analysed for skew attack with uni-directional strength and stiffness eccentricity (a) and bi-directional strength and stiffness eccentricity (b).

It is obvious that skew attack with one horizontal component does not reflect the ground motion excitation during an earthquake. Nevertheless, analyses of systems under skew attack were carried out for two reasons: First, this type of analysis had been performed by both Sommer [2000] and Castillo [2004] and hence the analyses were repeated here for confirmation; neither Sommer nor Castillo carried out analyses with two horizontal input components. Second, skew attack analysis might allow to identify weak directions of the building, i.e. directions of excitation that lead to large displacement demands on the structural elements.

a) Systems with uni-directional eccentricities.

Figure 7.23 shows the displacement demand on the CoM and the structural elements in the x direction (a-c) and in the z direction (d-f). For all three excess strength factors λ_1 that were considered, the displacement demand in the x direction on the CoM and the stiff and soft edge was largest when the direction of the input component was also in x direction ($\alpha = 90^\circ$). This corresponded to the type of analysis that had been carried out in the previous sections. The displacement demand on the transverse walls (Wall 3 and 4) was largest when the input component was applied in the z direction ($\alpha = 0^\circ$). It is interesting to note that for $\alpha = 90^\circ$ the displacement demand in the z direction was zero for the CoM but non-zero for Wall 3 and Wall 4 since the transverse walls were excited by the rotation of the building due to the strength and stiffness eccentricity in the x direction. The CoM, however, did not move since the input energy in the z direction was zero for $\alpha = 90^\circ$.

The findings from the skew attack analyses of the TR systems were not exactly in line with Castillo's observations (Section 7.2.4). He observed that the demand on the stiff edge was in some cases greatest when the direction of the input component was applied at some angle rather than parallel to the structural wall. He linked this observation to the greater rotations of the system due to the yielding of the transverse elements. When the wall was excited parallel to the stiff edge (i.e. in the x direction) the transverse elements remained either elastic or the imposed ductility demands were very small. Figure 7.24a shows the maximum rotation as a function of the angle α for the three analysed systems ($\lambda_1 = 1.0, 1.4$ and 1.8). As expected the rotations were largest for the largest values of λ_1 , i.e. for the largest strength eccentricity. For $\alpha = 0$, the rotation was zero since the systems were symmetric about the x -axis. For $\alpha = 90$, the rotation was non-zero since the system had a stiffness eccentricity and for $\lambda_1 = 1.0$ and 1.4 also a strength eccentricity in the z direction. However, as Castillo [2004] observed, the rotation was not largest when the structure was excited in the x direction but was largest for α between 45° and 60° . Unlike in Castillo's analyses, the larger rotation demand for $\alpha \neq 90^\circ$ did not yield in displacement demands greater than for $\alpha = 90^\circ$. The nominal rotations of Wall 1 and 2 (Figure 7.24b) were smaller than the maximum rotations but followed similar trends.

b) Systems with bi-directional eccentricities.

For systems with bi-directional eccentricities the response to skew attack was complex because, when the input component was rotated, the demand on the walls in the x and z directions as well as the "effective" eccentricity changed. The effective eccentricity is here defined as the distance of a line through the CoM in the direction of excitation to the centre of strength. The effective eccentricity is maximum for $\alpha = 59^\circ$ and it diminishes for $\alpha = 149^\circ$ (Figure 7.25). However, depending on the direction of excitation, not all the elements might yield. Hence,

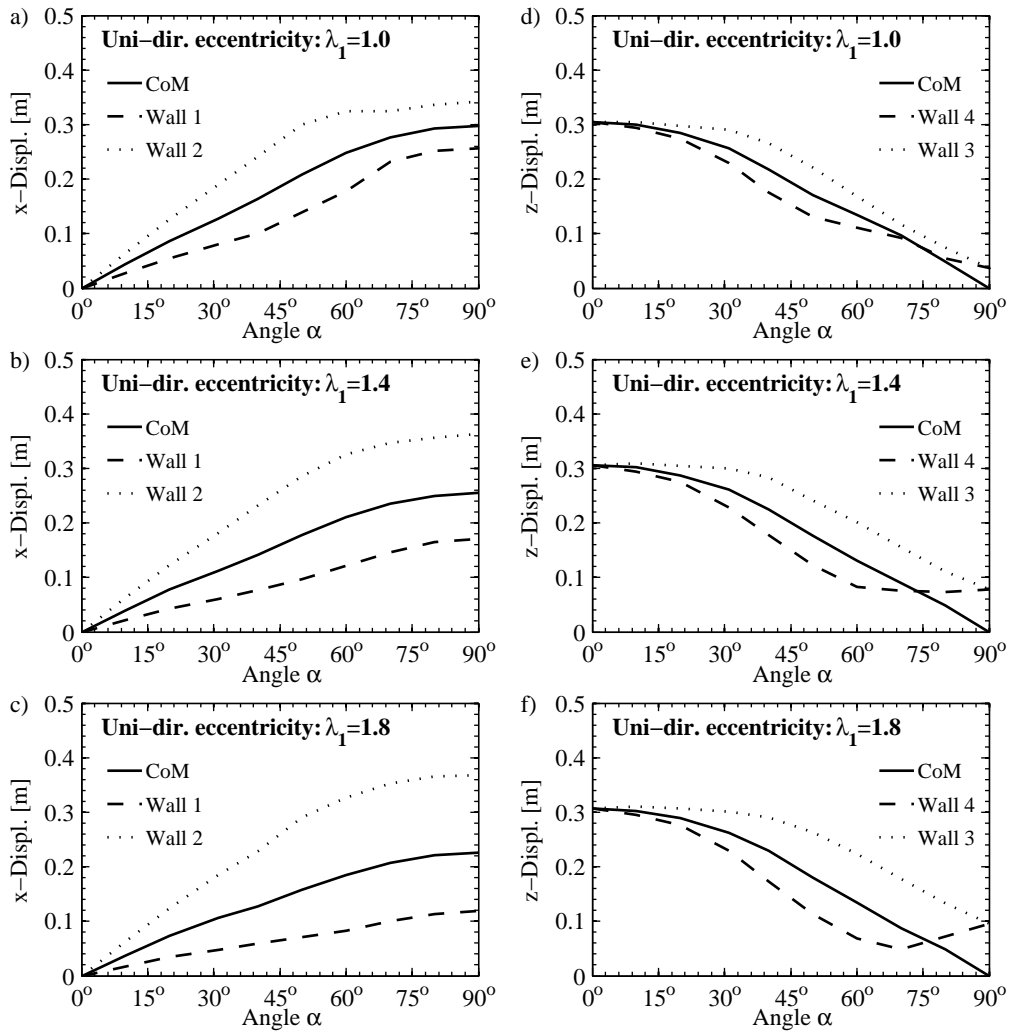


Figure 7.23. Skew attack of TR system with uni-directional strength and stiffness eccentricity: Displacement demand in the x direction (a-c) and the z direction (d-f) for different excess strength ratios λ_1 .

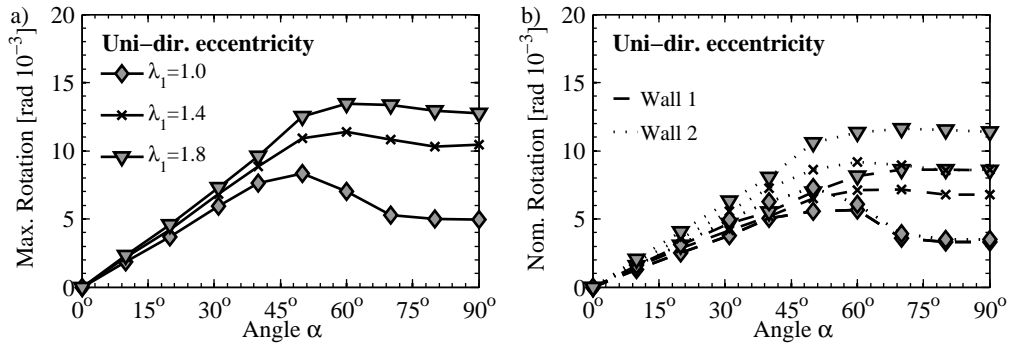


Figure 7.24. Skew attack of TR system with uni-directional strength and stiffness eccentricity: Maximum (a) and nominal rotation for Wall 1 and 2 (b) for different excess strength ratios λ_1 .

for example for a direction of excitation close to $\alpha = 90^\circ$, the centre of strength might be relevant for the torsional resistance of the elements in the x direction while the torsional resistance of the elements in the z direction, which are expected to remain largely elastic, might be better described by the centre of stiffness. In addition, any inelastic excursions of the elements in the x and z directions does most likely not occur simultaneously. Hence, the position of the centre of rotation changed during the duration of the seismic excitation. Apart from the effective eccentricity, the effective strength varied also with α . The effective strength was defined as the total strength projected along the direction of excitation. Since the strength in the x and z directions was the same, the effective strength was maximum for $\alpha = 45^\circ$ and $\alpha = 135^\circ$. Note that the effective stiffness was independent of the direction of excitation.

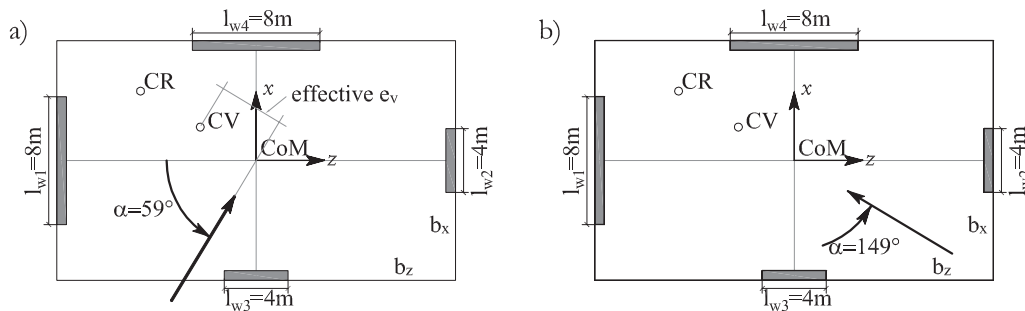


Figure 7.25. TR systems with bi-directional strength and stiffness eccentricity: Angle α for which the effective eccentricities are maximum (a) and for which the effective eccentricities diminished (b).

Figure 7.26 shows the displacement demand in the x direction (plots a-c) and the displacement demand in the z direction (plots d-f); the maximum rotation and the nominal rotations of Wall 1 and 2 are shown in Figure 7.27. The soft Wall 2, which was aligned with the x direction, was subjected to the largest displacements for $\alpha \cong 60^\circ$. This is the direction for which the effective eccentricities were greatest. By contrast, the stiff Wall 1 was subjected to the largest displacements when $\alpha \cong 110^\circ$. Wall 3 and 4 were subjected to the largest displacements when the input motion was applied in the z direction or at an angle very close to the z direction. The difference between the two directions was caused by the different lever arms: For excitation in the x direction, the large strength eccentricity was restrained by the transverse walls with the small lever arm while for excitation in the z direction the rotation resulting from the small strength eccentricity was restrained by the longitudinal walls with the large lever arm.

A note of caution is again issued against conclusions drawn from skew attack analyses: Real earthquake excitation consists of three translational components of which the vertical is often disregarded for structural analysis of systems that are not particularly sensitive to vertical excitations. Hence, in most cases it is sufficient to include the two horizontal components of ground motion in the seismic analysis of a system. However, when the two horizontal components are considered the intensity of the excitation along a certain direction does not vary much when the ground motion axes are rotated with respect to the structural axes. This is very different to skew attack with a single component where the intensity of the excitation along a certain direction changes significantly with the angle α .

7.4.7 Bi-directional input motion

Real seismic ground motion at a point consists of three translational and three rotational components. For structural analysis, it is customary to neglect the rotational components since their effect on the performance of structures is commonly considered as small [Kubo and Penzien, 1979]. It was assumed that the structural systems analysed here were not susceptible to vertical ground motions and hence only the two horizontal translational components of a ground motion were included in the records of Set C. The artificial ground motions in Set A and B consisted of only a single component, which did not reflect reality. They were used in the previous sections for the sake of simplicity and to make the analyses directly comparable to the parametric studies by Sommer [2000] and Castillo [2004], who had also used ground motions with a single component only. However, in particular for systems with bi-directional stiffness and/or strength eccentricities it is expected that the orthogonal component has some influence on the displacement demand of the structural elements. The objective of the analyses presented in this section is therefore to evaluate the difference in results between analyses carried out with a single horizontal component and analyses carried out with both horizontal

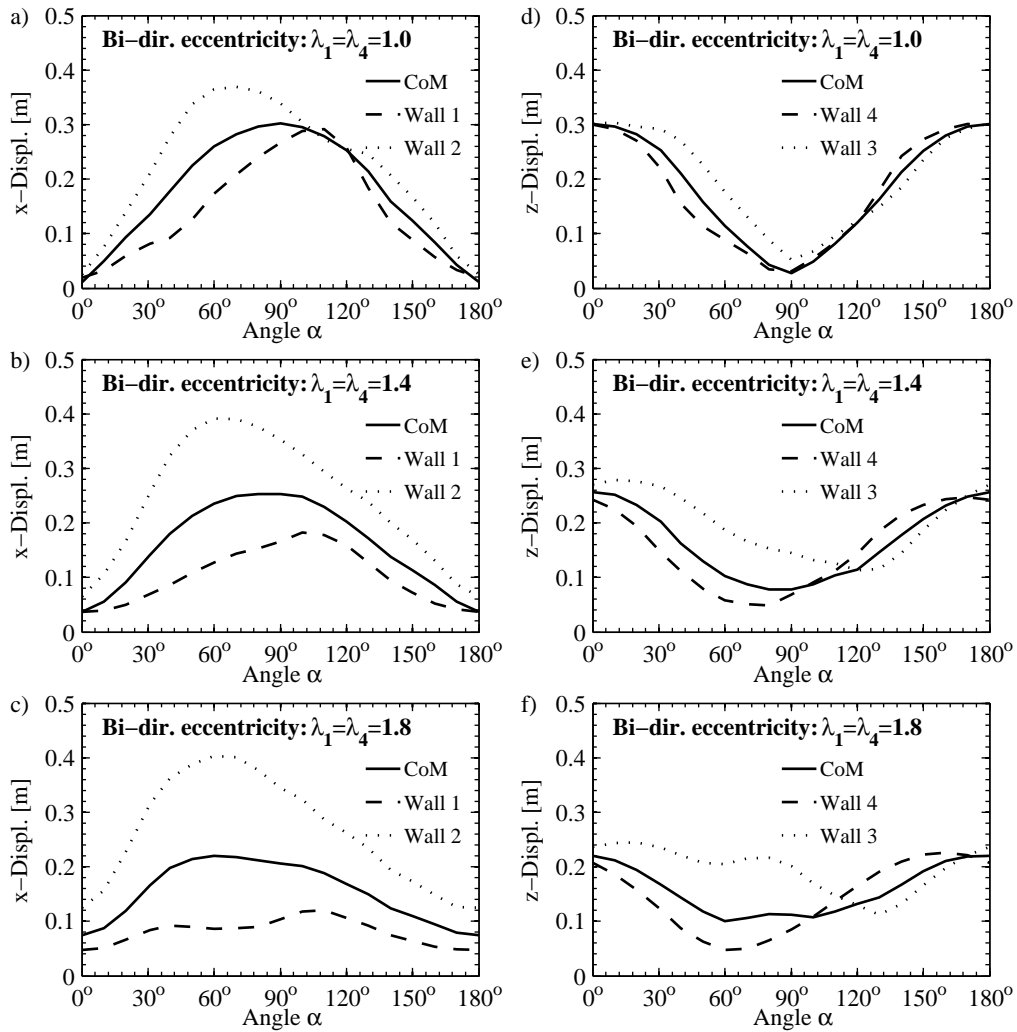


Figure 7.26. Skew attack of TR system with bi-directional strength and stiffness eccentricity: Displacement demand in the x direction (a-c) and the z direction (d-f) for different excess strength ratios λ_1 and λ_4 .

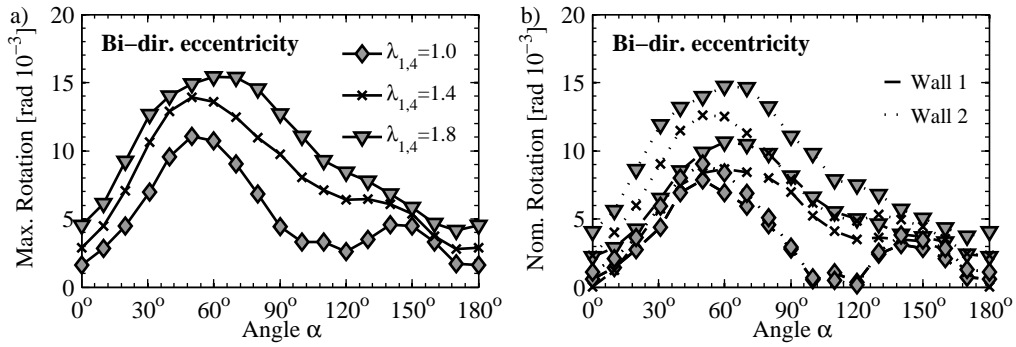


Figure 7.27. Skew attack of TR system with bi-directional strength and stiffness eccentricity: Maximum (a) and nominal rotation for Wall 1 and 2 (b) for different excess strength ratios λ_1 and λ_4 .

components. In Section 7.4.7a the response of the TR systems with uni-directional strength eccentricity that have been analysed in the previous sections is discussed. In Section 7.4.7b additional three sets of TR systems with bi-directional strength eccentricities were analysed and their median displacement demands for the 20 records of Set C determined.

a) Responses of TR systems to bi-directional excitation.

To demonstrate the effect of the second component of ground motion on the displacement demand the systems were first analysed for bi-directional excitation and then for uni-directional excitation. For the uni-directional case either the x or the z component of the ground motion was applied in the structural analysis. This is illustrated in Figure 7.28.

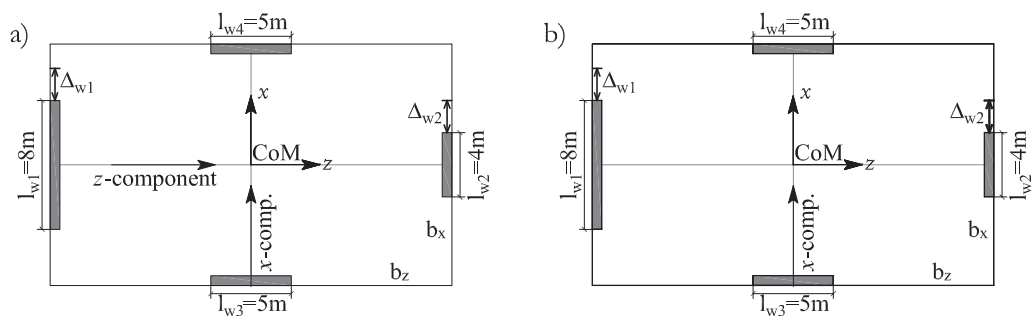


Figure 7.28. TR system: Analysis with bi-directional (a) and – as an example – analysis with uni-directional excitation for the component in the x direction (b).

Although the ground motions were selected and scaled to match the geometric mean displacement target spectrum (Section 7.3.3), the variation between the real records was considerably

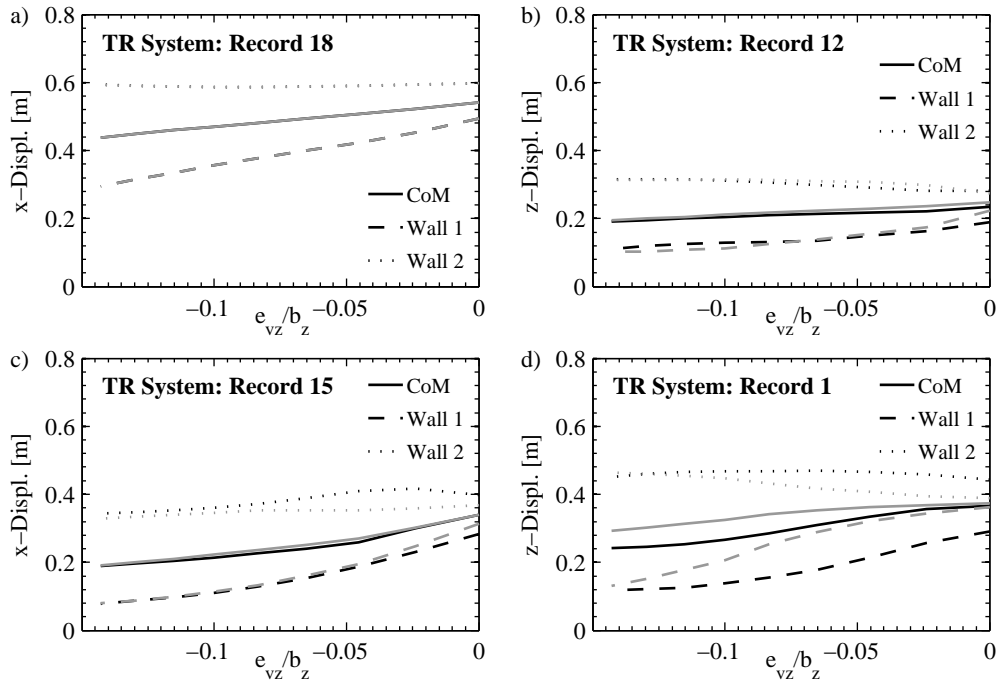


Figure 7.29. TR system: Comparison of analysis results for bi-directional to uni-directional excitation: Examples of records that led to approximately the same (a), a smaller (b), a larger (c) and dependent on the strength eccentricity a larger or a smaller (d) response for bi-directional excitation (black lines) than for uni-directional excitation (grey lines).

larger than between the artificial records of Set A and B. The variation also manifested itself in the effect of the second component of ground motion on the displacement demand of the structural analysis. Figure 7.29 shows four out of the 20 records for which the "reactions" of the systems to the second component of ground motion was very different: Plotted are the displacement demands in the x direction on the CoM and the stiff and soft edge. For the uni-directional analysis only the x component of the ground motion was applied to the system. For Record 18 (plot a) the displacement demand on the CoM, Wall 1 and 2 were not influenced by the orthogonal ground motion component; the results for uni- and bi-directional excitation were almost equal. For Record 12 and 15 (plots b and c) the second component of ground motion had only a small effect on the displacement demand whereas for Record 1 the difference was considerable different (plot d). These examples show that the ratio of bi- to uni-directional response can vary strongly between records and underline that it might be difficult to draw a general conclusion regarding the effect of the second component of ground motion on the displacement demand.

In Figure 7.30 the displacement demand in the x direction for bi-directional excitation is plotted against the displacement demand for uni-directional excitation; the data is shown for three different TR systems corresponding to $\lambda_1 = 1.0, 1.4$ and 1.8 . Equivalent plots for the displacement demand in the z direction are included in Figure 7.31. Each data point represents the results of one of the 20 records in Set C. Also included in these plots is a diagonal line; for data points that lie on the diagonal the displacement demands for bi- and uni-directional excitation were equal.

The displacement demand in the x direction was not strongly influenced by the orthogonal component of ground motion; most data points lie either on or in vicinity to the diagonal line. Plots a-c in Figure 7.30 show the x displacement demand on the CoM for uni- and bi-directional excitation; equivalent plots for the stiff and soft edge (Wall 1 and 2) are shown in plots d-f. It is believed that the effect of the orthogonal component (i.e. the ground motion component in the z direction) was small because the system was symmetric for excitation in the z direction. This orthogonal component did therefore not contribute to the torsional moment to which the system was subjected; it only subjected the transverse walls 3 and 4 to an additional demand and when these walls yielded the torsional stiffness of the system was reduced. Note that, had all elements of the system been elastic, the displacement in the x direction had been independent of the excitation in the z direction.

For the displacement demand in the z direction the situation is somewhat different: Figure 7.31d-f shows the displacement demand on Wall 3 and 4 (which have equal properties) for TR systems with $\lambda_1 = 1.0, 1.4$ and 1.8 . For $\lambda_1 = 1.0$ the displacement demands on Wall 3 and 4 were approximately equal for bi- and uni-directional excitation. For $\lambda_1 = 1.4$ and $\lambda_1 = 1.8$, however, the mean displacement demands were larger if both components of ground motions were applied. These plots suggest that considering only a single component of ground motion when analysing or designing the structure leads to biased low displacement demands.

b) Comparison of the median responses of different TR systems to uni- and bi-directional excitation.

Figures 7.30 and 7.31 showed that the variation between the results for the 20 records was very considerable. In particular in some cases there were a small number of "outliers" that produced significantly larger displacement demands than the other records. The mean displacement of all records will be unduely influenced by these few "outlier" records. The engineer is most often interested in a "typical" response value that is best represented by the median response. Unlike the mean response the median response is insensitive to outliers. For the two sets of artificial records considered in the previous sections the mean and median response were generally very similar. For the real records considered in this section, however, the median

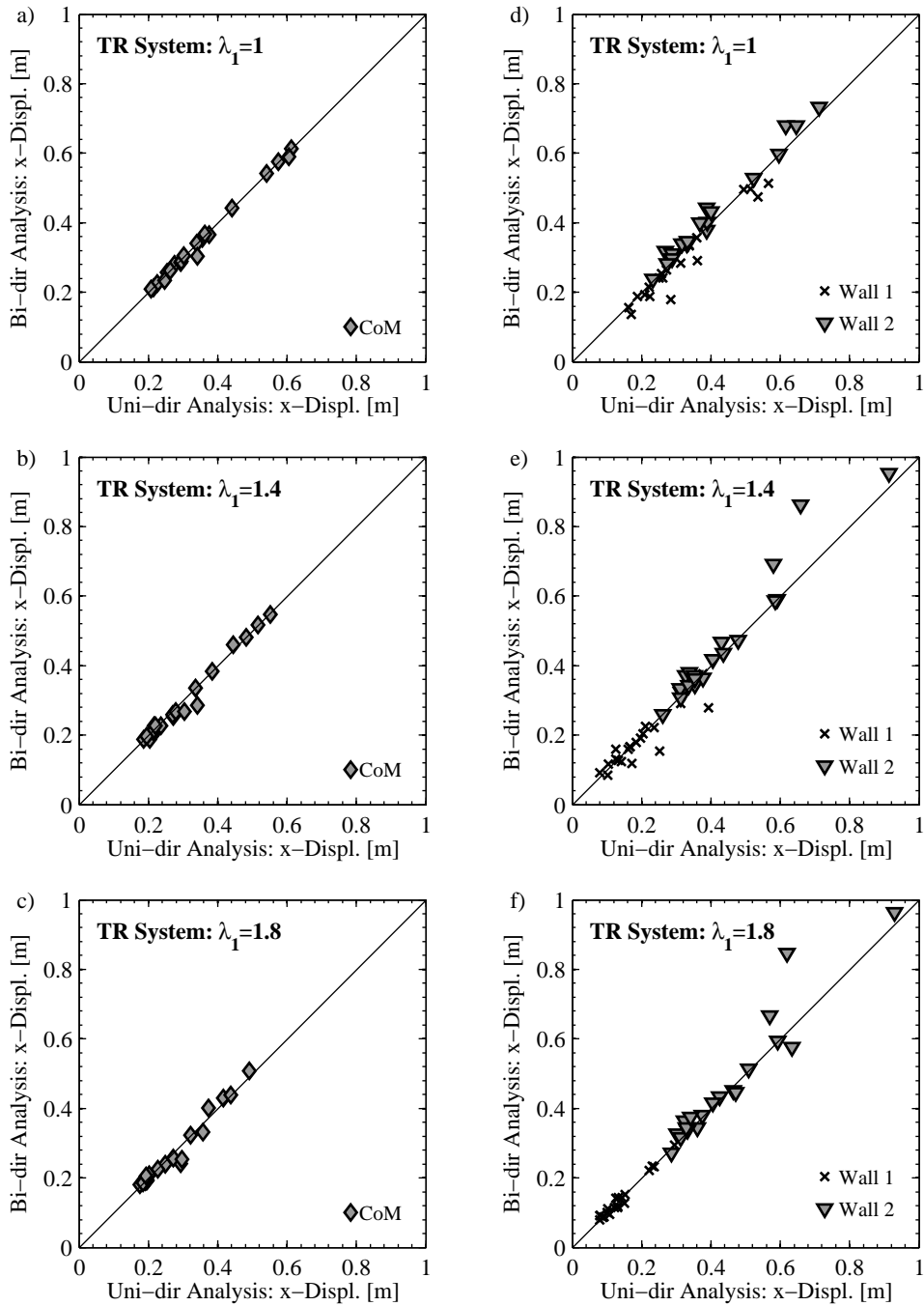


Figure 7.30. TR system: Comparison of bi-directional to uni-directional excitation with respect to the displacement demand in the x direction: Displacement demand on CoM (a-c) and stiff and soft edge (d-f) for $\lambda_1 = 1.0, 1.4$ and 1.8 .

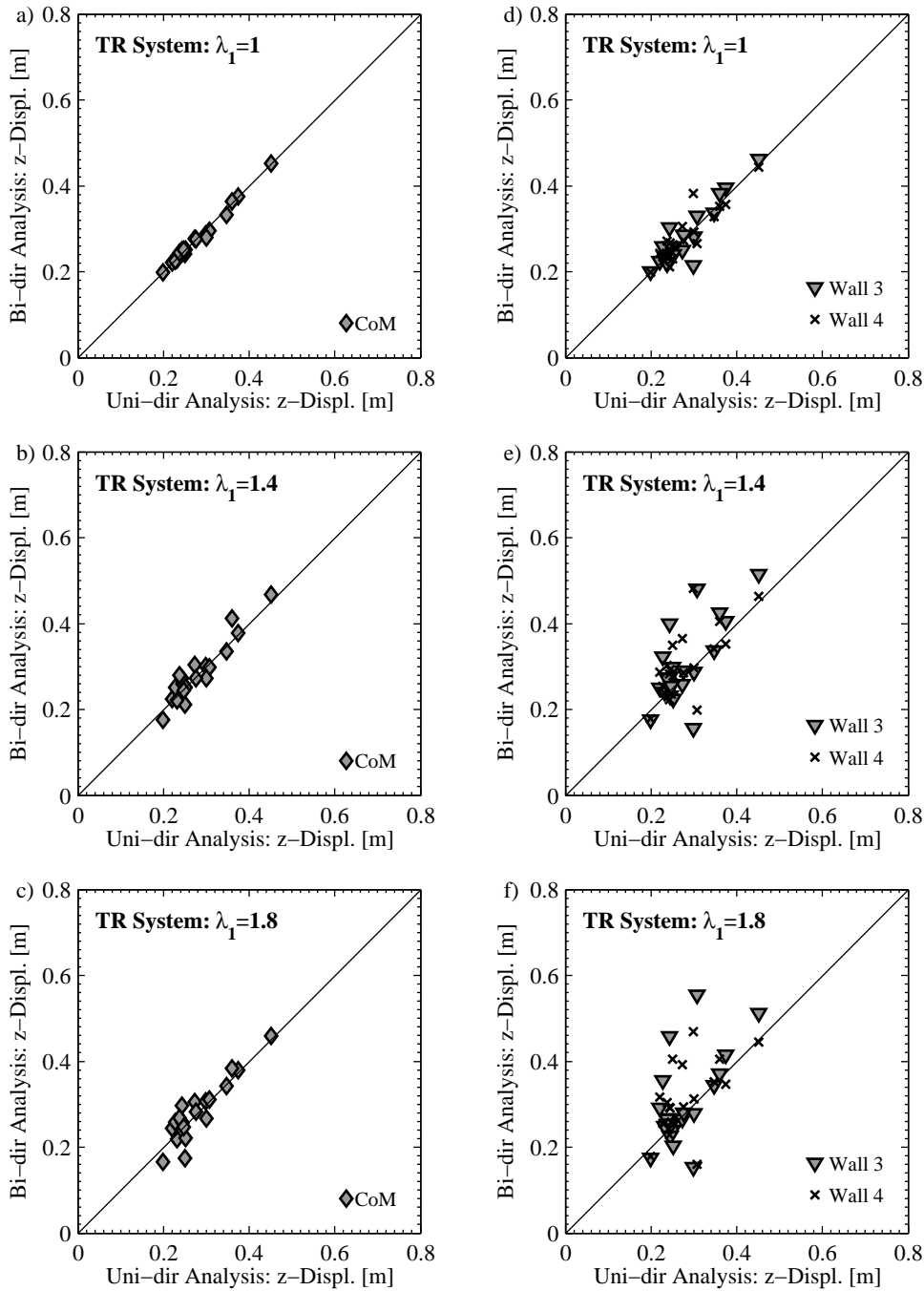


Figure 7.31. TR system: Comparison of bi-directional to uni-directional excitation with respect to the displacement demand in the z direction: Displacement demand on CoM (a-c) and Wall 3 and Wall 4 (d-f) for $\lambda_1 = 1.0, 1.4$ and 1.8 .

rather than the mean response will be evaluated although the elastic mean and median spectra were very similar (Figure 7.7). The median displacement demands are plotted in Figure 7.33.

To broaden the study, four different sets of TR systems were analysed; each set contained nine models:

- TR Systems: This set of TR systems with uni-directional strength and stiffness eccentricity was used for most of the parametric studies in the previous sections (Figure 7.9). The variation of the strength of Wall 1 corresponded to λ_1 -values between 1.0 and 1.8. The strengths of the four walls and the system strengths were given in Table 7.3.
- TR Systems 2: This set of system has bi-directional strength and stiffness eccentricities. The properties of Wall 3 equal those of Wall 2, and the properties of Wall 4 those of Wall 1. This set of systems was already analysed in the section on skew attack (Section 7.4.6); a plan view of it was presented in Figure 7.22.
- TR Systems 3: The properties of the walls in the z direction (Wall 3 and 4) of these system are identical to those of Systems 2. The properties of the walls in the x direction (Wall 1 and 2) were the same for all nine models of this set. The strength of Wall 1 was $V_1 = 1690\text{kN}$ and the strength of Wall 2 was $V_2 = 937\text{kN}$. This corresponded to excess strength factors of $\lambda_1 = 1.8$ and $\lambda_2 = 1.0$, respectively. A plan view of these systems with the excess strength factors of Wall 1-4 is shown in Figure 7.32a.
- TR Systems 4: The properties of the walls were identical to those of Systems 2. Unlike for Systems 2 the slab was square (25m x 25m) and not rectangular (Figure 7.32b).

Figure 7.33 shows the median displacement demands of the 20 records of Set C for the four sets of TR systems. In the left plot of these figures the displacement demands in the x direction are plotted, the right plots contain the information for the z direction. For both directions the response to bi-directional excitation (black lines) was compared with the response to uni-directional excitation (grey lines).

All graphs within Figure 7.33 show that the CoM displacement was not much affected by the orthogonal component of motion. The effect of the orthogonal component on the structural elements (Walls 1-4), however, varied between the different cases. In the following the reaction of the four sets of TR systems to the orthogonal component of ground motion are described and discussed. Figure 7.33a and b show the median displacement demand of the TR systems that have been used in previous sections; for these systems the single data points corresponding to the 20 records of Set C were already plotted in Figures 7.30 and 7.31. The effect of the orthogonal component of ground motion on the median displacement demand was noticeable

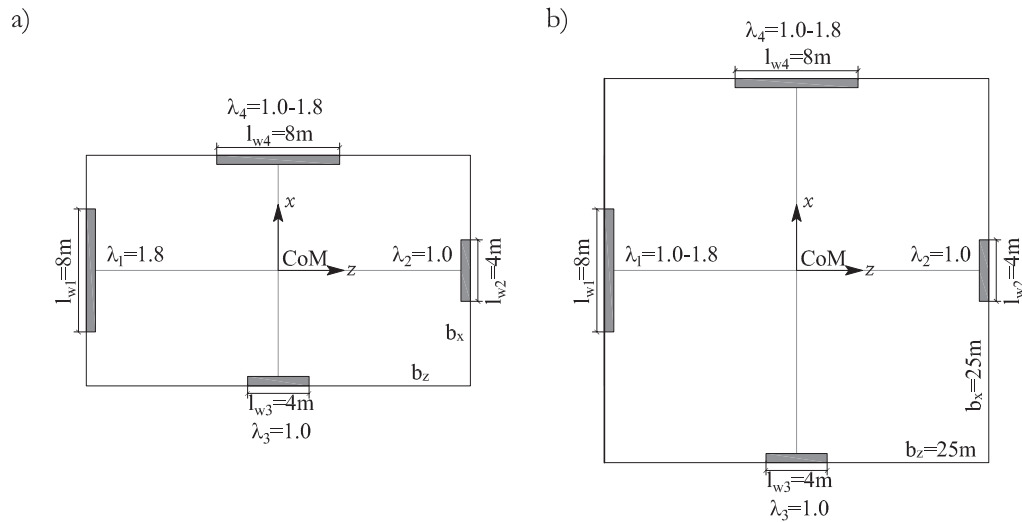


Figure 7.32. TR systems: Plan view of models of set TR Systems 3 (a) and models of set TR Systems 4 (b).

– although relatively small – for both the x and z directions. Figure 7.33b shows that, while the z displacement demand on CoM, Wall 3 and 4 were equal when only the z component of ground motion was considered, the displacement demands on Wall 3 and 4 exceeded the displacement demand on the CoM if the system was analysed for bi-directional excitation. The difference was caused by the rotation that was induced by the asymmetry of the walls in the x direction. Note that Figures 7.30 and 7.31 had suggested that the effect is negligible for the x but noticeable for the z direction. However, few outliers distorted the picture and the median response in the z direction was less affected than the plots in Figure 7.31 had suggested.

The analysis results for the second set of TR systems (TR Systems 2) are shown in plots c and d of Figure 7.33. These systems have bi-directional strength and stiffness eccentricities. As a consequence, the differences between the displacement demands on the soft edges (Wall 2 and Wall 3) for uni-directional analysis and bi-directional were considerably larger than those observed for the first set of systems (plots a and b). The displacement demand on the stiff edges and the CoM was hardly affected by the orthogonal component of ground motion.

For TR systems of set 3 (TR Systems 3) the properties of the walls in the x direction were the same for all nine models of this set while the properties of Walls 3 and 4 in the z direction varied. All nine models had a large stiffness and strength eccentricity in z direction; this

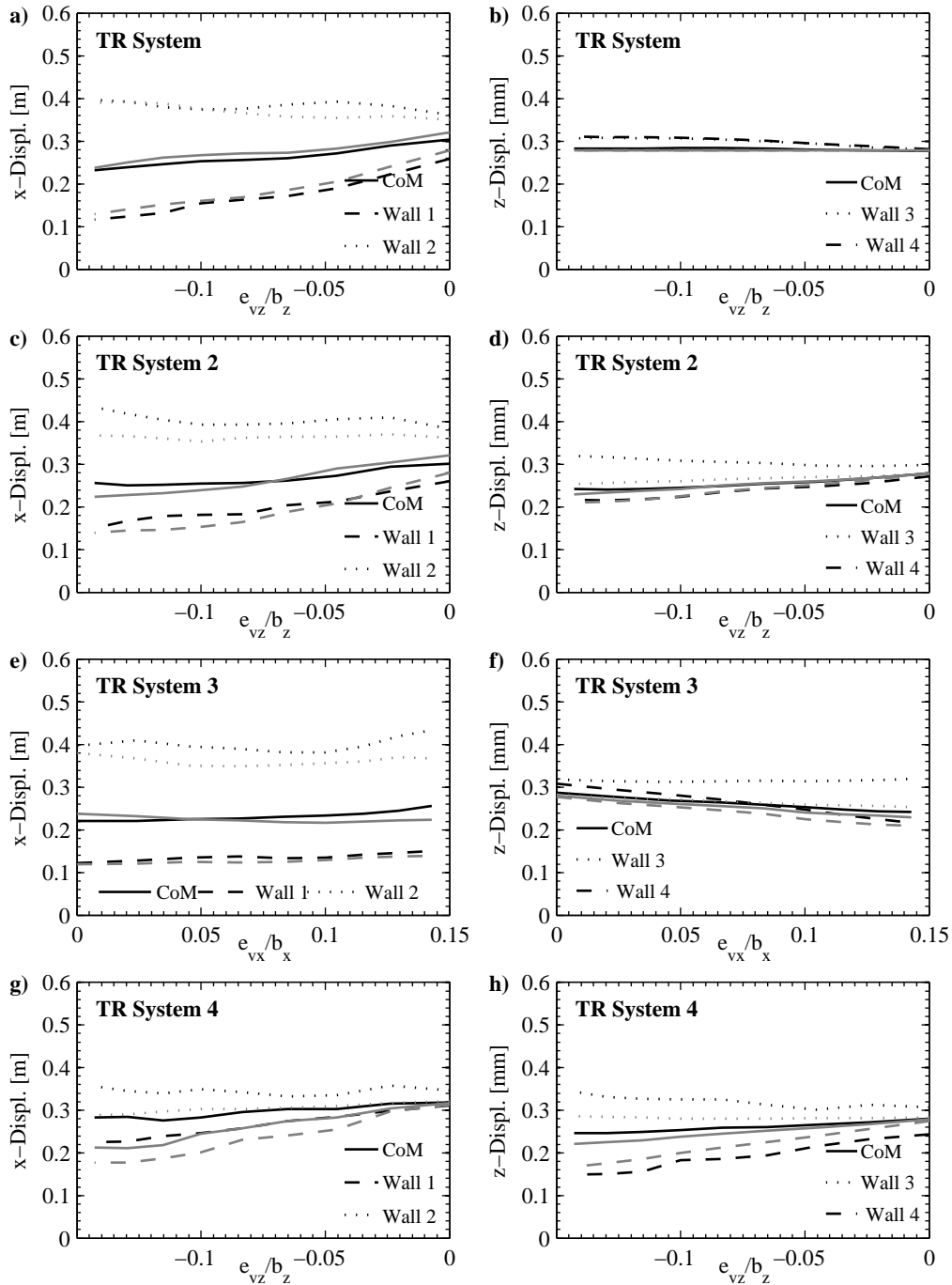


Figure 7.33. Different TR systems: Comparison of the median bi-directional excitation (black lines) to the median uni-directional excitation (grey lines) with respect to the displacement demand in the x direction (left plots) and in the z direction (right plots).

was reflected in the difference in displacement demands on the CoM, Wall 1 and Wall 2 (Figure 7.33e). This plot shows also that the difference between the x displacement demand for uni- and bi-directional excitation increased with increasing strength eccentricity in the x direction. Note that the strength eccentricity in plots e and f increases from the left to the right since Wall 4 with the positive x -coordinate was stronger than Wall 3. The displacement demand in the z direction on Wall 3 (Figure 7.33f) was also larger for bi-directional excitation than for uni-directional excitation.

The TR systems of set 4 (TR Systems 4), which only differed from the models of set 2 regarding the slab dimension b_x , show that for a square slab the nominal rotations for the two directions were almost equal. The difference between the displacement demands for uni- and bi-directional excitation were similar to those observed for the TR Systems 2.

On the whole, the comparison of displacement demands due to uni- and bi-directional excitation showed that the orthogonal component of excitation had little influence on the displacement demand of the CoM. However, it could not be neglected when determining the displacement demand on the structural elements (Walls 1-4). The influence of the orthogonal component of ground motion depended mainly on the strength eccentricity of the system in the orthogonal direction: If this strength eccentricity was small the effect of the orthogonal component of excitation was relatively small, although the orthogonal component reduced the stiffness of the elements in this direction and therefore also the overall torsional stiffness. This led typically to a slight increase of displacements along the soft edges (e.g. set 1, displacement demand on Wall 2). The effect of the orthogonal component increased with increasing strength eccentricity since the rotation induced by the strength eccentricity affected the displacement demand in both directions. The effect was stronger for the soft edges (e.g. set 2 and 4, Wall 2 and 3) whereas the effect of the orthogonal component on the stiff edges was typically less pronounced (e.g. set 2 and 4, Wall 1 and 4).

7.4.8 Summary of the results from the parametric study on 2D systems

Within the scope of the parametric study presented here, 2D systems representing structural wall buildings that were asymmetric in-plan were analysed. The systems were classified into torsionally restrained (TR) and torsionally unrestrained (TU) systems. TR systems were analysed for uni- and bi-directional excitation. TU systems were only considered marginally since the design approach proposed in the following section will be limited to TR systems. One reason for excluding TU systems is the relative large dependence of the displacement demands in particular on the soft edge on the rotational inertia (Section 7.4.3); this makes it considerably more difficult to identify a simple approach for estimating the nominal rotations. In the following the key findings for TR systems are summarised:

- Paulay [1999] proposed that for buildings that respond in the inelastic range when subjected to seismic excitation the strength eccentricity is a more important parameter than the stiffness eccentricity. Although strength eccentricity was considered an important parameter, it was found that for zero strength eccentricity but non-zero stiffness eccentricity the nominal rotations of the soft and stiff edge were also non-zero. Hence, the stiffness eccentricity had also some influence on systems that responded in the inelastic range.
- Castillo [2004] proposed a design rule for plan asymmetric buildings. According to this rule, strength eccentricity is acceptable as long as it results from excess strength of structural elements (Section 7.2.5). If this is the case, the displacement demand on the structural elements and the CoM of systems with strength eccentricity are not larger than for systems without strength eccentricity. More specifically, the displacement demand on the soft edge is approximately equal for systems with and without strength eccentricity while the displacement demands on the CoM and stiff edge reduce with strength eccentricity since the base shear capacity increases [Castillo, 2004]. The parametric analyses carried out here confirmed Castillo's finding provided the effective period of the system T_{eff} was smaller than the corner period T_D of the displacement spectrum. If $T_{eff} > T_D$ Castillo's design approach did not hold. For the stiff edge, Castillo [2004] proposed to estimate its displacement demand as the CoM displacement, which in turn can be estimated from an equivalent SDoF. In particular for larger strength eccentricities, approximating the stiff edge displacement by the CoM displacement was generally found to be very conservative.
- For zero strength eccentricity the displacement ductility demand on the long wall was larger than the ductility demand on the short wall. For the system analysed here, the displacement ductilities of the two walls were approximately equal for strength eccentricities between 0.05 and $0.1b_z$. This finding confirmed Sommer's observation [Sommer, 2000].
- In a first step, before the systems were analysed for bi-directional excitation, skew analyses were carried out. In this type of analysis a single component of excitation was applied to the system and the orientation of the component of motion to the system axes varied. For systems with uni-directional eccentricity the displacement demand on the elements was largest if the single component of excitation was applied parallel to the elements. The maximum and nominal rotations often peaked for different angles. This is, however, not of great significance since rotations are generally not considered as an important design quantity [Paulay, 1996]. For systems with bi-directional eccentricity the displacement demands were not always largest when the excitation was aligned with the considered element. The critical direction depended on whether the element was

on the stiff or soft edge of the building and on the torsional restraint offered by the transverse elements. It was cautioned against overrating the findings from skew analysis since seismic analysis with a single component does not reflect the real excitation during an earthquake. For in-plan asymmetric buildings that are insensitive to vertical excitations at least the two horizontal components of ground-motion should be considered. It is believed that including the orthogonal horizontal component is particularly important when systems with bi-directional eccentricities are considered.

- To investigate the effect of the orthogonal horizontal ground-motion component on the displacement demand of the elements analyses with bi-directional input motion were carried out and compared with results from uni-directional excitation. The results showed that the effect of the orthogonal component varied between the records. In general, however, the orthogonal component of ground motion increased the displacement demand on the soft edges by reducing the overall rotational stiffness of the system and by increasing the torsional moment, if the elements in the orthogonal direction were not symmetric. The effect of the orthogonal component of ground motion on the stiff edge and the CoM was typically fairly small.

7.5 Accounting for torsional response in DDBD

Based on the parametric studies presented in the previous sections the DDBD approach is extended to in-plan asymmetric buildings. In order to estimate the displacement demand on the stiff and soft edge an estimate of the nominal rotation is required. An approximate and simple method though without mathematical basis is proposed in Section 7.5.1. The design approach is limited to TR systems since it is generally recommended [Paulay, 1997] to refrain from TU systems.

7.5.1 Extending the DDBD approach to in-plan asymmetric buildings

In Section 7.4.2 it was shown that the CoM displacement is relatively independent of the stiffness and strength eccentricity if the total base shear capacity remains constant (Figure 7.16). Hence, as Castillo [2004] suggested, it is feasible to estimate the CoM displacement on the basis of an equivalent SDOF system assuming zero rotation, i.e. assuming that the stiff and the soft edge are subjected to the same displacement demands as the CoM. With this assumption the displacement demand on the CoM can be estimated by the DDBD approach. One of the objectives of DDBD is to protect the structural elements from undue displacement demands, which would lead to excessive damage or even element or system failure. Hence, it is necessary to estimate the displacement demands on the edges where the walls are placed. Castillo's [2004] approach for the soft edge displacement was introduced (Section 7.2.5) and its

shortcomings discussed (Section 7.4.8). In this section a different approach is proposed that is based on an estimate of the nominal rotation. The approach is limited to TR systems; when designing buildings care should be taken that – if the structure has to be asymmetric in-plan – the layout should at least correspond to that of a TR system in order to restrain the effects of seismic induced twists to a reasonable limit.

In Section 7.4.2 it was observed that at zero strength eccentricity the nominal rotation for both the stiff edge and the soft edge is not zero. Hence, the stiffness eccentricity causes some rotation of the system. It was also found (Section 7.4.4) that the nominal rotation at zero strength eccentricity was relatively independent of the intensity of the seismic demand since the transverse walls were always providing a good restraint against excessive rotations. The fact that the nominal rotation was in general smaller for the stiff edge than for the soft edge is in the following neglected.

First, an estimate of the nominal rotation for uni-directional excitation is proposed. It is then extended to bi-directional excitation. For uni-directional analysis it is proposed that the nominal rotation is estimated as:

$$\theta_x = \frac{V_{nsx} \cdot e_{rz}}{K_{rot,eff,x}} \quad (7.26)$$

where V_{nsx} is the system base shear in the considered direction, e_{rz} the stiffness eccentricity in the orthogonal direction and $K_{rot,eff,x}$ the effective rotational stiffness of the system. The latter is based on the effective stiffness of the walls in the x direction and the elastic stiffness of the walls in the z direction:

$$K_{rot,eff,x} = \sum \frac{k_{xi}}{\mu_{\Delta,i}} \cdot (z_i - e_{rz})^2 + \sum k_{zi} \cdot (x_i - e_{rx})^2 \quad (7.27)$$

The definition of all individual terms was given in Section 7.2.3b. It goes without saying that corresponding definitions for θ_z and $K_{rot,eff,z}$ apply when the system is considered for excitation in the z direction. The displacement ductility demand $\mu_{\Delta,i}$ on the stiff and soft edge can be estimated assuming a zero nominal rotation, i.e. approximating the displacement demand on the stiff and soft edge by the displacement demand on the CoM.

For bi-directional excitation the torsional moment $V_n \cdot e_r$ is computed as the sum of the moments in the two principal directions:

$$V_n \cdot e_r = V_{nsx} \cdot |e_{rz}| + V_{nsz} \cdot |e_{rx}| \quad (7.28)$$

The effective rotational stiffness of the system under bi-directional excitation is computed reducing the stiffness of all walls to their effective stiffness:

$$K_{rot,eff} = \sum \frac{k_{xi}}{\mu_{\Delta,i}} \cdot (z_i - e_{rz})^2 + \frac{k_{zi}}{\mu_{\Delta,i}} \cdot (x_i - e_{rx})^2 \quad (7.29)$$

As for the uni-directional analysis the effective stiffnesses of the structural wall elements is estimated assuming a zero nominal rotation. With these quantities the nominal rotation θ can be estimated as:

$$\theta_x = \frac{V_{nsx} \cdot |e_{rz}| + V_{nsz} \cdot |e_{rx}|}{K_{rot,eff}} \quad (7.30)$$

Having obtained an estimate for the nominal rotation the actual displacement demand on the stiff and soft edge is estimated by the following equations:

$$\begin{aligned} \text{Stiff edge: } \Delta_1 &= \Delta_{CoM} - \theta \cdot L_1 \\ \text{Soft edge: } \Delta_2 &= \Delta_{CoM} + \theta \cdot L_2 \end{aligned} \quad (7.31)$$

where L_1 and L_2 are the lengths of the lever arms between the centre of strength and the stiff and soft edge respectively. The CoM displacement and the nominal rotation θ are entered as absolute values. As explained before, the CoM displacement can be estimated using the DDBD approach assuming zero rotation of the system. Equation 7.31 then allows to find estimates for the displacement demands on the stiff and soft edge. In the following section this approach is applied to different TR systems.

7.5.2 Examples illustrating the design approach

In this section the design approach that was presented in the previous section is applied to a number of different TR systems, some of which have been already employed in the parametric studies in Section 7.4. The section is divided into two parts; in the first part, predictions for uni-directional excitation are compared with analyses results and in the second part the prediction and analyses results for bi-directional excitation are compared.

The design approach presented in the previous section is verified by comparing the predicted displacement demands on CoM, stiff and soft edge with the average displacement demands obtained from time-history analyses. This method of verification departs from the typical design situation in the respect that the element strengths are known a priori. The design process hence needs to be iterated until it yields the a priori chosen element strengths. Two different cases were distinguished: a) the effective period of the system is smaller than the

corner period T_D of the displacement spectrum and b) the effective period is larger than T_D . In the first case, the iterative procedure is commenced by assuming a design displacement Δ_d . Assuming zero nominal rotation, effective damping ratios of the walls on the stiff and the soft edge can be computed according to the equation proposed by Priestley [2003] including the correction factor $\lambda_1 \lambda_2$ on the elastic part of the equivalent viscous damping that was proposed by Priestley and Grant [2005]:

$$\xi_{eff} = 5 \cdot \lambda_1 \lambda_2 + 95 \cdot \frac{1 - \mu_{\Delta}^{-0.5}}{\pi} \quad (7.32)$$

where

$$\lambda_1 \lambda_2 = 1 - 0.095(\mu_{\Delta} - 1)(1 - r_F) \quad (7.33)$$

where r_F is the ratio of the post-yield stiffness to the initial elastic stiffness of the wall. The effective damping ratio of the system was then computed as

$$\xi_{eff,s} = \sum \frac{V_{ni}}{\sum V_{ni}} \xi_{eff,i} \quad (7.34)$$

Inserting $\xi_{eff,s}$ into Equation 7.23, the damped spectra was computed and assuming a displacement demand of Δ_d the effective period T_{eff} could be readily determined. Knowing also the effective mass of the systems ($m_{eff} = 1788t$, Section 7.4.1) the base shear demand could be computed. This base shear demand was then compared to the actual base shear capacity V_{nsx} and the initially assumed displacement Δ_d was modified until a match between the base shear demand and capacity was obtained. For the second case when $T_{eff} > T_D$ the displacement demand Δ_d was altered until a match with the spectral displacement $S_{d,\xi_{eff,s}}$ was obtained. The spectral displacement depends on the effective damping ratio $\xi_{eff,s}$, which in turn depends on the displacement demand.

a) Examples for uni-directional excitation.

For uni-directional excitation, for the following TR systems prediction and analysis results were compared: (i) systems with constant and non-constant base shear capacity in the x direction, (ii) different levels of lateral restraints in the z direction and (iii) systems with effective periods shorter and longer than the corner period T_D . Figures 7.34 to 7.36 show the comparison of the results from the inelastic time-history analyses (black lines) to the predictions (grey lines); for reasons of clarity a floor layout of the analysed system is shown to the right of the plots that compare the predicted and observed displacement demands as a function of the strength eccentricity. The wall properties are always those described in Section 7.4.2. The following observations regarding the prediction of the CoM displacement and the displacement demand on the stiff edge and the soft edge were made:

CoM displacement: The CoM displacement was in general well predicted. Hence, it is feasible to represent the asymmetric system by an equivalent SDoF system in order to estimate the CoM displacement; an observation that has also been made by Castillo [2004].

Soft edge displacement: In some cases the soft edge displacements were slightly underestimated. However, the design equation for the displacement demand captured the general trends and sensitivities rather well. The accuracy of the prediction was deemed satisfactory for design purposes.

Stiff edge displacement: The displacement demand on the stiff edge was in general overestimated; however, the discrepancy was considerably less than if the stiff edge displacement had been simply estimated as the CoM displacement, as Castillo [2004] proposed.

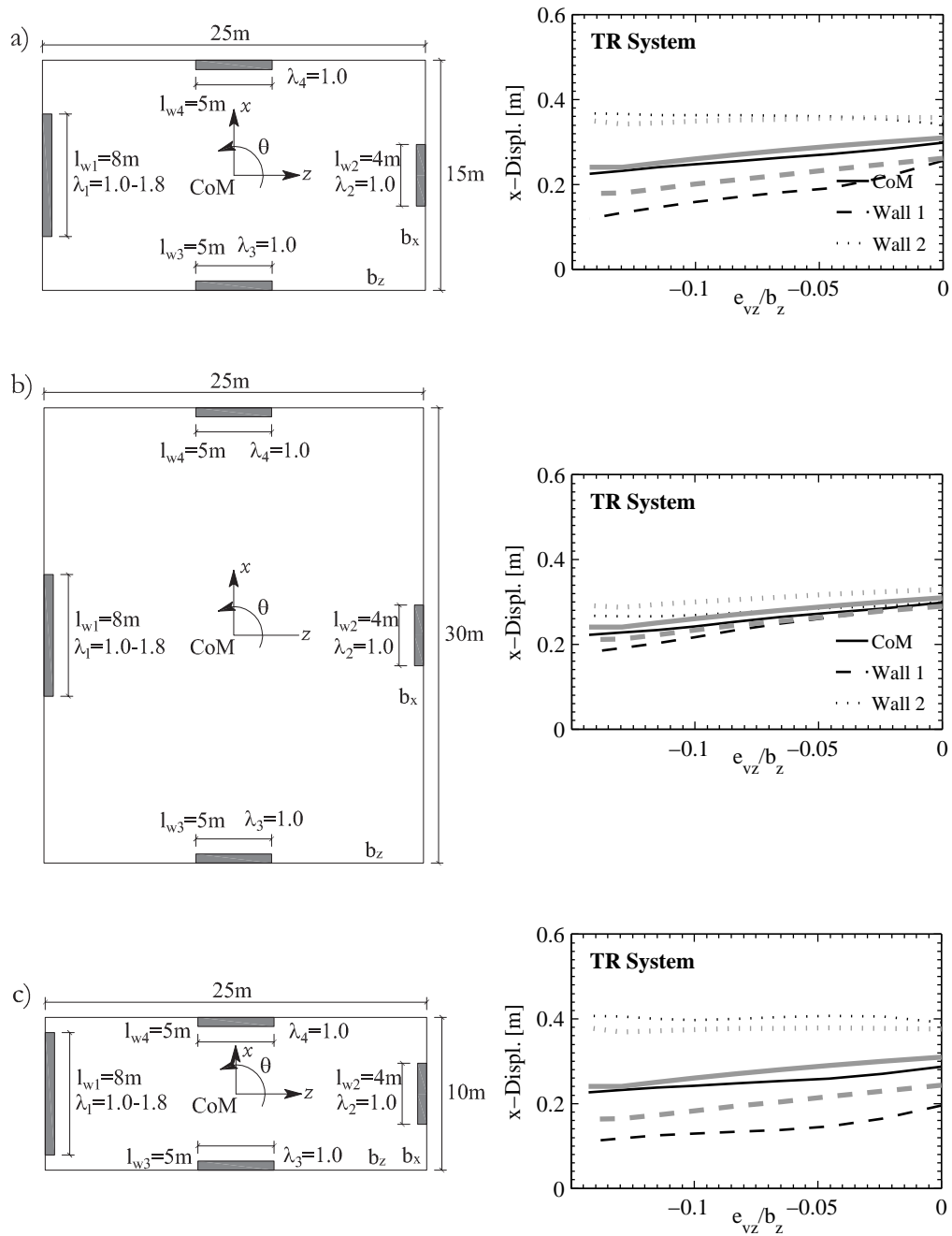


Figure 7.34. TR system with different slab lengths b_x : Comparison of analysis results for uni-directional excitation (black lines) to prediction (grey lines).

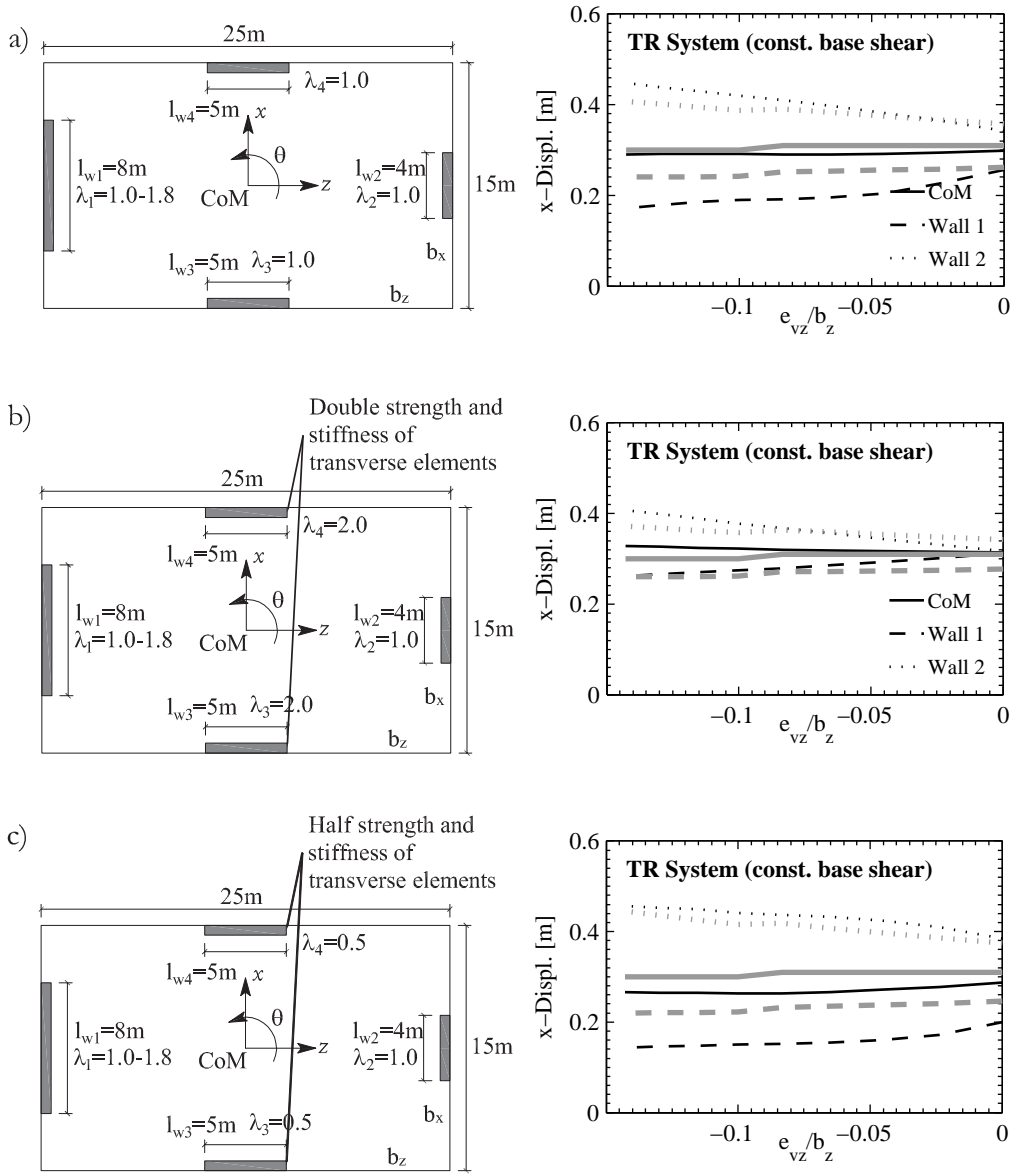


Figure 7.35. TR system with constant base shear and different strengths of transverse walls: Comparison of analysis results for uni-directional excitation (black lines) to prediction (grey lines).

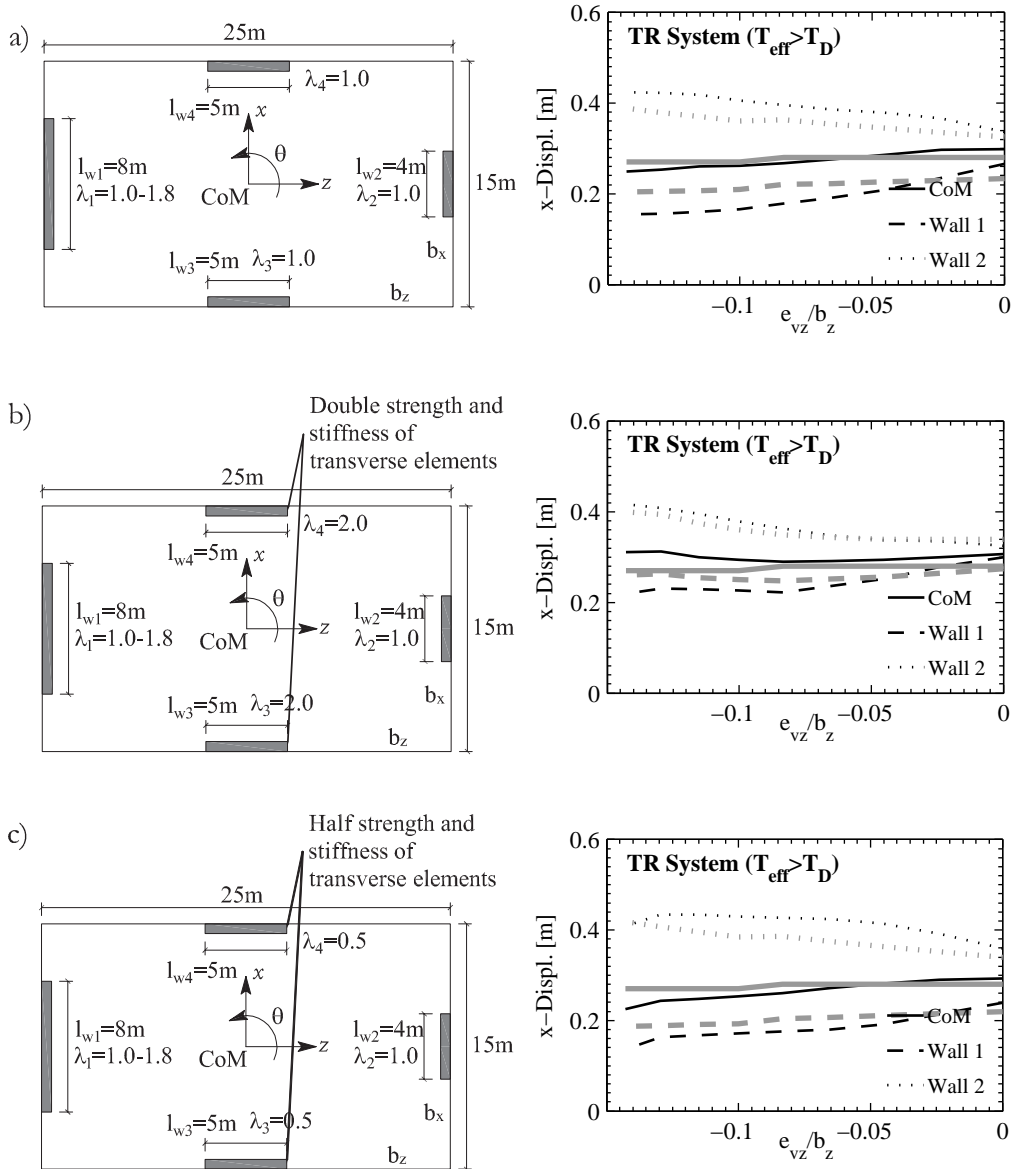


Figure 7.36. TR system with $T_{eff} > T_D$ and different strengths of transverse walls: Comparison of analysis results for uni-directional excitation (black lines) to prediction (grey lines).

b) Examples for bi-directional excitation.

Analysis results for bi-directional excitation were presented in Section 7.4.7. For the same systems that were considered in Section 7.4.7, the displacement demands were estimated according to the method presented in this section and plotted against the inelastic time-history analysis results (Figure 7.37). For the displacement demand in the x direction, the agreement between prediction and analysis results was generally good whereas the displacement demand on the CoM and the edges in the z direction was typically overestimated. For periods greater than 2.2s the spectral displacements of the z components of the records were in average lower than the design displacement (Figure 7.7). Since the fundamental period of the TR system with $e_v = 0$ is just below 2s, the effective periods were hence longer than 2s and therefore in the range of the spectrum for which the median spectrum was lower than the design spectrum. The difference between the prediction and the analysis results is therefore partly caused by the mismatch of the average displacement spectrum of the z component and the design spectrum. This mismatch is of course also reflected in the prediction of the edge displacements (Wall 3 and 4). For the systems for which the lever arm of the walls in the z direction was smaller than the lever arm of the walls in the x direction (Figure 7.37b, d and f), the nominal rotations were typically overestimated. For TR system of set 4 (Figure 7.37g and h), which had square slabs, the agreement between analysis results and prediction varied with strength eccentricity. For the x direction the stiff edge displacement was underestimated; this could be of concern from a design point of view. Castillo [2004] suggested to take the CoM displacement as an estimate of the stiff edge displacement. This, however, seems over conservative. It is suggested that, if a more conservative than the present estimate for the stiff edge is sought, the nominal rotation should be computed on the basis of the strength rather than the stiffness eccentricity:

$$\theta = \frac{V_{nsx} \cdot |e_{vz}| + V_{nsz} \cdot |e_{vx}|}{K_{rot,eff}} \quad (7.35)$$

7.6 Summary and recommendations for future research

Within the parametric study on 2D systems different parameters were investigated with respect to their effects on the torsional response of the systems. Among these parameters were the strength eccentricity, the rotational inertia, the orientation angle of a single ground motion component to the system axes, the seismic intensity, the spectral shape and the orthogonal component of ground motion. The first three of these have already been included in the parametric studies by Sommer [2000] and Castillo [2004] and in most respects the analyses carried out here confirmed their findings. Regarding the newly included factors, the analyses showed

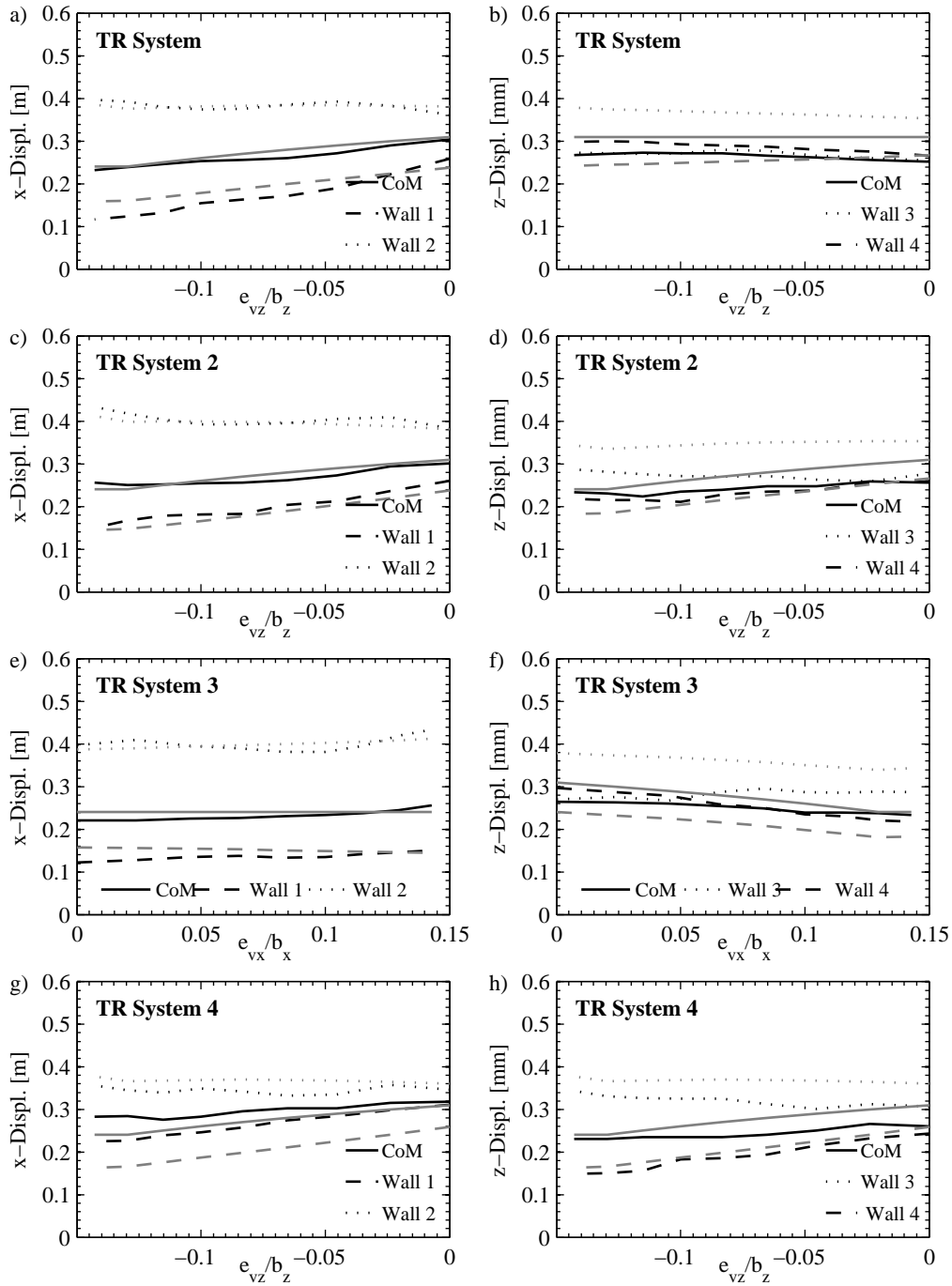


Figure 7.37. Different TR systems: Comparison of analysis results for bi-directional excitation (black lines) to prediction (grey lines).

that from a displacement-oriented design approach it is important to consider whether the effective period is longer or shorter than the corner period T_D of the spectrum: From the DDBD approach, it is known that, if the period is shorter than T_D , an increase in strength leads to a reduction in CoM displacement, while if it is longer than T_D , an increase in strength has little effect on the CoM displacement. Since the edge displacements are linked to the CoM displacement this characteristic is also reflected in the edge displacements. In particular, Castillo's postulate that the soft edge displacement is unaffected by strength eccentricity as long as the latter results from excess element strength of the stiff edge, does not hold for structures with effective periods longer than T_D . It was further shown that the second component of ground motion typically increases the displacement demand on the elements. This was linked to two effects: First, the second component softens the elements in the orthogonal direction and therefore reduces the rotational restraint. Second, if the orthogonal elements are not symmetric, the torsional moment is increased and hence the nominal rotations typically increase. The interplay of the different elements and the two ground motion components is, however, complex and varied between different records. The findings relate to the median displacement demands obtained from analyses of 20 real ground motion records with two horizontal components of motion.

Based on the observations from the parametric study semi-empirical equations were developed that allow estimating the nominal rotations and therefore also the displacement demands on the stiff and soft edges in TR systems. The predictions were compared to the analyses of different systems, some of which were analysed for uni-directional excitation and others for bi-directional excitation. The agreement was generally satisfactory. In some cases the stiff edge displacement was underestimated. A modification to the original design equations was proposed, which leads to safer displacement estimates for the stiff edge.

Since the proposed method for accounting for torsionally induced displacements is basically an empirical method, it bears the shortcoming of having to be verified for the entire range of system configurations to which it is later applied. Naturally, only a small portion of system configuration could be tested within the scope of this study. These could confirm that the method is capable of capturing the key effects but they cannot guarantee the method holds with the same accuracy for different systems. However, the method is only a design method and it is recommended that the displacement demand of systems that are suspected to show a significant rotational response should be verified by means of nonlinear time-history analysis.

A first investigation into the torsional response of 3D systems showed that if the systems are regular over the height, i.e. if the system fulfill the requirements listed in Section 7.1.1, then

the observed trends as well as the agreement between prediction and time-history analyses results were similar to those observed for 2D systems. The 3D systems that were analysed were structural wall buildings with a plan view similar to the one shown in Figure 7.2b and had two, four and eight storeys. For future studies, the analysis of 3D systems should be extended to frame-wall buildings. These buildings do not fulfill the requirements in Section 7.1.1. Although it is believed that the proposed estimates of the torsional response might be accurate enough for design purposes, the torsional response of wall-frame buildings should be analysed further. More so, since wall-frame buildings have often large strength and stiffness eccentricities since walls – and in particular cores – tend to be much stiffer than frames. An example for such a building is the reference building for the experimental work, which was shown in Figure 3.2.

8. SUMMARY, CONCLUSIONS AND OUTLOOK ON FUTURE RESEARCH

8.1 Summary

The objective of this project was to make a contribution to the performance-based seismic design of RC buildings with cores. Since cores are often placed at the perimeter of a building and are typically stiffer and stronger than other lateral strength providing structural elements, many of these buildings possess strength and stiffness eccentricities and are therefore prone to damage due to twist-induced displacements. The project focused on two aspects of the design for which the knowledge state was judged unsatisfactory. These were: (i) the inelastic behaviour of cores under different directions of seismic loading and (ii) the estimation of displacement demands on structural elements in torsionally eccentric buildings. Hence, the first aspect concerns the behaviour of a structural element while the second aspect concerns the overall behaviour of the building. In the following, contributions to these two aspects are summarised.

8.1.1 Seismic behaviour of U-shaped walls

The scope of this first part of the report was limited to cores with U-shaped sections. This is the simplest shape of a core, yet it has all the characteristics that set cores apart from, for example, rectangular walls. These are: its lateral strength and stiffness in both horizontal directions, its torsional stiffness and the open section that is composed of several rectangular wall sections. Although U-shaped walls are very popular in practice, their inelastic behaviour under seismic loading has not been examined in detail in the past. One drawback, when compared to the knowledge state of rectangular RC walls, was the scarce experimental evidence of only a single test series on U-shaped walls, which had been jointly conducted by the laboratories in Ispira and Saclay in 1999 and 2000 [Reynouard and Fardis, 2001]. It is believed that this lack of experimental data prevented a thorough calibration of analytical models and the derivation of appropriate design guidelines. One key objective of this project was, therefore, to conduct further quasi-static cyclic tests of U-shaped walls. Two test units were built at half scale and tested up to high ductility demands. The main difference between the two units

was their wall thickness. The objective of the experiments was to collect information on the behaviour of U-shaped walls for loading in different directions and therefore the walls were subjected to a bi-directional loading regime.

Both test units behaved very ductile. Depending on the direction of loading the maximum drifts at the point of failure were between 2.4% and 3.5%. The test unit with the larger wall thickness (TUA) failed during the diagonal cycle at $\mu_{\Delta} = 8.0$ due to rupture of longitudinal bars; most of the bars that ruptured had buckled during preceding cycles. This is a failure type that is also common for well-detailed and capacity designed rectangular walls. The second test unit (TUB) with the smaller wall thickness failed due to crushing of the compression struts in the web at the end of the $\mu_{\Delta} = 6.0$ cycles. This was not a targeted failure mechanism even though the well-confined corner elements prevented sudden crushing and maintained a residual strength capacity. The failure of the compression diagonal was caused by extensive spalling of the cover concrete of the web section. Spalling was not just limited to the boundary elements at the corners but due to the bi-directional loading history spalling extended into the non-confined regions. In these regions, spalling reduced the effective wall thickness even further than in the boundary elements. As a consequence, during the cycles of $\mu_{\Delta} = 6.0$, the effective wall thickness in the regions of the web where the crushing of compression struts finally initiated was reduced to only about one third of its original thickness. This significant reduction of the wall thickness had not been considered during the design of the test units.

a) Shear deformations.

One key difference of the tested U-shaped walls to rectangular walls concerned the magnitude of the shear deformations, which was for some directions of loading considerably larger for the U-shaped walls than for typical rectangular walls. The shear deformations of the U-shaped walls were evaluated using three different methods; differences between the results for the three methods showed that measurements of shear deformations are often associated with relative large uncertainties. Nevertheless, shear deformations deduced from the experimental measurements were used to identify trends in the magnitude of the shear deformations. In this study the shear deformations were described as the ratio of shear to flexural deformations (Δ_s/Δ_f). Dazio [2000] found that – unlike constant shear stiffness values would suggest – the Δ_s/Δ_f -ratio remained approximately constant over the entire ductility range; the shear stiffness reduced hence in proportion to the flexural stiffness. It could be shown that this finding is applicable to capacity designed walls, i.e. to walls whose shear transfer mechanisms are not degrading significantly. Considering the bi-axial strain state of an inelastic RC panel subjected to uniform shear and axial stresses showed that three sources of flexibility are contributing to the shear strain: (i) axial strains, which in RC walls are mainly associated with flexural deformations, (ii) tensile strains in the horizontal reinforcement, and (iii) compressive strains in the

concrete diagonal. For capacity designed walls the latter two components are relatively small and therefore the shear stiffness reduces in proportion to the flexural strains. If the walls are not capacity designed and either the shear reinforcement is yielding or the compression diagonals are softening considerably, the ratio of shear to flexural deformations are increasing with increasing ductility demand. Existing semi-empirical models [Hines *et al.*, 2004] and physical models [Priestley *et al.*, 2007] for determining the ratio of shear to flexural deformations were not capable of reflecting the large variation of shear to flexural deformations for U-shaped walls for different directions of loading; in particular the shear deformations of wall sections that were under net tension for loading in the diagonal direction were underestimated. Based on the results of 29 rectangular, barbelled, flanged and U-shaped walls that belonged to six different test series, a new empirical equation for the Δ_s/Δ_f -ratio was developed. Additionally, two structural analysis programs from the University of Toronto that are both based on the modified compression field theory were evaluated regarding their capability of modelling shear deformations. In particular one of these programs (VecTor2) seems suitable for this purpose. However, at present it is only available for 2D analysis while the 3D version is under development.

b) Plastic hinge analysis.

One of the most popular models for determining the force-displacement characteristics of flexural structural elements is the plastic hinge model. It is popular for the sake of its simplicity and because it results typically in good estimates of the displacement capacity of the structural element. However, only the moment-curvature relationship is derived from "first principles" whereas the relationships that are required to transform the curvature into a displacement and to determine the ultimate displacement capacity are largely empirical relationships. The key inputs that are required for this transformation are: (i) the curvature profile at first yield, (ii) the plastic hinge length, (iii) strain limits or ductility dependent shear capacities that determine the displacement capacity, and (iv) the ratio of shear to flexural displacements. The strain limits on concrete and reinforcement that have been derived from tests of RC walls or columns with different cross sections can be applied without limitations to walls with U-shaped cross sections. Ratios of shear to flexural deformations could be predicted with the newly developed empirical equation. State-of-the-art assumptions on the curvature profile and in particular existing estimates for the plastic hinge length, however, were derived from experimental evidence of uni-directional cyclic tests of mostly rectangular walls or columns. Before the current state-of-the-art equations are also applied to U-shaped walls, they should be validated against experimental results of U-shaped wall tests. While a comparison to results of two tests is certainly not sufficient, it can serve as starting point in the validation process.

Typically, the curvature profile at first yield is assumed as linear with zero curvature at the top and the first yield curvature at the base. By doing so, the flexural displacements are overestimated and the difference is attributed to account for shear displacements and displacements due to strain penetration into the foundation. Since shear deformations of U-shaped walls tend to be larger than shear deformations of rectangular walls, a more refined approach, which accounts explicitly for these two sources of flexibility and in return makes more realistic assumptions on the actual curvature profile at yield, was tested. It led only to marginally improved estimates of the nominal yield displacements when compared to the experimentally determined yield displacements. The difference between numerical and experimental results is, however, not only related to shortcomings of the numerical model; uncertainties related to determining the yield displacements from experimental data are also considerable. It was shown that good estimates of the yield curvature, which anchors the curvature profile at yield at the base, can be obtained from section analysis.

Plastic hinge lengths of the tested U-shaped walls varied for different directions of loading since the web and flange lengths were different as were the effective heights in the two principal directions of loading (i.e. the EW and the NS direction). It was shown that the existing empirical equations for the plastic hinge length yield conservative estimates of the experimentally determined hinge lengths. This also holds for the diagonal direction if the plastic hinge length in the diagonal direction is taken as the maximum of the plastic hinge lengths for the two principal directions; however, the degree of conservatism is less than for the principal directions. The existing equations for the plastic hinge length are design equation, which aim at providing conservative displacement capacity estimates. For assessment purposes some conservatism associated with the plastic hinge length component accounting for tension shift could be removed; the modified equation for the plastic hinge length resulted in better estimates of the experimentally determined plastic hinge lengths. The displacement capacities computed on the basis of the plastic hinge length equation for assessment purposes were reasonable, yet in most cases the actual displacement capacities were probably slightly overestimated. One of the drawbacks of testing a single unit under a bi-directional loading history is that the displacement capacity of the test unit can only be determined for one direction; for the other directions the maximum reached displacements can only serve as lower bound estimates of the actual displacement capacity and exact comparisons between analytical and experimental results are therefore not possible.

While the plastic hinge analysis predicted the moment capacities in the principal directions fairly accurately, the predicted moment capacities in the diagonal direction exceeded the maximum reached moments considerably. By means of wide-column analysis it could be shown that it is very likely that for the diagonal direction of loading the moment capacities were

never reached. This was due to the large shear flexibility, which had been underestimated when deciding on the loading pattern.

c) Wide-column models.

While plastic hinge models are convenient for estimating the displacement capacity, they do not give information on, for example, the force distribution between the web and flanges of the U-shaped section. This is, however, an important information for the shear design. From the experimental results it was found that in particular the force distribution between the two flanges during the diagonal cycles was very complex and was linked to two mechanisms, i.e. the forces required to impose the lateral displacements and the forces required to restrain the wall head from twisting. Depending on the direction of loading the force distribution between the two flanges varied considerably. To model the force distribution between the wall sections a three dimensional model of the U-shaped walls with inelastic properties is required. The wide-column analogy is the simplest model that fulfills these requirements. It is also a suitable analysis tool for practising engineers while other types of 3D models, such as shell and solid element models, are in most cases still limited to research applications if elements are assigned inelastic properties. For the wide-column models studied within the scope of this project nonlinear displacement-based beam elements with fibre sections were used for the vertical elements. Fibre sections have the advantage of capturing correctly the interaction of axial and flexural capacities. This was considered important since the axial force in the individual web and flange sections changed considerably over the course of the bi-directional loading history.

Existing guidelines for the properties of wide-column models of non-planar walls were almost exclusively derived from analysis of elastic models. When these guidelines were applied to inelastic models of the U-shaped walls, the models were generally too stiff. As a consequence, when the models were analysed for the entire loading history that was applied to the two test units, the maximum moments in the diagonal direction were – as for the plastic hinge analysis – overestimated. It was found that the shear flexibility of the vertical elements representing the web and flange sections and the shear flexibility of the horizontal link were the key parameters to improve the agreement of the numerical results with the experimental evidence.

In most structural analysis programs the shear and torsional stiffness of nonlinear beam elements are typically decoupled from the axial and flexural properties. Furthermore, the shear and torsional properties have to be assigned constant stiffness values which cannot be updated during the course of an analysis. However, it was explained above, that the shear stiffness of a RC member undergoing inelastic flexural deformations reduces in parallel to its flexural stiffness. Therefore, if an equivalent elastic shear stiffness is defined, it can only represent the correct shear stiffness for one particular top displacement. For top displacements that are

smaller or larger, the shear stiffness is underestimated or overestimated, respectively. It was shown that, if the often recommended shear stiffness corresponding to gross sectional properties (e.g. in FEMA 356 [American Society of Civil Engineers (ASCE), 2000]), is replaced by a shear stiffness equivalent to the shear stiffness at an intermediate ductility level, the agreement between numerical and experimental results in terms of force-displacement hystereses and force distribution between the two flanges is considerably improved.

Assigning also the horizontal links a shear flexibility was – to the best of our knowledge – a novel approach. This flexibility was introduced in order to account for deformations due to vertical shear stresses in the wall sections. While the shear flexibility of the links was necessary to model the global stiffness of the U-shaped walls correctly, it also led to a discrepancy of the vertical strains at the corners, which is physically not meaningful. Considering that the wide-column analogy is only a very simple modelling approach, which has the capability of reflecting the overall force-displacement characteristics of a structural member but not local phenomena, such as strains, this drawback was judged acceptable. Assigning a shear flexibility to the links reduced further the maximum moments in diagonal directions and as result the numerical model approximated the experimentally determined values fairly well.

Based on the results of sensitivity analyses and considerations regarding the representativeness of the modelling parameters for RC sections undergoing large inelastic deformations, guidelines for the modelling of U-shaped walls by means of the wide-column analogy were formulated. Apart from the already mentioned shear stiffnesses of vertical and horizontal members in the wide-column models, these comprise recommendations regarding the geometry of the model and the torsional stiffness of the links.

8.1.2 Displacement demands on in-plan asymmetric structures

The objective of the work on in-plan asymmetric structures was to extend the direct displacement-based design (DDBD) approach to structures that will not only translate but also twist when subjected to seismic excitation. The main consequence of the twist is the increased displacement demand on structural elements [Paulay, 1997], which should be accounted for in DDBD. The problem was approached in two steps: In a first step the key parameters influencing the twist displacements were identified by means of a parametric study on in-plan asymmetric structures. In a second step, a simple, semi-empirical approach was developed that allowed estimating the twist-induced displacements. The parametric study was the continuation of the work by Sommer [2000] and in particular by Castillo [2004]. Their work was extended regarding the type of ground motions that were included in the analysis. Both Sommer and Castillo carried out only analysis with a single horizontal component of ground motion which had a linearly increasing displacement spectrum for the period range of

interest. This study here complemented their analyses by using also components for which the spectral displacement for periods larger than a corner period T_D was constant. In addition, analyses with both horizontal components of ground motion were carried out. The analysis with records for which the spectral displacement for periods longer than T_D were constant showed that Castillo's design approach for torsionally eccentric structures, which stated that strength eccentricity is acceptable if it results from excess strength of the elements, is only applicable if the effective period of a structure is shorter than the corner period of the displacement spectrum. In New Zealand, where Castillo carried out his research, the corner period of the design displacement spectrum in NZS1170.5:2004 is at $T_D = 3s$ [New Zealand Standard, 2004]. Hence, a relatively large portion of structures will have effective periods $T_{eff} = T_{el}\sqrt{\mu\Delta}$ shorter than the corner period of the spectrum and therefore Castillo's design approach is applicable. In Europe, however, the corner period in the present seismic European code EC8 [CEN, 2003] is at $T_D = 2s$ and hence many structures subjected to medium to large displacement ductilities will have effective periods that are longer than the corner period. Analyses with the two horizontal components of ground motion showed that in most cases bi-directional analyses led to larger displacement demands than uni-directional analysis. The newly developed approach for estimating the displacement demand on structural elements of in-plan asymmetric structures can, independent of the spectral shape, cater for both uni- and bi-directional excitation although it is generally recommended to use at least the two horizontal components of a ground motion when analysing in-plan asymmetric structures. The design approach is limited to torsionally restrained systems that are regular over the height (Section 7.1.1). To compute the displacement demands on the structural elements an estimate of the seismic induced displacement demand on the centre of mass is required, which can be obtained from DDBD principles.

8.2 Conclusions

When searching the literature for publications on non-planar RC walls that respond in the inelastic range surprisingly few studies were found. Early studies ($\sim 1970-2000$) addressed mainly the response of elastic cores for which different types of models were developed. In these studies the torsional response of cores was a widely discussed research topic. For cores that are expected to respond in the inelastic range when subjected to seismic loading elastic models are of little relevance. The first studies to investigate the inelastic seismic behaviour of U-shaped walls were those related to the quasi-static cyclic and dynamic tests on U-shaped walls that had been jointly conducted by the laboratories in Ispra and Saclay [Reynouard and Fardis, 2001]. Within these studies the flexural behaviour for different directions of loading of one U-shaped wall configuration was investigated and complex shell models developed. This project attempted to complement the work on the inelastic seismic behaviour of U-shaped

walls commenced by Reynouard, Fardis and their co-workers in two respects: First, additional experiments on U-shaped walls were carried out. The walls had less compact sections than the ones tested in Ispra and Saclay and were detailed for high ductility demands while the specimens tested in Ispra and Saclay were designed for intermediate ductility demands. Second, more simple models, i.e. plastic hinge and wide-column models, were used for the analysis of the walls. Unlike shell or solid element models, these models are suitable for practical design applications since they are relatively easy to set up. Hence, this project improved the experimental evidence for U-shaped walls – instead of results for one wall configurations the results for three are now available – and also contributed to the modelling of such walls. It could be shown that both modelling approaches that were investigated, i.e. the plastic hinge model and the wide-column model, have their merits. In particular for the wide-column model guidelines were proposed, which should facilitate the setup of wide-column models with inelastic properties.

A topic that was originally not intended to be investigated in such depth were the shear deformations. However, during the analysis of the experimental database it was found that, depending on the direction of loading, shear deformations can constitute a major part of the lateral displacements and therefore they influenced considerably the overall behaviour of the test units. Since none of the existing approaches for estimating shear deformations could capture the strong dependence of the ratio of shear to flexural displacements on the directions of loading, it was decided to investigate this topic further. The result of this small study on shear deformations was mainly a new empirical equation for estimating the ratio of shear to flexural displacements. The large shear deformations influenced in particular the behaviour of the test units in diagonal direction. For some time the discrepancy between predicted and observed moment capacities in diagonal direction appeared like a mystery but it could be shown that, due to the underestimated shear flexibility, the moment capacity in diagonal direction was never reached. As a major consequence the flange in compression under diagonal loading was subjected to a smaller shear force than could occur, for example, for loading in diagonal direction only. Hence, the important aspect of the shear design of U-shaped walls could not be fully investigated and only few design guidelines were formulated when the design of the test units was described (Section 3.4). More research efforts are required to arrive at a complete set of design guidelines for U-shaped walls. In particular, additional experiments and analyses of U-shaped walls are required, that place emphasis on the shear force and displacement capacity for loading in diagonal direction.

Since damage to structural elements as well as many non-structural elements is related to imposed displacement and drift demands, performance-based seismic design requires estimates for these quantities. The direct displacement-based design approach is a well-established

performance-based design approach, which uses acceptable displacements and drifts as starting point in the design process. In its original form it could only be applied to structures that are symmetric in-plan, i.e. structures, that only translate but do not twist during an earthquake. This marked a considerable limitation to the range of structures to which the design method could be applied since many buildings have in-plan strength and stiffness eccentricities. The proposed method for estimating the twist-induced displacements was based on parametric studies of inelastic 2D systems. The basis for this study were the concepts on torsional behaviour by Paulay who first advocated that parameters describing the inelastic behaviour of buildings should be used when the twist induced displacements are estimated. Earlier design approaches which found their way into today's codes are based on elastic quantities. The parametric studies on 2D systems that were carried out within the scope of this project were a continuation of the work by Sommer and Castillo.

The proposed method for estimating the twist-induced displacements is limited to torsionally restrained structures that are regular over the height. This type of structure can be approximated by 2D systems, which facilitates parametric studies considerably. Not included in this group of systems are mixed wall-frame structures. Reinforced concrete cores are, however, often combined with a frame system and a design approach should also include this type of system. Although the 2D analyses are strictly speaking not applicable to mixed building systems, it is believed that for conceptual design purposes the proposed approach could also be applied. However, this should be verified by nonlinear time-history analysis of 3D models of mixed building systems that consist of a core and frames. Also not considered was the effect of the torsional stiffness of the U-shaped wall. While this is most likely not very important in torsionally restrained systems, it becomes more important in buildings in which the lever arm between walls is relatively small, e.g. for buildings in which the entire lateral strength is provided by the core or in which the lateral strength providing elements are placed close to the centre of mass. Neither of the two layouts are advisable but they may occur in existing buildings and therefore both the magnitude of the torsional stiffness of the core as well as the effect on the torsional response of the building should be quantified.

While the project treated two central aspects in the design of in-plan asymmetric RC buildings with U-shaped walls, more work is needed to bring the two pieces together. One important aspect that was not discussed, concerns, for example, the modelling of U-shaped walls as part of a building, i.e. the connection of the U-shaped wall to the surrounding structural elements. The following section gives a list of topics that should be investigated in the future in order to advance the understanding of the seismic behaviour of such buildings as well as to improve existing design and modelling guidelines.

8.3 Outlook on future research

Over the course of the project several aspects were identified that were beyond the scope of this project but should be investigated in the future. These are:

Torsional stiffness of U-shaped walls: The torsional stiffness of cores has not been covered within the scope of the thesis. However, during the loading of the two U-shaped test units small twists were applied in order to determine the torsional stiffness of the walls at different ductility levels and loading positions. The experimental data gained from these twists should be examined and the suitability of wide-column models for modelling the torsional stiffness should be addressed. In addition, the effect of the torsional stiffness of the U-shaped wall on the torsional response of buildings with different structural layouts should be examined.

Behaviour of U-shaped walls for loading in the diagonal direction: Since TUA failed in the diagonal direction of loading, this direction must be considered as one of the most critical ones. Moreover, the shear force demand on the flanges is largest for the diagonal direction. Due to the underestimated shear flexibility, the moment capacity in diagonal direction was never reached in the two tests which were carried out within the scope of this project and therefore this aspect could not be fully investigated. At present the diagonal direction is often not considered during the design process. To change this practice clear guidelines for determining the design base shear forces of the flanges due to translation and rotation are required. Also considered should be an increase of the shear forces in the flanges due to twist of the U-shaped wall. In addition the displacement capacity for loading in the diagonal direction must be addressed in more detail. An extension of this topic could cover the behaviour and retrofit of U-shaped walls for which the shear reinforcement in the flanges was determined based on the demand in the principal directions rather than the diagonal direction.

Derivation of design guidelines for non-planar walls: In this project, the design aspect was only touched on when the design of the test units was described (Section 3.4) and more research efforts are required to arrive at design guidelines for U-shaped walls. Apart from the additional experimental work regarding the behaviour for loading in the diagonal direction, analytical work is required on the basis of detailed models of U-shaped walls (e.g. shell or solid element models). The models should first be validated against the available experimental evidence for U-shaped walls before they are modified to cover a wider range of reinforcement layouts and geometries (different ratios of web to flange lengths and wall thicknesses). Also multi-cellular sections should be considered. However, the sections should remain simple enough to ensure that transparent design principles can be applied which result in a predictable and dependable inelastic

behaviour. Based on these models shear flexibilities, displacement capacities and failure modes could be assessed and favourable layouts distinguished from less favourable ones. The models could also be extended to investigate the effects of surrounding slabs, lintel beams across the opening and stairs in U-shaped walls on the inelastic behaviour of cores.

Assessment of U-shaped walls with inferior design details: The project was restricted to well detailed U-shaped walls with heavily confined boundary elements at the flange ends and the corners. It is believed (see Section 3.4) that in particular the boundary elements at the corners were essential for the ductile behaviour of the U-shaped walls. It would therefore be interesting to investigate the behaviour of U-shaped walls in which such boundary elements are either missing or poorly detailed. Since it is generally difficult to model the effect of inferior details numerically, this topic should also include an experimental part.

Analysis of buildings with U-shaped walls: The scope of the project was limited to the analysis of isolated U-shaped walls. In a future study U-shaped walls should be modelled as part of an entire building. While it is most likely advisable to represent U-shaped walls as wide-column models, other types of models such as stick models could also be investigated. In both cases, consideration should be given to the modelling of surrounding slabs and beam that are connected to the core. A preliminary discussion of this topic was given by Reynouard and Fardis [2001] but the given recommendations should be validated by numerical analyses and sensitivities to the modelling assumptions should be determined.

Torsional behaviour of buildings comprising a core and a frame system: Once guidelines on the modelling of core structures in an entire building are derived, a study on the torsional behaviour of in-plan asymmetric buildings with a core and a frame system can be carried out. It was outlined before that such structures strictly speaking do not fall into the category of "regular asymmetric systems" as defined by Hejal and Chopra [1989]. Only the behaviour of "regular asymmetric systems" can be represented by the 2D systems that were used for the parametric study on in-plan asymmetric buildings in Chapter 7. Since cores and frames are frequently combined, 3D models of such systems should be analysed regarding their torsional behaviour and conclusions regarding the comparativeness to the simple 2D models should be drawn.

Effect of non-structural components on the torsional response of buildings: Some non-structural components (e.g. masonry infill panels) are particularly stiff but have only small displacement capacities. An analytical study could investigate the effect of failure of non-structural components on the torsional response of a building. Appropriate

models for the interaction of the non-structural components with the structural components are a prerequisite for such a study.

REFERENCES

- ACI Committee 318 [2002] "Building code requirements for structural concrete (ACI 318-02) and commentary (ACI 318R-02)," Code and commentary, American Concrete Institute, Detroit, USA.
- American Society of Civil Engineers (ASCE) [2000] "FEMA 356: Prestandard and commentary for the seismic rehabilitation of buildings," Prestandard, Federal Emergency Management Agency (FEMA), Reston, Virginia, USA.
- Applied Technology Council [1992] "Improved seismic design criteria for California bridges," Report ACT-24, Applied Technology Council, Redwood City, California, USA.
- Avramidis, I. E. [1991] "Zur Kritik des äquivalenten Rahmenmodells für Wandscheiben und Hochhauskerne (Criticism of the equivalent frame model for structural walls and cores in high-rise buildings)," *Bautechnik*, Vol. 68, No. 8, pp. 275-285.
- Bachmann, H. [1967] "Zur plastizitätstheoretischen Berechnung statisch unbestimmter Stahlbetonbalken (A contribution to the analysis of indeterminate reinforced concrete beams using plasticity theory)," Ph.D. thesis N° 4069, Swiss Federal Institute of Technology (ETH), Zürich, Switzerland.
- Bathe, K. J. [1996] *Finite Element Procedures*, Prentice Hall, Upper Saddle River, New Jersey, USA.
- Bentz, E. [2000] "Sectional analysis of reinforced concrete members," Ph.D. thesis, Department of Civil Engineering, University of Toronto, Canada.
- Bentz, E. [2001] *Response-2000, Shell-2000, Triax-2000, Membrane-2000 User Manual*, University of Toronto.
- Bergmeister, K. and Wörner, J.-D. [2003] *BetonKalender (Concrete calendar)*, Ernst und Sohn, Berlin, Germany.
- Berry, M. P. and Eberhard, M. O. [2005] "Practical performance model for bar buckling," *ASCE Journal of Structural Engineering*, Vol. 131, No. 7, pp. 1060-1070.
- Beyer, K., Dazio, A., and Priestley, M. J. N. [2006] "Quasi-static cyclic tests on U-shaped RC walls: Test design and preliminary results," *Proceedings of the First European Conference on Earthquake Engineering and Seismology*, Geneva, Switzerland.

- Beyer, K., Dazio, A., and Priestley, M. J. N. [2008] “Quasi-static cyclic tests of two U-shaped walls,” Ibk report, Institut für Baustatik und Konstruktion, Swiss Federal Institute of Technology (ETH), Zürich, Switzerland, to be published.
- Carr, A. J. [2003] *Simqke – A program for artificial motion generation*, Department of Civil Engineering, University of Canterbury, Christchurch, New Zealand.
- Carr, A. J. [2004] *Ruaumoko – A program for inelastic dynamic analysis*, Department of Civil Engineering, University of Canterbury, Christchurch, New Zealand.
- Castillo, R. [2004] “Seismic design of asymmetric ductile systems,” Ph.D. thesis, Christchurch, New Zealand.
- Castillo, R., Carr, A. J., and Restrepo, J. I. [2001] “The rotation of asymmetric plan structures,” *Proceedings of the NZSEE Annual Conference*, Wairakei, New Zealand.
- Castillo, R., Paulay, T., and Carr, A. J. [2002] “Design concepts for ductile single-mass asymmetric systems,” *Proceedings of the 3rd European Workshop on the Seismic Behaviour of Irregular and Complex Structures*, Firenze, Italy.
- CEN [1994] “Eurocode 8: Design provisions for earthquake resistance of structures, Part 1: General rules, seismic actions and rules for buildings,” First Draft ENV 1998 – 1 – 1, European Committee for Standardization, Brussels.
- CEN [2001] “Eurocode 8: Design provisions for earthquake resistance of structures, Part 1: General rules, seismic actions and rules for buildings,” Draft No. 4 prEN 1998 – 1, European Committee for Standardization, Brussels.
- CEN [2003] “Eurocode 8: Design provisions for earthquake resistance of structures, Part 1: General rules, seismic actions and rules for buildings,” Final Draft prEN 1998–1, European Committee for Standardization, Brussels.
- Chopra, A. K. and Goel, R. K. [2004] “A modal pushover analysis procedure to estimate seismic demands for unsymmetric-plan buildings,” *Earthquake Engineering and Structural Dynamics*, Vol. 33, No. 8, pp. 903–927.
- Clough, R. W., King, I. P., and Wilson, E. L. [1964] “Structural analysis of multistory buildings,” *Journal of the Structural Division, ASCE*, Vol. 90, No. ST 3, pp. 19–34.
- Coleman, J. and Spacone, E. [2001] “Localization issues in force-based frame elements,” *Journal of Structural Engineering*, Vol. 127, No. 11, pp. 1257–1265.

- Combesure, D., Chaudat, T., and Moutafidou, A. [1999a] "Seismic tests of ICONS U-shaped walls – Description of the experimental set-up. Main results." Rapport DMT SEMT/EMSI/RT/99-062, CEA, France.
- Combesure, D., Chaudat, T., and Moutafidou, A. [1999b] "Seismic tests of ICONS u-shaped walls - description of the experimental set-up. main results," SEMT/EMSI/RT/ 99-062, Direction des réacteurs nucléaires, Département de mécanique et de technologie, Saclay, France.
- Dazio, A. [2000] "Entwurf und Bemessung von Tragwandgebäuden unter Erdbebeneinwirkung (Seismic design of buildings with structural walls)," Ph.D. thesis, Zürich, Switzerland.
- Dazio, A., Wenk, T., and Bachmann, H. [1999] "Versuche an Stahlbetontragwänden unter zyklisch-statischer Einwirkung (Quasi-static cyclic tests of RC structural walls)," IBK Report N° 239, Institut für Baustatik und Konstruktion, Swiss Federal Institute of Technology (ETH), Zürich, Switzerland.
- De la Llera, J. C. and Chopra, A. K. [1995] "Understanding the inelastic seismic behaviour of asymmetric-plan buildings," *Earthquake Engineering and Structural Dynamics*, Vol. 24, No. 4, pp. 549–572.
- De Stefano, M. and Pintucchi, B. [2006] "EAAE Task Group (TG) 8: Seismic behaviour of irregular and complex structures: Progress since 2002," *First European Conference on Earthquake Engineering and Seismology*, Geneva, Switzerland.
- Fajfar, P., Marusic, D., and Perus, I. [2005] "Torsional effects in the pushover-based seismic analysis of buildings," *Journal of Earthquake Engineering*, Vol. 9, No. 6, pp. 831–854.
- Greifenhagen, C. [2006] "Seismic behavior of lightly reinforced concrete squat shear walls," Ph.D. Thesis N° 3512, Ecole Polytechnique Fédérale de Lausanne, Switzerland.
- Hejal, R. and Chopra, A. K. [1989] "Earthquake analysis of a class of torsionally-coupled buildings," *Earthquake Engineering and Structural Dynamics*, Vol. 18, No. 3, pp. 305–323.
- Hines, E., Dazio, A., Chou, C., and Seible, F. [2002a] "Structural testing of the San Francisco-Oakland bay bridge East span skyway piers," Tech. rep. SSRP-2002/1, Department of Structural Engineering, University of California (UCSD), San Diego, California, USA.
- Hines, E. M. [2002] "Seismic performance of hollow rectangular reinforced concrete bridge piers with confined corner elements," Ph.D. thesis, University of California (UCSD), San Diego, USA.

- Hines, E. M., Dazio, A., and Seible, F. [2002b] "Seismic performance of hollow rectangular reinforced concrete piers with highly-confined boundary elements, Phase III: Web crushing tests," Tech. rep. SSRP-2001/27, Department of Structural Engineering, University of California (UCSD), San Diego, California, USA.
- Hines, E. M., Restrepo, J. I., and Seible, F. [2004] "Force-displacement characterization of well-confined bridge piers," *ACI Structural Journal*, Vol. 101, No. 4, pp. 537-548.
- Hines, E. M. and Seible, F. [2004] "Web crushing capacity of hollow rectangular bridge piers," *ACI Structural Journal*, Vol. 101, No. 4, pp. 569-579.
- Hines, E. M., Seible, F., and Priestley, M. J. N. [1999] "Cyclic tests of structural walls with highly-confined boundary elements, Phase I: Flexural tests, Phase II: Shear tests," Tech. rep. SSRP-99/15, Department of Structural Engineering, University of California (UCSD), San Diego, California, USA.
- Hiraishi, H. [1984] "Evaluation of shear and flexural deformations of flexural type shear walls," *Bulletin of the New Zealand Society for Earthquake Engineering*, Vol. 17, No. 2, pp. 135-144.
- Ile, N. [2000] "Contribution à la compréhension du fonctionnement des voiles en béton armé sous sollicitation sismique: Apport de l'expérimentation et de la modélisation à la conception (A contribution towards the understanding of the behaviour of RC walls under seismic loading: Report on the experimental work and from the modelling approach to the design concept)," N° d'ordre 98SAL0010, L'Institut National des Sciences Appliquées de Lyon, France.
- Ile, N., Plumier, C., and Reynouard, J. M. [2002a] "Test program on U-shaped walls leading to model validation and implication to design," *Proceedings of the 12th European Conference on Earthquake Engineering*, Elsevier Science Ltd.
- Ile, N. and Reynouard, J. M. [2000] "Nonlinear analysis of reinforced concrete shear wall under earthquake loading," *Journal of Earthquake Engineering*, Vol. 4, No. 2, pp. 183-213.
- Ile, N. and Reynouard, J. M. [2005] "Behaviour of U-shaped walls subjected to uniaxial and biaxial cyclic lateral loading," *Journal of Earthquake Engineering*, Vol. 9, No. 1, pp. 67-94.
- Ile, N., Reynouard, J. M., and Georgin, J. F. [2002b] "Non-linear response and modelling of RC walls subjected to seismic loading," *ISSET Journal of Earthquake Technology*, Vol. 39, No. 1-2, pp. 1-21.
- Kan, C. and Chopra, A. [1977] "Elastic earthquake analysis of a class of torsionally coupled buildings," *ASCE Journal of the Structural Division*, Vol. 103, No. ST4, pp. 821-838.

- Kaneko, T. [1975] "On Timoshenko's correction for shear in vibrating beams," *Journal of Physics D: Applied Physics*, Vol. 8, pp. 1927-1936.
- Kilar, V. and Fajfar, P. [1997] "Simple pushover analysis of asymmetric buildings," *Earthquake Engineering and Structural Dynamics*, Vol. 26, No. 2, pp. 233-249.
- Kilar, V. and Fajfar, P. [1999] "Application of the BST surface for seismic evaluation of an asymmetric multi-storey building," *Proceedings of the 3rd European Workshop on the Seismic Behaviour of Irregular and Complex Structures*, Firenze, Italy.
- Kowalsky, M. J. and Priestley, M. J. N. [2000] "Improved analytical model for shear strength of circular reinforced concrete columns in seismic regions," *ACI Structural Journal*, Vol. 97, No. 3, pp. 388-396.
- Krawinkler, H. [1996] "Cyclic loading histories for seismic experimentation on structural components," *Earthquake Spectra*, Vol. 12, No. 1, pp. 1-12.
- Kubo, T. and Penzien, J. [1979] "Analysis of three-dimensional strong ground motions along principal axes, san fernando earthquake," *Earthquake Engineering and Structural Dynamics*, Vol. 7, No. 3, pp. 265-278.
- Kwan, A. K. H. [1991] "Analysis of coupled wall/frame structures by frame method with shear deformation allowed," *Proceedings of the Institution of Civil Engineers*, Vol. 91, No. 2, pp. 273-297.
- Kwan, A. K. H. [1993] "Improved wide-column-frame analogy for shear/core wall analysis," *ASCE Journal of the Structural Engineering*, Vol. 119, No. 2, pp. 420-437.
- Kwan, A. K. H. [1994] "Unification of existing frame analogies for coupled shear/core wall analysis," *Computers & Structures*, Vol. 51, No. 4, pp. 393-401.
- Lopez, O. A., Chopra, A. K., and Hernandez, J. J. [2000] "Critical response of structures to multicomponent earthquake excitation," *Earthquake Engineering and Structural Dynamics*, Vol. 29, No. 12, pp. 1759-1778.
- MacLeod, I. and Hosny, H. [1977] "Frame analysis of shear wall cores," *Journal of the Structural Division, ASCE*, Vol. 103, No. ST10, pp. 2037-2047.
- MacLeod, I. A. [1974] "Analysis of shear wall buildings by the frame method," *Proceedings of the Institution of Civil Engineers*, Vol. 55, No. 2, pp. 593-603.
- Mander, J. B., Priestley, M. J. N., and Park, R. [1988a] "Observed stress-strain behavior of confined concrete," *ASCE Journal of Structural Engineering*, Vol. 114, No. 8, pp. 1827-1849.

- Mander, J. B., Priestley, M. J. N., and Park, R. [1988b] "Theoretical stress-strain model for confined concrete," *ASCE Journal of Structural Engineering*, Vol. 114, No. 8, pp. 1804–1826.
- Massone, L. M. and Wallace, J. W. [2004] "Load-deformation responses of slender reinforced concrete walls," *ACI Structural Journal*, Vol. 101, No. 1, pp. 103–113.
- Mazzoni, S., McKenna, F., and Fenves, G. L. [2005] *OpenSees Command Language Manual, OpenSees v. 1.6.2f*, University of California, Berkeley, USA.
- Menegotto, M. and Pinto, P. E. [1973] "Method of analysis for cyclically loaded R.C. plane frames including changes in geometry and non-elastic behavior of elements under combined normal force and bending," *IABSE Symposium on Resistance and ultimate deformability of structures acted on by well defined repeated loads*, pp. 15–22, IABSE, Lisbon, Portugal.
- Myslimaj, B. and Tso, W. K. [2002] "A strength distribution criterion for minimizing torsional response of asymmetric wall-type structures," *Earthquake Engineering and Structural Dynamics*, Vol. 31, No. 1, pp. 99–120.
- New Zealand Standard [2004] "Structural design actions: Part 5: Earthquake actions – New Zealand," Code and commentary, Wellington, New Zealand.
- Oesterle, R. G., Aristizabal-Ochoa, J. D., Fiorato, A. E., Russell, H. G., and Corley, W. G. [1979] "Earthquake resistant structural walls – Tests of isolated walls – Phase II," Tech. rep., Portland Cement Association, Skokie, Illinois, USA.
- Oesterle, R. G., Aristizabal-Ochoa, J. D., Shiu, K. N., and Corley, W. G. [1984] "Web crushing of reinforced concrete structural walls," *ACI Journal*, Vol. 81, No. 3, pp. 231–241.
- Oesterle, R. G., Fiorato, A. E., Johal, L. S., Carpenter, J. E., Russell, H. G., and Corley, W. G. [1976] "Earthquake resistant structural walls – Tests of isolated walls," Tech. rep. NSF/RA-760815, Portland Cement Association, Skokie, Illinois, USA.
- Park, R. [1988] "Ductility evaluation from laboratory and analytical testing – State-of-the art report," *Proceedings of the Ninth World Conference on Earthquake Engineering*, Vol. VIII, pp. 605–616, Tokyo-Kyoto, Japan.
- Park, R. and Paulay, T. [1975] *Reinforced Concrete Structures*, John Wiley and Sons, Inc.
- Paulay, T. [1996] "Seismic design for torsional response of ductile buildings," *Bulletin of the New Zealand National Society for Earthquake Engineering*, Vol. 29, No. 3, pp. 178–198.
- Paulay, T. [1997] "Displacement-based design approach to earthquake-induced torsion in ductile buildings," *Engineering Structures*, Vol. 19, No. 9, pp. 699–707.

- Paulay, T. [1999] "Some principals relevant to the seismic torsional response of ductile buildings," *Proceedings of the 2nd European Workshop on the Seismic Behaviour of Asymmetric and Irregular Structures*, Istanbul, Turkey.
- Paulay, T. [2001] "Some design principles relevant to torsional phenomena in ductile buildings," *Journal of Earthquake Engineering*, Vol. 5, No. 3, pp. 273–308.
- Paulay, T. [2002] "An estimation of displacement limits for ductile systems," *Earthquake Engineering and Structural Dynamics*, Vol. 31, No. 3, pp. 583–599.
- Paulay, T. and Priestley, M. J. N. [1992] *Seismic design of reinforced concrete and masonry buildings*, John Wiley and Sons, Inc.
- PEER [2005] "NGA database (where NGA stands for "Next Generation of Attenuation" with records orientated fault-normal and fault-parallel direction," on CDs, Pacific Earthquake Engineering Research Center, Berkeley, USA.
- Pégon, P., Plumier, C., Pinto, A., Molina, J., Gonzalez, P., Colombo, A., Tognoli, P., and Hubert, O. [2000a] "U-shaped walls: Quasi-static test in the X direction – Test report," TMR-ICONS-TOPIC5 JRC Special Publication No.I.01.28, JRC Ispra, Italy.
- Pégon, P., Plumier, C., Pinto, A., Molina, J., Gonzalez, P., Colombo, A., Tognoli, P., Hubert, O., and Tirelli, D. [2000b] "U-shaped walls: Description of the experimental set-up," TMR-ICONS-TOPIC5 JRC Special Publication No.I.00.141, JRC Ispra, Italy.
- Pégon, P., Plumier, C., Pinto, A., Molina, J., Gonzalez, P., Tognoli, P., and Hubert, O. [2000c] "U-shaped walls: Quasi-static bi-axial test in the X and Y directions – Test report," TMR-ICONS-TOPIC5 Draft, JRC Ispra, Italy.
- Pégon, P., Plumier, C., Pinto, A., Molina, J., Gonzalez, P., Tognoli, P., Hubert, O., and Tirelli, D. [2000d] "U-shaped walls: Quasi-static test in the Y direction – Test report," TMR-ICONS-TOPIC5 JRC Special Publication No.I.00.143, JRC Ispra, Italy.
- Pettinga, J. D. and Priestley, M. J. N. [2005] "Dynamic behaviour of reinforced concrete frames designed with direct-displacement based design," *Journal of Earthquake Engineering*, Vol. 9, Special Issue 2, pp. 309–330.
- Priestley, M. J. N. [2000] "Performance-based seismic design," *Keynote address, Proceedings of the 12th World Conference on Earthquake Engineering*, Auckland, New Zealand.
- Priestley, M. J. N. [2003] "Myths and fallacies in earthquake engineering, revisited," The Mallet Milne Lecture 2003, IUSS Press, Pavia, Italy.

- Priestley, M. J. N. and Amaris, A. D. [2002] "Dynamic amplification of seismic moments and shear forces in cantilever walls," Research Report ROSE 2002/01, ROSE School, Pavia, Italy.
- Priestley, M. J. N., Calvi, G. M., and Kowalsky, M. [2007] *Displacement-based seismic design of structures*, IUSS Press, Pavia, Italy.
- Priestley, M. J. N. and Grant, D. N. [2005] "Viscous damping in seismic design and analysis," *Journal of Earthquake Engineering*, Vol. 9, Special Issue 2, pp. 229–255.
- Priestley, M. J. N. and Kowalsky, M. J. [1998] "Aspects of drift and ductility capacity of rectangular cantilever structural walls," *Bulletin of the New Zealand Society for Earthquake Engineering*, Vol. 31, No. 2, pp. 73–85.
- Priestley, M. J. N. and Kowalsky, M. J. [2000] "Direct-displacement-based seismic design of concrete buildings," *Bulletin of the New Zealand Society for Earthquake Engineering*, Vol. 33, No. 4, pp. 421–444.
- Priestley, M. J. N. and Park, R. [1987] "Strength and ductility of concrete bridge columns under seismic loading," *ACI Structural Journal*, Vol. 84, No. 1, pp. 61–76.
- Priestley, M. J. N., Seible, F., and Benzoni, G. [1994] "Seismic response of columns with low longitudinal steel ratios," Research Report SSRP-94/08, UCSD, San Diego, California, USA.
- Priestley, M. J. N., Seible, F., and Calvi, G. M. [1996] *Seismic design and retrofit of bridges*, John Wiley and Sons, Inc.
- Rabbat, B. and Collins, M. [1978] "A variable angle space truss model for structural concrete members subjected to complex loading," *Proceedings of the Douglas McHenry International Symposium on Concrete and Concrete Structures*, No. SP-55, pp. 547–587, American Concrete Institute, Detroit, USA.
- Restrepo, J. I. [1993] "Seismic behaviour of connections between precast concrete elements," Ph.D. thesis 93-3, Department of Civil Engineering, University of Canterbury, Christchurch, New Zealand.
- Restrepo, J. I. [2006] *Lectures notes to the course "Seismic design of reinforced concrete buildings"*, ROSE School, Pavia, Italy.
- Reynouard, J.-M. and Fardis, M. N. [2001] *Shear wall structures*, No. 5 in CAFEEL-ECOEST/ICONS Thematic Report, Laboratório Nacional de Engenharia Civil (LNEC), Lisboa, Portugal.

- Rutenberg, A. [1992] "Nonlinear response of asymmetric building structures and seismic codes: A state of the art review," *European Earthquake Engineering*, Vol. VI, No. 2, pp. 3–19.
- Rutenberg, A. [2002] "EAEE Task Group (TG) 8: Behaviour of irregular and complex structures and asymmetric structures," *12th European Conference on Earthquake Engineering*, London, UK.
- Rutenberg, A. and De Stefano, M. [1997a] "The force reduction factor and seismic stability of code-designed asymmetric structures," *Proceedings of the 1st Japan-Turkey Workshop on Earthquake Engineering*, pp. 41–51, Istanbul, Turkey.
- Rutenberg, A. and De Stefano, M. [1997b] "On the seismic performance of yielding asymmetric multistorey buildings: A review and a case study," *Seismic Design Methodologies for the Next Generation of Codes*, eds. P. Fajfar and H. Krawinkler, Balkema, Rotterdam, Netherlands.
- Rutenberg, A., Hsu, T.-I., and Tso, W. K. [1978] "Response spectrum techniques for asymmetric buildings," *Earthquake Engineering and Structural Dynamics*, Vol. 6, No. 5, pp. 427–435.
- Rutenberg, A., Shtarkman, M., and Eisenberger, M. [1986] "Torsional analysis methods for perforated cores," *ASCE Journal of Structural Engineering*, Vol. 112, No. 6, pp. 1207–1227.
- Scott, B. D., Park, R., and Priestley, M. J. N. [1982] "Stress-strain behavior of concrete confined by overlapping hoops at low and high strain rates," *ACI Journal*, Vol. 79, No. 2, pp. 13–27.
- Shing, B. and Tanabe, T., eds. [2001] *Modeling of inelastic behavior of RC structures under seismic loads*, Tokyo and at Lake Yamanaka, Japan, ASCE, proceedings of the US-Japan Seminar on "Post-Peak Behavior of Reinforced Concrete Structures Subjected to Seismic Loads: Recent Advances and Challenges on Analysis and Design".
- SIA 160 [1989] "SIA 160: Einwirkungen auf Tragwerke (Structural loads)," Building code, Swiss Society of Engineers and Architects, Zürich, Switzerland, in German.
- Sommer, A. [2000] "Torsion und Duktilitätsbedarf bei Hochbauten unter Erdbebeneinwirkung (Torsion and ductility demand of buildings subjected to seismic loading)," Ph.D. thesis, Zürich, Switzerland.
- Stafford-Smith, B. and Abate, A. [1981] "Analysis of non-planar shear wall assemblies by analogous frame," *Proceedings of the Institution of Civil Engineers*, Vol. 71, No. 2, pp. 395–406.
- Stafford-Smith, B. and Girgis, A. [1984] "Simple analogous frames for shear wall analysis," *Journal of Structural Engineering, ASCE*, Vol. 110, No. 11, pp. 2655–2666.

- Stafford-Smith, B. and Girgis, A. [1986] "Deficiencies in the wide column analogy for shearwall analysis," *Concrete International*, pp. 58–61.
- Sullivan, T. J., Priestley, M. J. N., and Calvi, G. M. [2006] "Direct displacement-based design of frame-wall structures," *Journal of Earthquake Engineering*, Vol. 10, Special Issue 1, pp. 91–124.
- Taucer, F. F., Spacone, E., and Filippou, F. C. [1991] "A fiber beam-column element for seismic response analysis of reinforced concrete structures," Tech. rep. Report No. UCB/EERC-91/17, Earthquake Engineering Research Centre, College of Engineering, University of California, Berkeley, USA.
- Trombetti, T., Gasparini, G., and Silvestri, S. [2002] "A new simplified approach to the analysis of torsional problems in eccentric systems: The "alpha" method," *27th Conference on "Our World in Concrete & Structures"*, Singapore.
- Tso, W. K. and Moghadam, A. S. [1997] "Seismic response of asymmetrical buildings using pushover analysis," *Seismic Design Methodologies for the Next Generation of Codes*, eds. P. Fajfar and H. Krawinkler, pp. 311–321, Balkema, Rotterdam, Netherlands.
- Vecchio, F. and Collins, M. [1986] "The modified compression-field theory for reinforced concrete elements subjected to shear," *ACI Journal*, Vol. 83, No. 2, pp. 219–231.
- Vecchio, F. and Collins, M. [1988] "Predicting the response of reinforced concrete beams subjected to shear using the modified compression field theory," *ACI Journal*, Vol. 85, No. 3, pp. 258–268.
- Wong, P. S. and Vecchio, F. J. [2002] *VecTor2 and Formworks User's Manual*, University of Toronto, Canada.
- Wood, S. L. [1989] "Minimum tensile reinforcement requirements in walls," *ACI Journal*, Vol. 86, No. 4, pp. 582–591.
- Xenidis, H., Athanatopoulou, A., and Avramidis, I. [1993] "Modelling of shear wall cores under earthquake loading using equivalent frames," *Proceedings of the 2nd European Conference on Structural Dynamics: EURODYN '93*, pp. 901–910, Balkema, Rotterdam, Trondheim, Norway.
- Xenidis, H. and Avramidis, I. [1999] "Comparative performance of code prescribed analysis methods for R/C buildings with shear wall cores," *Proceedings of the 4th European Conference on Structural Dynamics: EURODYN '99*, pp. 869–875, Balkema, Rotterdam.

A. EXPERIMENTALLY DETERMINED RATIOS OF SHEAR TO FLEXURAL DISPLACEMENTS FOR RC WALLS

In this section experimental data related to shear deformations of RC walls tested under cyclic loading is presented. Each test unit is characterised regarding the reinforcement layout and ratios, the axial load ratio, the failure mode and the ratio of shear to flexural deformations. Additional information on these tests regarding maximum shear force, the observed cracking angle and values derived from section analysis are given in Table A.10. The database is used for the empirical study on shear displacements which is presented in Chapter 5. The mean ratio of shear to flexural displacements Δ_s/Δ_f is the target parameter of this study. There is no doubt a certain degree of interserial variability of the Δ_s/Δ_f -ratios due to different instrumentation and different evaluation techniques used by different authors. The shear displacement measurements seem particularly sensitive to these factors (see Section 2.6) while the flexural displacements are always evaluated by double-integrating average curvatures and differences between test series are mainly associated with different baselengths over which elongations are measured. Interserial variability of flexural displacement is therefore believed to be smaller than for shear displacements. It was therefore decided to compute the Δ_s/Δ_f -ratios according to the indirect method for evaluating the shear displacements (Equation 4.10). This method has also the advantage that it can be applied to all test units in the database while Hiraishi's method for example could only be applied to test units for which the data is available in electronic format.

The database includes 29 walls which belong to six different test series. These are: PCA, Phase I (Section A.1), PCA, Phase II (Section A.2), the test series by Dazio (Section A.3), the test series by Hines (Section A.4), the three U-shaped walls tested in Ispra (Section A.5) and the U-shaped walls TUA and TUB, which were tested within the scope of this project (Section 4.4). Out of the 29 walls, 26 walls were tested under a uni-axial loading history and three walls under a bi-axial loading history (Ispra XY, TUA and TUB). Among the 26 walls tested under uni-directional loading, there were 7 rectangular walls, 15 barbelled walls, 2 flanged walls and 2 U-shaped walls (Ispra X and Ispra Y). All walls were slender walls with shear span ratios larger than two. The reasoning behind excluding squat walls was given in Section 5.1.

A.1 PCA Tests, Phase I

Within the scope of the first phase of the PCA research project Oesterle *et al.* [1976] tested seven structural walls under cyclic loading. In addition, one of the seven walls was repaired and tested again under cyclic loading and an eighth wall was tested under monotonic loading. These two experiments are not considered in the following. All walls were 1.905m long and had an effective height of 4.57m. Among the seven walls were two rectangular walls, four barbelled walls and one flanged wall. All walls were tested with no axial load apart from their selfweight. The loading history was a uni-directional loading history with symmetric cycles about the zero position. At each displacement level a wall was subjected to three cycles of the same amplitude before the displacement demand was increased by 1in (25.4mm). Details of the specimens are summarised in Table A.2; additional information on the experiments can be found in Wood [1989].

From the experimental results Oesterle *et al.* [1976] derived flexural and shear displacements at the positive peak loads of the first cycle of a ductility level. For the reasons stated in the introduction to this appendix, the shear displacements were computed with the indirect method. Aside from the consistency, which demands that the indirect method is applied, there are further reasons that support the choice of the indirect method: Oesterle *et al.* [1976] computed shear deformations according to the original method from diagonal displacement measures. However, these shear deformations cannot be considered as accurate for the following reasons because the shear deformations were measured across the base construction joints and the base rotation due to strain penetration into the foundation distorts the computed shear deformations. Although the Δ_s/Δ_f -ratios obtained from the shear displacements according to the original method are not used in the study in Chapter 5, the values were evaluated and compared with those of the indirect method. The Δ_s/Δ_f -ratios obtained for the indirect and original method are plotted as functions of the top displacement in Figure A.1; the "mean" ratios obtained for the two methods are compared in Table A.1. While for the larger ratios the difference between the two methods is relatively small, there is a significant difference for walls where the indirect method yields small ratios. The shear displacements were evaluated at the top of the wall, i.e. at $h = 4.57\text{m}$. For the PCA walls of Phase I the development of the ratios Δ_s/Δ_f with top displacement was discussed in detail in Section 5.1.1; in this section also the derivation of the "mean" ratios was explained. Note also that all values for the displacement quantities were obtained as readings from graphs of the test report. The image quality of the figures in the copy of the test report was relatively poor since the copy had been obtained by scanning an original hard-copy of the test report. The data is hence less accurate than for the experiments where the results were available in electronic format. This should be kept in mind when interpreting the test data.

Table A.1. PCA, Phase I: Comparison of ratios of shear to flexural deformations for the different methods of evaluating the shear displacements.

	$\frac{\Delta_{s2}}{\Delta_f}$	$\frac{\Delta_{s3}}{\Delta_f}$
R ₁	0.15	0.33
R ₂	0.27	0.40
B ₁	0.21	0.36
B ₃	0.33	0.54
B ₂	0.45	0.45
B ₅	0.47	0.47
F ₁	0.47	0.55

Δ_{s2} Indirect method: $\Delta_{s2} = \Delta_{top} - \Delta_f - \Delta_{sl}$
 Δ_{s3} Original method

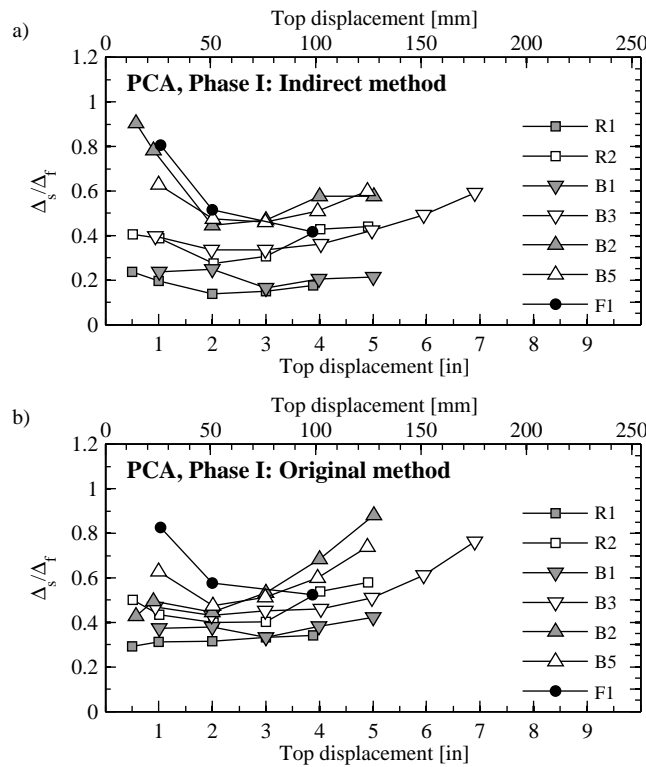


Figure A.1. PCA walls, Phase I: Ratio of shear to flexural displacements as a function of the top displacement if the shear displacements are computed according to the indirect method (a) and the original method (b).

Table A.2. PCA Tests, Phase I: Characteristics of walls [Oesterle *et al.*, 1976].

Specimen	Reinforcement layout	ρ_t [%]	ρ_{web} [%]	ρ_h [%]	$\nu^{(1)}$ [%]	Description	Failure Mode
R1		0.48	0.25	0.31	0.4	No boundary elements.	Flexure ¹⁾ ; first buckling during cycles with $\Delta_{top} = 3$ in; first fracture during cycles with $\Delta_{top} = 5$ in; concrete did not crush.
R2		1.00	0.25	0.31	0.4	Confined boundary elements with concentrated reinforcement.	Flexure ¹⁾ ; onset of out-of-plane deformation of compression end was observed after a maximum top displ. of 3in; bowing progressed further but load bearing capacity remained stable up to 2nd cycle with $\Delta_{top} = 5$ in; during first cycle with $\Delta_{top} = 6$ in several bar fractured, further out-of-plane displacement and concrete crushing occurred.
B1		0.77	0.29	0.31	0.3	Almost no confinement of boundary elements.	Flexure ¹⁾ ; during cycles with $\Delta_{top} = 3$ in first bar buckled and onset of concrete crushing; end hooks of shear reinforcement started to open during the first cycle with $\Delta_{top} = 4$ in; first bar fracture occurred during the first cycle with $\Delta_{top} = 5$ in; in subsequent cycles the boundary elements deteriorated significantly.
B3		0.77	0.29	0.31	0.4	As B1 but with well confined boundary elements.	Flexure ¹⁾ ; very similar behaviour to B1 but first bar buckling during cycles with $\Delta_{top} = 7$ in; from $\Delta_{top} = 4$ in onwards significant crushing and grinding of the web concrete; failure during cycles with $\Delta_{top} = 8$ in due to bar fracture associated with large shear displacements of the boundary element.
B2		2.27	0.29	0.63	0.4	Heavily reinforced boundary element but little confining reinforcement.	Shear ¹⁾ ; first indication of crushing of concrete at $\Delta_{top} = 3$ in; during cycles with $\Delta_{top} = 4$ in 2 bars buckled; sudden failure of web compression strut during cycle with $\Delta_{top} = 5$ in.
B5		0.48	0.29	0.63	0.3	As B2 but with well confined boundary elements.	Shear ¹⁾ ; no bar buckling reported; onset of compression strut failure during cycles with $\Delta_{top} = 3$ in but load could be transferred to other struts; web crushing occurred during second cycle with $\Delta_{top} = 5$ in.
F1		2.16	0.30	0.71	0.4	No confining reinforcement, only some stabilising reinforcement.	Shear ¹⁾ ; steepest diagonal strut crushed during cycle with $\Delta_{top} = 4$ in which led to the failure of the total wall.

1) Failure mode according to Wood [1989]

A.2 PCA Tests, Phase II

In the second phase of the PCA tests [Oesterle *et al.*, 1979], six walls were tested. One wall of these six walls was repaired and retested; the data of the repaired wall is not considered here. The wall dimensions were the same as those of the walls tested during Phase I. During Phase II, however, axial load was applied to the specimens. The six walls comprised five barbelled walls and one flanged wall. Apart from specimen B₉ and B₁₀ the walls were tested using the same loading regime as for Phase I, i.e. three cycles of the same amplitude with top displacement increments of 1in (25.4mm).

One pair of barbelled walls (B₇ and B₉) were used to investigate the effect of the loading history. Specimen B₇ was tested under the incrementally increasing loading history while specimen B₉ was tested using a loading regime under which the wall was subjected to cracking during the first cycle while in the second cycle the wall was already taken to the predetermined displacement capacity. After three cycles at this level the displacement demand was reduced to 80% for three cycles before the displacement demand was reduced further to $\mu_{\Delta} = 1.1$ for six more cycles. Specimen B₁₀ was also tested using this modified loading regime; however, the vertical reinforcement content of the boundary elements was smaller for B₁₀ than for B₇. Further details on these experiments can be found in Wood [1989]. As for all other walls, the ratios of shear to flexural displacements were determined in the indirect way (Figure A.2a). For the sake of completeness, however, also the shear displacements according to the original method (i.e. the shear displacements computed by Oesterle *et al.* [1979]) are plotted in Figure A.2b and the Δ_s/Δ_f -ratios obtained for the two methods are compared in Table A.3.

Table A.3. PCA, Phase II: Comparison of ratios of shear to flexural deformations for the different methods of evaluating the shear displacements.

	$\frac{\Delta_{s2}}{\Delta_f}$	$\frac{\Delta_{s3}}{\Delta_f}$
B ₆	0.54	0.35
B ₇	0.53	0.32
B ₈	0.40	0.27
B ₉	0.31	0.45
B ₁₀	0.35	0.26
F ₂	0.58	0.42
Δ_{s2}	Indirect method: $\Delta_{s2} = \Delta_{top} - \Delta_f - \Delta_{sl}$	
Δ_{s3}	Original method	

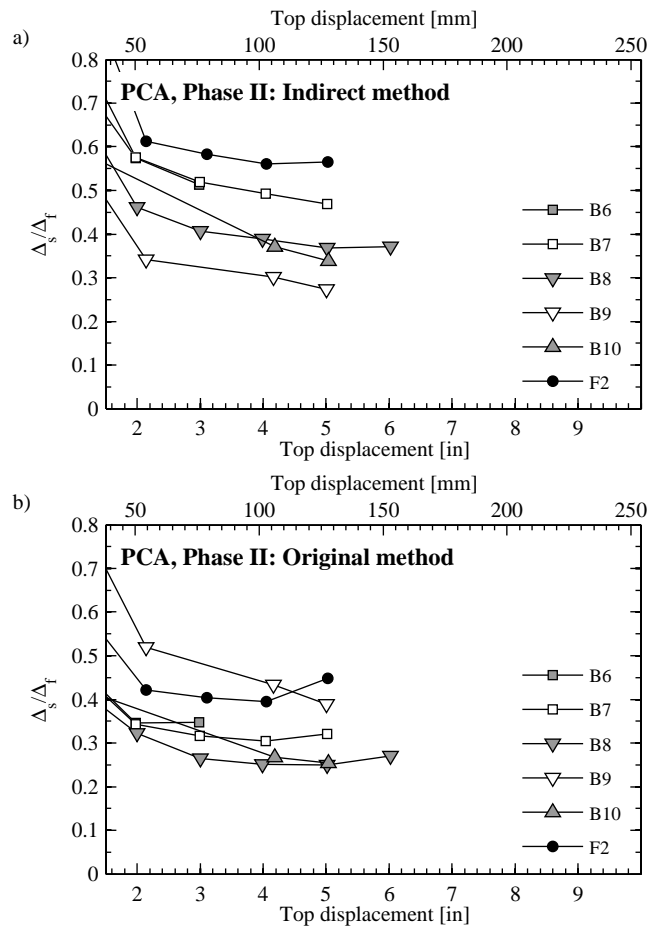


Figure A.2. PCA walls, Phase II: Ratio of shear to flexural displacements as a function of the top displacement if the shear displacements are computed according to the indirect method (a) and the original method (b).

A.3 Tests by Dazio

Dazio *et al.* [1999] tested six rectangular RC walls of similar outer dimensions as the rectangular walls tested by Oesterle *et al.* [1976]. Only the wall thickness was approximately 1.5 times larger than the wall thickness of the PCA walls. The first of the six walls was used to test the experimental setup and a different type of instrumentation than for the remaining five walls was used. In the following only the walls WSH2-6 are considered. The walls were capacity-designed and hence all five walls failed in flexure either due to bar fracture (WSH2, WSH3, WSH5) or due to failure of the compression zone (WSH4, WSH6). Details of the walls are given in Table A.6.

Dazio *et al.* [1999] determined the shear displacements without accounting for the effect of the location of the centre of rotation on the shear deformations (original method, Section 2.6). The shear deformations were recomputed according to Hiraishi's method and the indirect method. Figure A.3 shows the corresponding Δ_s/Δ_f -ratios at the top of the walls ($h = 4.56\text{m}$, WSH6: 4.52m) for displacement ductilities $\mu_\Delta \geq 2.0$; the ratios were computed as the average of the ratios at the first positive and negative peak of one ductility level. Table A.5 summarises the mean ratios. Note that since the sliding displacement at the wall base had not been measured the shear displacements according to the indirect method were estimated as $\Delta_{top} - \Delta_f$. Sliding displacements were also not reported in the test documentation and it is therefore expected that the resulting error in the ratio Δ_s/Δ_f is relatively small. Figure A.3 shows the Δ_s/Δ_f -ratios at the top of the walls ($h = 4.56\text{m}$, WSH6: 4.52m) for displacement ductilities $\mu_\Delta \geq 2.0$. The ratios are considerably smaller than the ratios observed for the PCA-walls.

Table A.5. Dazio: Comparison of ratios of shear to flexural deformations for the different methods of evaluating the shear displacements.

	$\frac{\Delta_{s1}}{\Delta_f}$	$\frac{\Delta_{s2}}{\Delta_f}$	$\frac{\Delta_{s3}}{\Delta_f}$
WSH2	0.09	0.13	0.14
WSH3	0.13	0.22	0.16
WSH4	0.08	0.17	0.13
WSH5	0.05	0.12	0.10
WSH6	0.09	0.15	0.14
Δ_{s1}	Computed according to Hiraishi [1984]		
Δ_{s2}	Indirect method: $\Delta_{s2} = \Delta_{top} - \Delta_f$		
Δ_{s3}	Original method		

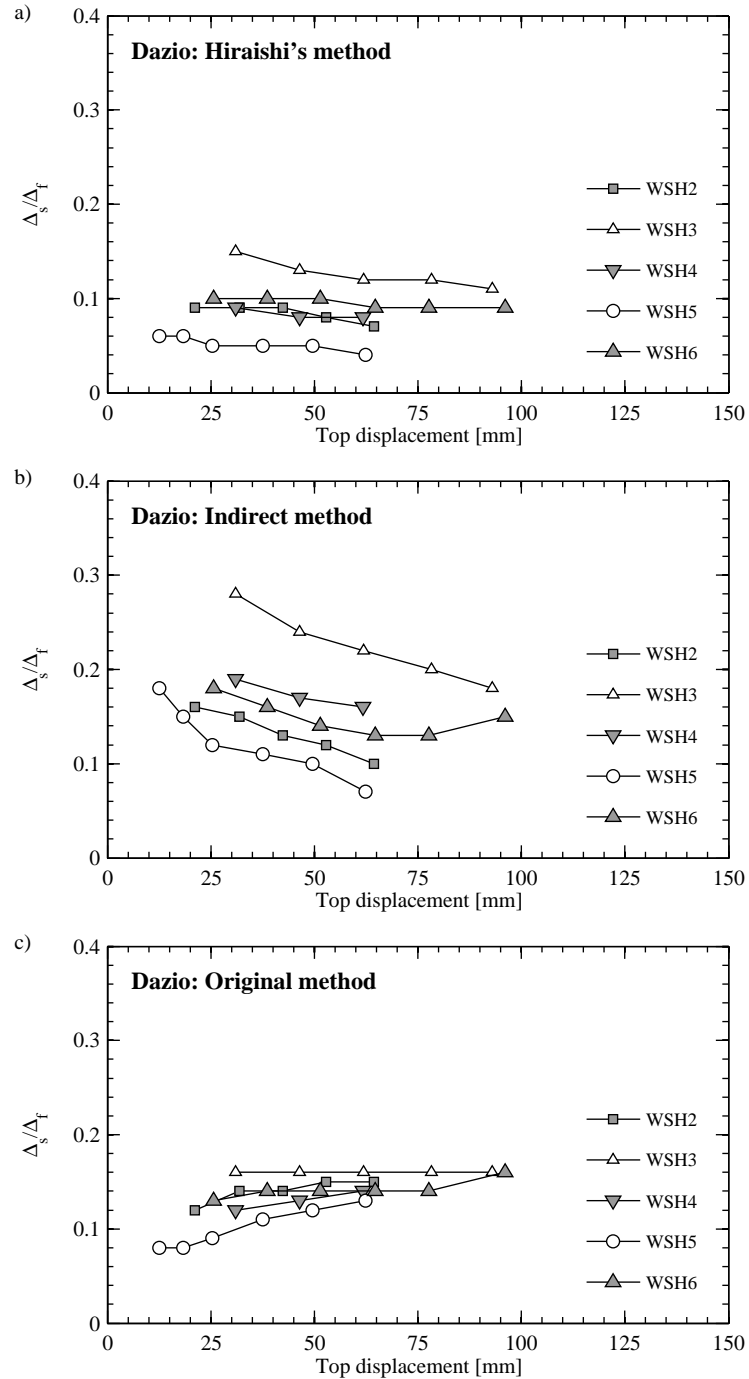
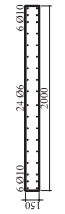
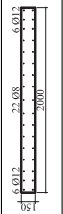
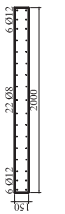
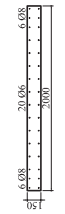
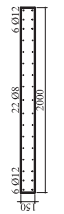


Figure A.3. Dazio: Ratio of shear to flexural displacements as a function of the top displacement if the shear displacements are computed according to Hiraishi's method (a), the indirect method (b) and the original method (c).

Table A.6. Dazio *et al.* [1999]: Characteristics of walls WSH₂-WSH₆.

Specimen	Reinforcement layout	ρ_t [%]	ρ_{web} [%]	ρ_h [%]	ν^1 [-]	Description	Failure Mode
WSH ₂		0.54	0.30	0.25	5.0	Boundary elements are confined but not very strong (i.e. relative small vertical reinf. ratio).	First fracture of web reinforcing bar during cycle of $\mu_\Delta = 5.0$ (limited ductility of web reinforcement); buckling of the boundary reinforcement at $\mu_\Delta = 5.0$; failure due to fracture of boundary reinforcement at $\mu_\Delta = 6.0$
WSH ₃		0.82	0.54	0.25	5.0	Confined and strong boundary elements.	Onset of buckling of the boundary reinforcement at $\mu_\Delta = 5.0$; fracture of the boundary reinforcement at $\mu_\Delta = 6.0$
WSH ₄		0.82	0.54	0.25	5.0	Difference to WSH ₃ : no confinement, shear reinforcement has no end hooks.	Onset of buckling of the boundary reinforcement at $\mu_\Delta = 3.0$; at $\mu_\Delta = 4.0$ the crushing of the concrete in the compression zone led to a reduction of the internal lever arm and hence to a reduction in the moment capacity (point of failure).
WSH ₅		0.39	0.27	0.25	11.0	Boundary elements are confined but not very strong.	At $\mu_\Delta = 4.0$ fracture of the first longitudinal reinforcing bars in the web and buckling of the boundary reinforcement; failure due to fracture of boundary reinforcing bar.
WSH ₆		0.82	0.54	0.25	11.0	Boundary elements are confined and strong.	Onset of buckling of the boundary reinforcement at $\mu_\Delta = 6.0$; failure due to failure of the confined compression zone (fracture of confining reinforcement).

A.4 Tests by Hines

Hines tested eight walls with strong boundary elements [Hines *et al.*, 1999, 2002b]. All walls had similar shapes but different web lengths, web widths and wall heights. The specimens also differed in horizontal and vertical reinforcement ratios and axial load ratios. All specimens were subjected to a symmetric cyclic loading history with three cycles at each displacement level. Testing was divided into three phases; two of the eight walls were tested during Phase I and three walls each during Phase II and III. The objective of Phase I was to validate for walls with strong boundary elements the plastic hinge analysis approach as well as existing estimates for plastic hinge lengths. The two walls tested within this phase were identical apart from the shear reinforcement ratios. The units of Phase II were designed to fail in three different modes, i.e. flexural failure, shear failure due to inadequate transverse reinforcement and shear failure due to web crushing. Phase III of the test series was used to investigate further the aspect of web crushing of walls with boundary elements. For all three phases, Hines evaluated the different displacement components and included graphs in the tests reports which showed the different displacement components at peak displacements during the first cycle of one displacement level. Since the data was not available in electronic format graphs from the test reports were scanned in and the data points were read from these graphs.

Unit 2B failed as intended due to excessive transverse strains. As a consequence, the ratios of shear to flexural displacement were very large (ratios varied between $\Delta_s/\Delta_f = 0.4 - 2.3$). The focus of this study is to determine shear displacements for walls that did not fail in shear. The wall 2B will hence not be considered in this study. For the remaining walls the Δ_s/Δ_f -ratios for the original and the indirect method are plotted in Figure A.4; the mean ratios for the two methods are compared in Table A.7. When computing the mean Δ_s/Δ_f -ratio for a wall, ultimate cycles for which the Δ_s/Δ_f -ratio increased significantly were disregarded. Also excluded were ratios of small cycles if they differed strongly from those of larger cycles. As outlined in the introduction to this appendix, the indirect method of computing the shear displacements was the preferred method of computing the shear displacements. For the sake of completeness, also the Δ_s/Δ_f -ratios based on the shear displacements computed according to the original method are included here. The comparison between the Δ_s/Δ_f -ratios for the indirect and original method showed that they only differed significantly for test units 1A and 1B. For these two test units Hines *et al.* [1999] stated that instruments in the upper part of the wall were missing hence both flexural and shear deformations were underestimated; the indirect method therefore resulted in misleading ratios. Hence, for test units 1A and 1B the Δ_s/Δ_f -ratios according to the original method will be used in the study in Chapter 5. For all subsequent test units, the instrumentation was improved and hence the Δ_s/Δ_f -ratios according to the indirect method will be used in Chapter 5.

Table A.7. Hines: Comparison of ratios of shear to flexural deformations for different methods of evaluating the shear displacements.

	$\frac{\Delta_{s2}}{\Delta_f}$	$\frac{\Delta_{s3}}{\Delta_f}$
1A	0.27	0.10
1B	0.43	0.10
2A	0.25	0.26
2B	1.69	1.32
2C	0.46	0.45
3A	0.27	0.30
3B	0.26	0.27
3C	0.25	0.23

Δ_{s2} Indirect method: $\Delta_{s2} = \Delta_{top} - \Delta_f$
 Δ_{s3} Original method

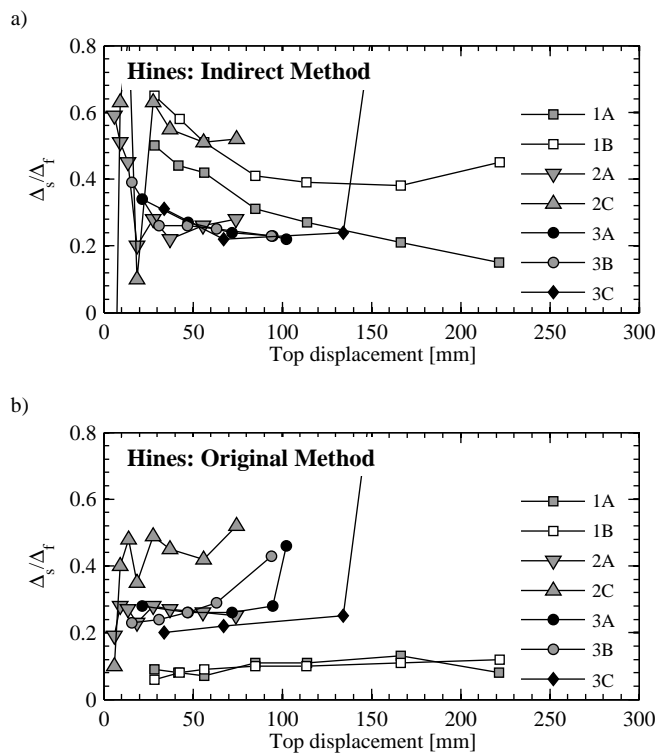
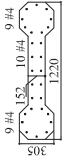
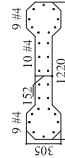
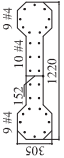
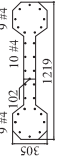
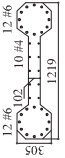
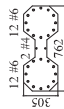
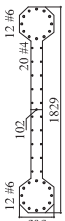


Figure A.4. Hines: Ratio of shear to flexural displacements as a function of the top displacement if the shear displacements are computed according to the indirect method (a) and the original method (b).

Table A.8. Hines: Characteristics of walls with highly-confined boundary elements [Hines *et al.*, 1999, 2002b].

Spec.	Reinforcement layout	ρ_t [%]	ρ_{web} [%]	ρ_h [%]	ν [-]	Description	Failure Mode
1A		1.44	1.39	0.61	9.0	Transverse steel designed for section overstrength; $H = 4.93\text{m}$.	First bar fracture during $\mu_\Delta = 6.0$ cycles (bar fracture without having buckled before); during the cycles at $\mu_\Delta = 8.0$ the concrete of the boundary element degraded significantly when in tension; this led to a reduction of the internal lever arm when the load was reversed (point of failure).
1B		1.44	1.39	0.21	8.1	Similar to unit 1A but transverse steel designed for shrinkage control only; $H = 4.93\text{m}$.	Onset of bar buckling during third cycle of $\mu_\Delta = 6.0$; bar fracture during cycles at $\mu_\Delta = 8.0$ which ultimately led to failure.
2A		1.44	1.39	0.61	9.4	Designed to fail in flexure; $H = 2.44\text{m}$.	Onset of bar buckling during the first cycle of $\mu_\Delta = 6.0$; first bar fractured during second cycle of $\mu_\Delta = 8.0$ which led to failure during the third cycle of $\mu_\Delta = 8.0$.
2C		1.64	2.08	0.61	12.0	Designed to fail due to web crushing; Similar to 2A but smaller web thickness; $H = 2.44\text{m}$.	Onset of bar buckling during cycles at $\mu_\Delta = 6.0$ leading to bar fracture during cycles at $\mu_\Delta = 8.0$.
3A		3.42	1.15	1.38	8.4	Similar to unit 2C but larger longitudinal reinforcement ratio; $H = 3.05\text{m}$.	Sudden web crushing failure during first cycle of $\mu_\Delta = 5.0$.
3B		4.01	0.92	1.38	8.4	Similar to unit 3A but smaller height; $H = 1.91\text{m}$.	Sudden web crushing failure during first cycle of $\mu_\Delta = 6.0$ (cycles at $\mu_\Delta = 5.0$ were omitted).
3C		2.92	1.15	1.38	8.4	Similar to unit 3A but longer wall; $H = 4.57\text{m}$.	Sudden web crushing failure during second cycle of $\mu_\Delta = 4.0$. Loading was continued up to $\mu_\Delta = 5.0$ although the web concrete had degraded extensively.

A.5 Ispra-Tests on U-shaped walls

The three U-shaped walls that were tested in Ispra (Section 3.1) were instrumented with 98 devices measuring local and global deformations as well as forces. Unfortunately the sliding displacements along the wall base were not measured and there were also no continuous chains of LVDTs along the edges, which could be used for computing the flexural deformations. The provided instruments measuring vertical displacements along the edges did not form continuous chains and for different heights the measurements were taken at different positions in plan. The available instruments measured the deformations between $h = 0 - 0.28\text{m}$, $h = 0 - 0.78\text{m}$, $h = 0 - 2.3\text{m}$, $h = 1.3 - 2.6\text{m}$ and $h = 0 - 3.6\text{m}$ which renders it necessary to subtract readings to determine for example the average strain between $h = 0.28 - 0.78\text{m}$ (note: for the first test in the Y -direction the vertical spacings were slightly different). The varying location as well as the subtraction of small deformations introduces an error, which magnitude is difficult to determine. Nevertheless, the measurements were used to compute the flexural displacements Δ_f at the top of the wall. As an alternative it was investigated to determine the shear displacements from the diagonal LVDTs that covered the three outer faces of the U-shaped walls (each face was equipped with two crosses of LVDTs). Unfortunately, the lower diagonals were connected to the foundation and measured deformations across the base crack. It is believed that this distorts the shear measurements (see also Section A.1). In addition, due to the lacking chain of vertical readings, it was not possible to compute the shear deformations following the method by Hiraishi [1984]. Hence, both the computation of the flexural and the shear deformations will be biased and it is difficult to judge whether the ratio Δ_s/Δ_f should be better computed as $(\Delta_{top} - \Delta_f)/\Delta_f$ or as $\Delta_s/(\Delta_{top} - \Delta_s)$. For the two approaches the resulting ratios are given in Table A.9. All values were computed for a top displacement of 40mm, which corresponded approximately to a displacement ductility of 2.0; for most directions of loading later readings seemed unreliable. In many cases the ratios obtained from the two approaches are quite similar while in a few cases the difference is more significant (e.g. Position F, West and East flange). To be consistent with the other test series in this database the ratio based on the flexural displacement Δ_f is used within this study.

A.6 Tests of TUA and TUB

The ratios of shear to flexural displacements for TUA and TUB were presented in Section 4.4.1. In Table 4.5 of this section the ratios according to the three different experimental methods of evaluating the shear displacements were presented. For the empirical study the ratios based on Δ_{s2} , i.e. the shear displacements according to the indirect method, were used. Details on the section analysis of TUA and TUB can be found in Section 6.1.1.

Table A.9. Ispra: Δ_s/Δ_f -ratios for the different wall sections for different directions of loading (flange labels correspond to those of TUA and TUB).

			$\frac{\Delta_s}{\Delta_f} = \frac{\Delta_s}{\Delta_{top} - \Delta_s}$	$\frac{\Delta_s}{\Delta_f} = \frac{\Delta_{top} - \Delta_f}{\Delta_f}$
Ispra X	Position A, B	Web	0.28	0.31
Ispra Y	Position C	Flanges	0.16	0.12
	Position D	Flanges	0.19	0.12
Ispra XY	Position E	Web	0.95	0.78
		West flange	-0.02	0.05
		East flange	0.12	0.06
	Position F	Web	0.28	0.31
		West flange	0.54	0.20
		East flange	0.14	0.27

A.7 Summary of quantities used for the empirical study

For the empirical study on the ratios of shear to flexural displacement that was presented in Section 5.1 a number of experimental and analytical quantities were used. These are defined in the following and summarised in Table A.10:

- V_{max} : Maximum reported shear force.
- θ : Cracking angle towards the vertical; if the cracking angle was not reported or could not be determined from photographs a value of 45° was assumed.
- L_{ph} : The plastic hinge length was estimated using Equation 2.12.
- c/l_w , ε_m , φ : These quantities were determined from section analyses; c/l_w is the normalised compression zone depth, ε_m the strain at the wall centre and φ the curvature. The three quantities were evaluated at the point of nominal moment, i.e. when the steel strain reached 1.5%. For the walls that were loaded uni-axially the section analyses were carried out using the program Response2000 [Bentz, 2001], for the U-shaped walls the program Opensees [Mazzoni *et al.*, 2005] was used. Although Response2000 offers the option to include the effects of shear strains, these were neglected when computing the moment-curvature relationships, i.e. the sections were analysed for zero shear forces, a constant axial load and an incrementally increasing bending moment about the major axis.
- P : For rectangular, barbelled and flanged walls P is the total axial load applied to the wall. For the U-shaped walls P was determined separately for the two flanges and the web. For a web or flange N was determined by integrating over the axial stresses in the

concrete and reinforcement fibres of the particular wall section. The axial stresses were obtained from the section analysis at the point of nominal moment. The area of the web and the flanges both included the corner area; hence the sum of axial forces on the web and the two flanges does not correspond to the total applied axial force.

- f'_c : The concrete cylinder strength at the day of testing.
- Δ_s/Δ_f : Mean ratio over cycles for which the ratio was approximately constant (exceptions for PCA, Phase I and Ispra test units were discussed in Section 5.1.1).

Table A.10. Summary of experimental and analytical quantities used for the empirical study on the ratio of shear to flexural displacements for RC walls.

Test Serie	Specimen	V_{max} [kN]	θ [°]	L_{ph} [m]	c/l_w [-]	ε_m [10 ⁻³]	φ [1/km]	P [kN]	f'_c [MPa]	Δ_s/Δ_f [-]
PCA, Phase I	R1	118	64	0.85	0.09	6.68	8.55	34	44.75	0.15
	R2	217	62	0.87	0.11	6.43	8.55	34	46.4	0.27
	B1	271	49	0.87	0.07	6.96	8.55	47	53.0	0.21
	B3	276	54	0.87	0.07	6.95	8.55	47	47.3	0.33
	B2	704	45	0.91	0.10	6.45	8.55	47	53.6	0.45
	B5	762	50	0.91	0.10	6.34	8.55	47	45.3	0.47
	F1	836	43	0.87	0.07	7.06	8.55	52	38.4	0.47
PCA, Phase II	B6	825	40	0.93	0.16	6.06	9.40	932	21.8	0.54
	B7	980	37	0.94	0.14	6.49	9.40	1200	49.3	0.53
	B8	978	35	0.93	0.14	6.38	9.40	1200	42.0	0.40
	B9	977	34	0.93	0.14	6.43	9.40	1200	44.1	0.31
	B10	775	43	0.90	0.13	6.69	9.40	1200	45.6	0.35
	F2	887	38	0.87	0.09	6.70	8.55	1190	45.6	0.58
Dazio	WSH2	359	52	0.81	0.14	6.39	8.95	691	40.5	0.13
	WSH3	451	38	0.75	0.17	5.95	8.96	686	39.2	0.22
	WSH4	441	40	0.71	0.18	5.79	8.96	695	40.9	0.17
	WSH5	436	53	0.76	0.19	5.57	8.96	1470	38.3	0.12
	WSH6	592	37	0.71	0.20	5.44	8.96	1480	45.6	0.15
Hines	1A	320	45	0.77	0.19	5.88	15.4	881	38.1	0.10
	1B	310	35	0.77	0.18	6.02	15.4	881	42.8	0.10
	2A	600	45	0.57	0.19	5.85	15.4	881	36.6	0.25
	2C	600	35	0.58	0.20	5.55	15.4	881	31.1	0.46
	3A	800	38	0.67	0.19	5.85	15.4	761	40.9	0.27
	3B	685	38	0.48	0.25	4.83	25.2	601	40.9	0.26
	3C	980	40	0.91	0.21	5.44	10.2	988	40.9	0.25
TUA	Pos. A, B	456	40	0.54	0.06	7.2	12.6	-215	77.9	0.25
	Pos. C	208	40	0.47	0.12	6.8	16.8	483	77.9	0.143
	Pos. D	181	40	0.47	0.06	7.3	15.8	-357	77.9	0.166
	Pos. E, web	294	45	0.54	0	9.5	8.4	-628	77.9	0.28
	Pos. E, W-fl.	265	30	0.47	0.23	1.6	6.8	1700	77.9	0.26
	Pos. E, E-fl.	55	45	0.47	0	11.3	6.8	-738	77.9	-0.06
	Pos. F, web	401	40	0.54	0.19	3.4	8.4	1145	77.9	0.32
	Pos. F, W-fl.	62	50	0.47	0	11.3	6.8	-739	77.9	0.43
	Pos. F, E-fl.	157	45	0.47	0.27	1.6	6.8	1282	77.9	0.15
TUB	Pos. A, B	434	40	0.531	0.06	7.2	12.6	-215	54.7	0.38
	Pos. C	212	40	0.46	0.17	6.2	17.7	498	54.7	0.2
	Pos. D	176	45	0.46	0.06	7.2	15.7	-291	54.7	0.22
	Pos. E, web	303	43	0.53	0	9.4	8.8	-643	54.7	0.63
	Pos. E, W-fl.	260	25	0.46	0.33	0.7	7.1	1690	54.7	0.28
	Pos. E, E-fl.	18	45	0.46	0	11.3	7.1	-693	54.7	-0.01
	Pos. F, web	366	40	0.53	0.23	3	8.5	917	54.7	0.35
	Pos. F, W-fl.	98	45	0.46	0	11.4	6.86	-694	54.7	0.76
	Pos. F, E-fl.	118	45	0.46	0.33	1.2	6.86	1180	54.7	0.16
Ispra	Pos. A, B	904	45	0.59	0.11	6.8	13.2	33	23.7	0.31
	Pos. C	760	45	0.54	0.20	5.8	18.5	1279	23.7	0.12
	Pos. D	692	50	0.54	0.11	6.8	13.9	-99	23.7	0.12
	Pos. E, web	564	40	0.59	0	8.9	7.6	-987	20.8	0.78
	Pos. E, W-fl.	460	45	0.54	0.44	0.57	7.6	3637	20.8	0.05
	Pos. E, E-fl.	159	45	0.54	0	9.8	7.6	-1081	20.8	0.06
	Pos. F, web	785	40	0.59	0.32	1.9	7.3	2468	20.8	0.31
	Pos. F, W-fl.	136	45	0.54	0	10.1	7.3	-1082	20.8	0.20
	Pos. F, E-fl.	387	45	0.54	0.37	1.2	7.3	2528	20.8	0.27